SHEAR BAND AND LANDSLIDE DYNAMICS IN SUBMERGED AND SUBAERIAL SLOPES

A Dissertation
Presented to
The Academic Faculty

by

Sihyun Kim

In Partial Fulfillment
of the Requirements for the Degree
Doctor of Philosophy in the
School of Civil and Environmental Engineering

Georgia Institute of Technology
December 2014

SHEAR BAND AND LANDSLIDE DYNAMICS

IN SUBMERGED AND SUBAERIAL SLOPES

Approved by:

Dr. Leonid N. Germanovich, Advisor
School of Civil and Environmental Engineering
Georgia Institute of Technology

Dr. Haiying Huang
School of Civil and Environmental Engineering
Georgia Institute of Technology

Dr. Hermann M. Fritz
School of Civil and Environmental Engineering
Georgia Institute of Technology

Dr. Arash Yavari
School of Civil and Environmental Engineering
Georgia Institute of Technology

Dr. Robert P. Lowell
School of Earth and Atmospheric Science
Georgia Institute of Technology

Dr. Alexander M. Puzrin
Institute for Geotechnical Engineering
Swiss Federal Institute of Technology, Zurich

Date Approved: August 22, 2014

ACKNOWLEDGEMENTS

I am immensely grateful to my advisor Dr. Leonid Germanovich for his generous mentoring and guidance during the work on this thesis. I am very much thankful to Dr. Puzrin for encouraging me in working on such a challenging topic.

I would like to thank my Ph.D. dissertation committee members, Drs. L.N. Germanovich, H.M. Fritz, H. Huang, R.P. Lowell, A.M. Puzrin, and A. Yavari for taking time to read this thesis and providing valuable comments.

I am also indebted to the members of the Rock and Fracture Mechanics Laboratory at Georgia Tech for their technical and personal support throughout this work. I thank Jongwon Choi, Gence Genc, Devon Gwaba, Robert Hurt, Cem Ozan, Pierre Ramondenc, Youngjong Sim, Josh Smith, and Ruiting Wu for many days and nights spent during the several years of my graduate studies. I am particularly grateful to Josh Smith who kindly edited the manuscript of this thesis.

My PhD work at Georgia Tech was supported by the National Science Foundation (grant CMC-0421090), Shell petroleum company, US Department of Energy (contract DE FE0004542), and Georgia Tech - Schlumberger Foundation.

Last but not least, I would like to thank my parents Mr. and Mrs. Kim, wife Jiyeon, son Jongwoo, and daughter Yeonwoo. I am deeply grateful for the invaluable and generous support I have received from them during all these years and for encouraging and supporting me devotedly in my decisions.

TABLE OF CONTENTS

LIST OF TABLES

LIST OF FIGURES

LIST OF SYMBOLS

Symbol	Definition	Equation[1]
	Latin symbols	
A	point with coordinates $x = l_0$, $t = 0$, where the discontinuity initiates (Figure 4a)	
A_w	coefficient of water resistance	(9.3)
$a_1(x)$	function defined by (M.8)	(M.5)
$a_2(x)$	function defined by (M.7)	(M.5)
B	arbitrary point on the discontinuity line AC (Figure 4a)	
B	point on line EF, which corresponds to point Z in Figure G.1a (Appendix G)	
B_1	arbitrary point on the discontinuity line LX in Figure G.1b	
b	slide width (Figure 26, Table A.1)	
c	$(E / \rho_0)^{1/2}$, speed of elastic waves	(2.4)
C	point on plane (x, t) of the first arrival of the discontinuity at $x = 0$ (Figure 4a)	
C	cohesion in the Mohr-Coulomb criterion (Section 8.1)	
C_D	drag coefficient	(K.8)
c_w	$(gH)^{1/2}$, long gravitational (shallow water) wave velocity (Section 9.1)	
d/dx	$\partial/\partial x + (\partial t/\partial x)\partial/\partial t$, total derivative	(4.1)
D	point on the band tip line, $x = l(t)$, which corresponds to point B in Figure 4a	
D	point on line EF, which corresponds to point S in Figure G.1a	
D_1	point on line $x = l_3(t)$ in Figure G.1b	
D_h	hydraulic diffusivity (diffusion coefficient) (Section 2.1)	
E	tangent (plane-strain) elastic modulus	(2.2)
E	point on plane (x, t) where the discontinuity arrives first at the band tip $x = l(t)$ (Figure 4a)	
E	infinite point when the discontinuity does not intersect curve $x = l(t)$ (Figure 4b)	
$\bar{E}$	average plane strain modulus of the sliding layer	(L.1)
E_l	tangent (plane-strain) elastic modulus in loading regime (Section 2.1)	
E_u	tangent (plane-strain) elastic modulus in unloading regime (Section 2.1)	
F	point on plane (x, t) of the second arrival of the discontinuity at $x = 0$ (Figure 4)	
Fr	v / c_w, Froude number (Section 9.1)	
$F(\Gamma)$	energy flux to the crack tip (Figure C.1)	(C.1)
$F(\bar{\Omega})$	$T_w(\bar{\eta})/T_0 = T_w(\gamma_0 c\bar{\Omega})/T_0$, normalized $T_w(\bar{\eta})$	(K.6)

G	arbitrary point (x, t) above the discontinuity line FL in Figure G.1a	
h	slide (layer) thickness	(2.1)
H	point on line $x = l(t)$ corresponding to points Z (Figure 6) and G (Figure F.1)	
H_0	initial depth of the top of the submerged slide (Table A.1, Figure 19)	
h_s	bottom uplift due to the slide motion (Section 9.2)	
h_w	tsunami wave height (Section 9.2)	
$H(x)$	ocean depth as a function of horizontal coordinate, x (Figure 19b and Section 9.1)	
I	point on line AC, which corresponds to point P in Figure E.1b	
I	point on line AC, which corresponds to points P and S in Figure G.1a	
$I(l)$	integral in (4.8)	(4.8)
i, j	indices indicating x, y in (C.1)	(C.1)
J	energy release rate (Section 2.1, and Appendix C)	
J	point on line AC, which corresponds to point R in Figure E.1b	
J	point on line AC, which corresponds to points R and U in Figure G.1a	
J_0	surface energy for a static fracture	(2.12)
J_c	surface energy for a dynamically growing fracture	(2.12)
K	kinetic energy density (per unit volume)	(C.1)
K	arbitrary point (x, t) above the discontinuity line CE in Figure 4b	
k_0	p_0 / σ'_v, earth pressure coefficient at rest	(L.2)
k_E	E / τ_p, ratio of elastic modulus to peak shear resistance	(L.2)
k_p	τ_p / σ'_v, ratio of peak shear resistance to vertical effective stress	(L.2)
k_r	τ_r / τ_p, ratio of residual to peak shear resistance	(L.3)
$l,\ l(t)$	length of the shear band (Figure 2a)	
L	point on plane (x, t) where the discontinuity arrives at the band tip the second time(Figure E.1a)	
L	infinite point when the discontinuity line does not intersect curve $x = l(t)$ again (Figure 6)	
l_0	initial shear band length at mobile equilibrium, critical length	(3.6), (5.3)
l_1	coordinate of the lower end of the shear band (Figure 25)	
l_2	coordinate of the upper end of the shear band (Figure 25)	
l_E	shear band length, which corresponds to point E on (x, t) plane (Figure 4a)	(4.20)
L_f	length of static (or progressively propagating) band at slope failure	(7.9)
l_f	length of dynamic shear band at slope failure	(6.1)
l_f^w	shear band length at slope failure when the water resistance is not negligible	(K.11)
l_L	shear band length, which corresponds to point L (Figure 11)	(6.13)
l_P	shear band length, which corresponds to point P in Figure 4	(4.10)

l_R	shear band length, which corresponds to point *R* in Figure 4	(4.15)
l_s	length of the shear band when it stops propagating	(10.15)
M	arbitrary point on the discontinuity line *CE*, which corresponds to point *K* (Figure 4b)	
n	J_0/J_c, bluntness parameter	(2.12)
N	arbitrary point on the discontinuity line *EF*, which corresponds to point *Z* (Figure 6)	
n_i	external normal to contour Γ (Figure C.1)	
P	local pore pressure in the sliding layer	(2.1)
P	point on the band tip line, $x = l(t)$, which corresponds to point *Q* in Figure 4a	
P	point on the curve, $x = l(t)$, which corresponds to point *S* in Figure G.1a (Appendix G)	
p	pore pressure averaged across the sliding layer	(2.1)
P_0	initial pore pressure in the slope	(B.1)
p_0	effective stress in the infinite slope, s'_x, averaged across the potential sliding layer	(2.2)
p_a	active "pressure" (stress) at the upper end, $x = 0$, of the shear band (Section 2.2)	
p_h	hydrostatic pressure at the upper end, $x = 0$, of the shear band (Section 10.1)	
p_p	passive "pressure" (stress) at the band tip, $x = l_f$, at slope failure (Section 6.1)	(6.1)
Q	arbitrary point (x, t) above the discontinuity line *AC* (but below *CE*) in Figure 4a	
Q_1	arbitrary point (x, t) above the discontinuity line *LX* (but below XX_1) in Figure G.1b	
$q(x)$	auxiliary function defined in (M.8)	(M.8)
R	point on line $x = l(t)$, which corresponds to *K* (Figure 4b), *Z*, *U*, *H* (all in Figure 6), and *G* (Figure F.1)	
RH	notation for point *R* in connection with point *H* (Figure 6)	
RL	notation for point *R* in connection with point *L* (Figure 11)	
RS	notation for point *R* in connection with point *S* (Figure G.1a)	(G.11)
RU	notation for point *R* in connection with point *U* (Figure 6)	
s	curvilinear coordinate along the slope (Figure N.1)	(M.1)
S	point on line $x = 0$, which corresponds to point *K* in Figure 4b	
s_x, s_y, s_{xy}	total stresses in the infinite slope	(B.2)
s'_x, s'_y	effective stresses in the infinite slope (Appendix B)	
$s(x)$	curvilinear coordinate along the shear band, which parallels the slope (Figure N.1)	(N.1)
$S(\lambda)$	$\overline{T_1}(\lambda l_0)/T_0$, normalized value of $T(l)$ averaged along the shear band of	(K.6)

	length l	
t	time	(2.1)
T	τ / E, normalized longitudinal load (along the slope)	(2.4)
T	point on line AC, which corresponds to points W and H in Figure G.1a	
T_0	normalized, homogeneous longitudinal load in the slope	(5.1)
t_0	l_f / c_w, characteristic time (Section 9.1)	
t_1	t / t_0, dimensionless time	(9.6)
$T_1(x)$	$(\tau_g - \tau_r)/E$, dimensionless shear load	(K.1)
t_B	time when the discontinuity arrives at point B ($x = x_B$)	(4.2)
t_E	time of the shear band arrival at point E	(4.20)
t_f	time of the shear band arrival at point $x = l_f$ where passive failure takes place (Section 6.1)	
t_f	dimensionless time during which the slide moves distance l_f (or when the slide of length comes out from the original position) (Section 9.2)	
t_L	time, which corresponds point L (Figure 11)	(6.13)
t_s	dimensionless time during which the slide moves dimensionless distance x_s (or when the slide fully stops)	(9.15)
$T_D(\bar{\eta})$	$C_D \rho_w h \bar{\eta}^2 / (2El)$, effective dimensionless longitudinal load (Appendix K)	
$T_S(\bar{\eta})$	$C_S \rho_w \bar{\eta}^2 / (2E)$, effective dimensionless shear load	(K.8)
$T_w(\bar{\eta})$	$\tau_w(\bar{\eta})/E$, dimensionless water resistance	(K.1)
$\bar{T}(l)$	average value of $T(x)$ along the shear band of length l	(4.8)
u	displacement (along the slope) averaged across the layer	(2.1)
U	elastic energy density (per unit volume)	(C.1)
U	point on $x = l(t)$ corresponding to point Z (Figure 6)	
u	$u_x d_0 / (h c_w)$, dimensionless fluid particle velocity along the x-axis	(9.6)
u_i	displacement components in (x, y) coordinate set (Figure C.1)	
$u_s(x)$	static displacement at point x	(2.6)
u_x	displacement along the slope	(2.1)
u_x	fluid particle velocity along the x-axis (Section 9.2)	
v	dl/dt, velocity of the shear band tip (Figure 2)	(2.7)
v	velocity of slide motion (Section 9.1)	
V	v / c, dimensionless band tip velocity	(5.5)
V	point on $x = 0$ corresponding to point G in Figure G.1a	
$v(t)$	landslide velocity as a function of the position t (Section 9.1)	
$v(x)$	landslide velocity as a function of the position x	(9.2)
v_0	initial velocity of the shear band	(4.14)
v_1	velocity of the shear band tip before it is reached by the discontinuity	(4.5)
V	volume of the material displaced by the slide (Table A.1)	
V_1	v_1 / c	(5.5)

v_2	velocity of shear band tip after it is reached by the discontinuity	(4.18)
V_2	v_2 / c	(G.13)
W	point on $x = l(t)$ corresponding to points H (Figure 6 and Figure F.1) and G (Figure F.1)	
x	coordinate along the slope (Figure 2a)	(2.1)
x	horizontal coordinate (Figure 19b)	
X	point of the third arrival of the discontinuity at $x = 0$ (Figure E.1a)	
x_0	point where $\gamma_s(x)$ changes sign	(10.14)
x_1	x / l_f, dimensionless horizontal coordinate	(9.6)
X_1	an infinite point or point that the discontinuity arrives the third times at the band tip in Figure G.1b	
x_B	physical location of point B along the shear band	(4.2)
x_c	horizontal coordinate of the slide center of mass	(M.1)
x_s	horizontal distance when the slide stops (Section 9.1)	
y	coordinate perpendicular to the slope (Figure 2a)	(2.1)
Y	arbitrary point on the characteristic discontinuity line FL (Figure 11)	
Z	arbitrary point (x, t) above the discontinuity line EF (but below FL) in Figure 6	
z	vertical coordinate (Figure 19b)	

Greek symbols

α	slope angle with respect to the horizontal (Figure 2a)	(B.1)
$\alpha(x)$	slope angle as a function of position x	(N.1)
β	dimensionless drag coefficient	(K.8)
γ	$\partial u/\partial x$, material strain (Section 2.2)	
$\gamma^{\pm}$	limits of γ obtained by approaching a characteristic line from different sides	(3.5)
γ_0	$[2J_0 / (hE)]^{1/2}$, strain level required at the tip of a static band to start propagating	(2.10)
$\gamma_1(l)$	strain at the band tip, $x = l$, before it is reached by the discontinuity at point E (Figure 7a)	(4.9)
$\gamma_2(l)$	strain at the shear band tip, $x = l$, after it is reached by the discontinuity at point E (Figure 7a)	(4.22)
γ_a	$(p_0 - p_a)/E$, strain of active loading at the slide end, $x = 0$	(2.8)
γ_c	$[2J_c / (hE)]^{1/2}$, minimal strain level at the tip of the growing, dynamic shear band (i.e., immediately after it begins growing)	(2.9)
γ_p	$(p_p - p_0)/E$, strain of passive loading at the band tip, $x =$	(6.1)
$\gamma_s(x)$	static strain at point $x \le l$	(2.11)
Γ	simple, closed contour surrounding the band tip (Figure C.1)	
Γ	$-\gamma / \gamma_0$, normalized strain	(4.29)
Γ_1	$-\gamma_1 / \gamma_0$, normalized strain at the band tip, $x = l$, before it arrives at point	(5.8)

	E (Figure 7a)	
Γ_2	$-\gamma_2 / \gamma_0$, normalized strain at the band tip, $x = l$, after it arrives at point E (Figure 7a)	(5.8)
Γ_s	$-\gamma_s / \gamma_0$, normalized static strain	(5.7)
δ	relative shear displacement (slip) along the shear band (Figure 3)	
$\delta\tau$	limit of $\Delta\tau$ when $\xi \to \infty$	(F.3)
$\delta(l, B)$	auxiliary strain function	(E.4)
δ_r	relative shear displacement required for τ_r to develop (Figure 3b)	
$\delta(x)$	Dirac's δ-function	(9.12)
$\bar{\delta}$	characteristic displacement (slip) in the shear band tip zone (Section 8.1)	
Δ_0	magnitude of the discontinuity before it arrives at point E at the band tip	(H.2)
Δ_1	magnitude of the discontinuity after it arrives at point E at the band tip	(H.8)
ΔK	change of kinetic energy density (per unit volume) of the sliding layer, which corresponds to the displacement change Δu	(C.10)
Δl	change of the shear band length when time changes by Δt	(C.7)
ΔP	excess pore pressure on the rupture surface (shear band) (Section 8.1)	
Δp	excess pressure averaged across the sliding layer (Section 8.2)	
Δt	time change, which corresponds to the band propagation by Δl	(C.6)
Δt	difference between the arrival times of the discontinuity and the band tip at the same point (Figure 4b)	(F.1)
Δu	displacement change, which corresponds to the band length change; Δl	(C.6)
ΔU_S	energy dissipated at the tip of the band when it propagates distance Δl	(C.22)
ΔW	increment of work done on the layer above the band over Δu	(C.9)
ΔW_a	increment of work done on the layer above the band by load p_a	(C.7)
ΔW_i	change of elastic (internal) energy density over Δu	(C.15)
ΔW_τ	increment of work done on the layer above the band by load τ	(C.7)
$\Delta\gamma_s$	difference between the tip strains at $x = l_1$ and $x = -l_2$	(10.9)
$\Delta\lambda$	change of the dimensionless failure length after the first arrival of the discontinuity	(6.6)
ε	small parameter	(9.1)
ε_a	$-\gamma_a$, strain of active loading at the slide end, $x = 0$	(L.4)
ε_p	γ_p, strain of passive loading at the band tip, $x = l_f$	(L.4)
η	$\partial u/\partial t$, material velocity (Section 2.2)	
$\eta^{\pm}$	limits of η obtained by approaching a characteristic line from different sides	(3.5)
$\eta_1(l)$	material velocity at the band tip, $x = l$, before it is reached by the discontinuity at point E	(4.9)
$\eta_2(l)$	material velocity at the shear band tip, $x = l$, after it is reached by the	(4.22)

	discontinuity at point E	
η_s	h_s/h, dimensionless varying thickness of the moving slide	(9.6)
$\bar{\eta}(t)$	slide velocity or material velocity, averaged along the band, at time t	(6.7)
κ	$\lambda_f/\Lambda_f = l_f/L_f$, ratio of dynamic and static failure lengths	(7.11)
λ	l/l_0, dimensionless length of the shear band	(5.5)
λ_*	$\gamma_0/(\gamma_a + \gamma_0)$, dimensionless strain parameter	(4.29)
λ_*	$\gamma_0/(\gamma_0 - \gamma_h)$, dimensionless strain parameter in the dynamic Palmer and Rice model [1973] (Figure 24)	(10.2)
Λ_f	L_f/l_0, dimensionless static (or progressively propagating) band length at slope failure	(7.9)
λ_f	l_f/l_0, dimensionless shear band length at slope failure	(6.3)
λ_P	l_P/l_0, dimensionless shear band length, which corresponds to point P	(5.9)
λ_R	l_R/l_0, dimensionless shear band length, which corresponds to point R	(5.10)
μ	coefficient of friction at the slide bottom	(9.2)
μ	coefficient of residual friction (Section 2.2)	
ξ	x/l_0, dimensionless coordinate along the slope	(5.9)
ξ	h_w/h, dimensionless tsunami wave height	(9.6)
ϕ_p	peak friction angle (Section 8.2)	
ρ_0	material density	(2.3)
ρ_w	density of water	(K.8)
σ	x-component of the total stress averaged across the layer	(2.1)
σ_{ij}	stress components in the infinite slope with shear band in (x, y) coordinate set (Figure C.1)	
σ'_v	$-\sigma'_y = (\rho_0 - \rho_w)g\cos\alpha$, effective stress normal to the slope (Section 8.1)	
σ_{xx}	total stress parallel to the slope	(2.1)
τ	ct/l_0, dimensionless time	(4.29)
τ_0	$\tau_g - \tau_r - \tau_w$	(2.3)
τ_1	$\tau_g - \tau_b - \tau_r$, combined distributed gravitational and frictional load	(2.5)
τ_b	$\rho_w g\sin\alpha$, buoyancy load	(2.5)
τ_g	component of the gravitational stress along the shear band (Figure 2a)	(2.5)
τ_p	peak shear resistance (Figure 3)	
τ_r	residual shear resistance (Figure 2a)	(2.5)
τ_w	water resistance on the sediment-water interface	(2.5)
τ_{xy}	shear resistance on the rupture plane or shear band sides (Figure 3)	
τ_*	$\tau_g - \tau_b - \tau_r - \tau_w$, combined distributed gravitational, frictional, and viscous loads in the slope direction (net driving stress)	(2.5)
$\overline{\tau_p}$	average peak shear resistance of the sliding layer	(L.2)
$\overline{\tau_r}$	average residual shear resistance of the sliding layer	(L.2)
ω	process zone size (Figure 2a)	

Ω	$\eta/(c\gamma_0)$, normalized material (slip) velocity	(4.29)
Ω_1	η_1 / γ_0, normalized material velocity at the band tip, $x = l$, it is reached by the discontinuity at point E	(5.8)
$\overline{\Omega}(\lambda)$	$\bar{\eta}(l)/(c\gamma_0)$, dimensionless slide velocity	(6.14)

[1]If a parameter shows in more than one equation, only the first one is listed.

SUMMARY

Submarine landslides, commonly triggered by earthquakes, can generate tsunamis. Subaerial landslides can also be catastrophic in nature, causing human casualties and property damage. This work focuses on landslides associated with shear band that develops beneath the slipping mass. We consider a landslide as a dynamic process when a shear band emerges along the potential rupture surface. Within this band, the shear strength decreases due to the softening behaviour of the particulate material. Material above the band moves downwards, causing the band to propagate dynamically. As a result, the landslide body acquires finite velocity before it begins separating from the substrata, reaches the post-failure stage, displaces material downhill, and generates tsunami. Existing models of tsunamigenic landslides, however, assume zero initial slide velocity.

Previous analyses of the catastrophic shear band propagation in slopes of normally-consolidated and overconsolidated sediments have shown that a relatively short initial failure zone is sufficient to cause a full-scale landslide. For the shear band to propagate, the energy produced in the body by an incremental propagation of the shear band must exceed the energy required for the propagation. This consideration separates the shear band growth into progressive (stable) and catastrophic (dynamic) stages and treats the band growth as a true physical process rather than an instantaneously appearing discontinuity.

For a dynamic shear band propagating parallel to the slope, we obtain the exact, closed-form solution for the band and landslide velocities as well as for the spatial and temporal distributions of strain and material velocity. This solution assesses when the slide fails due to a limiting condition (e.g., passive failure) near the propagating tip of the shear band. We also obtain a simple asymptotic solution, which is compared to the exact solution. The obtained solutions are used in landslide and tsunami height analyses. Our results suggest that the conventional static approach to the slope stability analysis leads to a significant underestimation of the slide size (volume). It appears that the volumes of catastrophic slides can exceed the volumes of progressive slides by nearly factor of two.

CHAPTER 1. INTRODUCTION

1.1. Landslides and their consequences

The term 'landslide' refers to a broad range of processes that result in gravity-assisted, downslope movement of slope-forming materials (Appendix A). The largest landslides known on Earth occurred in the submarine environment and involved $\sim 10^3 - 10^4$ km^3 of sediment [e.g., *Dingle*, 1977; *Nisbet and Piper*, 1998; *Legros*, 2002; *Haflidason et al.*, 2004; *Haflidason et al.*, 2005; *Gee et al.*, 2007]. This is one to two orders greater than volumes displaced by the largest known subaerial landslides [*Legros*, 2002; *Locat and Lee*, 2002; *Masson et al.*, 2006; *Clare et al.*, 2014]. Submarine landslides have been observed in most, if not all, oceanic settings [e.g., *Martinsen*, 1994; *Hampton et al.*, 1996; *Blackman et al.*, 2002], but they are particularly abundant on continental slopes and represent a major mechanism of sediment transfer across continental margins to deep ocean [e.g., *Masson et al.*, 2006; *Lee et al.*, 2007]. Their occurrence, morphology, distribution, scale, and consequences have been discussed in detail by *Moore* [1961; 1977], *Dott* [1963], *Prior and Coleman* [1979], *Prior* [1984], *Coleman and Prior* [1988], *O'Leary* [1991], *Hampton et al.* [1996], *Locat and Lee* [2002; 2009], *Canals et al.* [2004], *Hühnerbach and Masson* [2004], *Masson et al.* [2006], *Lee et al.* [2007], *De Blasio* [2011], *Lu and Godt* [2013], *Talling et al.* [2014], and *Vanneste et al.* [2014] among others. Consequences of submarine landslides include [e.g., *Hampton et al.*, 1996; *Bryn et al.*, 2005; *Masson et al.*, 2006; *ten Brink et al.*, 2007; *Locat and Lee*, 2009; *Vanneste et al.*, 2014] damaging and disappearance of valuable land near the shoreline in populated areas (e.g., by headwords cutting onto land), destabilizing and damaging marine engineering structures (such as offshore platforms and pipelines), breaking telecommunication cables, altering environments (e.g., benthic ecosystems and fishing habitats), and generating tsunamis. Subaerial landslides can also generate tsunamis if the land flows into a body of water [e.g., *Miller*, 1960; *Walder et al.*, 2003] and can be catastrophic, causing human casualties and property damage [e.g., *Cornforth*, 2005; *Cecinato*, 2009; *Chowdhury et al.*, 2010; *De Blasio*, 2011; *Lu and Godt*, 2013]. Landslides that generate tsunamis are called *tsunamigenic*.

Tsunami waves represent a serious hazard for the coastlines of the world [e.g., *Bryant*, 2008; *Joseph*, 2011; *Watts*, 2012; *Dominey-Howes and Goff*, 2013]. Although tsunamis often

occur directly due to coseismic uplift of the seafloor caused by a fault slip [e.g., *Kanamori*, 1972; *Ruff*, 2003; *Stein and Okal*, 2005; *Synolakis and Bernard*, 2006; *Segur*, 2007; *Levin and Nosov*, 2009; *Crozier*, 2010], submarine landslides, triggered by earthquakes, can significantly affect the tsunami wave magnitude [*Plafker et al.*, 1969; *Bardet et al.*, 2003; *Baba et al.*, 2012; *Miyazawa et al.*, 2012; *Satake*, 2012]. On July 17, 1998, for example, the coast of Papua New Guinea was demolished by a 15-m tsunami, generated by a submarine earthquake accompanied by an underwater landslide [*Geist*, 2000; *Heinrich et al.*, 2000; *Tappin et al.*, 2001; *Imamura and Hashi*, 2002; *Synolakis et al.*, 2002; *Levin and Nosov*, 2009]. On December 12, 1992, an earthquake in the Flores Island (Indonesia) triggered a submarine landslide and a subsequent 26-m tsunami [*Hidayat et al.*, 1995; *Imamura et al.*, 1995; *Levin and Nosov*, 2009]. The tsunami caused by the Atacama Earthquake (Chile) on November 11, 1922 was generated by the submarine landslide with earthquake waves as a trigger and earthquake rupture (fault movement) occurred inland, more than 100 km away from the coast [*Gutenberg*, 1939]. This tsunami would not have happened had the landslide had not taken place.

1.2. Slides induced by shear bands

In this work we focus on slides caused by a shear band (discontinuity) that develops below the sliding mass (Appendix A) in submerged [e.g., *Prior and Coleman*, 1979; *Bugge et al.*, 1988; *Gardner et al.*, 1999; *Huvenne et al.*, 2002; *Lee et al.*, 2007; *Locat et al.*, 2009] or subaerial [e.g., *Chowdhury*, 1978; *Skempton*, 1985; *Bertini et al.*, 1986; *Trenter and Warren*, 1996; *D'Elia et al.*, 1998; *Troncone*, 2005; *Urciuoli et al.*, 2007; *Locat et al.*, 2008; *Quinn et al.*, 2011a] slopes. Below, the terms 'landslide' and 'slide' are used interchangeably and are synonymous. 'Failure surface', 'rupture surface', and 'slip surface' are all equivalent to the basal detachment boundary created by shear band propagation sub-parallel to the slope surface during the failure stage (Appendix A and Figure A.2a). Also, 'shear band' is synonymous to 'mode II crack' or 'in-plane shear fracture' with contacting sides. In landslide literature, terms 'progressive' and 'retrogressive' usually indicate the direction of the slide development, that is, downslope and upslope, respectively. The term 'progressive', however, can also be used as the opposite to 'catastrophic' meaning that progressive shear band propagation is quasi-stable (slow) [e.g., *Bernander*, 2011] in contrast to the catastrophic (fast) growth when dynamic effects (inertia

terms) are important. How fast the shear band propagates is of main interest in this work. Hence, we use the temporal meaning of term 'progressive' without regards to the direction of band growth.

(a)

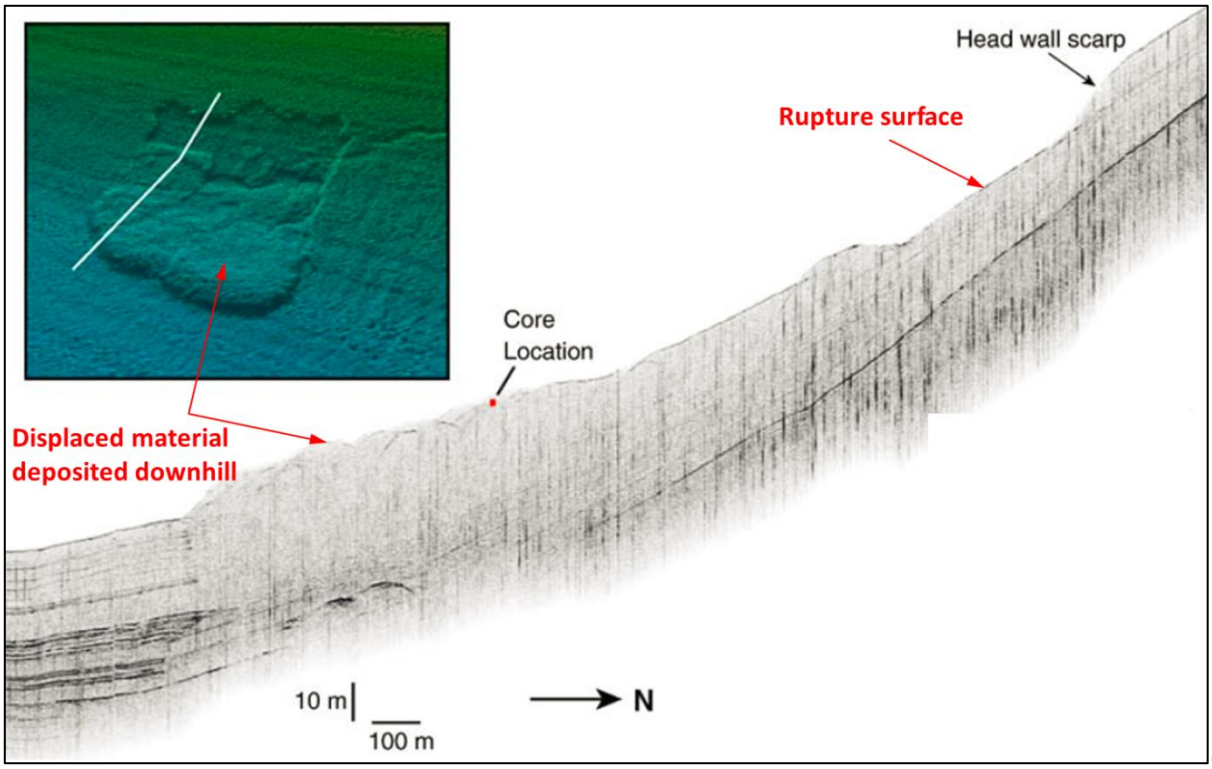

(b)

Figure 1. (a) Sidescan sonar image from *Martel* [2004] of the Gaviota slide, offshore Santa Barbara, CA [*Lee and Edwards*, 1986; *Edwards et al.*, 1995; *Hampton et al.*, 1996; *Greene et al.*, 2006; *Schwehr et al.*, 2007; *Blum et al.*, 2010]. The slope is interpreted as undeformed to the left (west) of the slide, while the fracture (≈8 km long [*Schwehr et al.*, 2006]) to the right (east) of the slide (marked by arrows spaced by ≈4 km) is produced by the developing rupture surface and represents the future location of a head scarp [*Martel*, 2004]. (b) A CHIRP [*Schock et al.*, 1989] seismic profile image of the Gaviota Slide in the Santa Barbara basin, southern California [*Schwehr et al.*, 2007].

A landslide example is shown in Figure 1, which depicts the Gaviota slide on the northern slope of the Santa Barbara basin [*Edwards et al.*, 1995; *Schwehr et al.*, 2006; *Schwehr et al.*, 2007; *Blum et al.*, 2010]. The subhorizontal crack (Figure 1a) extends for ≈8km east-west along the slope [*Schwehr et al.*, 2006]. This is interpreted as the site of slide initiation due to the shear surface that starts at the crack and develops downslope subparallel to the slope surface [*Martel*, 2004]. Both the crack and the Gaviota slide are considered to be seismically triggered [*Edwards et al.*, 1995; *Blum et al.*, 2010].

Wright and Rathje [2003] provided an overview of earthquake-related triggering mechanisms of submarine and shoreline slope instabilities. They distinguished between direct (e.g., acceleration- or liquefaction-induced sliding) and indirect (e.g., delayed failure due to the excess pore water pressure) triggering mechanisms. The general tendency, however, is to assume that the landslide fails simultaneously along the entire rupture surface [*Denlinger and Iverson*, 1990; *Harbitz*, 1992; *Hampton et al.*, 1996; *Leynaud et al.*, 2004; *Strasser et al.*, 2007], which can be tens of kilometres long [e.g., *Jansen et al.*, 1987; *Bugge et al.*, 1988; *Dawson et al.*, 1988; *Bondevik et al.*, 2005; *Gee et al.*, 2007]. While justified in modelling faulting-induced tsunamis [e.g., *Hammack*, 1973; *Ruff*, 2003; *Okal and Synolakis*, 2004; *Segur*, 2007], this assumption may have led to an underestimation of the tsunami wave height in numerical simulations of landslide-induced tsunamis [*Harbitz*, 1992; *Bondevik et al.*, 2005], which can be seen from the following argument.

Consider the landslide as a slope failure process (Appendix A) when a shear band (discontinuity) emerges along the potential rupture surface [e.g., *Palmer and Rice*, 1973; *Chowdhury*, 1978; *Puzrin and Germanovich*, 2005a; *Bernander*, 2011]. Within the band, the shear strength drops due to the softening behaviour of the particulate material. The sediment above this weakened zone moves downwards, causing the shear band to propagate and creating the rupture surface (Figure A.2a in Appendix A). When the shear band reaches a sufficiently large size, the propagation becomes dynamic (fast) and is supported by the energy stored in the body and released during the propagation [*Palmer and Rice*, 1973]. This dynamic propagation produces a finite slide velocity already before the slide separates from the substrata (Figure 1a) and moves downslope (Figure 1b), displacing water and generating a

tsunami (Figure A.2b). The resulting tsunami magnitude may, therefore, be higher than in the case of zero initial slide velocity assumed by the existing models of tsunamigenic landslides [e.g., *Pelinovsky and Poplavsky*, 1996; *Watts*, 1998; *Ward*, 2001; *Levin and Nosov*, 2009].

When the shear band begins growing dynamically, the induced dynamic wave propagates in the overlaying sediment layer away from the band tip and unloads the layer near the tip. Hence, the failure in the static band (passive or active; Figure A.2a) is expected to take place for a shorter band length than in the dynamic case. Therefore, the static approach can result in an underestimation of the displaced volume, and the magnitude of this underestimation is unknown *a priori*. Underestimating the displaced volume, in turn, could result in underestimating the tsunami magnitude [e.g., *Murty*, 2003; *Haugen et al.*, 2005; *Lovholt et al.*, 2005] or the slide damage potential.

Therefore, it is tempting to evaluate the dimensions and velocities of a dynamic landslide and the corresponding shear band. An attempt to assess the landslide velocity at failure was made by *Puzrin et al.* [2010] who used a simplified approach to the solution of the dynamic problem for the layer of sediment moving above the shear band. They modeled the layer as a solid block that slides downhill and increases in length as the shear band grows. They assumed that all points in the sliding block have the same velocity, which is a function of time. In other words, *Puzrin et al.* [2010] considered the layer as being a rigid (with respect to motion) yet deformable (with respect to loading) body with displacements and particle velocities depending on time, but not on the space coordinate. By adding the inertia terms and water resistance to the steady-state formulation of *Palmer and Rice* [1973] and *Puzrin and Germanovich* [2005a], they computed the stress, strain, and particle velocity in the moving layer. *Puzrin et al.* [2010] did not include, however, the elastic waves generated by a dynamically growing shear band. As a result, the block length (mass) increased faster than the resistance to the block growth, so the sliding material continued to accelerate. This is why they obtained shear band and slide velocities that were unbound in time.

In this work, we have not invoked the simplifying assumptions utilized by *Puzrin et al.* [2010]. Our analysis is based on the energy balance approach of *Palmer and Rice* [1973], which has been the basis for understanding the progressive shear band growth in natural slopes [e.g.,

Chowdhury, 1978; *McClung*, 1979; *Farrell*, 1984; *Martel*, 2004; *Puzrin et al.*, 2004; *Puzrin and Germanovich*, 2005b; a; *McClung*, 2009; *Chowdhury et al.*, 2010; *Quinn et al.*, 2011a; *Dey et al.*, 2012; *Quinn et al.*, 2012]. For a shear band to propagate, the energy surplus produced in the body during an incremental propagation should exceed the energy required for this propagation [*Rice*, 1968; *Cherepanov*, 1979; *Broberg*, 1999]. The main advantage of this approach is that it distinguishes explicitly between the progressive (quasi-static) and catastrophic (dynamic) stages of the band propagation (Figure A.2b) and treats the band growth as a true physical process rather than an instantaneously appearing rupture surface. Analysis of the band propagation in a submerged slope, built of normally-consolidated clays, has shown that a relatively short initial weakness zone [*L'Heureux et al.*, 2014; *Locat et al.*, 2014] or progressively-propagating shear band is sufficient to cause a full-scale landslide [*Puzrin et al.*, 2004; *Puzrin and Germanovich*, 2005a].

Therefore, the dynamic problem for a propagating shear band is formulated below within the framework of the *Palmer and Rice*'s [1973] approach. We obtain the exact solution for the landslide size and velocity as well as for the distributions of strain and material (slip) velocity in space and time. The dynamic version of the *Palmer and Rice*'s [1973] model appears to be a particular case of our formulation. We also obtain a simple asymptotic solution and check its accuracy by comparing it to the exact solution. We then use the obtained solutions in the analysis of several landslide examples and discuss the effects of the landslide size and velocity on tsunami wave height (in the case of submerged slopes).

1.3. Goals and objectives

The main goal of this work is to understand the shear band mechanism of submarine and subaerial landslides. Specifically, we consider the scenario when the shear band growth in a slope separates the sliding material, triggering a tsunami if the slope is submerged. The principal objectives of this work are to

- identify the criterion for the shear band propagation in a slope;
- develop a model describing the catastrophic (unstable) propagation of a shear band;
- identify post-failure parameters such as slide length and velocity at failure; and

- compare generated tsunami heights from static and dynamic submarine landslides.

The structure of this thesis is as follows.

Chapter 1 briefly describes the background and motivation for this study.

Chapter 2 introduces a dynamic model with the governing equations of the shear band propagation in a slope and the onset of band growth.

Chapter 3 formulates the initial-boundary value problem for dynamic shear band propagation near the boundary.

Chapter 4 presents the exact closed-form solution of this initial-boundary value problem and obtains the material velocity and strain at the arbitrary spatial and temporal coordinates.

Chapter 5 provides a quantitative example in the case of homogeneous loading along the band length.

Chapter 6 calculates the slide length and velocity at failure.

Chapter 7 obtains an asymptotic solution and estimates the effect of water resistance on the band length and slide velocity.

Chapter 8 employs the obtained solutions in discussion of several landslide examples including the Gaviota slide in the Santa Barbara basin, Currituck slide on the western North Atlantic continental slope, and Storegga slide on the mid-Norwegian continental margin.

Chapter 9 assesses the motion of the submerged landslides and generated tsunami heights.

Chapter 10 discusses the obtained dynamic solution in context of the direction of band growth (upslope or downslope), mechanism of the band growth arrest caused by the variable slope angle, and applicability of the developed model to landslides of more realistic geometry.

Chapter 11 summarizes main results obtained in this dissertation.

CHAPTER 2. SHEAR BAND IN AN INFINITE SLOPE

2.1. One-dimensional model

Landslides may develop by the shear rupture propagating both in the upslope and downslope directions [e.g., *Gardner et al.*, 1999; *Quinn et al.*, 2011a], although downslope propagation (Figure 1; see also Figure 17 in Section 8.3) is probably more common**.** For example, in a saturated poroelastic body, interaction with the free surface provides a downslope directionality to the surface-parallel rupture, propagating in the undrained, dynamic regime [*Bradshaw et al.*, 2010; *Viesca*, 2011]. Consider, therefore, a shear band of length l at depth h, parallel to the surface of the infinite slope, which is inclined at angle α to the horizontal (Figure 2a). Starting from some *initial weak zone* (e.g., Figure A.2a in Appendix A), the shear band (rupture) propagates down the slope and parallel to the surface.

Various mechanisms such as earthquake-triggered liquefaction [*Newmark*, 1965; *Seed*, 1979; *Wright and Rathje*, 2003; *Nadim et al.*, 2007], methane hydrate decomposition [*Sultan et al.*, 2004; *Masson et al.*, 2006; *Xu and Germanovich*, 2006; 2007; *Scholz et al.*, 2011], overpressure (i.e., pressure above hydrostatic) induced by rapid sedimentation [*Locat and Lee*, 2002; *Flemings et al.*, 2008a; 2008b; *Dugan and Stigall*, 2010; *Flemings et al.*, 2012] (see also *Viesca and Rice* [2012] for a quantified account), and local fluid fluxes [*Screaton et al.*, 1990; *Dugan and Flemings*, 2000; *Viesca and Rice*, 2012] may cause the initial weak zone. The landslide evolution, therefore, may be rather complex (Appendix A). In this work, we focus on the stage of dynamic (catastrophic) growth of the shear band that underlines the landslide. Hence, we simply assume that the dynamic stage is preceded by the stage of stable (progressive) growth until the band size becomes equal to some *critical length*, l_0 (yet to be determined). After that, the shear band propagates dynamically along the slope surface (Figure 1 and Figure 2a), eventually causing the global landslide [*Puzrin et al.*, 2004; *Puzrin and Germanovich*, 2005a; *Quinn et al.*, 2011a; *Dey et al.*, 2012].

The value of l_0 is defined based on the static analysis using the energy balance criterion [*Palmer and Rice*, 1973; *Rice*, 1973; *Puzrin et al.*, 2004; *Puzrin and Germanovich*, 2005a; *Quinn et al.*, 2011a; *Dey et al.*, 2012]. The initial weak zone does not need to be of the observed landslide length, l_f, which can be up to $\sim 10^2$ km [*Jansen et al.*, 1987; *Bugge et al.*, 1988; *Dawson*

et al., 1988; *Bondevik et al.*, 2005]. It is sufficient, instead, that the initial zone is equal to or exceeds the critical length, l_0, which is smaller than l_f.

We also assume that the length, l, of the shear band is sufficiently larger than its depth, h, which, in turn, is much greater than the size, ω, of the process zone (Figure 2a) at the band tip, $x = l(t)$ (i.e., $l >> h >> \omega$). Within this small zone, the shear resistance, τ_{xy}, of the material gradually decreases from the peak, τ_p, to the residual, τ_r, value as a function of the relative slip displacement [*Palmer and Rice*, 1973] (Figure 3b). Everywhere else in the band, the shear resistance is constant and equal to τ_r. At the tip of the process zone, the shear resistance is equal to the peak value, τ_p. The downhill component, τ_g, of the gravitational stress is the driving force that causes the material above the band to move downwards, which makes the band propagate along the slope (Figure 2a), until the slope fails (Section 6.1). If the band grows in a submerged slope, the slope slides down and mobilizes the water resistance, τ_w, on the seafloor, which is a function of the sliding velocity (Appendix K). Conditions $l >> w$ and $h >> w$ represent the asymptotic approximation of the small scale yielding. As $l >> h$, the slab above the shear band is considered thin when compared to its length. This condition is essential for the 1-D model developed below. Both conditions, $l >> h$ and $h >> \omega$, are relaxed by *Viesca* [2011] and *Viesca and Rice* [2012], who studied slide (including submarine slide) initiation due to slip surface nucleation and growth driven by locally elevated pore pressure. In this work, we keep these assumptions as focus on the dynamic aspects of the shear band growth.

Although the total normal stress in the x-direction is a function of depth, we follow *Palmer and Rice* [1973] and consider the average values

$$\sigma(x,t)=\frac{1}{h}\int_0^h \sigma_{xx}(x,y,t)dy, \quad u(x,t)=\frac{1}{h}\int_0^h u_x(x,y,t)dy, \quad p(x,t)=\frac{1}{h}\int_0^h P(x,y,t)dy \qquad (2.1)$$

of the total stress, σ_{xx}, displacement, u_x, and pore pressure, P, across the sliding layer. Here t is time, x, y is the chosen coordinate set with x being the longitudinal coordinate (Figure 2a), and h is the thickness of the sliding layer. We assume that P does not change during the shear band growth and consider the dynamic deformation being undrained at the scale of the thickness of the sliding layer. Specifically, we assume that $\sqrt{D_h t_f} << h$, where D_h is the hydraulic diffusivity (diffusion coefficient) of the host sediment and t_f is the time to global failure when the shear

band reaches the size of l_f. Then, we consider both local, P, and averaged, p, pore pressure as not changing with time and equal their values at $t = 0$. Note that, in general, diffusion at the scale of the shear band thickness and at the scale of the process zone of the shear band (Figure 2a) may or may not be neglected, which affects the sediment strength at these scales.

Before the shear band appears, the average normal effective stress in the intact slope is $\sigma + p = -p_0$ ($p_0 > 0$). Although stress state is not uniform in natural slopes [e.g., *Picarelli et al.*, 2000], p_0 does not change sharply along a long, mild slope, which, therefore, is approximated by an infinite slope with constant p_0 [e.g., *Prior and Suhayda*, 1979; *Denlinger and Iverson*, 1990; *Davis and Selvadurai*, 1996]. Hereafter, compressive stresses and strains are defined to be negative, and displacements and strains are measured with respect to the undeformed state in the infinite slope with homogeneous, undisturbed, longitudinal effective stress of magnitude p_0 (Figure 2b).

Following *Puzrin et al.* [2010], we assume that at the top end, $x = 0$, of the sliding slab, the sediment undergoes *active* failure (i.e., due to the sediment unloading compared to the infinite slope). In a sediment with sufficient cohesion, a tensile crack may develop connecting the shear band with the slide surface. As the seawater fills the crack, the slide becomes loaded at the upper end by the hydrostatic pressure, which corresponds to zero effective stress. In either case, we denote the average longitudinal effective stress at $x = 0$ by p_a (Figure 2a).

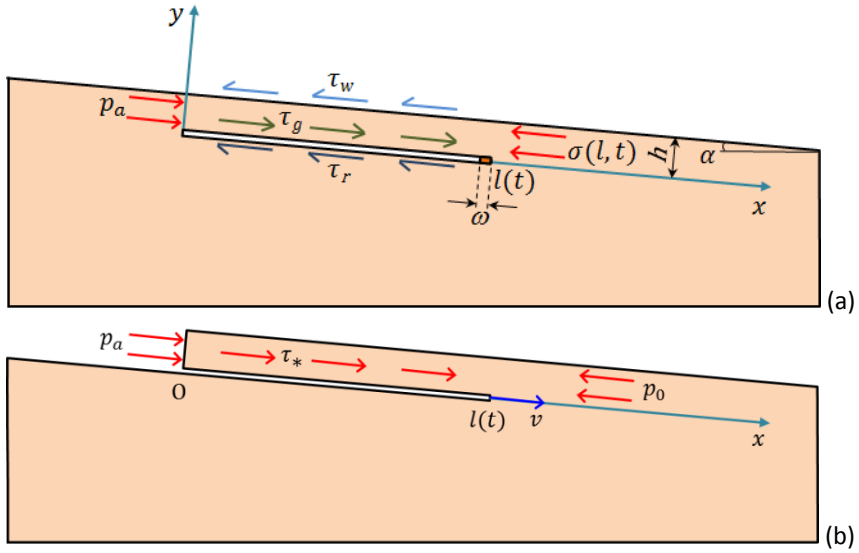

Figure 2. (a) Shear band propagation in an infinite slope. The slab above the failed zone already has deformation accumulated during the stable (progressive) stage of the shear band growth, while the sliding velocity appears in the dynamic stage that begins at $t = 0$. (b) One-dimensional model of a landslide

developing by the mechanism of dynamic propagation of the underlying shear band.

The soil behavior in the sliding layer is described by a one-dimensional model (Appendix B)

$$\sigma + p = E\frac{\partial u}{\partial x} - p_0 \qquad (p_0 = \text{const} > 0) \tag{2.2}$$

where $E = E_0/(1-\nu^2)$ is the tangent (plane-strain) elastic modulus of the particulate material, E_0 and ν are the Young's modulus and Poisson's ratio, respectively. In general, soil moduli in loading, E_l, and unloading, E_u, are different. For the sake of simplicity, however, we consider the case of $E_l = E_u = E$. In this formulation, the constitutive behavior of the material is equivalent to that in linear elasticity.

2.2. Dynamic motion

Governing equations are formulated in terms of quantities (2.1) averaged across the landslide. Substituting the constitutive relation (2.2) into the momentum balance condition [*Hellan*, 1984; *Freund*, 1998]

$$\rho_0\frac{\partial^2 u}{\partial t^2} = \frac{\tau_0}{h} + \frac{\partial \sigma}{\partial x} \tag{2.3}$$

results in an inhomogeneous wave equation (Appendix B)

$$\frac{\partial^2 u}{\partial x^2} - \frac{1}{c^2}\frac{\partial^2 u}{\partial t^2} = -\frac{T}{h} \qquad (0 < x < l, \;\; t > 0) \tag{2.4}$$

where $c = (E/\rho_0)^{1/2}$ is the speed of the longitudinal elastic waves, ρ_0 is the total material density (which accounts for both solid matrix and pore water), $l(t)$ is the length of the propagating shear band, $T = \tau_* / E > 0$ is the normalized longitudinal load, $\tau_0 = \tau_g - \tau_r - \tau_w$,

$$\tau_* = \tau_1 - \tau_w \qquad (\tau_1 = \tau_g - \tau_b - \tau_r) \tag{2.5}$$

is the combined distributed gravitational, $\tau_g = \rho_0 gh\sin\alpha$, buoyancy, $\tau_b = \rho_w gh\sin\alpha$, frictional, $\tau_r = \mu(\rho_0 - \rho_w)gh\cos\alpha$, and viscous (water resistance in the case of submerged slopes), τ_w, loads in the slope direction (Figure 2b). Until indicated otherwise, we consider the general case of this load dependent on both x and t.

The initial conditions are

$$u(x,t) = u_s(x), \qquad \frac{\partial u}{\partial t}(x,t) = 0 \quad (0 < x < l_0, \;\; t \to 0) \tag{2.6}$$

where l_0 is the initial length of the shear band and $u_s(x)$ is the static displacement just before the band begins propagating dynamically.

The slide (slope) is initially at rest, but has already moved during the quasi-static stage of the deformation process. The boundary condition, $u(l(t), t) = 0$ $(t > 0)$, at the tip, $x = l(t)$, of the propagating shear band can be written as [*Hellan*, 1984; *Freund*, 1998]

$$\frac{\partial u}{\partial t} = -v\frac{\partial u}{\partial x} \quad (x = l(t), \;\; t > 0) \tag{2.7}$$

where $v = dl/dt$ is the velocity of the band tip. Because the model developed here is based on the assumption of small strains ($|\partial u/\partial x| << 1$), (2.7) implies that $\partial u(l, t)/\partial t < v$, so the material at the band tip moves slower than the crack tip, which is a necessary condition for our model to be physically acceptable. In Section 6.1, it will be shown that this condition is satisfied.

The boundary condition at the upper end, $x = 0$, of the slide (Figure 2b) represents the effective stress $\sigma(0, t) + p = -p_a$ ($p_a = \text{const} > 0$, $t \geq 0$), which per Hooke's law (2.2), is expressed as

$$\frac{\partial u}{\partial x}(0,t) = \gamma_a \quad (t \geq 0) \tag{2.8}$$

where $\gamma_a = (p_0 - p_a)/E$ is the strain at $x = 0$. Note that at $x = 0$, the effective stress $\sigma + p = -p_a$ is compressive (negative) while strain $\partial u / \partial x = \gamma_a$ is tensile (positive) due to the chosen undeformed state, which is reflected by the difference in signs. As mentioned above, if a tensile fracture develops at the upper end of the slide in a sediment with sufficient cohesion, p_a can also be interpreted as zero effective stress ($p_a = 0$) due to the hydrostatic water pressure in the fracture and in the sediment (Appendix B) [*Puzrin et al.*, 2010]. Hence, $p_a < p_0$, which also holds when p_a is the active pressure. Therefore, in both cases, $\gamma_a > 0$. This does not result in a loss of generality, as the solution of the dynamic problem obtained below is also mathematically applicable to the case of negative γ_a. The absolute value, $|\gamma_a| = -\gamma_a$, of this compressive strain, however, should be smaller than the tip strain, γ_0 (defined in the next section), at the onset of dynamic growth.

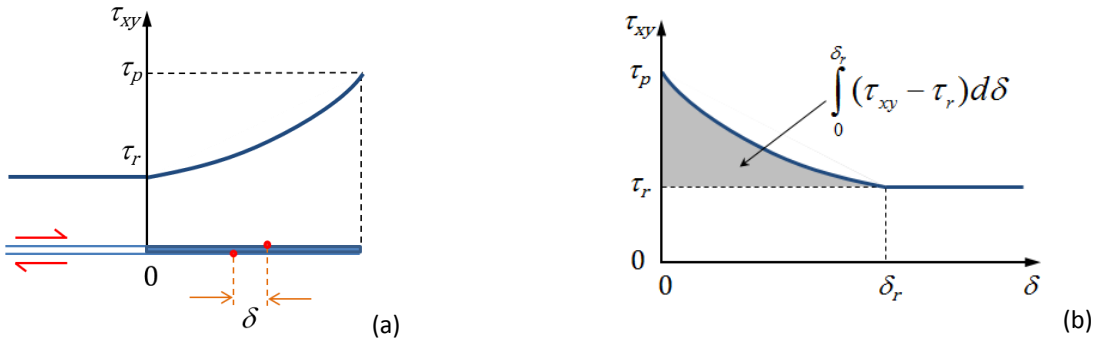

Figure 3. (a) Shear traction (resistance), τ_{xy}, along the shear band and (b) relationship between τ_{xy} and relative shear displacement, δ [*Palmer and Rice*, 1973]. The shear strength of the material decreases from peak, τ_p, to residual, τ_r, values with shear deformation based on a strain-softening constitutive behavior. The integral shows the energy surplus available per unit area of the shear band advance, and δ_r is the relative displacement required for τ_r to develop. The surplus is the excess of the work input of the applied forces over the sum of (*i*) the net energy absorbed in the deforming material outside the band and (*ii*) the frictional dissipation against the residual part, τ_r, of the slip resistance within the shear band [*Palmer and Rice*, 1973].

2.3. Energy balance

Following *Palmer and Rice* [1973], we treat the propagating shear band as an ideal, mode II fracture. We assume that the fracture process zone is small compared to the layer thickness and the band size. The propagation of such a fracture is controlled by the energy balance at the fracture tip. For a dynamically propagating fracture, the energy release rate J is balanced by rate of the energy dissipation at the tip [*Rice*, 1968; *Cherepanov*, 1979]. Hence, $J = J_c$, where J_c is the effective surface energy for a growing fracture. It is assumed constant, although in the landslide context, this is not necessarily the case even for small scale yielding because different weakening mechanisms may take place during the shear band growth. As noted by *Viesca and Rice* [2012], for example, rapid slip may result in shear heating, which, in turn, may cause thermal pressurization or material decomposition to occur in a sediment [*Voight and Faust*, 1982; *Vardoulakis*, 2002; *Cecinato*, 2009; *Goren et al.*, 2010; *Pinyol and Alonso*, 2010].

For a sliding 1-D layer, the condition of $J = J_c$ results (Appendix C) in the squared strain

$$\left[\frac{\partial u}{\partial x}(l,t)\right]^2 = \frac{\gamma_c^2}{1-v^2/c^2} \qquad (l(t) > l_0,\ t > 0) \tag{2.9}$$

at the propagating band tip $x = l(t)$. Hereafter, $\gamma_c = [2J_c/(hE)]^{1/2}$ is the minimal strain level at the tip of the propagating fracture (when $v \to 0$). As follows from (2.9), for a physically meaningful solution, $v < c$. Condition (2.9) is identical to that obtained by *Freund* [1998] in the case of $p_0 = 0$, but it is also applicable when $p_0 \neq 0$ (Appendix C).

When $t = 0$, the initial shear band is in a state of mobile equilibrium [*Barenblatt*, 1962] and has a length l_0 such that at the given level T of the applied loads, it is just about to start propagating. This length, therefore, is defined by (2.9) with $v = 0$ and γ_c replaced by $\gamma_0 = [2J_0 / (hE)]^{1/2}$, which is the strain level required at the tip for the static band to begin propagating. Here J_0 is the surface energy for the static shear band [*Palmer and Rice*, 1973; *Chowdhury*, 1978; *Saurer and Puzrin*, 2011; *Dey et al.*, 2012]. In this case, (2.9) reads

$$\gamma_s^2(l_0) = \gamma_0^2 \tag{2.10}$$

where $\gamma_s(l_0) = \gamma(l_0, 0)$ is the static deformation of the initial 1-D layer above the shear band at its tip $x = l_0$ (Figure 2b). It is determined from

$$\gamma_s(x) = \gamma_a - \frac{1}{h}\int_0^x T(x,0)dx \tag{2.11}$$

which is the deformation of a static layer of size $l \geq l_0$ at point $x \leq l$. This deformation is obtained by integrating (2.4) with $\partial^2 u / \partial t^2 = 0$ and boundary condition (2.8). In reality, the layer is in a state of dynamic motion as the shear band grows, but introducing the auxiliary function (2.11) is handy to characterize its virtual steady state (if the layer were not moving). Deformation $\gamma_s(x)$ implicitly depends on the layer size in the sense that $x \leq l$, but we do not indicate this to simplify notations.

Because $J_0 \neq J_c$, and, hence, $\gamma_0 \neq \gamma_c$, comparing (2.10) and (2.9) shows that at $t = +0$, either the band tip instantaneously acquires (if $\gamma^2(l_0, +0) = \gamma_s^2(l_0)$) some finite propagation velocity, v_0, or the strain, $\gamma(l, t)$, at the tip instantaneously changes (if $v_0 = 0$) from $\gamma(l_0, 0) = \gamma_s(l_0)$ to some $\gamma(l_0, +0) \neq \gamma_s(l_0)$, or both. Hereafter, symbol $+0$ indicates the limit of $t \to 0$ $(t > 0)$. In general, J_0 is greater than J_c [e.g., *Shukla*, 1983; *Marur et al.*, 2004; *Jajam and Tippur*, 2012], and we adopt the notation of

$$n = J_0 / J_c = \gamma_0^2 / \gamma_c^2 \tag{2.12}$$

where $n > 1$ is called the bluntness parameter [*Freund*, 1998] as applied to open (mode I) cracks, but n is also used for shear fractures [*Hellan*, 1984; *Freund*, 1998]. Transition from J_0 to J_c could be addressed, in principle, by considering more accurate friction laws that depend upon displacement discontinuity and/or the relative slip velocity [*Ida*, 1972; *Dieterich*, 1979; *Rice*, 1980; *Ruina*, 1983]. Then, the material motion and/or strain at the band tip would initiate from

the state of rest [*Garagash and Germanovich*, 2012; *Viesca and Rice*, 2012]. Within the framework of the simplified 1-D model, considered here, this transition time from rest to dynamic motion is considered to be relatively short, and is approximated by the abrupt increase in propagation velocity from zero to some v_0 or/and by the instantaneous strain change at the tip from $\gamma_s(l_0)$ to $\gamma(l_0, +0)$. In this case, (2.9) becomes $\gamma^2(l_0, +0) = \gamma_c^2/(1 - v_0^2/c^2)$), where the values of v_0 to be found.

CHAPTER 3. INITIAL-BOUNDARY VALUE PROBLEM

3.1. Governing equations

Equations (2.4) - (2.8) are written with respect to the unknown functions $u(x, t)$ and $l(t)$. Following *Freund* [1998], they can be rewritten in terms of the longitudinal strain, $\gamma(x, t) = \partial u/\partial x$, material velocity (slip rate), $\eta(x, t) = \partial u/\partial t$, and fracture length, $l(t)$, as

$$\frac{\partial \gamma}{\partial t} = \frac{\partial \eta}{\partial x}, \qquad \frac{\partial \gamma}{\partial x} - \frac{1}{c^2}\frac{\partial \eta}{\partial t} + \frac{T}{h} = 0 \quad (0 < x < l(t), \ t > 0) \tag{3.1}$$

$$\gamma(x,0) = \gamma_s(x), \qquad \eta(x,0) = 0 \quad (0 < x < l_0) \tag{3.2}$$

$$\gamma(0,t) = \gamma_a, \qquad \eta(l(t),t) = -v(t)\gamma(l(t),t) \qquad (t > 0) \tag{3.3}$$

To close this set, we also use an additional condition at the tip of the propagating shear band that combines (2.10) and (2.9) into

$$\frac{\gamma^2}{\gamma_0^2} = \begin{cases} 1 & (x = l_0, \ \ t = 0) \\ n^{-1}(1 - v^2/c^2)^{-1} & (x = l(t), \ t > 0) \end{cases} \tag{3.4}$$

where we took into account (2.12). The initial value l_0 of $l(t)$ is defined by (2.10), (2.11) and further assumed known. In Chapter 5, l_0 is defined explicitly for a particular type of dependence $T(x, t)$.

Note that the term 'material velocity' is synonymous to the term 'particle velocity'. 'Particle velocity' refers to both the (random) velocity of individual particles in the sediment displaced by the slide and to the mean velocity of particles in the representative elementary volume. To avoid confusion and to emphasize that our model is developed within the framework of continuum mechanics, we prefer the term 'material velocity'.

3.2. Conditions on discontinuities

Set (3.1) of first-order linear differential equations is hyperbolic [e.g., *Whitham*, 1999]. It has two sets of characteristics represented by the straight lines $dt/dx = \pm 1/c$ in plane (x, t). At $t = +0$, the tip boundary condition changes instantaneously, i.e., the band velocity jumps from zero to $v_0 \neq 0$ or/and the tip strain changes instantaneously from its static, $\gamma_s(l_0)$, to dynamic, $\gamma(l_0, +0)$, value. Such an instantaneous change causes a discontinuity (generally, in both γ and η) that begins propagating from the shear band tip $x = l_0$ towards the other boundary at $x = 0$. Because

of the hyperbolicity of set (3.1), discontinuities can only propagate along its characteristics [*Courant and Friedrichs*, 1948; *Whitham*, 1999; *Lax*, 2006]. Therefore, the discontinuity propagates with velocity c (line AC of $x = l_0 - ct$ in Figure 4), and at time $t = l_0/c$, it reflects on the slide end, $x = 0$, and propagates back towards the band tip, $x = l(t)$ (line CE of $x = ct - l_0$ in Figure 4). As will be shown below, the band tip propagates with velocity $v < c$, and the discontinuity may (Figure 4a) or may not (Figure 4b) reach the propagating tip. If it does, then it reflects at the tip and propagates again towards $x = 0$ (line EF of $x = l_E + c(t_E - t)$ in Figure 4, where l_E and t_E are found in (4.17)). Within the framework of elastic theory, this process can continue indefinitely, although it is also possible that, after a number of reflections from $x = 0$, the discontinuity will cease to reach the band tip. Until Section 4.3, the consideration is common for both cases of the discontinuity lagging behind and reaching the band tip, that is, for both CE intersecting (Figure 4a) and not intersecting (Figure 4b) the band tip line of $x = l(t)$.

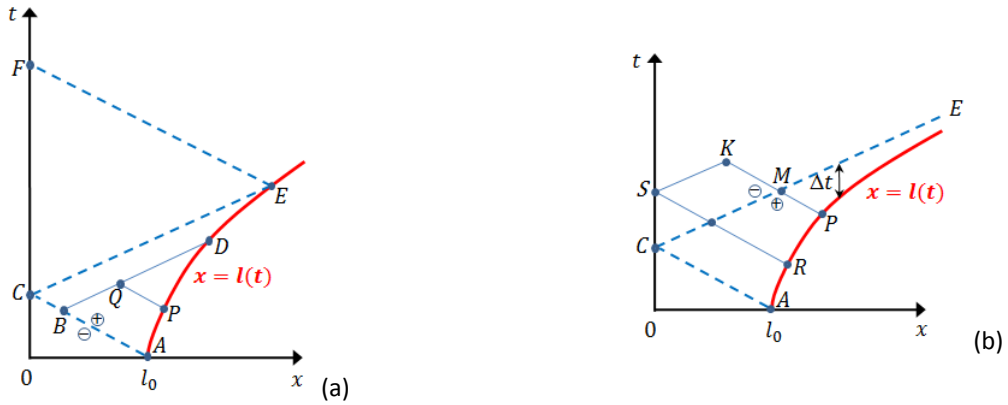

Figure 4. Location $x = l(t)$ of the shear band tip at time t (solid, curved line AE) and characteristics AC ($x = l_0 - ct$) and CE ($x = ct - l_0$) of the propagating discontinuity (dashed lines). "Regular" characteristics (a) BD and PQ (thin lines) and (b) RS, SK, and KP (thin lines) are in domains of continuous values of γ and η (and their derivatives of the first order). Plus and minus correspond to the limits of γ and η while approaching to the discontinuity lines AC in (a) and CE in (b). (a) When the discontinuity reaches the propagating tip, it reflects and starts propagating back along line EF ($x = l_E + c(t_E - t)$, dashed lines). (b) After the discontinuity, propagating from the band tip, $x = l_0$, at A is reflected back from the slide end, $x = 0$, at C, it is not able to reach the moving band tip, $x = l(t)$, again. In this case, E is the infinite point (compare to (a)). Characteristics RS and PK intersect line CE of the reflected discontinuity. Solution in domain CEF in (a) is similar to that above the characteristic line CE in (b).

Mathematically, we look for functions $\gamma(x, t)$ and $\eta(x, t)$ that are continuous and have continuous derivatives of the first order in the domains between the discontinuity characteristics (for example, between AC and CE, or CE and EF in Figure 4a). The values of η and γ on these characteristics are discontinuous with the jump condition [*Courant and Friedrichs*,

1948; *Whitham*, 1999; *Davison*, 2008]

$$\eta^+ - \eta^- = \pm c(\gamma^+ - \gamma^-) \qquad (dt/dx = \mp 1/c) \tag{3.5}$$

where $\eta^{\pm}$ and $\gamma^{\pm}$ are the limits of $\eta(x, t)$ and $\gamma(x, t)$, respectively, obtained by approaching the discontinuity characteristics from different sides. For example, we further use notations $\eta^+(x, t)$, $\gamma^+(x, t)$ and $\eta^-(x, t)$, $\gamma^-(x, t)$ for values of $\eta(x, t)$, $\gamma(x, t)$, obtained by approaching line *AC* in Figure 4a from above and below, respectively.

In summary, the initial-boundary value problem for $\gamma(x, t)$, $\eta(x, t)$, and $l(t)$ is given by the closed, hyperbolic set of equations (3.1) with boundary conditions (3.3), (3.4) and initial conditions (3.2) and

$$l(t) = l_0 \quad (t = 0) \tag{3.6}$$

Solution of this problem is considered in the next chapter.

CHAPTER 4. SOLUTION OF THE INITIAL-BOUNDAY VALUE PROBLEM

4.1. Shear band velocity

The set of linear equations on characteristics, which is equivalent to (3.1), can be written as [*Courant and Friedrichs*, 1948; *Whitham*, 1999],

$$\frac{d}{dx}\left(\gamma \pm \frac{\eta}{c}\right) = -\frac{T}{h} \qquad \left(\frac{dt}{dx} = \mp\frac{1}{c}\right) \tag{4.1}$$

where $d/dx = \partial/\partial x + (\partial t/\partial x)\partial/\partial t$ is the total derivative. Following *Burridge and Keller* [1978], we first integrate (4.1) along the characteristic line, $t = t_B + (x - x_B)/c$, between point, $B(x_B, t_B)$, which is on the characteristic line AC, $t = (l_0 - x)/c$, and point $D(l_D, t_D)$ at the band tip $x_D = l_D = l(t)$ (Figure 4). We obtain

$$\gamma(D) - \frac{\eta(D)}{c} - \gamma^+(B) + \frac{\eta^+(B)}{c} = -\frac{1}{h}\int_{x_B}^{l_D} T(x, t_B + (x - x_B)/c)dx \tag{4.2}$$

where $\gamma^+(B)$ and $\eta^+(B)$ are the limits of $\gamma(x, t)$ and $\eta(x, t)$, respectively, when $x \to x_B$, $t \to t_B$, and $t - (l_0 - x)/c \to +0$. Functions $\gamma(x, t)$ and $\eta(x, t)$ are continuous and have continuous derivatives in domain ACE in Figure 4a. Because the initial discontinuity propagates along line AC, $\gamma^-(B)$ and $\eta^-(B)$ on this line are simply the initial static strain and material velocity, respectively. They are undisturbed until the initial discontinuity arrives at x_B at time $t_B = (l_0 - x_B)/c$. Therefore, in (2.11),

$$\gamma^-(B) = \gamma_s(x_B), \qquad \eta^-(B) = 0 \tag{4.3}$$

so the jump condition (3.5) becomes

$$\eta^+(B)/c - \gamma^+(B) = -\gamma_s(x_B) \tag{4.4}$$

Since point $D(l_D, t_D)$ corresponds to the propagating tip, the second (dynamic) fracture condition in (3.4) applies. Substituting this, (4.4), and the second equation in (3.3) into (4.2), results in equation

$$\sqrt{\frac{1 + v_1/c}{1 - v_1/c}} = -\frac{1}{\gamma_c}\left[\gamma_s(x_B(l,t)) - \frac{1}{h}\int_{x_B(l,t)}^{l} T(x, t + (x - l)/c)dx\right] \tag{4.5}$$

for the crack tip velocity v_1, where $x_B(l, t) = (l + l_0 - ct)/2$ and we used notations $l_D = l$, $t_D = t$ because $D(l_D, t_D) = D(l, t)$ is the arbitrary point on the line, $x = l(t)$, of band tip locations. The right hand side in (4.5) is positive because $\gamma_s(x_B(l, t)) < 0$ and $T(x, t) > 0$ for any $t \geq 0$. Hereafter,

$v_1(l)$ is the velocity of the band tip before it is reached by the discontinuity (at point E in Figure 4a and never in Figure 4b, where E is at infinity).

Equation (4.5) for $l(t)$ is to be solved with the initial condition (3.6). To simplify the solution, we further assume that function $T(x, t) = T(x)$ is independent of t. In this case, solution of (4.5) with (3.6) can be written in the closed form

$$t = \int_{l_0}^{l} \frac{dl}{v_1(l)} = \frac{1}{c}\left[l - l_0 + 2\gamma_c^2 \int_{l_0}^{l} \frac{dl}{\gamma_s^2(l) - \gamma_c^2} \right] \tag{4.6}$$

where

$$\frac{v_1(l)}{c} = \frac{\gamma_s^2(l) - \gamma_c^2}{\gamma_s^2(l) + \gamma_c^2} \tag{4.7}$$

Taking into account condition (2.10) for l_0, expression (2.11) can be rewritten for $x = l$ as

$$\gamma_s(l) = \gamma_a - \frac{l}{h}\bar{T}(l) = -\gamma_0 - I(l), \qquad \bar{T}(l) = \frac{1}{l}\int_0^l T(x)dx, \qquad I(l) = \frac{1}{h}\int_{l_0}^{l} T(x)dx \tag{4.8}$$

with $\bar{T}(l)$ being the average value of $T(x)$ for the band of length l.

Since $T(x) > 0$, $I(l)$ in (4.8) increases monotonically with l and so does $\gamma_s^2(l)$ (since $\gamma_0 > 0$). Initially, $\gamma_s^2(l_0) = \gamma_0^2 > \gamma_c^2$. Hence, $\gamma_s^2(l) - \gamma_0^2 > 0$, and $v(l) > 0$ for any $l \geq l_0$. Furthermore, according to (4.7), the shear band propagation velocity is always smaller than the speed of elastic waves, $v_1 < c$. Because of the monotonic increase of $\gamma_s^2(l)$ with l, function $l(t)$ defined by (4.6) also monotonically increases with t.

In the simplest case, the reflected discontinuity does not ever reach the crack tip, which corresponds to the characteristic line CE not crossing line $x = l(t)$ of the tip location (Figure 4b). In this case, the mathematical limit of $l \to \infty$ is possible in (4.6) and (4.7), resulting in $v_1 \to c$ as $l \to \infty$ and $l \to \infty$ as $t \to \infty$. Therefore, (4.6) and (4.7) give a physically meaningful solution for the shear band size, $l(t)$, and the propagation velocity, $v_1(t)$ (Figure 5). It is straightforward to show that assumption $T(x, t) = T(x)$ does not result in a loss of generality and the same conclusions remain valid in the general case of $T(x, t) > 0$.

It should be noted that from the physical standpoint, the material may fail or start exhibiting significant inelastic strain before the shear band size becomes infinitely large. This will be discussed in Section 6.2. Until then, we consider the mathematical aspects of the

obtained solution and formally allow l to be unbounded.

Finally, solution (4.6)-(4.8) was obtained based on the concept of propagating discontinuities arising from the hyperbolicity of the initial-boundary value problem (3.1) - (3.4). It can be shown (Appendix D) that this problem does not have physically acceptable continuous solutions.

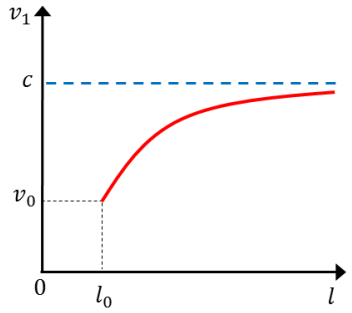

Figure 5. Dependence of the band propagation velocity, v_1, on its length, l, for arbitrary $T(x, t) > 0$ in the case of the discontinuity not reaching the band tip (Figure 4b).

4.2. Strain and material velocity

To obtain the strain, γ_1, and material velocity, η_1, at the shear band tip, we insert (4.7) into the second relation of (3.4) and use the second (compatibility) condition at the band tip in (3.3). This gives

$$\gamma_1(l) = \frac{\gamma_s^2(l) + \gamma_c^2}{2\gamma_s(l)}, \qquad \frac{\eta_1(l)}{c} = -\frac{\gamma_s^2(l) - \gamma_c^2}{2\gamma_s(l)} \tag{4.9}$$

where, as shown above, $\gamma_s^2(l)$ monotonically increases with $l \geq l_0$. Therefore, both $|\gamma_1(l)|$ and $\eta_1(l)$ increase as the shear band grows.

To find strain, γ, and slip velocity, η, at the arbitrary point $Q(x, t)$, located between lines AC and CE in Figure 4a, we next consider point $P(l_P, t_P)$, which is at the band tip and is connected to $Q(x, t)$ by the characteristic line, $x - l_P = -c(t - t_P)$. Here l_P and t_P are related by (4.6), and l_P can be found from

$$t + \frac{x - l_P}{c} = \int_{l_0}^{l_P} \frac{dl}{v_1(l)} \tag{4.10}$$

once x and t are specified. Integrating then (4.1) from P to Q and taking into account (4.9) (because P is at the band tip), we arrive at

$$\gamma(Q)+\frac{\eta(Q)}{c}=\frac{\gamma_c^2}{\gamma_s(l_P)}+\frac{1}{h}\int_x^{l_P}T(x)dx \tag{4.11}$$

while integration of (4.1) from *B* to *Q* is similar to (4.2). Using (4.4) with the result of this integration, we have

$$\gamma(Q)-\frac{\eta(Q)}{c}=\gamma_s(x) \tag{4.12}$$

Finally, we obtain from (4.12) and (4.11) that

$$\gamma(x,t)=\gamma_s(x)+\eta_1(l_P)/c,\quad \eta(x,t)=\eta_1(l_P) \tag{4.13}$$

where $(l_0-x)/c<t<(l_0+x)/c$, $x<l(t)$, l_0 is defined by (2.10), and $l_P(x,t)$ is the solution of (4.10).

Note that the second equation in (4.13) means that inside *ACE* (Figure 4a), the slip velocity $\eta(x,t)$ is constant on characteristics $dt/dx=1/c$. The value of $\eta(x,t)$ is not constant, however, along characteristics $dt/dx=-1/c$ because $\eta_1(l_P)$ is the material velocity at the band tip and, therefore, depends upon the position of *P* on line $x=l(t)$.

Equations (4.13) give γ and η at the arbitrary point (x,t) in domain *ACE* in Figure 4a. Values $\gamma(l,t)$ and $\eta(l,t)$ of these quantities at the band tip are given by (4.9). Equations (4.7) and (4.6) define the dependence of the shear band velocity upon l and t, respectively. In particular, at the initial moment, $t=+0$, at the band tip, $x=l_0$,

$$v(+0)=v_0=c\frac{n-1}{n+1},\quad \eta(l_0,+0)=\eta_1(l_0)=c\gamma_0\frac{n-1}{2n},\quad \gamma(l_0,+0)=\gamma_1(l_0)=-\gamma_0\frac{n+1}{2n} \tag{4.14}$$

Material strain and velocity for the arbitrary point $K(x,t)$ inside domain *CEF* in Figure 4a or outside domain *ACE* in Figure 4b are given by (Appendix E)

$$\gamma(x,t)=\frac{\eta_1(l_P)}{c}-\frac{\eta_1(l_R)}{c}+\gamma_s(x),\qquad \eta(x,t)=\eta_1(l_P)+\eta_1(l_R) \tag{4.15}$$

where for the specified x and t, $l_P(x,t)$ is obtained from (4.10) and $l_R(x,t)$ from

$$t-\frac{x+l_R}{c}=\int_{l_0}^{l_R}\frac{dl}{v_1(l)} \tag{4.16}$$

for the same x and t.

4.3. Solution after the discontinuity reaches the band tip

Once the discontinuity propagating along *CE* in Figure 4a reaches the shear band tip, it reflects

and propagates again towards $x = 0$. Whether this indeed happens is discussed in Appendix F. At point F (Figure 4 and Figure 6), the incident discontinuity reflects for the second time from the upper slide end, $x = 0$. The solution for the region above line EF (but below line FL) in Figure 6 (and for all other regions between the incident and reflected discontinuities) is obtained in Appendix E. The band tip arrives at point $x = l \geq l_E$ at time

$$t = t_E + \int_{l_E}^{l} \frac{dl}{v_2(l, l_{RU}(l))} \tag{4.17}$$

where

$$\frac{v_2(l, l_{RU})}{c} = \frac{[-\gamma_s(l) + 2\eta_1(l_{RU})/c]^2 - \gamma_c^2}{[-\gamma_s(l) + 2\eta_1(l_{RU})/c]^2 + \gamma_c^2} \quad (l \geq l_E,\ l_0 \leq l_{RU}(l) < l_E) \tag{4.18}$$

is the tip velocity after the tip is reached by the discontinuity. After the discontinuity reflects from the band tip at E, the tip $x = l(t)$ arrives at point $U(l_U, t_U)$ together with the wave that originates at $R(l_R, t_R)$ and then reflects from $x = 0$ (Figure 6). This means that $l = l_U > l_E$, $t = t_U > t_E$, $t_R = t_{RU} > t_E$, $l_0 < l_R = l_{RU} < l_E$, and we further use notation $l_{RU} = l_R$ when we want to emphasize that R and U are connected by the characteristics lines (Figure 6). Hence, substituting $t = t_R + (l_R + l)/c$ into (4.17) and differentiating the result with respect to t, we see that $l_{RU}(l)$ is the solution of the initial value problem

$$\frac{dl_{RU}}{dl} = \left[\frac{c}{v_2(l, l_{RU})} - 1\right]\left[\frac{c}{v_1(l_{RU})} + 1\right]^{-1}, \quad l_{RU}(l_E) = l_0 \quad (l \geq l_E,\ l_0 \leq l_{RU}(l) < l_E) \tag{4.19}$$

with the crack length, l_E, at point E (Figure 6) determined from

$$t_E = \int_{l_0}^{l_E} \frac{dl}{v_1(l)}, \quad l_E + l_0 = ct_E \tag{4.20}$$

Since $0 < v_2 < c$ and $v_1 > 0$, $dl_{RU}/dl > 0$ in (4.19), which implies that $l_{RU}(l)$ monotonically grows with l.

The material strain and velocity at the arbitrary point $Z(x, t)$ above the discontinuity line EF (in region EFL in Figure 6) are given by (Appendix G)

$$\begin{cases} \gamma(x,t) = \dfrac{\eta_2(l_H) - \eta_1(l_W) - \eta_1(l_R)}{c} + \gamma_s(x) \\ \eta(x,t) = \eta_2(l_H) - \eta_1(l_W) + \eta_1(l_R) \end{cases} \tag{4.21}$$

while these quantities at the fracture tip (after it is reached by the discontinuity) can be written as (Appendix G)

$$\begin{cases} \gamma_2(l) = \dfrac{1}{2}\dfrac{[\gamma_s(l) - 2\eta_1(l_R)/c]^2 + \gamma_c^2}{\gamma_s(l) - 2\eta_1(l_R)/c} \\ \dfrac{\eta_2(l)}{c} = \dfrac{1}{2}\dfrac{\gamma_c^2 - [\gamma_s(l) - 2\eta_1(l_R)/c]^2}{\gamma_s(l) - 2\eta_1(l_R)/c} \end{cases} \quad (l \ge l_E,\ l_0 \le l_R(l) < l_E) \tag{4.22}$$

Here l_R, l_H, and l_W, are the lengths of the shear band at points $R(l_R, t_R)$, $H(l_H, t_H)$, and $W(l_W, t_W)$, respectively, and these points are related to point $Z(x, t)$ through the corresponding characteristics (Figure 6). This means that a wave, originating at the crack tip at R, reflects from $x = 0$ and arrives at Z at the same time as another wave, originating at W, arrives at Z after it reflects from $x = 0$ and H (both W and H are also at the band tip). Hence, we have

$$t = \frac{x + l_R}{c} + \int_{l_0}^{l_R} \frac{dl}{v_1(l)}, \quad t + \frac{x - l_H}{c} = t_E + \int_{l_E}^{l_H} \frac{dl}{v_2(l, l_{RH}(l))} \tag{4.23}$$

and

$$t = \frac{2l_H + l_W - x}{c} + \int_{l_0}^{l_W} \frac{dl}{v_1(l)} \tag{4.24}$$

where for any given x and t (such that $Z(x, t)$ is above EF), $l_R(x, t)$ and $l_H(x, t)$ are first found from (4.23) and then $l_W(x, t)$ from (4.24). Function $l_{RH}(l)$ is obtained (Appendix G) by replacing l_{RU} with l_{RH} in (4.19) and solving the resulting equation.

The material strain and velocity at the arbitrary point $G(x, t)$ above the discontinuity line FL (Figure G.1a, where point G is not shown to simplify the drawing) are given by (Appendix G)

$$\begin{cases} \gamma(x,t) = \dfrac{\eta_2(l_H) - \eta_2(l_S) - \eta_1(l_W) + \eta_1(l_P)}{c} + \gamma_s(x) \\ \eta(x,t) = \eta_2(l_H) + \eta_2(l_S) - \eta_1(l_W) - \eta_1(l_P) \end{cases} \tag{4.25}$$

where l_H, l_W, l_S, and l_P are the band lengths at points $H(l_H, t_H)$, $W(l_W, t_W)$, $S(l_S, t_S)$, and $P(l_P, t_P)$, respectively, and these points are related to point $G(x, t)$ through the corresponding characteristics (Figure G.1a in Appendix G). Specifically, functions $l_H(x, t)$ and $l_W(x, t)$ are given by (4.23) (second equation) and (4.24), respectively, while points $l_S(x, t)$ and $l_P(x, t)$ are defined by

$$t+\frac{x+l_S}{c}=t_E+\int_{l_E}^{l_S}\frac{dl}{v_2(l,l_{RS}(l))},\qquad t=\frac{2l_S+l_P+x}{c}+\int_{l_0}^{l_P}\frac{dl}{v_1(l)} \tag{4.26}$$

Function $l_{RS}(l)$ is obtained (Appendix G) by replacing l_{RU} with l_{RS} in (4.19).

Note that the material velocity (4.9) at the crack tip is always positive, $\eta_1(l) > 0$, while the static strain corresponding to the band length is always negative (compressive), $\gamma_s(l) < 0$. Therefore, the material velocity, η, at the arbitrary point in (4.21) is always positive (because $l_R > l_W$).

As common in the method of characteristics for hyperbolic equations [*Courant and Friedrichs*, 1948; *Whitham*, 1999; *Lax*, 2006], finding the solution of partial differential equations (3.1) is reduced to solving ordinary differential equation (4.19), which represents no difficulty (when solved numerically) since it has a unique solution and function v_2 is known from (4.18). Some conclusions can be derived, however, even without explicitly solving (4.19).

Consider, for example, the shear band velocities right before and right after the discontinuity reaches the band tip at point E (Figure 6) and reflects back towards $x = 0$. In this case, $l \to l_E$ and $l_R \to l_0$, and these velocities are obtained from (4.18) and (4.7), respectively, as

$$\frac{v_2(l_E)}{c}=\frac{[-\gamma_s(l_E)/\gamma_0+1-1/n]^2-1/n}{[-\gamma_s(l_E)/\gamma_0+1-1/n]^2+1/n},\qquad \frac{v_1(l_E)}{c}=\frac{\gamma_s^2(l_E)/\gamma_0^2-1/n}{\gamma_s^2(l_E)/\gamma_0^2+1/n} \tag{4.27}$$

Because function $(z^2 - a^2)/(z^2 + a^2) = 1 - 2a^2/(z^2 + a^2)$ monotonically increases with increasing $z^2 = [-\gamma_s(l_E) / \gamma_0 + 1 - 1/n]^2$ (and $a^2 = 1/n$), this implies that $v_2(l_E, l_0) > v_1(l_E)$ (because $n > 1$). In other words, the band tip velocity increases when the tip is overtaken by the discontinuity. This velocity increase is shown schematically in Figure 6 by breaking the slope of $x = l(t)$ at point E.

Further, because both l_{RU} in (4.18) and $\eta_1(l)$ in (4.9) increase with l, a similar argument (with $z^2 = [-\gamma_s(l) + 2\eta_1(l_E)/c]^2$ and $a^2 = \gamma_c^2$) suggests that $v_2(l, l_0)$ in (4.18) monotonically grows as the band propagates. Yet, as can be observed from (4.18), $v_2(l, l_0) < c$, although $v_2(l, l_0) \to c$, if $l \to \infty$ (since $\gamma_s(l)$ is a monotonic and unbounded function).

Mathematically, the limit transition $l \to \infty$ corresponds to the discontinuity that does not catch up with the band tip again, i.e., after it reflects from the $x = 0$ end for the second time. If, however, the discontinuity reaches the band tip, a nearly identical consideration leads to the same result; that is, the velocity of the shear band approaches c as it propagates. In a similar

manner, it is straight-forward to show (Appendix H) that the discontinuity magnitude reduces after each reflection from the band tip.

Below we are mostly interested either in the discontinuity lagging behind the band tip (Figure 4b) or in the discontinuity reflected once from the tip (i.e., twice from $x = 0$; Figure 4a and Figure 6). These cases are of primary interest for this work (Chapters 5 and 6) as they illustrate all important features of the general solution (Appendix E) for the arbitrary number of reflections.

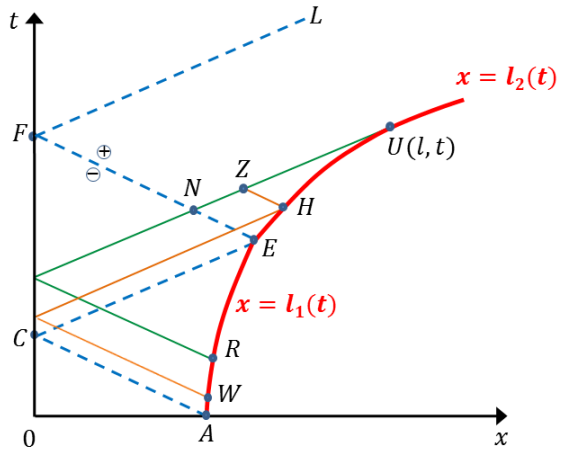

Figure 6. Discontinuity (dashed lines) originated at $t = 0$, $x = l_0$ (point A) and reflected consequently from points C, E, and F. $Z(x, t)$ is the arbitrary point above the discontinuity line EF (but below FL). N and H are points related to Z and located on lines $x = l(t)$ and EF, respectively (above E). Points N and H correspond to waves reflected once from $x = 0$ and initiated at points R and W (both below E) on $x = l(t)$, respectively. $U(l, t)$ is another point on $x = l(t)$ (above E) that also corresponds to point Z. On a few occasions, point R is referred to as RU and RH to stress its relation to points U and H, respectively.

4.4. Range of dimensionless parameters

The solutions presented above can be written in terms of dimensionless quantities

$$\Gamma = -\frac{\gamma}{\gamma_0}, \quad \Omega = \frac{\eta}{c\gamma_0}, \quad V = \frac{v}{c}, \quad \xi = \frac{x}{l_0}, \quad \tau = \frac{ct}{l_0} \tag{4.28}$$

and used with appropriate indices that correspond to the non-normalized parameters. Below, we use both normalized and non-normalized quantities. Note the change of sign in the first equation in (4.28), which corresponds to the normalized compressive strain being positive.

It turns out that the obtained solution, written in terms of quantities (4.28), depends upon only two dimensionless parameters, that is, the "bluntness" number, n, and the characteristic, dimensionless number

$$\lambda_* = \frac{\gamma_0 h}{T_0 l_0} = \frac{\gamma_0}{\gamma_a + \gamma_0} \qquad (T_0 = \bar{T}(l_0)) \tag{4.29}$$

where function $\bar{T}(l)$ is defined by (4.8). Both parameters are relatively well constrained. Because $\gamma_a > 0$ (Section 2.2) and $\gamma_0 > 0$, the range of parameter λ_* is $0 \le \lambda_* \le 1$. It is difficult to further narrow down this range without addressing the specifics of progressive growth of the shear band, until the band reaches the critical length of l_0. Per (4.29), the value of λ_* depends upon the relative values of γ_a and γ_0. If $\gamma_a << \gamma_0$, $\lambda_* \approx 1$, for $\gamma_a \to \gamma_0$, $\lambda_* = 0.5$, and for $\gamma_a >> \gamma_0$, $\lambda_* \approx 0$.

In principal, parameter n is only constrained by condition $n > 1$. It is difficult to constrain it further without explicitly considering the slip and specific weakening mechanisms (e.g., in the band process zone (Figure 2). We note, however, that per (4.14), the crack tip velocity jumps from zero to $v_0 = c/2$ already at the initial moment when $n = 3$ and to $v_0 = c/3$ when $n = 2$. In the absence of better data for n for shear bands in particulate materials, we further consider $1 < n < 2$ and, in most cases, $1 < n < 1.5$. The obtained mathematical results, however, are valid for arbitrary $n > 1$. Furthermore, as shown in Section 8.1, the asymptote of a large n ($n >> 1$) becomes applicable already at $n \sim 1.01$ in many practically important cases.

The value of T in (4.8) and (4.29) is a function of x only, which implies that in (2.5), not only is $\tau_1 = \tau_g - \tau_b - \tau_r$, but also τ_w is independent of time t. The water resistance to the slide motion, however, does depend on the relative velocity of water and, therefore, is not constant over time. The effect of τ_w will be explicitly included in Chapter 8. Until then, τ_w is considered to be negligible.

CHAPTER 5. SLIDE IN HOMOGENEOUS LOADING

5.1. Discontinuity approaching the band tip

Homogeneous load distribution

$$T(x) = T_0 = \bar{T}(l_0) = \text{const} \tag{5.1}$$

in a slope with a propagating shear band represents an important particular case that has been employed in many works on shear bands in soils and sediments [*Palmer and Rice*, 1973; *Chowdhury*, 1978; *Chowdhury et al.*, 2010; *Quinn et al.*, 2011a; *Dey et al.*, 2012; *Quinn et al.*, 2012; *Viesca and Rice*, 2012]. The approximation of constant quantities τ_g, τ_b, and τ_r is also commonly used in the conventional slope stability analysis [*Lambe and Whitman*, 1986; *Das*, 1994; *Craig*, 1997; *Duncan and Wright*, 2005; *Budhu*, 2007; *Chowdhury et al.*, 2010]. In this case, (4.8) simplifies to

$$\gamma_s(l) = -\gamma_0 - T_0(l - l_0)/h \tag{5.2}$$

and the initial value of the band length

$$l_0/h = (\gamma_a + \gamma_0)/T_0 \tag{5.3}$$

is obtained by using (5.1) with (2.11) and (2.10).

Since in our model $l_0/h \gg 1$, (5.3) implies that

$$\gamma_a + \gamma_0 \gg T_0 \tag{5.4}$$

where $T_0 = \tau/E \ll 1$. Because $0 \le \lambda_* \le 1$, this is consistent with $\gamma_0 \gg \lambda_* T_0$, which follows from (4.29) for $l_0/h \gg 1$. These inequalities provide an additional constraint on the choice of parameters, which was satisfied in all numerical examples below.

In the normalized formulation (4.28), equation (4.7) rewrites as

$$\frac{d\lambda}{d\tau} = V_1(\lambda) = \frac{\left[1 + (\lambda - 1)/\lambda_*\right]^2 - 1/n}{\left[1 + (\lambda - 1)/\lambda_*\right]^2 + 1/n} \tag{5.5}$$

where $V_1 = v_1/c$. Substituting (5.5) into (4.6) and integrating yields

$$\tau = \int_1^{\lambda} \frac{d\lambda}{V_1(\lambda)} = \lambda - 1 + \frac{\lambda_*}{\sqrt{n}}\left[\ln\frac{\sqrt{n}+1}{\sqrt{n}-1} + \ln\frac{\lambda - 1 + \lambda_*(1 - 1/\sqrt{n})}{\lambda + 1 + \lambda_*(1 + 1/\sqrt{n})}\right] \tag{5.6}$$

which defines the dimensionless band length $\lambda(\tau)$ as a function of time.

With (5.1) and (4.28), the static strain (5.2) rewrites as

$$\Gamma_s(\lambda) = -\frac{\gamma_s(l)}{\gamma_0} = 1 + \frac{\lambda - 1}{\lambda_*} \tag{5.7}$$

while expressions (4.9) for the material strain and velocity at the crack tip (before the tip is overtaken by the discontinuity) become

$$\Gamma_1 = -\frac{\gamma_1}{\gamma_0} = \frac{1}{2}\left[1 + \frac{\lambda - 1}{\lambda_*} + \frac{1/n}{1 + (\lambda - 1)/\lambda_*}\right], \quad \Omega_1 = \frac{\eta_1}{c\gamma_0} = \frac{1}{2}\left[1 + \frac{\lambda - 1}{\lambda_*} - \frac{1/n}{1 + (\lambda - 1)/\lambda_*}\right] \tag{5.8}$$

Normalized strain and material velocity

$$\Gamma(\xi, \tau) = 1 + \frac{\xi - 1}{\lambda_*} - \Omega_1(\lambda_P), \qquad \Omega(\xi, \tau) = \Omega_1(\lambda_P) \tag{5.9}$$

below *CE* (but above *AC*) in Figure 4a and Figure 4b are obtained from (4.13) while (4.15) results in strain and velocity

$$\Gamma(\xi, \tau) = \Omega_1(\lambda_R) - \Omega_1(\lambda_P) - \Gamma_s(\xi), \qquad \Omega(\xi, \tau) = \Omega_1(\lambda_P) + \Omega_1(\lambda_R) \tag{5.10}$$

at the arbitrary point (ξ, τ) above *CE* in Figure 4a and Figure 4b (but below *EF* in Figure 4 and Figure 6). Here functions $\lambda_P(\xi, \tau)$ and $\lambda_R(\xi, \tau)$ are the solutions of equations

$$\tau + \xi - \lambda_P = \int_1^{\lambda_P} \frac{d\lambda}{V_1(\lambda)}, \qquad \tau - \xi - \lambda_R = \int_1^{\lambda_R} \frac{d\lambda}{V_1(\lambda)} \tag{5.11}$$

where elementary expression for the integrals are given by (5.6). Equations (5.11) are the dimensionless versions of (4.10), (4.16).

Hence, expressions (5.5) – (5.11) provide the closed-form solution for the material strain and velocity and for the shear band size and tip velocity in the case of homogeneous loading (5.1). They are valid before the band tip is reached by the discontinuity.

We observe from (5.8) that both strain and material velocity at the band tip monotonically grow with the band length starting from their initial values $\Gamma_1(1) = (n + 1)/(2n)$ and $\Omega_1(1) = (n - 1)/(2n)$, respectively, which are defined by (5.8), or, equivalently, by (4.14) and (4.28). For $\lambda \to \infty$, both $\Gamma_1(\lambda)$ and $\Omega_1(\lambda)$ formally approach the same asymptote $[1 + (\lambda - 1)/\lambda_*]/2$, always remaining greater and less than, respectively, this asymptote. This can also be seen in Figure 7a, where $\Gamma_1(\lambda)$ and $\Omega_1(\lambda)$ are plotted for $n = 1.1$ and $\lambda_* = 0.25$ and 0.75.

Dimensionless length of the shear band and the corresponding discontinuity characteristics are plotted in Figure 7b in ξ, τ coordinates for $\lambda_* = 0.75$ and $n = 1.1$, 1.2, and 1.4. As can be

seen, the reflected discontinuity will catch up with the band tip for $n = 1.1$, but not for $n = 1.4$. For $n = 1.2$, the curves intersect at $\xi = 8.430$, which is beyond the drawing domain in Figure 7b. To put these values of n in perspective, we note that according to (5.5), $n = 1.1$, 1.2, and 1.4 correspond to an initial velocity v_0 of the band tip equal to 4.8%, 9.1%, and 16.7% of c, respectively.

The velocity v of the band tip quickly approaches c (within approximately two or three initial band sizes), which can be observed in Figure 7c. This observation holds for the entire range of $0 \le \lambda_* \le 1$ and $n > 1$, and v approaches c faster for smaller λ_* and greater n. By the time v becomes comparable to c (when $\lambda \approx 3$), the material velocity Ω_1 at the tip becomes roughly ~ 1, at which stage the normalized strain Γ_1 at the tip is still ~ 1 (Figure 7a). For $\gamma_0 \sim 0.01$, these values of Γ_1 and Ω_1 correspond to the values of $\eta_1 \sim 0.01c$ and $|\gamma_1| \sim 1\%$, respectively. At the moment of reflection of the discontinuity from the band tip, the band velocity jumps (Figure 7c), which is discussed in more details below.

Note that the shear band velocity approaches c but remains slower than c, which is in contrast with the result of *Puzrin et al.* [2010]. They obtained the shear band velocity *unbounded* in time because they did not account for the elastic waves in their formulation. Comparison of our result to *Puzrin et al.* [2010] is given in Appendix I.

Distributions of Γ and Ω along the slope (i.e., in the physical space) are shown in Figure 8a and Figure 8b, respectively, for dimensionless times $\tau = 0.2$, 0.5, and 0.8 (i.e., before the discontinuity hits the slide end, $x = 0$). They are also in Figure 8c and Figure 8d for $\tau = 1.3$, 1.7, and 2 (i.e., after it reflects from the end at $\tau = 1$ but before it reaches the band tip, $x = l$), and in Figure 8e and Figure 8f for $\tau = 3.2$, 3.8, and 4.4 (i.e., after the discontinuity reflects from the tip, which is further discussed in Section 5.2). All lines in Figure 8 are plotted for $\lambda_* = 0.75$ and $n = 1.1$. At time $\tau = 2$, the discontinuity passes the initial position $\xi = 1$ (or $x = l_0$) of the band tip (Figure 8c and d). By that time, however, the tip has already advanced to the new position of $\xi = 1.3865$. The band tip propagation can be seen in Figure 8a through Figure 8f by observing where the curves end to the right of the vertical line $\xi = 1$.

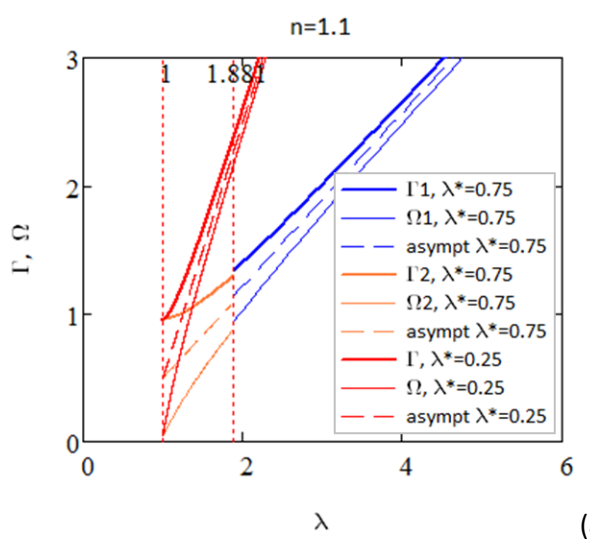

(a)

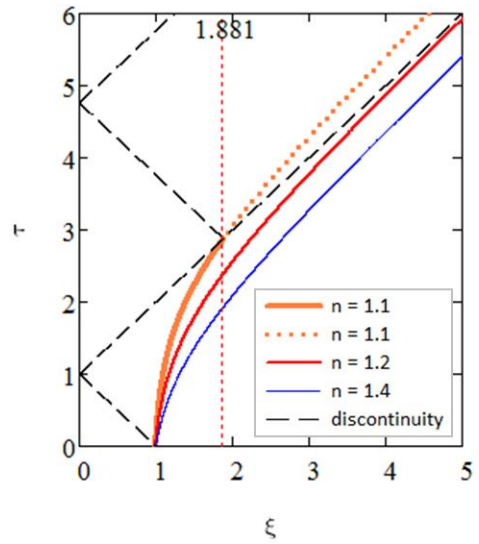

(b)

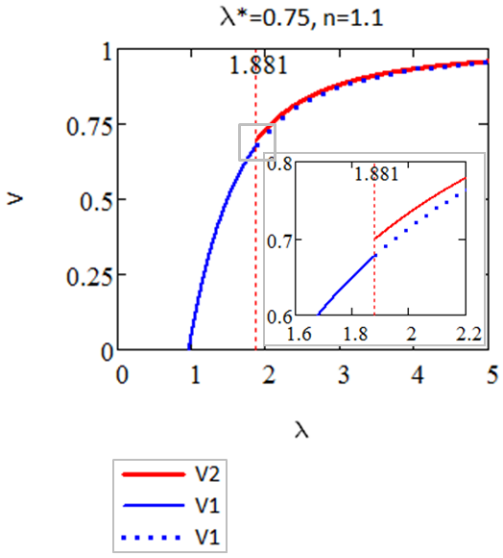

(c)

Figure 7. (a) Normalized strain (bold lines), and material velocity (thin lines), at the shear band tip as functions of $\lambda = l/l_0$ for $\lambda_* = 0.25$ (black lines) and $\lambda_* = 0.75$ (red and blue lines) and $n = 1.1$. Asymptotes of Γ_1 and Ω_1 at $\lambda \to \infty$ are shown by the dashed lines. (b) Dependence of the normalized band size, $\lambda = l/l_0$, on $\tau = ct/l_0$ for $\lambda_* = 0.75$ (i.e., $\gamma_0/\gamma_0 = 1/3$) and $n = 1.4$ (thin, blue line), $n = 1.2$ (red line of medium thickness), and $n = 1.1$ (bold, orange line). In the latter case, the discontinuity (thin dashed line) reaches the propagating tip at $\xi = 1.881$, where it reflects at $\tau = \xi + 1 = 2.881$. Both solid and dotted parts of the orange line are plotted using (5.6). (c) Dimensionless velocity, $V = v/c$, of the shear band as a function of $\lambda = l/l_0$ for $n = 1.1$ and $\lambda_* = 0.75$ (equation (4.18) or (G.13), bold blue and red lines before and after the discontinuity reflects from the tip at $\xi_E = 1.881$, $\tau_E = 2.881$, respectively). For the sake of comparison, dotted lines are plotted using (4.18), but after the reflection. Inset shows a magnified view near the discontinuity.

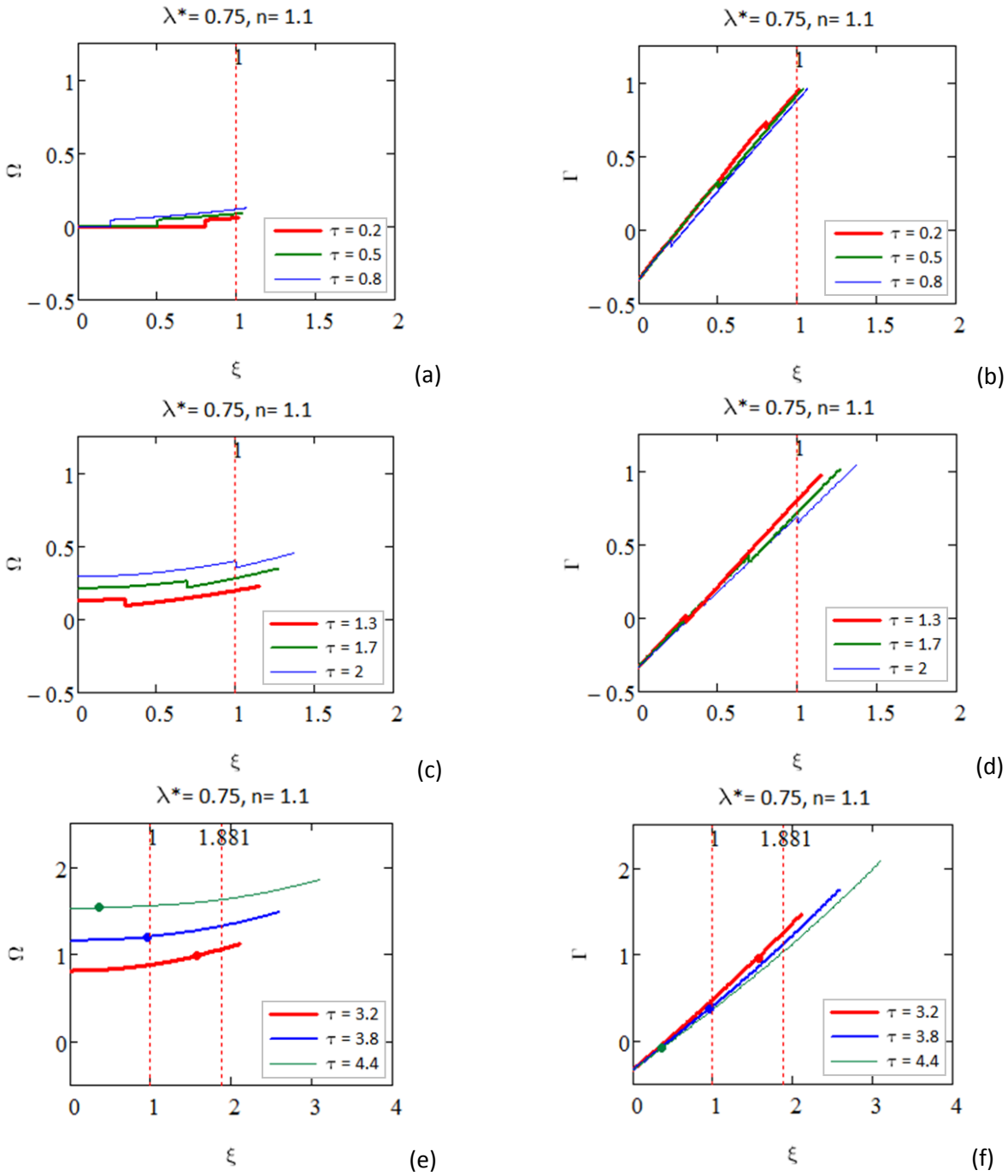

Figure 8. Distributions of (a, c, e) normalized material velocity, $\Omega = \eta/(c\gamma_0)$, and (c, d, f) strain, $\Gamma = -\gamma/\gamma_0$, along the slope as functions of dimensionless coordinate, $\xi = x/l_0$, at different dimensionless times, $\tau = ct/l_0$, when (a, b) the discontinuity has not reflected yet from $x = 0$ ($\tau = 0.2$, 0.5, 0.8), (c, d) after it reflected from $x = 0$ ($\tau = 1.3$, 1.7, 2), but before it reached the band tip $\xi = 1.881$ at $\tau = 2.881$, and (e, f) after the reflection from the tip ($\tau = 3.2$, 3.8, and 4.4) for $\lambda_* = 0.75$ and $n = 1.1$. The discontinuity magnitude, $\Delta_1 = 8.382\times10^{-3}$, after it reflects from the band tip (the same for all curves in (e) and (f)) is an order smaller than magnitude $\Delta_0 = 4.545\times10^{-2}$ (the same for all curve in (a) through (d)) after the reflection. Note that in (a),(b), (e), (f) and (c), (d), the discontinuity moves towards the slide end, $x = 0$, and the band tip, $x = l(t)$, respectively. The discontinuity is not visible in (e) and (d), so its location is indicated by dots.

5.2. Discontinuity reflected from the band tip

In a similar manner, equations (4.17) – (4.24) can be rewritten in the normalized form (4.28) in the case of homogeneous loading (5.1) and discontinuity reflection from the band tip (Appendix G). As can be seen from (G.14), both $\Gamma_2(\lambda)$ and $\Omega_2(\lambda)$ monotonically grow with the band length approaching the same asymptote $[\Gamma_s(\lambda) + 2\Omega_1(\lambda_{RU}(\lambda))]/2$ for $\lambda \to \infty$, remaining always greater and less than the asymptote, respectively. This can also be observed in Figure 7a and Figure 9a where $\Gamma_2(\lambda)$ and $\Omega_2(\lambda)$ are plotted for $n = 1.1$ and 1.2, respectively (in both cases, $\lambda_* = 0.75$). As expected, both $\Gamma_2(\lambda)$ and $\Omega_2(\lambda)$ experience a jump when the crack tip is overtaken by the discontinuity.

Figure 7b and Figure 9b show in ξ, τ coordinates the dimensionless length of the shear band and discontinuity characteristics for the same parameters ($n = 1.1$ or 1.2 and $\lambda_* = 0.75$). While the velocity changes at point E (Figure 4 and Figure 6), the change is hardly noticeable in Figure 7c, where the lines, computed with (solid curves) and without (dotted lines) taking into account that the discontinuity reaches the band tip, practically coincide. A small (compared to the magnitude) velocity jump, when the discontinuity reflects from the band tip is present though, as evident in the inset in Figure 7c, which gives a magnified view of the discontinuity for $\lambda_* = 0.75$ and $n = 1.1$. The velocity behavior for $\lambda_* = 0.75$ and $n = 1.2$ is similar. In general, the tip velocity jump decreases as the band becomes larger (i.e., with more reflections of the discontinuity from the band tip). This can be directly observed from expressions (4.27), the difference of which decreases with increasing l_E (and not only for the homogeneous load (5.1)).

It is important to note that although in Figure 9b, the discontinuity reflects from $x = 0$ for the second time, it will never reach the band tip again; at least, from the practical standpoint. This is in fact the case for most of the parameter combinations under consideration. For example, the discontinuity lags behind the band tip until at least when $\xi \le 10^3$ for $\lambda_* = 1$ and $n \ge 1.04$, for $\lambda_* = 0.75$ and $n \ge 1.02$ and for $\lambda_* = 0.5$ and $n \ge 1.01$ (Appendix F). With increasing n, the value of ξ where the discontinuity arrives to the band tip becomes larger. This simplifies further analysis as it is unlikely that the size of real landslides would exceed l_0 by more than three orders of magnitude (although one could envision two orders; Chapter 8).

Distributions of Ω and Γ along the slope are shown in (Figure 8e and f) for the same parameters ($\lambda_* = 0.75$, $n = 1.1$) as in Figure 8a through Figure 8d, but for larger dimensionless times $\tau = 3.2$, 3.8, and 4.4, i.e., after the discontinuity reflects from the shear band tip $\xi = 1.881$ at $\tau = 2.881$. The end of each curve in Figure 8e for Ω and in Figure 8d for Γ corresponds to the propagating band tip. The discontinuity (marked by dots) is not visible at the scales of Figure 8e and Figure 8f because after the reflection from the tip, it became an order of magnitude smaller (4.545×10^{-2} before reflection and 8.382×10^{-3} after). Therefore, similar to the band tip velocity, the magnitudes of the propagating discontinuities of Ω and Γ also quickly reduce with each reflection from the band tip. This is a general trend, which is independent of the choice of parameters λ_* and n.

Figure 9 and Figure 10, plotted for $\lambda_* = 0.75$, $n = 1.2$, show similar patterns as those presented in Figure 7 and Figure 8 for $\lambda_* = 0.75$, $n = 1.1$. For example, both $\Gamma_2(\lambda)$ and $\Omega_2(\lambda)$ in Figure 9a monotonically grow approaching the same asymptote $\Omega_1(\lambda_{RU}(\lambda) + \Gamma_s(\lambda)/2$ for $\lambda \to \infty$. The band velocity trends in Figure 7c are also similar and so are the distributions of Γ and Ω along the slope displayed in Figure 10 and Figure 8 for $\tau = 0.2$, 0.5, and 0.8 (i.e., before the discontinuity reflects from $x = 0$ at $\tau = 1$) and for $\tau = 1.3$, 1.7, and 2 (i.e., after it reflects from $x = 0$).

There are differences, however, with respect to the location of point E where the discontinuity reflects from the band tip. For $\lambda_* = 0.75$ and $n = 1.1$, the reflection happens at $\xi_E = \lambda_E = 1.881$ while for $\lambda_* = 0.75$, the discontinuity does not reach the crack tip at all when $n = 1.24$ tip (Figure F.1 in Appendix F). Hence, for $\lambda_* = 0.75$ when n changes from 1.1 to 1.24, λ_E changes from 1.881 to ∞. In particular, because in Figure 9b is plotted for $n = 1.2$ instead of $n = 1.1$, the point where the crack tip is overtaken by the discontinuity is extended to $\xi_E = \lambda_E = 8.43$. As a result, both strain and velocity distributions in Figure 9 and Figure 10 can now be observed at a larger scale, which presents some new features.

For $n = 1.1$, for example, the dimensionless time $\tau = 2$ (last in Figure 8) is relatively close to time $\tau_E = 2.881$, when the discontinuity reaches the band tip, while for $n = 1.2$, the discontinuity is still relatively far from the tip (Figure 10c and Figure 10d) since $\tau_E = 9.43$. For dimensionless times $\tau = 3$, 5, and 8 in Figure 10e and Figure 10f, which are closer to $\tau_E = 9.43$,

the actual magnitudes of the discontinuity are the same in both figures, but the discontinuity is less visible because the magnitudes of strain and material velocity become considerably larger at $\tau = 3$, 5, 8 than before. Also, the physical location of the discontinuity is closer to the propagating band tip for these times.

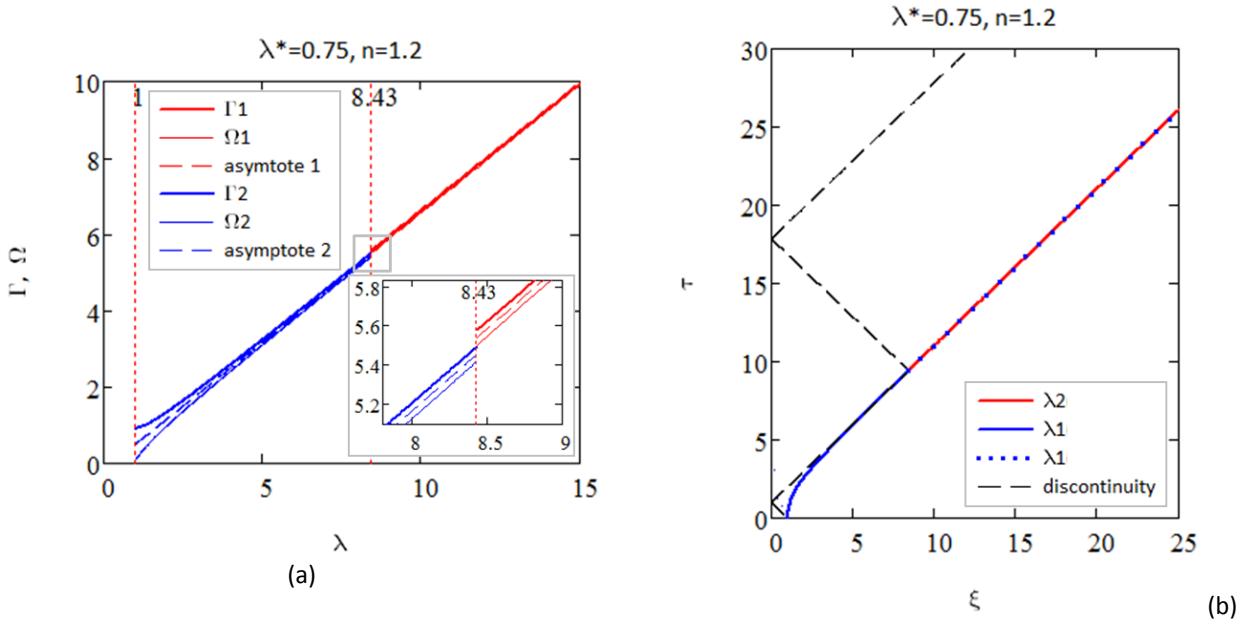

Figure 9. (a) Normalized strain, $\Gamma_1 = -\gamma_1 / \gamma_0$ (bold lines), and normalized material velocity, $\Omega_1 = \eta_1 / (c\gamma_0)$ (thin lines), at the shear band tip as functions of the normalized band length, $\lambda = l/l_0$, for $\boldsymbol{\lambda}_* = 0.75$ and $n = 1.2$ before (blue lines) and after (red lines) the discontinuity arrives at the band tip $\xi_E = 8.43$ at $\tau_E = 9.43$. Asymptotes of Γ_1 and Ω_1 at $\lambda \to \infty$ are shown by the dashed lines (blue and red, respectively). (b) Dependence of the normalized band size, $\lambda = l/l_0$, on dimensionless time, $\tau = ct/l_0$, for $\boldsymbol{\lambda}_* = 0.75$ (i.e., $\gamma_a / \gamma_0 = 1/3$) and $n = 1.2$ before (blue, solid and dotted lines) and after (red line) the discontinuity arrives at the band tip at $\xi_E = 8.43$ and reflects back at $\tau_E = 9.43$.

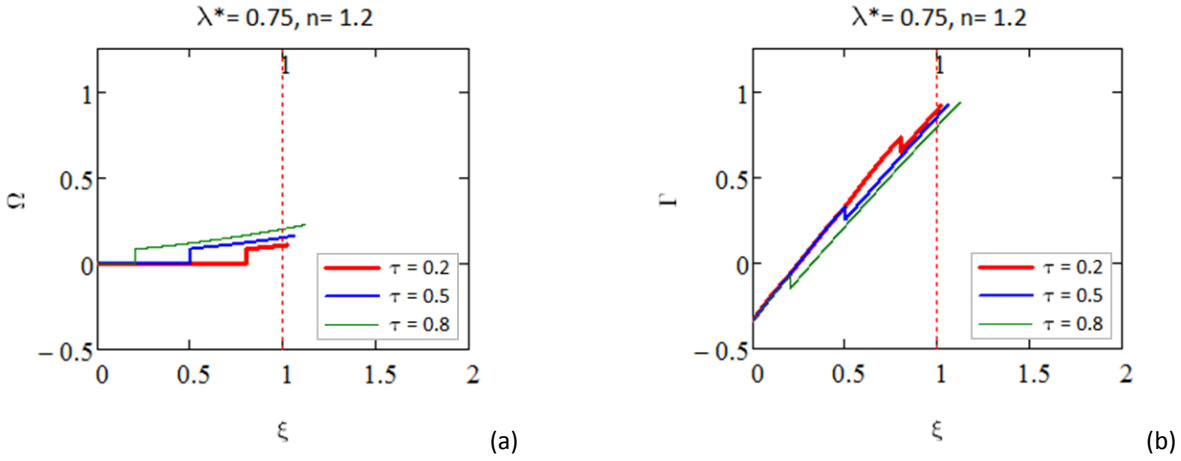

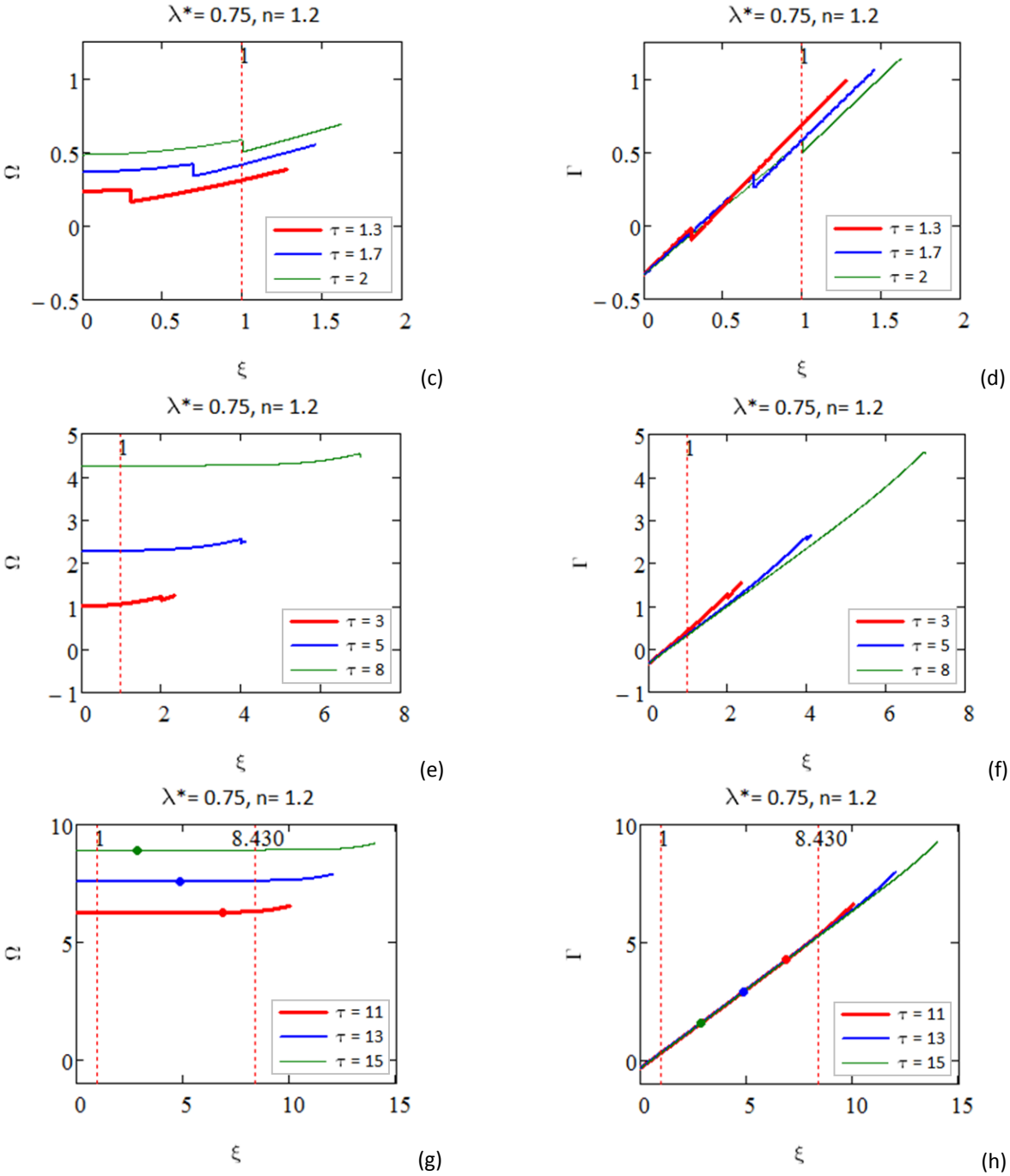

Figure 10. Distributions of (a, c, e, g) dimensionless material velocity, $\Omega = \eta/(c\gamma_0)$, and (b, d, f, h) normalized strain, $\Gamma = -\gamma/\gamma_0$, along the slope as functions of dimensionless coordinate, $\xi = x/l_0$, at dimensionless times, $\tau = ct/l_0$, of (a, b) 0.2, 0.5, 0.8 (when the discontinuity has not reflected yet from $x = 0$), (c, d) 1.3, 1.7, 2 (soon after it reflected from $x = 0$), (e, f) 3, 5, 8 (shortly before the discontinuity arrives at the band tip), and (g, h) 11, 13, 15 (after the discontinuity is reflected from the tip) for $\lambda_* = 0.75$ and $n = 1.2$. The magnitude $\Delta_1 = 5.741\times10^{-4}$ of the discontinuity after it reflects from the tip (the same in (g) and (h)) is two orders smaller than magnitude $\Delta_0 = 8.333\times10^{-2}$ before the reflection (the same in (a) through (f)). Note that in (a), (b), (g), (h) the discontinuity moves towards the slide end, $x = 0$, while in (c), (d), (e), (f) it moves towards the band tip, $x = l(t)$.

Figure 10g and Figure 10h display the distributions of Γ and Ω along the slope for even larger times $\tau = 11$, 13, 15 and the same parameters $\lambda_* = 0.75$, $n = 1.2$. These are times before the discontinuity reflects again from $x = 0$, but after its reflection from the band tip at E. Because of this reflection, the magnitude of the discontinuity decreases by two orders (from $\Delta_0 = 8.333\times10^{-2}$ before the reflection to $\Delta_1 = 5.741\times10^{-4}$ after) while the magnitudes of both material strain and velocity further increase with time. This again is a common trend, independent of parameters, which justifies allowing discontinuities in our model as further discussed below (Section 10.1).

When n is relatively close to 1, its value is important with respect to the magnitudes of the shear band and material velocities. We can see from (4.14) that when n changes, for example, from 1.1 to 1.2, the factor of $n - 1$ in (4.14) doubles and so do the initial magnitudes of the band and material velocities. In turn, this translates in the magnitude of material velocity in Figure 10 being roughly doubled compared to Figure 8.

CHAPTER 6. SLIDE PROPERTIES

6.1. Slope failure and slide length

As above, in this chapter, we consider the case of negligible water resistance, τ_w, so the homogeneous load (5.1) in the infinite slope is $T_0 = (\tau_g - \tau_r)/E$. The effect of τ_w will be addressed in Appendix K.

As the shear band propagates, the strain magnitude at the tip $x = l(t)$ increases until it reaches the critical magnitude of the passive failure strain $\gamma_p = (p_p - p_0)/E > 0$ [*Puzrin and Germanovich*, 2005a], which corresponds to the passive failure stress $\sigma(l_f, t_f) = -p_p$ ($p_p > 0$). At this point, the shear band can be visualized as turning abruptly towards the surface, which effectively ends its propagation at $x = l_f$, $t = t_f$. We refer to this event as 'global failure' or 'slope failure', and first obtain $\gamma_1(l_f)$ from (4.9) or (5.5) with $x = l_f$. In the case of the discontinuity that has not reflected yet from the band tip, condition of the global failure can be expressed from (4.9) as

$$\frac{\gamma_s^2(l_f) + \gamma_c^2}{2\gamma_s(l_f)} = -\gamma_p \tag{6.1}$$

In turn, (6.1) yields

$$\gamma_s(l_f) = -\gamma_p \pm \sqrt{\gamma_p^2 - \gamma_c^2} \tag{6.2}$$

where the static strain $\gamma_s(l_f) = -\gamma_0 - T_0(l_f - l_0)/h$ is defined by (5.2) with $l = l_f$. Using then (2.12), substituting (5.2) in (6.2), and solving the resulting equation for l_f, we obtain the dimensionless failure length

$$\lambda_f = \frac{l_f}{l_0} = 1 + \lambda_* \left[\frac{\gamma_p}{\gamma_0} - 1 + \sqrt{\frac{\gamma_p^2}{\gamma_0^2} - \frac{1}{n}} \right] \tag{6.3}$$

where λ_* is given by (4.29) and we assumed that the global failure does not occur for $l < l_0$, which implies that $|\gamma_p| \geq \gamma_0$ (otherwise, the global failure would occur before the shear band even starts propagating dynamically). Hence, because $n > 1$, the solution (6.3) exists, and because $\lambda_f > 1$, we chose the minus sign in (6.2), which corresponds to the plus sign before the square root in in (6.3).

If the discontinuity reaches the band tip, the left hand side in (6.1) needs to be replaced by

the tip strain in (4.22) (with $l = l_f$), so expression (6.2) becomes

$$\gamma_s(l_f)+\gamma_s(l_R)-\gamma_c^2/\gamma_s(l_R)=-\gamma_p\pm\sqrt{\gamma_p^2-\gamma_c^2} \tag{6.4}$$

where l_R is found from

$$\frac{l_f+l_R}{c}+\int_{l_0}^{l_R}\frac{dl}{v_1(l)}=t_E+\int_{l_E}^{l_f}\frac{dl}{v_2(l,l_{RH}(l))} \tag{6.5}$$

Function $l_{RH}(l)$ is the same as in (4.23). In this case, the dimensionless failure length

$$\lambda_f=1+\lambda_*\left[\frac{\gamma_p}{\gamma_0}-1+\sqrt{\frac{\gamma_p^2}{\gamma_0^2}-\frac{1}{n}}\right]+\Delta\lambda_f,\qquad \Delta\lambda_f=\lambda_*\left[\frac{1}{n\Gamma_s(\lambda_R)}-\Gamma_s(\lambda_R)\right] \tag{6.6}$$

is obtained by solving (6.4) with $\lambda_R = l_R/l_0$ and Γ_s defined by (5.7). Because $\lambda_* > 0$, $\lambda_R > 1$, and $n > 1$, $\Delta\lambda_f < 0$, so for λ_f to be greater than 1, we chose again the plus sign before the square root in (6.6).

The value of γ_p/γ_0 depends upon the sediment properties, which will be considered in Chapter 8. Here we only note that assuming $\tau_w = 0$ overestimates T_0, and, hence, overestimates λ_* in (4.29). Therefore, λ_f computed based on (6.3) or (6.6) is also overestimated. In other words, (6.3) and (6.6) provide an upper estimate of the slide size, which, in turn, provides an additional safety factor.

As discussed in Section 2.2, our model is applicable for $\eta_1(l) < c$. Substituting $l = l_f$ into (4.9) and using (6.1), we see that $\eta_1(l_f)/c = \gamma_p + \gamma_c^2/\gamma_s(l_f)$. Here $\eta_1(l)$ is a positive function monotonically increasing with l while terms in the right hand side have different signs and the absolute values smaller than one. We conclude, therefore, that for $l \le l_f$, condition $\eta_1(l) < c$ is satisfied when the discontinuity does not reach the band tip. When it does, a similar argument applies after using $\gamma_2(l)$ from (4.29) in the failure condition $\gamma_2(l_f) = -\gamma_p$ and rewriting the tip velocity at failure in (4.29) as $\eta_1(l_f)/c = \gamma_p + \gamma_c^2/[\gamma_s(l_f) - 2\eta_1(l_R)/c]$. Therefore, up to the time τ_f of global failure, the model is physically consistent in the sense that the material at the band end moves slower than the band tip grows.

6.2. Slide velocity

To understand the slide potential to generate a tsunami of a considerable magnitude, we

evaluate below the average material velocity

$$\bar{\eta}(t)=\frac{1}{l}\int_0^l \eta(x,t)dx \tag{6.7}$$

which is further called “slide velocity.”

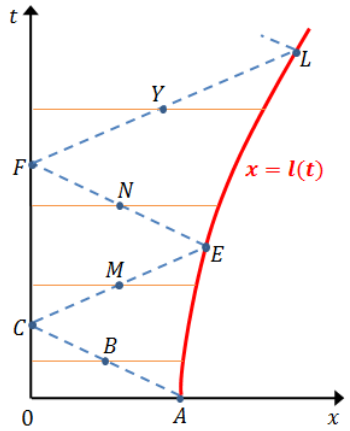

Figure 11. Integration intervals (horizontal lines) for calculating the average material velocity in (6.7) at given moments of time. Points *B*, *M*, *N*, and *Y* are the positions of the discontinuity at these times. The discontinuity, initiated from point *A*, consequently reflects from points *C*, *E*, *F*, *L*, and so on. Integration in (6.11), (6.12), and (6.14) is done over two adjacent intervals separated by the discontinuity position.

We first integrate the second equation in (3.1) with respect to x for constant time $t < l_0 / c$ (along the horizontal line that passes through point *B* in Figure 11) and obtain

$$\frac{1}{c^2}\int_{x_B}^{l}\frac{\partial\eta(x,t)}{\partial t}dx=\int_0^l\frac{\partial\gamma(x,t)}{\partial x}dx+\frac{1}{h}\int_0^l T(x)dx \tag{6.8}$$

where $x_B = l_0 - ct$ (Figure 11). Changing the order of integration and differentiation in the left hand side and taking into account that both l and x_B are functions of time yields

$$\frac{\partial}{\partial t}\int_{x_B}^{l}\eta dx=v_1\eta_1(l)+c\eta^+(x_B,t)+c^2[\gamma_1(l)-\gamma_s(l)+\gamma_s(x_B)-\gamma^+(x_B,t)] \tag{6.9}$$

where we used (2.11), (4.8), and that $\gamma(l, t) = \gamma_1(l)$, $\eta(l, t) = \eta_1(l)$ given by (4.9). Using then the jump condition (4.4) and integrating (6.9) with respect to time results in

$$\int_0^l\eta dx=\int_{l_0}^{l}\eta_1(l)dl+c^2\int_{l_0}^{l}\frac{\gamma_1(l)-\gamma_s(l)}{v_1(l)}dl \tag{6.10}$$

where we took into account that $dl = v_1 dt$ and $\eta(x, t) = 0$ for $0 < x < l_0 - ct$ (which allowed us to replace x_B with 0 in the lower limit of the integration in the left hand side of (6.10)). Finally,

substituting (6.10) into (6.7) and using (4.9) gives

$$\frac{\bar{\eta}(l)}{c} = -\frac{1}{l}\int_{l_0}^{l} \gamma_s(l)dl \qquad (0 < t < l_0 / c) \tag{6.11}$$

For time $l_0/c < t < (l_0 + l_E)/c$, where l_E is defined by (4.20), the integration interval is the horizontal line that passes through point *M* in Figure 11. Otherwise, consideration is similar and results (Appendix J) in the same expression (6.11) for $\bar{\eta}(l)$. Therefore, (6.11) is valid when $0 < t < (l_0 + l_E)/c$, when the discontinuity starts at point *A* and continues propagating until it reaches point *E* (with *M* replacing *B* as needed; Figure 11).

For $(l_0 + l_E)/c < t < (l_0 + 2l_E + l_L)/c$, when the discontinuity moves from point *E* through point *F* to point *L* (horizontal integration intervals that include points *N* and *Y* in Figure 11), the slide velocity is given by (Appendix J)

$$\frac{\bar{\eta}(l)}{c} = -\frac{1}{l}\int_{l_0}^{l} \gamma_s(l)dl + \frac{1}{l}\int_{l_E}^{l}\left[\frac{\eta_2(l)}{c} + c\frac{\gamma_2(l) - \gamma_s(l)}{v_2(l)} + \gamma_s(l)\right]dl \qquad (t_E < t < t_L) \tag{6.12}$$

where $t_E = (l_0 + l_E)/c$, t_L and l_L are defined by

$$t_L = t_E + \int_{l_E}^{l_L} \frac{dl}{v_2(l, l_{RL}(l))}, \quad l_L + 2l_E + l_0 = ct_L \tag{6.13}$$

and function $l_{RL}(l)$ is obtained (Appendix G) by replacing l_{RU} with l_{RL} in (4.19) and solving the resulting equation. Comparing (6.12) to (6.11), we observe that $\bar{\eta}(l)$ remains continuous at $l = l_E$, although the band velocity jumps at point *E* due to the reflection of the discontinuity from the band tip (Figure 7c). Points *Y* and *N* in Figure 11 correspond to points *M* and *B*, respectively.

Equations (6.11) and (6.12) represent the cases when the discontinuity does not reach the crack tip after the first or the second reflection from $x = 0$ (Appendix F), respectively. These equations exhibit all features of the general solution (Appendix J) for the arbitrary number of reflections.

For homogeneous distribution (5.1) of $T(x)$, expressions (6.11), (6.12) become

$$\bar{\Omega}(\lambda)=\frac{\bar{\eta}(l)}{\gamma_0 c}=\begin{cases}\left(1-\dfrac{1}{\lambda}\right)\left(1+\dfrac{\lambda-1}{2\lambda_*}\right) & (0<\tau<1+\lambda_E)\\ \displaystyle\int_{\lambda_E}^{\lambda}\left\{\Omega_2(\lambda)-\frac{\Gamma_2(\lambda)-\Gamma_s(\lambda)}{V_2(\lambda)}-\Gamma_s(\lambda)\right\}d\lambda+ & \\ +\left(1-\dfrac{1}{\lambda}\right)\left(1+\dfrac{\lambda-1}{2\lambda_*}\right) & (1+\lambda_E<\tau<1+2\lambda_E+\lambda_L)\end{cases} \tag{6.14}$$

where $\Gamma_2(\lambda)$ and $\Omega_2(\lambda)$ are given by (G.14) and λ_E is defined by (G.16) (Appendix G). Dependence $\bar{\Omega}(\lambda)$ is shown in Figure 12 for $n = 1.1$ and the values of $\lambda_* = 0.1$, 0.5, and 1. For these parameters, the discontinuity lags behind the tip after the first (for $\lambda_* = 0.1$ and 0.5) or second (for $\lambda_* = 1$) reflection from $x = 0$ (i.e., point L can be considered being at infinity in Figure 4b, Figure 6a, and Figure 11). Before the discontinuity arrives at E, $\bar{\Omega}(\lambda)$ is independent of n, but the position of point E itself (or the value of λ_E) does depend upon n and so does $\bar{\Omega}(\lambda)$ in (6.14) after the reflection at E. In Figure 12, for $\lambda = 1 - 10^2$ and $\lambda_* = 0.2$, 0.5, $\bar{\Omega}(\lambda) \sim 10^{-2} - 10^2$. This implies that by the time the shear band increases its initial length by two orders of magnitude, the average slide velocity becomes $\sim 0.1c$ for $\gamma_0 = 0.001$. For $\gamma_0 = 0.01$, $\bar{\eta}(l)$ may reach a value $\sim c$, although it remains smaller than c. Indeed, as shown in Section 6.1, $\eta_1(l) < c$ for $l < l_f$. Hence, because $\eta(l(t), t) < \eta_1(l(t))$ (e.g., Figure 7a, Figure 8, Figure 9a, Figure 10), we see that $\bar{\eta}(l) < c$ for $l < l_f$ as well.

It should be noted that neglecting τ_w overestimates the value τ in (2.5), which increases T_0 and, therefore, the slide velocity. This can be seen in Figure 12, where a larger slide velocity corresponds to a smaller value of λ_*, which per (4.29), corresponds to a larger T_0.

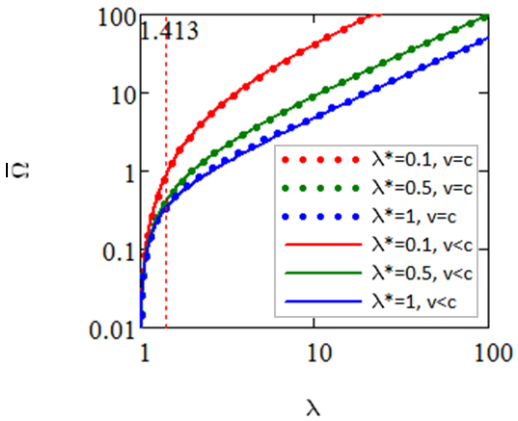

Figure 12. Dimensionless slide velocity, $\bar{\Omega} = \bar{\eta}/(c\gamma_0)$, as a function of the dimensionless length, $\lambda = l/l_0$. Solid lines correspond to the exact solution, $v = v(l)$ (in (6.14)), with $n = 1.1$, while dotted lines represent the asymptotic solution, $v = c$ (in (K.10) with $\beta = 0$). Red, green, and blue lines correspond to $\lambda_* = 0.1$, 0.5 and 1, respectively. For $\lambda_* = 0.1$ and 0.5 with $n = 1.1$, the discontinuity does not reach the band tip in the exact solution (red and green, solid lines) (Figure F.1). For $\lambda_* = 1$ and $n = 1.1$, however, blue, solid line is plotted for solutions in (6.14) before and after the discontinuity visits the tip, respectively, at $\xi = \lambda_E = 1.413$ ($\tau_E = 2.413$).

CHAPTER 7. ASYMPTOTIC SOLUTION

7.1. Asymptote of long bands

As discussed above, the shear band typically acquires the velocity of propagation comparable to the speed c of elastic waves after it propagates the distance of approximately two or three times its original lengths. If we are interested in much greater lengths ($\sim 10^1 l_0 - 10^2 l_0$), it is natural to simplify the solution by assuming the band velocity, v, reaching c already at $t = 0$ and remaining constant after that.

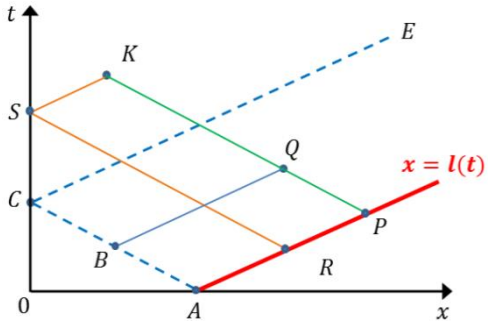

Figure 13. Shear band propagation with the speed, c, of elastic waves. Tip location line $x = l(t) = l_0 + ct$ and characteristic line CE of the propagating discontinuity have the same slopes $dl/dx = 1/c$ and do not intersect. Q and K are arbitrary points below and above CE, respectively. They are similar to point Q in domain ACE in Figure 4a and point K in domain CEF in Figure 4b, respectively.

For $v = c$, the band length at time t

$$l(t) = l_0 + ct \tag{7.1}$$

and the boundary condition (2.7) yields

$$\eta(l)/c + \gamma(l) = 0 \tag{7.2}$$

In this approximation, the discontinuity, once reflected at $x = 0$, never reaches the band tip (Figure 13) since the band propagates with the same speed as the discontinuity. This approximation is asymptotic for large band sizes because in the exact solution, $v(l)/c \to 1$ as $l \to \infty$ (even if the discontinuity arrives at the band tip one or several times).

It should be noted that $v(l)/c \to 1$ also when $\gamma_c \to 0$ or, which is the same for any given n, when $\gamma_0 \to 0$. This implies that asymptotics of a large l and small γ_0 (or small γ_c) are the same, which indicates that in the absence of the resistance to the fracture growth (since $\gamma_c \to 0$ or $\gamma_0 \to 0$), the band velocity jumps to c (but not higher than c) immediately at the onset of growth. Similarly, $\gamma_c \to 0$ if $n \to \infty$ for any given γ_0, so the asymptotes of $l \to \infty$ and $n \to \infty$ are

equivalent as well. Comparison of these asymptotes to the exact solution is presented in Section 8.1.

Similar to (4.13), for the arbitrary point *Q*(*x*, *t*) below the discontinuity line *CE* in Figure 13,

$$\begin{cases} \gamma(x,t) = \gamma_s(x) + \eta(x,t)/c \\ \eta(x,t)/c = -\gamma_s(l_P)/2 \end{cases} \qquad (l/l_0 >> 1 \text{ or } n >> 1) \tag{7.3}$$

and similar to (4.15), for the arbitrary point *K*(*x*, *t*) above line *CE* in Figure 13,

$$\begin{cases} \gamma(x,t) = \gamma_s(x) + [\gamma_s(l_R) - \gamma_s(l_P)]/2 \\ \eta(x,t)/c = -[\gamma_s(l_R) + \gamma_s(l_P)]/2 \end{cases} \qquad (l/l_0 >> 1 \text{ or } n >> 1) \tag{7.4}$$

where l_P and l_R are related to (*x*, *t*) (below and above *CE* in Figure 13, respectively) by

$$l_P = (ct + l_0 + x)/2, \qquad l_R = (ct + l_0 - x)/2 \tag{7.5}$$

At the band tip, $x = l_f$, the boundary condition (2.7) (for $v = c$) combined with the slope failure condition, $\gamma(l_f, t_f) = -\gamma_p$ (Section 6.1), results in the material velocity, $\eta(l_f, t_f)/c = \gamma_p$, at the band tip at failure. Hence, similar to the exact solution (Section 6.1), $\eta(l_f, t_f)/c < 1$.

In the case of homogeneous load (5.1), the static strain is given by (5.2). Therefore, using (4.28), (5.2), and (7.5), the material strain and velocity below *CE* (Figure 13) are obtained from (7.3) as

$$\begin{cases} \dfrac{\gamma(x,t)}{-\gamma_0} = \dfrac{1}{2} + \dfrac{1}{4\lambda_*}\left(\dfrac{3x - ct}{l_0} - 3\right) \\ \dfrac{\eta(x,t)}{c\gamma_0} = \dfrac{1}{2} + \dfrac{1}{4\lambda_*}\left(\dfrac{ct + x}{l_0} - 1\right) \end{cases} \qquad (l/l_0 >> 1 \text{ or } n >> 1) \tag{7.6}$$

Similarly, strain and material velocity above *CE* (Figure 13) are found from (7.4) as

$$\begin{cases} \dfrac{\gamma(x,t)}{-\gamma_0} = 1 + \dfrac{1}{2\lambda_*}\left(\dfrac{x}{l_0} - 2\right) \\ \dfrac{\eta(x,t)}{c\gamma_0} = 1 + \dfrac{1}{2\lambda_*}\left(\dfrac{ct}{l_0} - 1\right) \end{cases} \qquad (l/l_0 >> 1 \text{ or } n >> 1) \tag{7.7}$$

where η is independent of *x*, although it is changing with time. Note that a part of the slide (along the slope) where $\eta(x, t)$ is spatially constant becomes larger with time (as the shear bands grows).

Expressions (7.6) and (7.7) can also be obtained directly from (5.9) and (5.10), respectively,

by considering the limit of $n \to \infty$ or $l \to \infty$. Because the discontinuity does not ever reach the band tip for $n \geq 1.4392$ (Appendix F and Figure F.1a), the limit of $n \to \infty$ (or $l \to \infty$) can also be applied directly to (4.13) and (4.15), which results again in (7.6) and (7.7), respectively, if $T(x) = T_0 = \text{const}$. At the moment of slope failure, $l_f = l_0 + ct_f$, and the failure condition $\gamma(l_f, t_f) = -\gamma_p$, used with the first equation in (7.6), yields the shear band length at failure

$$l_f / l_0 = 1 + \lambda_*(2\gamma_p/\gamma_0 - 1) \tag{7.8}$$

Given that the expected value of γ_p is at least several times greater than γ_0 (Chapter 8) and that $n > 1$, l_f in (7.8) is only slightly larger than in the exact solution (6.3).

The normalized strain, Γ, and material velocity, Ω, are given by (4.28) with (7.3) and (7.4). Distributions of Ω along the slope (i.e., in the physical space) are shown in Figure 14a (solid lines) for dimensionless times $\tau = 10$, 20 and $\lambda_* = 0.5$. For comparison, the exact solution (5.9), (5.10) is also plotted (dashed lines) in Figure 14a for the same times and λ_*. The exact solution, however, also depends upon n, so we used $n = 1.1$ when the discontinuity does not reach the band tip (Figure F.1 in Appendix F). As can be seen, the patterns of Ω are similar for the exact and asymptotic solutions, although the magnitudes of the discontinuity jump differ by an order (0.5 and 0.045, respectively). These magnitudes do not change with time, but their relative values decrease (Figure 14a). The difference between the asymptotic and exact solutions is insignificant for large enough values of τ (Figure 14a).

Effect of n on the distributions of Ω along the slope is shown in Figure 14b for $n = 1.1$ (blue, thin line), 1.2 (green, dashed line) and $\tau = 9$. The physical locations of the discontinuity are the same, but the magnitude, Δ_0, of the discontinuity of Ω increases with n. For example, $\Delta_0 = 4.545\times10^{-2}$ and 8.333×10^{-2} for $n = 1.1$ and 1.2, respectively. Note that at any given time, the band length (solid lines in Figure 14) in the asymptotic solution is slightly longer than in the exact one (dashed lines in Figure 14) because the band tip velocity is larger in the asymptotic solution.

The slide velocity, $\overline{\Omega}$, can be obtained either by averaging the material velocity in (7.3) and (7.4) at a given time or directly from (6.10) by replacing $v_1(l)$ with c. This results in (6.11) (with $v_1(l) = c$), which is valid for any time, since the discontinuity does not reach the band tip if $v = c$. Dependence $\overline{\Omega}(\lambda)$ is shown in Figure 12 for $\lambda_* = 0.1$, 0.5, 1 and $n = 1.1$. For $\lambda_* = 0.1$, 0.5 and

$n = 1.1$, the discontinuity does not reach the tip (Figure F.1 in Appendix F), and in this case, the exact and asymptotic solutions are nearly identical. But even for $\lambda_* = 1$ and $n = 1.1$ (blue solid and dotted lines), when the discontinuity arrives at the tip at $\tau_E = 2.413$ and $\lambda_E = 1.413$ (in the exact solution), the asymptotic solution still provides a close match to the exact solution.

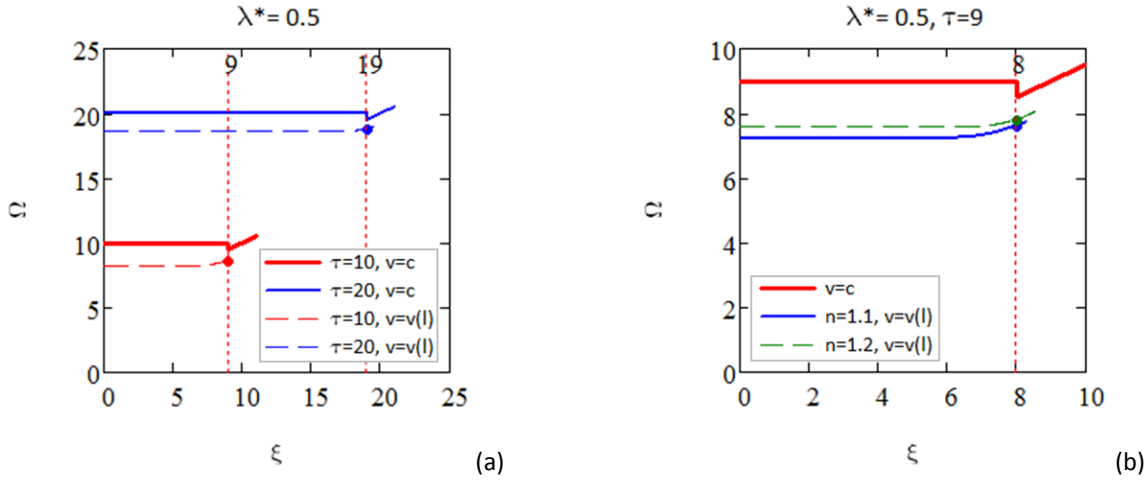

Figure 14. (a) Distribution of dimensionless material velocity, $\Omega = \eta/(c\gamma_0)$, along the slope as a function of dimensionless longitudinal coordinate, $\xi = x/l_0$, at dimensionless times, $\tau = ct/l_0$, of 10 and 20. Solid lines show the asymptotic solution (7.3), (7.4) (when $v = c$), while dashed lines correspond to the exact solution (when $v = v(l)$) in (4.7) and (4.18) with $\lambda_* = 0.5$ and $n = 1.1$ (when the discontinuity never reaches the band tip). The magnitude of the discontinuity is $\Delta_0 = 0.5$ in asymptotic (solid line) and 4.545×10^{-2} exact (dashed line) solutions. Dots indicate locations of the discontinuities, which are not visible at the figure scale. (b) Effect of the values of n on Ω in the exact solution (4.7), (4.18) for $n = 1.1$ (blue, thin line) and $n = 1.2$ (green, dashed line) at $\tau = 9$. The corresponding magnitudes of discontinuity are $\Delta_0 = 4.545\times10^{-2}$ and 8.333×10^{-2}, respectively. The asymptotic solution given by (7.3) and (7.4) (bold line) is independent of n because this solution corresponds to $n \to \infty$.

7.2. Static versus dynamic failure lengths

Expressions (6.3) and (6.4) for the dimensionless failure lengths, $\lambda_f = l_f/l_0$, before and after the discontinuity reaches the band tip at $t = t_E$ were obtained from conditions $\gamma_1(l_f) = -\gamma_p$ and $\gamma_1(l_f) = -\gamma_p$, respectively, where the dynamic tip strains are given by (4.9) and (4.22). Parameter l_f is important because it defines the amount of material available for the actual slide. It would typically be evaluated based on the static considerations such as limiting equilibrium condition [*Hampton et al.*, 1996; *Leynaud et al.*, 2004; *Sansoucy et al.*, 2007; *Bradshaw et al.*, 2010]. This is equivalent to neglecting the dynamic effect and assuming the static strain at the tip of the growing band. The corresponding length, L_f, of the static (or progressively propagating) band at

failure is obtained from the tip condition $\gamma_s(L_f) = -\gamma_p$. Using then (5.7), results in the dimensionless static failure length

$$\Lambda_f = \frac{L_f}{l_0} = 1 + \lambda_* \left(\frac{\gamma_p}{\gamma_0} - 1 \right) \tag{7.9}$$

which can also be obtained directly from expression $L_f/h = (p_p - p_a)/\tau_* = (\gamma_p + \gamma_a)/T_0$ used, for example, by *Puzrin and Germanovich* [2005a]. Hence, taking into account the dynamic failure length from the asymptotic solution (7.8), we have

$$\lambda_f = \Lambda_f + \lambda_* \gamma_p / \gamma_0 \tag{7.10}$$

Equations (7.9) and (7.10) imply that ratio of the dynamic to static failure lengths is given by

$$\kappa = \frac{l_f}{L_f} = \frac{\lambda_f}{\Lambda_f} = 1 + \left[1 - \frac{\gamma_0}{\gamma_p} \left(1 - \frac{1}{\lambda_*} \right) \right]^{-1} \tag{7.11}$$

Because $\gamma_0/\gamma_p < 1$, κ is always greater than 1, which suggest that the dynamic effect increases the slide volume (mass) compared to the static (progressive) band growth and/or static analysis. Furthermore, in the case of retrogressive slide (Section 10.1), $\lambda_* > 1$, and (7.11) suggests that $\kappa > 2$ and close to 2 (> 1.5) for the most of the cases of $0 < \lambda_* < 1$ when $\gamma_p >> \gamma_0$ (Figure 15). For shear bands propagating downhill (Figure 2), $0 < \lambda_* < 1$ (Chapters 2 through 7) and as follows from (7.11), $1 + \lambda_* \le \kappa \le 2$. Hence, λ_* is an important parameter, defining the lower bound of κ. Isoclines of κ are shown in Figure 15. It can be seen that for small values of γ_0/γ_p, κ becomes relatively close to 2. For example, $\kappa > 1.8$ if $\gamma_0/\gamma_p < 0.2$ and $\lambda_* > 0.444$ or $\gamma_0/\gamma_p < 0.1$ and $\lambda_* > 0.286$.

The reason of l_f being greater than L_f is that the elastic wave, which starts propagating away from the tip at $t = 0$, unloads the material, which is initially at static strain $\gamma_s(x)$. As a result, $\gamma_1(l) < \gamma_s(l)$ and a larger l_f is required to satisfy the dynamic failure condition $\gamma_1(l_f) = -\gamma_p$ than L_f satisfying the static failure condition $\gamma_s(L_f) = -\gamma_p$.

Finally, (7.11) defines the value of κ in the asymptote of large length of the shear band. In the exact solution, we would use (6.3) instead of (7.10), which results in

$$\kappa = \frac{\lambda_f}{\Lambda_f} = 1 + \sqrt{1 - \frac{1}{n}\left(\frac{\gamma_0}{\gamma_p} \right)^2} \cdot \left[1 - \frac{\gamma_0}{\gamma_p} \left(1 - \frac{1}{\lambda_*} \right) \right]^{-1} \tag{7.12}$$

Although expression (7.12) now includes the bluntness parameter, n, it still shows that for small values of γ_0/γ_p, κ becomes relatively close to 2. For example, now $\kappa > 1.8$ if $\gamma_0/\gamma_p < 0.2$ and $\lambda_* > 0.468$ or $\gamma_0/\gamma_p < 0.1$ and $\lambda_* > 0.290$.

Expressions (7.11) - (7.12) have been obtained without accounting for the water resistance to the slide motion during the failure stage (Appendix A). In general, water resistance reduces the magnitude of slip and tip strain. Thus, for the same band length, the tip strain computed with accounting for the water resistance is smaller than the one without. More details on the effect of water resistance on slide parameters is given in Appendix K. For typical submarine landslides this effect is not significant (Chapter 8).

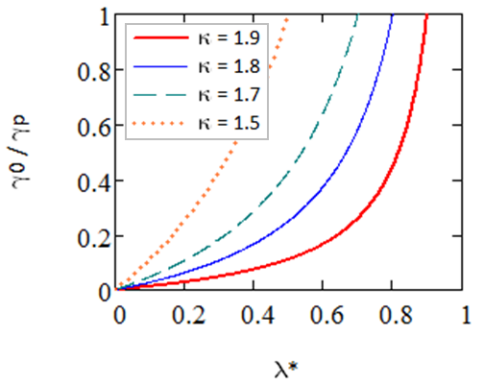

Figure 15. Ratio $\kappa = \lambda_f / \Lambda_f$ as a function of λ_* and the normalized failure tip strain γ_0/γ_p. The curves are plotted for the magnitude of λ_f / Λ_f as 1.9 (red bold line), 1.8 (blue thin line), 1.7 (green dashed line), and 1.5 (orange dotted line).

CHAPTER 8. APPLICATION TO REAL LANDSLIDES

8.1. Properties of displaced material

Literature on submarine slides [e.g., *Chowdhury*, 1978; *Bugge et al.*, 1988; *Hampton et al.*, 1996; *Fine et al.*, 2003; *Sweet and Silver*, 2003; *Hühnerbach and Masson*, 2004; *Fine et al.*, 2005; *Saurer*, 2009; *Chowdhury et al.*, 2010; *Quinn et al.*, 2011a; *Viesca*, 2011; *Dey et al.*, 2012; *Quinn et al.*, 2012; *Steiner et al.*, 2012; *Viesca and Rice*, 2012; *Wiemer et al.*, 2012] indicates a relatively wide range of the characteristic sediment, slide, and shear band parameters. The observed or inferred failure length, l_f, ranges from $\lesssim 1$ km to $\gtrsim 10^2$ km slope angle, α, from 0.01° to $\approx 20°$, and the aspect ratio, h/l_f, of the displaced material from $\lesssim 0.01$ to ≈ 0.1 (Appendix A). The density of the deposit, ρ_0, is typically within 1500 to 2000 kg/m^3; for example, $\rho_0 = 1790$ kg/m^3 in Grand Banks [*Fine et al.*, 2005] and 1850 kg/m^3 in the Izmit Bay, Turkey [*Yalciner et al.*, 2002]. The peak shear strength, τ_p, generally varies from $0.2\sigma'_v$ [*Dey et al.*, 2012] to $0.58\sigma'_v$ [*Locat et al.*, 2009], the elastic soil modulus, E, from $250\tau_p$ [*Quinn et al.*, 2011a] to $360\tau_p$ [*Viesca*, 2011], and the residual shear strength, τ_r, from $0.013\tau_p$ [*Quinn et al.*, 2011a] to $0.45\tau_p$ [*Viesca*, 2011]. Here, $\sigma'_v = -\sigma'_y = (\rho_0 - \rho_w)gh\cos\alpha$, is the y-component (normal to the slope and the shear band) of the effective stress.

The critical value of the energy release rate, J, at the onset of the dynamic band growth scales as $J_0 = (\tau_p - \tau_r)\bar{\delta}$ [*Palmer and Rice*, 1973]. The characteristic displacement, $\bar{\delta}$, in the process zone (Figure 3b) is probably the most ambiguous parameter in the landslide literature, ranging from 2 mm to 50 cm. For example, *Palmer and Rice* [1973] varied $\bar{\delta}$ from 2 mm to 1 cm, *Puzrin et al.* [2004] and *Puzrin and Germanovich* [2005a] assumed $\bar{\delta} = 2$ mm, *Chowdhury* [1978], *Chowdhury et al.* [2010], *Viesca* [2011], and *Viesca and Rice* [2012] employed 1 cm, *Saurer* [2009] and *Puzrin et al.* [2010] adopted $\bar{\delta} = 5$ cm, and *Dey et al.* [2012] and *Quinn et al.* [2011a; 2012] used 10 cm and 50 cm, respectively.

Many, if not most, submarine slopes are composed of normally-consolidated and lightly-overconsolidated sediments [e.g., *Bjerrum*, 1967; *Levin and Nosov*, 2009; *De Blasio*, 2011]. Hence, we consider a typical landslide with $\alpha = 6°$, $h = 50$ m, and sediment properties $\tau_p = 0.25\sigma'_v$, $\tau_r = 0.4\tau_p$, $E = 350\tau_p$, $\rho_0 = 1800$ kg/m^3. Density of seawater $\rho_w = 1000$ kg/m^3. Since σ'_v depends upon depth, so do τ_p, τ_r, and E. At the depth of $h = 50$ m, $\sigma'_v(h) = (\rho_0 - \rho_w)gh\cos\alpha =$

390 kPa, τ_p = 97.5 kPa, and τ_r = 39.0 kPa. Mean properties of the sliding layer ($0 < y < h$) are estimated by their values at $y = h/2$ = 25 m and denoted by bars above the corresponding symbol. We have $\bar{\sigma}'_v \approx (1/2)(\rho_0 - \rho_w)gh\cos\alpha$ = 195 kPa, $\bar{\tau}_p \approx 0.25\bar{\sigma}'_v$ = 48.8 kPa, and $\bar{E} \approx 350\bar{\tau}_p$ = 17.1 MPa. For these parameters and $\bar{\delta}$ = 10 cm, $c = (\bar{E}/\rho_0)^{1/2}$ = 97.4 m/s, $\tau_g = (\rho_0 - \rho_w)gh\sin\alpha$ = 41.0 kPa, $J_0 = (\tau_p - \tau_r)\bar{\delta}$ = 5.85 kPa·m, $\gamma_0 = [2J_0/(h\bar{E})]^{1/2}$ = 0.370%, and $T_0 = (\tau_g - \tau_r)/\bar{E}$ = 1.17×10^{-4}.

Failure of fully saturated, normally-consolidated sediments under fast (dynamic) loading can be described by the Von Mises criterion [e.g., *Desai and Siriwardane*, 1984; *Chen and Baladi*, 1985], which results in $p_a = \bar{\sigma}'_v - 2\bar{\tau}_p$ = 97.5 kPa and $p_p = \bar{\sigma}'_v + 2\bar{\tau}_p$ = 292.6 kPa. The corresponding average active and passive strains are $\varepsilon_a = -\gamma_a = (p_a - p_0)/\bar{E}$ = –0.114% and $\varepsilon_p = \gamma_p = (p_p - p_0)/\bar{E}$ = 1.029%, where $p_0 = K_0\bar{\sigma}'_v \approx 0.6\bar{\sigma}'_v$ = 117 kPa is the characteristic initial longitudinal stress in the sliding layer.

The above parameters are further used as a baseline, and we deviate from the baseline to test the dependence on one or another parameter.

The critical length, $l_0 = h(\gamma_0 - \varepsilon_a)/T_0$ = 2.08 km, is computed from (5.3). The asymptotic solution (7.8) for the failure length gives l_f = 9.31 km, and the strain ratio of λ_* = 0.764 is found from (4.29). This failure length, however, reduces to L_f = 4.90 km in the static analysis (equation (7.9)) conducted for the same parameters. Hence, in this case, the dynamic-to-static length ratio (7.11) is $\kappa = l_f/L_f$ = 1.9. The value of $\lambda_f = l_f/l_0$ = 4.48 indicates that the results of the asymptotic and exact solutions are close. The ratio of l_0/h = 41.5 suggests that the condition of $l_0/h >> 1$ for the developed model to be applicable to this case is reasonably satisfied. This condition has been checked in all calculations described in this work.

Our dynamic analysis, therefore, results in a failure length magnitude typical for many landslides [e.g., *Hühnerbach and Masson*, 2004; *Lee et al.*, 2007] (Appendix A). It also shows that the corresponding static analysis may underestimate this length by nearly a factor of two.

As the slide develops, the shear band separates a layer (slab) of sediments, which eventually fails near the band tip. The layer velocity $\bar{\eta}$ at this point is the *final* slide velocity at the slide initiation stage (i.e., before the slide body separates from the slope) (Appendix A). This velocity, however, is also the *initial* velocity, v_0, of the slide (i.e., of the slab of sediments separated from

the substrata) just before it begins moving downslope. Using the value $C_S = 0.002$ [e.g., *Pelinovsky and Poplavsky*, 1996; *Levin and Nosov*, 2009; *De Blasio*, 2011] of the surface friction coefficient (equation (K.8) in Appendix K) results in the dimensionless drag coefficient $\beta = 8.55\times10^{-5}$. Such a small value of β indicates that the effect of water resistance on the initial slide velocity, $v_0 = \bar{\eta}$, is relatively small. Indeed, accounting for the water resistance to the slide motion during the shear band growth (equation (K.10) in Appendix K), results in $\bar{\eta} = 0.61$ m/s. Without accounting for the water resistance, $\bar{\eta} = 0.92$ m/s is obtained from (6.11). Water resistance, therefore, does not have a significant effect in this case.

It is important to stress that although for sediment materials, the value of the bluntness parameter $n = J_0/J_c = \gamma_0^2/\gamma_c^2$ is not currently constrained, it does not appear in the developed asymptotic solution (Section 6.1). Technically, this asymptotic solution corresponds to the limit of $n \to \infty$ since according to (4.14), the shear band propagation velocity $v = c$ already at $t = +0$. Therefore, using the asymptotic solution corresponds to using a sufficiently large value of n. To test how large this value may be, we also performed computations based on the exact solution (5.5) - (5.11), but for different values of n. The results (Table 1) show a good agreement of the asymptotic and exact solutions for $\lambda_* = 0.764$ (baseline case) and n as small as 1.001. Per (4.14), for $n = 1.001$, the initial shear band velocity is $v_0 = 0.0005c = 0.049$ m/sec. Once the band propagates a distance of three times its initial lengths (i.e., $l = 3l_0$), the band tip velocity reaches $\approx 92\%$ of c for $n = 1.001$ and $\bar{\delta} = 1$ cm, and $\approx 87\%$ of c for $n = 1.01$ and $\bar{\delta} = 10$ cm. The corresponding results for $l = 2l_0$ are 80% and 71% of c. Hence, from a practical standpoint, even $n = 1.001$ can be considered sufficiently large for using the asymptote of $n \to \infty$.

The agreement between the exact and asymptotic solutions becomes even better for smaller values of elastic modulus, E. Table 2 shows the same results as Table 1, but for $E = 250\tau_p$, which is a typical lower limit for normally-consolidated sediments. Band length of the asymptotic solution in (7.8) is same in both Table 1 and Table 2. Exact solutions of the band length (6.3) and (6.6) in Table 2, however, are in better agreement with the asymptotic values than in the case of $E = 350\tau_p$ in Table 1. This is also the case for the dynamic-to-static length ratio $\kappa = l_f/L_f$ and shear band velocity at $l = 2l_0$ and $l = 3l_0$. Slide velocity, $\bar{\eta}$, is also better in Table 2, as the difference between exact and asymptotic solution is 10% and 8% in Table 1 and Table

2, respectively, for the case of n = 1.01 and $\bar{\delta}$ = 10 cm.

Table 1. Results of the dynamic shear band model for baseline parameters, $E = 350\tau_p$, and different values of n. Values computed after the second arrival (equations (4.7), (4.14), (G.23), (J.4), (7.8), and (7.11)), between the first and second arrivals (equations (4.7), (4.14), (4.18), (6.12), (7.8), and (7.11)), and before the first arrival of the discontinuity to the band tip (equations (4.7), (4.14), (6.11), (7.8), and (7.11)) are denoted by two asterisks, one asterisk, and no asterisk, respectively. Bold font is used for the baseline case.

n	1.001	1.01	1.05	**1.1**	1.5	2	Asymptotic solution
Characteristic slip, $\bar{\delta}$ = 10 cm							
l_f (km)	8.802**	8.810*	8.794*	**8.799***	9.111	9.161	9.306
$\bar{\eta}$ (m/s)	0.826**	0.825*	0.829*	**0.841***	0.895	0.901	0.918
κ	1.797**	1.799*	1.796*	**1.796***	1.860	1.870	1.9
v_0 (m/s)	0.049	0.484	2.375	**4.637**	19.48	32.46	97.40
v_0/c	0.0005	0.005	0.024	**0.048**	0.200	0.333	1
v/c at $l = 2l_0$	0.703**	0.705*	0.717*	**0.729***	0.778	0.828	1
v/c at $l = 3l_0$	0.866**	0.867*	0.873*	**0.878***	0.903	0.926	1
Characteristic slip, $\bar{\delta}$ = 1 cm							
l_f (km)	9.249**	9.247*	9.249*	9.280	9.287	9.292	9.306
$\bar{\eta}$ (m/s)	0.939**	0.936*	0.939*	0.943	0.944	0.944	0.946
κ	1.888**	1.888*	1.888*	1.895	1.896	1.897	1.9
v_0 (m/s)	0.049	0.484	2.375	4.637	19.48	32.46	97.40
v_0/c	0.0005	0.005	0.024	0.048	0.200	0.333	1
v/c at $l = 2l_0$	0.802**	0.803*	0.806*	0.814	0.860	0.893	1
v/c at $l = 3l_0$	0.923**	0.924*	0.922*	0.929	0.947	0.960	1

Table 2. Results of the dynamic shear band model for baseline parameters, $E = 250\tau_p$, and different values of n. Values computed after the second arrival (equations (4.7), (4.14), (G.23), (J.4), (7.8), and (7.11)), between the first and second arrivals (equations (4.7), (4.14), (4.18), (6.12), (7.8), and (7.11)), and before the first arrival of the discontinuity to the band tip (equations (4.7), (4.14), (6.11), (7.8), and (7.11)) are denoted by two asterisks, one asterisk, and no asterisk, respectively.

n	1.001	1.01	1.05	1.1	1.5	2	Asymptotic solution
Characteristic slip, $\bar{\delta}$ = 10 cm							
l_f (km)	8.925**	8.929*	8.918*	8.922*	9.168	9.203	9.306
$\bar{\eta}$ (m/s)	1.014**	1.012*	1.017*	1.044*	1.078	1.083	1.097
κ	1.822**	1.823*	1.821*	1.822*	1.872	1.879	1.9
v_0 (m/s)	0.041	0.409	2.007	3.919	16.46	27.43	82.30
v_0/c	0.0005	0.005	0.024	0.048	0.200	0.333	1
v/c at $l = 2l_0$	0.713**	0.715*	0.727*	0.738*	0.787	0.836	1
v/c at $l = 3l_0$	0.873**	0.874*	0.879*	0.885*	0.909	0.931	1

Characteristic slip, $\bar{\delta}$ = 1 cm							
l_f (km)	9.267*	9.267*	9.287	9.287	9.292	9.296	9.306
$\bar{\eta}$ (m/s)	1.112*	1.113*	1.117	1.118	1.118	1.119	1.120
κ	1.892*	1.892*	1.896	1.896	1.897	1.898	1.900
v_0 (m/s)	0.041	0.409	2.007	3.919	16.46	27.43	82.30
v_0/c	0.0005	0.005	0.024	0.048	0.200	0.333	1
v/c at $l = 2l_0$	0.820*	0.822*	0.825	0.833	0.874	0.904	1
v/c at $l = 3l_0$	0.932*	0.933*	0.935	0.938	0.954	0.965	1

Changing the characteristic slip $\bar{\delta}$ at the tip zone of the shear band by even two orders of magnitude does not significantly affect the slide length, l_f (Table 3). Because the energy dissipated at the band tip is characterized by $J_0 = (\tau_p - \tau_r)\,\bar{\delta}$ and $J_c = J_0/n$, this indicates that from the energy balance standpoint, the propagation of a sufficiently long band is mainly controlled by the frictional resistance at the band sides. For a shorter band, corresponding to a thinner layer, i.e., h = 10 m, the band length in the exact solution (6.6) is l_f = 1.804 km and l_f = 1.466 km for $\bar{\delta}$ = 1 cm and $\bar{\delta}$ = 10 cm, respectively. Although the difference is not too large (≈ 19%), it is much greater than for h = 50 m when l_f = 9.280 km and l_f = 8.799 km, respectively (Table 3). This difference, however, becomes large (≈ 17%), for h = 50 m and $\bar{\delta}$ = 50 cm (Table 3). The difference between the exact and asymptotic values of l_f (or $\kappa = l_f/L_f$) also increases with $\bar{\delta}$ (Table 3). For $\bar{\delta}$ = 10 cm and 50 cm, it is ≈ 5% and ≈ 21%, respectively. Note that the asymptotic solution (7.8) can be rewritten as $l_f/h = (2\gamma_p + \gamma_a)/T_0 = (2\varepsilon_p - \varepsilon_a)/T_0$ and is independent of $\bar{\delta}$ and n (per (L.4) in Appendix L). Hence, the asymptotic value of l_f = 9.306 km does not change with $\bar{\delta}$ for h = 50 m in Table 3, and for h = 10 m, l_f = 1.861 km for both $\bar{\delta}$ = 1 cm and $\bar{\delta}$ = 10 cm. Likewise, the asymptotic expression (7.11) for the dynamic-to-static length ratio $\kappa = l_f/L_f$ can be rewritten using (4.29) as $\kappa = (2\gamma_p + \gamma_a)/(\gamma_p + \gamma_a) = (2\varepsilon_p - \varepsilon_a)/(\varepsilon_p - \varepsilon_a)$, which is also independent of $\bar{\delta}$ and n. Furthermore, κ is independent of h and α. This is why the asymptotic value of $\kappa = l_f/L_f$ = 1.9 does not change with α, h, and $\bar{\delta}$ in Table 3. Similarly, the crack grows velocity, v, in (4.7), (4.18), and (E.6) (Appendix E) is independent of $\bar{\delta}$ (but not of n), so the values of v in Table 1 are the same for $\bar{\delta}$ = 1 cm and $\bar{\delta}$ = 10 cm.

Table 3. Results of the dynamic shear band model for baseline parameters, $E = 350\tau_p$, and different values of characteristic displacement, $\bar{\delta}$, slide thickness, h, and slope angle, α. Values computed between the first and second arrivals (equations (4.7), (4.14), (4.18), (6.12), (7.8), and (7.11)) of the discontinuity to the tip are denoted by the asterisk. All other values are computed before the first arrival of the discontinuity to the band tip (equations (4.7), (4.14), (6.11), (7.8), and (7.11)). Bold font is used for the baseline case.

	l_0/h	λ_*	l_f (km)		$\bar{\eta}$ (m/s)		$\kappa = l_f/L_f$	
			Asymp.	Exact	Asymp.	Exact	Asymp.	Exact
Slip, $\bar{\delta}$ (cm)								
1*	19.8	0.506	9.306	9.280	0.946	0.943	1.9	1.895
5	32.2	0.696	9.306	9.022	0.933	0.892	1.9	1.842
10	**41.5**	**0.764**	**9.306**	**8.799**	**0.918**	**0.841**	**1.9**	**1.796**
50	80.8	0.879	9.306	7.328	0.795	0.514	1.9	1.496
Thickness, h (m)								
10	80.8	0.879	1.861	1.466	0.356	0.230	1.9	1.496
50	**41.5**	**0.764**	**9.306**	**8.799**	**0.918**	**0.841**	**1.9**	**1.796**
100	32.2	0.696	18.61	18.05	1.320	1.262	1.9	1.842
200	25.7	0.618	37.22	36.63	1.882	1.845	1.9	1.870
Slope angle, α								
1° ($\Delta P/\sigma'_v = 0.875$)*[1,2]	21.6	0.534	9.560	9.527	0.948	0.944	1.9	1.893
1° ($\Delta P/\sigma'_v = 0.6$)[1,2]	35.0	0.712	9.581	9.247	0.933	0.886	1.9	1.834
3° ($\Delta P/\sigma'_v = 0.525$)[1]	32.4	0.691	9.538	9.261	0.936	0.897	1.9	1.845
6°	**41.5**	**0.764**	**9.306**	**8.799**	**0.918**	**0.841**	**1.9**	**1.796**

[1]Excess pore pressure ΔP is applied on the rupture surface (shear band, including the tip zone) to reduce friction and allow slides to move.
[2]Since $0.875 > k_0 = 0.6$, hydraulic fracturing may take place before the slide occurs. This is why, $\Delta P/\sigma'_v$ is reduced to 0.6, which, however, is insufficient for the slide body to move on the 1° slope. Hence, the residual friction was also reduced to $\tau_r = 0.125\tau_p$ in this case.

Table 4. Results of the dynamic shear band model for baseline parameters, $E = 250\tau_p$, and different values of characteristic displacement, $\bar{\delta}$, slide thickness, h, and slope angle, α. Values computed between the first and second arrivals (equations (4.7), (4.14), (4.18), (6.12), (7.8), and (7.11)) of the discontinuity to the tip are denoted by the asterisk. All other values are computed before the first arrival of the discontinuity to the band tip (equations (4.7), (4.14), (6.11), (7.8), and (7.11)).

	l_0/h	λ_*	l_f (km)		$\bar{\eta}$ (m/s)		$\kappa = l_f/L_f$	
			Asymp.	Exact	Asymp.	Exact	Asymp.	Exact
Slip, $\bar{\delta}$ (cm)								
1*	18.3	0.464	9.306	9.287	1.120	1.118	1.9	1.896
5	28.8	0.659	9.306	9.096	1.110	1.076	1.9	1.857
10	36.6	0.733	9.306	8.922	1.097	1.029	1.9	1.822
50	69.8	0.860	9.306	7.857	0.993	0.744	1.9	1.604
Thickness, h (m)								
10	69.8	0.860	1.861	1.571	0.444	0.333	1.9	1.604

50	36.6	0.733	9.306	8.922	1.097	1.029	1.9	1.822
100	28.8	0.659	18.612	18.19	1.569	1.521	1.9	1.857
200*	23.2	0.578	37.224	37.04	2.232	2.220	1.9	1.890
Slope angle, α								
1° ($\Delta P/\sigma'_v = 0.893$) *[1,2]	14.0	0.472	7.018	7.003	1.123	1.120	1.9	1.896
1° ($\Delta P/\sigma'_v = 0.6$)[1,2]	33.2	0.776	7.084	6.655	1.084	0.982	1.9	1.785
3° ($\Delta P/\sigma'_v = 0.543$)[1]	21.0	0.649	7.004	6.859	1.113	1.082	1.9	1.861
6°	36.6	0.733	9.306	8.922	1.097	1.029	1.9	1.822

[1]Excess pore pressure ΔP is applied on the rupture surface (shear band, including the tip zone) to reduce friction and allow slides to move.
[2]Since $0.893 > k_0 = 0.6$, hydraulic fracturing may take place before the slide occurs. This is why, $\Delta P/\sigma'_v$ is reduced to 0.6, which, however, is insufficient for the slide body to move on the 1° slope. Hence, the residual friction was also reduced to $\tau_r = 0.043\tau_p$ in this case.

Slide velocity, $\bar{\eta}$, is more greatly affected by the value of $\bar{\delta}$ than the failure length, l_f, both in the exact (6.14) and asymptotic (first equation in (6.14)) solutions. With increasing $\bar{\delta}$, the energy lost to failure at the band tip also increases, and the slide is expected to have lower velocity. This can be observed in Table 3, where $\bar{\eta} = 0.841$ m/s for $\bar{\delta} = 10$ cm and $\bar{\eta} = 0.514$ m/s for $\bar{\delta} = 50$ cm in the exact solution. We also observe 35% difference in $\bar{\eta}$ between the exact and asymptotic solutions for $\bar{\delta} = 50$ cm; that is, $\bar{\eta} = 0.795$ m/s and $\bar{\eta} = 0.514$ m/s, respectively. Similarly, the asymptotic dynamic-to-static length ratio, $\kappa = l_f/L_f = 1.9$, overestimates the exact value of $\kappa = 1.496$ by nearly 21% for $h = 50$ m and $\bar{\delta} = 50$ cm (Table 3). This is because the dimensionless failure length $\lambda_f = l_f/l_0 = 1.912$ is relatively low at failure, and the asymptotic solution is less accurate than for larger lengths (typically, for $l_f \geq 3l_0$). The same effect can be observed for the thinner slide of $h = 10$ m, when in the exact solution (6.14), $\bar{\eta} = 0.399$ m/s, $\kappa = 1.842$ and $\bar{\eta} = 0.230$ m/s, $\kappa = 1.496$ for $\bar{\delta} = 1$ cm and $\bar{\delta} = 10$ cm, respectively. In the asymptotic solution, the corresponding values are $\bar{\eta} = 0.417$ m/s, $\kappa = 1.9$ and $\bar{\eta} = 0.356$ m/s, $\kappa = 1.9$. For $h = 10$ m, $\lambda_f = 5.691$ for $\bar{\delta} = 1$ cm and $\lambda_f = 1.912$ for $\bar{\delta} = 10$ cm, so the asymptotic solution is less applicable to the latter case than to the former. Therefore, for short and thin bands (typically, $h < 10$ m) and large tip displacements (typically, $\bar{\delta} > 50$ cm), the asymptotic solution needs to be applied with care. The simplest check is computing λ_f to confirm that $\lambda_f > 3$. These conclusions are confirmed by results given in Table 4 for a softer material with $E = 250\tau_p$ but otherwise having the same baseline properties as in Table 3.

The baseline slope angle of 6° cannot be considerably reduced with the chosen baseline parameters. Submarine landslides, however, can occur on slopes as small as 0.5° [e.g., *Hühnerbach and Masson*, 2004; *Haflidason et al.*, 2005] and even smaller (Appendix A). This is commonly explained by the excess pore pressure, which developed in the sediment by or at the time of the event [*Screaton et al.*, 1990; *Dugan and Flemings*, 2000; *Locat et al.*, 2009; *Pinyol and Alonso*, 2010; *Viesca and Rice*, 2012]. Excess pore pressure is attributed to such factors as seismic load [*Newmark*, 1965; *Seed*, 1979; *Puzrin et al.*, 1995; 1997; *Wright and Rathje*, 2003; *Nadim et al.*, 2007; *Locat et al.*, 2009], methane hydrate dissociation [*Sultan et al.*, 2004; *Masson et al.*, 2006; *Xu and Germanovich*, 2006; 2007; *Scholz et al.*, 2011], fast sedimentation rates [*Locat and Lee*, 2002; *Flemings et al.*, 2008a; 2008b; *Dugan and Stigall*, 2010; *Flemings et al.*, 2012], and high artesian pressure [*Prior and Suhayda*, 1979; *Bonzanigo*, 1997; *Neuffer and Schultz*, 2006; *L'Heureux et al.*, 2010]. In this case, σ'_v (which includes only hydrostatic pressure) should be replaced by $\sigma'_v + \Delta P$ with ΔP being the excess pressure on the rupture surface (Appendix B). For example, in the case of baseline parameters, an excess pressure ΔP of 87.5% and 52.5% of σ'_v along the shear band in slopes of $\alpha = 1°$ and $\alpha = 3°$, respectively, would result in slope slip (shear band growth) and the same dynamic failure length, $l_f \approx 9.5$ km for both slopes (Table 3).

The overpressure of $\Delta P = 0.875\sigma'_v$ (i.e., greater than $k_0\sigma'_v$) may be possible if generated by fast earthquake loading. Otherwise, such a high ΔP is unlikely to realize because the sediment will be fractured hydraulically before ΔP reaches this level, that is, at $\Delta P \approx k_0\sigma'_v$ [e.g., *Xu and Germanovich*, 2007; *Viesca and Rice*, 2012]. Hence, we also present in Table 3 the slide parameters that correspond to $\Delta P = k_0\sigma'_v$ ($k_0 = 0.6$) when $\alpha = 1°$. Since this level of overpressure is insufficient for the slide body to move, we reduced the residual friction to $\tau_r = 0.125\tau_p$.

The requirement of a high level of excess pressure for low-angle faults is not unusual. *Viesca and Rice* [2012], for example, suggest that at a depth of 20 m below a 2° sloping seafloor under an initially hydrostatic condition, the failure corresponds to a pore pressure increase by ≈ 93% of the effective initial pore pressure. Excess pore pressure may develop not only along the slip surface, but also within the sediment (slide) body. Recently, *Viesca* [2011] and *Viesca and Rice* [2012] reviewed possible mechanisms for locally elevated pressure for submarine landslides

conditions. Evidence of these mechanisms included fluid pathways such as faults and coarse-grained, buried turbidity deposits. Resulting high-permeability conduits may elevate the subsurface pore pressure to the lithostatic level and even create horizons of liquefied sediments. Without analyzing detailed data for specific landslides (which is beyond the scope of this work), we only consider the excess pore pressure, localized along the potential slip surface (shear band). In the models of *Viesca and Rice* [2012] and *Garagash and Germanovich* [2012], the pressure only needs to be elevated in the source region, which can be sufficient for the slip to be driven by pressure diffusion along the slip surface. There are the initial conditions, however, when the residual friction is sufficiently great, so that the pressurized zone spreads from the local region with highly-elevated pressure before the nucleation of dynamic slip [*Garagash and Germanovich*, 2012; *Viesca and Rice*, 2012]. This extreme case can be visualized as an initial state for the scenario considered in this work.

It should be noted that in sensitive clays, slides can take place even in the absence of overpressure. Sensitive clays are characterized by fast strength decrease during deformation [e.g., *Thakur et al.*, 2013], which translates in low residual friction coefficient. *Quinn et al.* [2011a] for example, suggest $k_r = \tau_r / \tau_p = 0.013$ for sensitive clays in Quebec area (Canada). Sensitivity of the sediment material appears to be a major factor in the deformation softening process [*Bernander*, 2011], and promotes strain localization and propagation of shear bands [e.g., *Vanneste et al.*, 2014]. As a result, many landslides occurred in slopes composed of sensitive clays [e.g., *Mitchell and Markell*, 1974; *Bernander and Olofsson*, 1981; *Locat and Demers*, 1988; *Kvalstad et al.*, 2005; *Quinn et al.*, 2011a; *Kovacevic et al.*, 2012; *Thakur et al.*, 2013]. Hence, we also considered a scenario when a landslide is caused by reducing the frictional resistance not by rising pressure, but by mobilizing soil sensitivity in a thin zone where the rupture surface (shear band) develops. For the baseline parameters, for example, reducing k_r to 0.005 [*Quinn et al.*, 2011a] (i.e., below the range of (L.3) in Appendix L) allows the slide to develop in the slope of $\alpha = 0.5°$. This results in $l_f = 12.75$ km, $\bar{\eta} = 0.90$ m/s, and $\kappa = 1.9$.

In an analysis of real submarine landslides, the slope failure length, l_f, is typically better constrained (e.g., from bathymetry data) then the sediment properties. Hence, we also conducted a similar analysis, but using a static slide model (Section 7.2). That is, we ignored the

dynamic effects and assumed that even after the shear bands reaches the critical value of l_0, the static equilibrium conditions are applicable. This results in equations (7.10) - (7.12), and given the same properties, the static and dynamic failure lengths can differ nearly by a factor of 2 (Section 7.2). Alternatively, one can use the observed failure length to constrain the sediment properties, which can be done both within the static and dynamic frameworks. It appears, that the same failure lengths, $l_f = L_f$, can be achieved for the 3° slope (Table 5) by only slightly chaging the residual friction (from $\tau_r = 0.4\tau_p$ in dynamics to $\tau_r = 0.42\tau_p$ in statics) or excess pore pressure in the band (from $\Delta P = 0.525\sigma'_v$ to $\Delta P = 0.502\sigma'_v$, respectively). The peak friction, however, needs to be raised nearly twice (from $\tau_p = 0.25\sigma'_v$ to $\tau_p = 0.47\sigma'_v$) as can be seen from Table 5. Hence, the static analysis may work reasonably well for the back calculations of τ_r and τ_p, but it should be used with care for recovering τ_p from field observations. This observation is also valid for 6° slope (Table 6) and confirmed below using examples of different slides.

Below, we consider examples of four submarine slides and one subaerial slide (Table 6 through Table 10). Since the failure length, l_f, is probably the most constrained parameter, we test if it would be possible to obtain values of l_f consistent with field data. For the case of submerged slides, we also estimate the magnitude of the tsunami that could have been generated by these slides (Section 9.2).

Table 5. Results of the shear band model for baseline parameters, $\alpha = 6°$, and $\alpha = 3°$. Excess pore pressure $\Delta P \neq 0$ on the rupture surface (shear band) was used to allow the slide body to move in the case of 3° slope.

Parameters	6° slope (dynamic analysis)	6° slope (static analysis)		3° slope (dynamic analysis)	3° slope (static analysis)		
		varying τ_r	varying τ_p		varying ΔP	varying τ_r	varying τ_p
Slope angle, α	6°	6°	6°	3°	3°	3°	3°
Thickness, h (m)	50	50	50	50	50	50	50
Density, ρ_0 (kg/m^3)	1800	1800	1800	1800	1800	1800	1800
Characteristic slip, $\bar{\delta}$ (cm)	10	10	10	10	10	10	10
$k_p = \tau_p / \sigma'_v$	0.25	0.25	**0.48**	0.25	0.25	0.25	**0.47**
$k_r = \tau_r / \tau_p$	0.4	**0.41**	0.208	0.4	0.4	**0.42**	0.213
$k_E = E / \tau_p$	350	350	350	350	350	350	350
$k_0 = p_0 / \sigma'_v$	0.6	0.6	0.6	0.6	0.6	0.6	0.6
$\mu = \tau_r / \sigma'_v$	0.1	0.103	0.1	0.1	0.1	0.105	0.1
Elastic modulus, E (MPa)	17.1	17.1	32.8	17.1	17.1	17.1	32.2
Excess pore pressure ratio, $\Delta P / \sigma'_v$	0	0	0	0.525	**0.502**	0.525	0.525
Active failure strain, ε_a (%)	–0.11	–0.11	–0.33	–0.11	–0.11	–0.11	–0.33
Passive failure strain, ε_p (%)	1.03	1.03	0.81	1.03	1.03	1.03	0.82
Fracture energy, J_0 (kPa·m)	5.9	5.8	14.8	2.8	5.9	2.7	6.9
Surface friction coefficient, C_S	0.002	0.002	0.002	0.002	0.002	0.002	0.002
Fracture strain, γ_0 (%)	0.370	0.367	0.425	0.255	0.261	0.251	0.292
$T_0 = (\tau_g - \tau_r)/E$	1.2×10^{-4}	6.0×10^{-5}	6.1×10^{-5}	1.1×10^{-4}	6.1×10^{-5}	6.0×10^{-5}	6.1×10^{-5}
Strain ratio, λ_*	0.764	0.763	0.561	0.691	0.696	0.687	0.471
Critical length, l_0 (km)	2.08	4.05	6.24	1.62	3.07	3.06	5.1
l_0 / h	41.5	90.9	124.9	32.4	61.4	61.2	102.5
Dynamic failure length, l_f (km)	9.3	18.2	16.1	9.5	17.7	18.2	16.2
$\lambda_f = l_f / l_0$	4.5	4.5	2.6	5.9	5.8	5.9	3.2
Static failure length, $L_f = l_f / \kappa$ (km)	4.9	**9.6**	**9.4**	5.0	**9.3**	**9.6**	**9.4**
Failure length ratio, κ	1.90	1.90	1.71	1.90	1.90	1.88	1.71
Water resistance coefficient, β	8.5×10^{-5}	1.7×10^{-4}	3.0×10^{-4}	8.5×10^{-5}	8.9×10^{-5}	8.5×10^{-5}	1.7×10^{-4}
Slide velocity, $\bar{\eta} = v_0$ (m/s)	0.61	0.59	0.43	0.72	0.71	0.72	0.58
Slide velocity when $\beta = 0$, $\bar{\eta} = v_0$ (m/s)	0.92	0.92	0.84	0.94	0.94	0.94	0.8

8.2. Currituck Slides

The Currituck slide complex is located northwest of Cape Hatteras (36°20'N, 74°40'W), offshore North Carolina. *Prior et al.* [1986] reported a detailed stratigraphic description and the geomorphological analysis of the slide area. Using deep-tow sidescan sonar and high resolution seismic data, they concluded that the slide complex is the result of two slides, Slide 1 and Slide 2 (Figure 16a). Their analysis of the slide geometry and dimensions (Figure 16b) agrees well with more recent multibeam bathymetry imaging [*Locat et al.*, 2009].

Bunn and McGregor [1980] collected 11 cores from the slide area, but 10 of these cores only penetrated up to 5.5 m of the sediment drape, which blankets the entire region and was deposited post-slide. One core (core 4 in *Bunn and McGregor* [1980]), however, sampled 2.3 m of dry friable clay beneath the drape. The core location along the slope is shown in Figure 16c. Since it is nearly at the base of Slide 2, *McGregor* [1981] suggested that the slip surface may have occurred within the sedimentary sequence at a discontinuity in physical properties sampled by this core.

Based on the thickness (4 to 9 m) of the sediment drape, identified acoustically and by coring, *Prior et al.* [1986] used the available deposition rates and estimated that the slides took place from 48 to 16 ka. *Lee* [2009] recently reanalyzed this range to 25 - 50 ka. Core analysis at the Currituck slide complex and surrounding areas suggests that the surface drape is composed of silty clays with occasional thin lenses of sand [*Prior et al.*, 1986]. Little else is known about the Currituck slide sediments, but presumably they are clays or silty clays that were normally- or lightly over-consolidated at the time of the slides [*Geist et al.*, 2009; *Locat et al.*, 2009].

Prior et al. [1986] argue that Slide 1 was the first mobilized slope segment, which involved ≈ 78 km^3 of sediments and evolved on a surface slope of $\approx 4°$ and a basal shear plane inclined at 2° (Figure 16b). They also argue that Slide 2 was developing upslope and represents a shallower, retrogressive extention of Slide 1. They suggest that ≈ 50 km^3 of the displaced sediment from Slide 2 moved into the trough created by Slide 1, but did not sufficiently fill it. Accordingly, they concluded that some of the material from Slide 1 remained in its trough and was subsequently covered by the Slide 2 sediments.

Locat et al. [2009] noted that Slide 2 developed sufficiently fast to completely clear the slip surface above and at the side of Slide 1 (Figure 16a). Retrogressive slides typically exhibit a distinct pattern of a highly perturbed slope surface with alternating grabens and horsts [*Bryn et al.*, 2004, Fig. 16; *Gauer et al.*, 2005, Fig. 2 and 3; *Kvalstad et al.*, 2005, Fig. 4; *Quinn et al.*, 2011a, Fig. 2]. This pattern contrasts with the smooth, clean failure surface (Figure 16b) left by Slide 2 [*Bunn and McGregor*, 1980; *Prior et al.*, 1986; *Locat et al.*, 2009]. The interpretation of *Prior et al.* [1986], however, did not consider the actual retrogressive slide development. In fact, the concept of retrogressive slides does not really contribute to their reasoning. In essence, they suggest that because the Slide 2 area is located above Slide 1 (Figure 16a), it is likely that Slide 2 initiated at the headscarp of Slide 1, 150 to 175 m below the original slope surface. Incidently, this would be consistent with the slip surface (Figure 16c) interpreted from core 4 [*Bunn and McGregor*, 1980; *McGregor*, 1981].

Therefore, an alternative to the retrogressive slide mechanism could be an upslope propagation of the shear band beneath the sliding slab. This was suggested by *Chowdhury* [1978], *Chowdhury et al.* [2010], and by *Quinn et al.* [2011a; 2011b] as a mechanism of translational slides. This mechanism could leave the failure/slip surface relatively intact, as observed in the Slide 2 area. *Quinn et al.* [2011a; 2011b], *Chowdhury* [1978] and *Chowdhury et al.* [2010] used the original *Palmer and Rice* [1973] model for an open cut slope in overconsolidated clays. The dynamic version of their model is a particular case of the model developed in this work (Figure 24 in Section 10.1), and we use it here to test if Slide 2 could hve developed upslope from the headscarp of Slide 1.

For the Currituck slide sediments, *Locat et al.* [2009] suggested a Mohr-Coulomb failure criterion with a peak friction angle $\phi_p = 30°$ and cohesion $C = 10$ kPa to 100 kPa. Then, the frictional traction in the intact material on the future rupture (shear band) surface, $\tau_p = C + k_p\,(\sigma'_v + \Delta P)$, where $k_p = \tan\phi_p$, $\sigma'_v = -\sigma'_y$ is the effective stress at the depth of the shear band in the intact sediment (in the infinite slope), and ΔP is the excess pore pressure at the same depth at the time of slide. On the sliding sides of the rupture surface (after the shear band propagates through a given place), cohesion C drops to zero and residual friction becomes $\tau_r = k_r\,(\sigma'_v + \Delta P)$. In the case of upslope shear band development, the slab is unloaded at the

upper end where the failure would happen. Furthermore, the sediment at the upper end experiences tensile longitudinal stress (to counteract the weight of the "hanging" slab) and should have at least some cohesion (perhaps, being in the overconsolidated state). In such conditions, using the active critical load $p_a = k\overline{\sigma}'_v + \overline{\Delta P} - C_0$ (where $k = (1 - \sin\phi_p)/(1 + \sin\phi_p)$, $C_0 = 2C\cos\phi_p/(1 + \sin\phi_p)$, $\Delta p = \overline{\Delta P}$ and $\overline{\sigma}'_v$ are the excess pressure and effective stress, normal to the slope, respectively, averaged across the sliding layer) may not be advisable since Mohr-Coulomb criterion may not be suitable in the tensile stress conditions. Hence, we use the simplest tensile failure criterion $\sigma' = \sigma_t$, where σ_t is the tensile strength, which, for simplicity, we estimate as $\sigma_t \approx C$. As will be seen below, this estimate is not critical for the derived conclusions.

At the lower slab end, the longitudinal effective stress $\sigma' = \sigma + p = 0$. For the Currituck slide sediments, $\rho_0 \approx 1800$ kg/m^3 [*Locat et al.*, 2009], and for Slide 2, $h \approx 180$ m. As noted by *Locat et al.* [2009], such a slide with $\phi = 30°$ would not move on the 4° slope, even in the case of zero cohesion, so some level of excess pore pressure is required. *Locat et al.* [2009] considered sediment accumulation and earthquake load as two potential mechanisms. *Viesca and Rice* [2012] argue that the possibility of the sedimentation-induced excess pressure generating landslides at the depths of < 100 m could be excluded. The depth of the Currituck slides is > 100 m, however. In the absence of data, we simply assume $\Delta P \approx 0.75\sigma'_v$. This level of excess pressure is required for the slide to move, but deviating from this value also does not affect the conclusion below.

The main result of our analysis is that an unrealistically high magnitude of cohesion (tensile strength) of at least 1 MPa (Table 6) is required for the shear band to propagate ≈ 11 km (Figure 16b) before the failure. The final failure length, l_f, is ≈ 11 km [*Prior et al.*, 1986; *Locat et al.*, 2009]. To maintain such a large l_f, the tensile stress magnitude has to be sufficiently large, however. Unless some special conditions are realized, the value of $\sigma_t = C > 1$ MPa appears to be too excessive for the Currituck slide sediments that are more likely to be normally-consolidated than highly overconsolidated. Therefore, we rule out the possibility for the shear band to develop upslope as a single event.

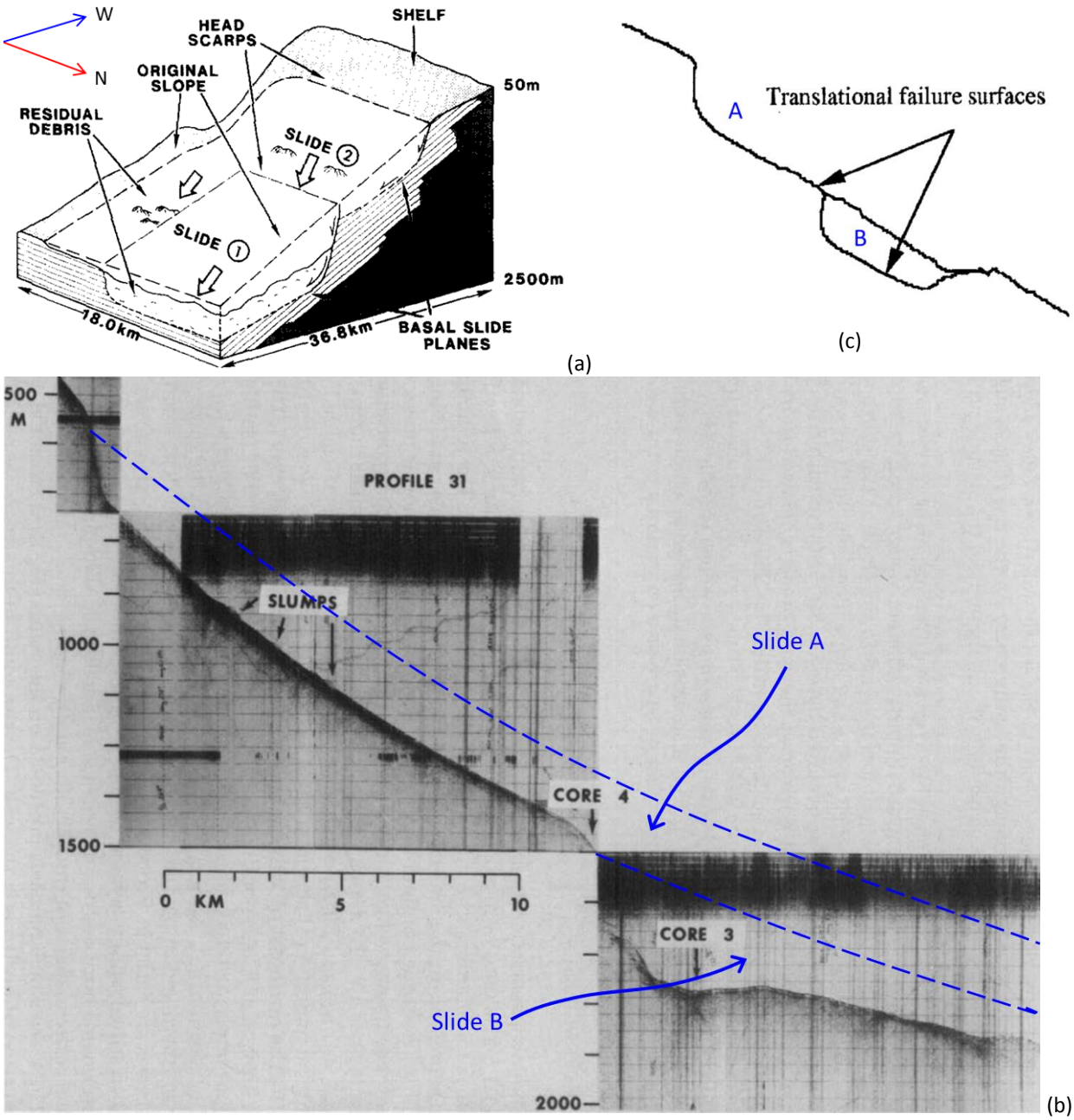

Figure 16. (a) Schematic view of the Currituck slide complex [*Prior et al.*, 1986]. (b) Seismic reflection (at 3.5 kHz) profile [*Bunn and McGregor*, 1980]. Dashed lines show the Currituck Slide A hypothesized in this work. (c) *Mulder and Cochonat*'s [1996] scenario similar to that in figure (b). Slide A displaces material above Slide B, which follows Slide A.

Note that in the propagating band, the residual shear stress τ_r is mobilized, and cohesion $C = 0$. The value of cohesion at the tip zone of the shear band affects τ_p and can be reduced to 100 kPa or 10 kPa [*Locat et al.*, 2009] or even to zero. This only affects the value of l_0, the shear

band length when the band begins propagating dynamically. It should be also noted, that we only considered the excess pressure developing in the band. If the excess pressure also develops inside the sliding layer, this would reduce the sediment strength σ_t to $\sigma_t - \Delta p$ and make l_f smaller. Hence, even higher σ_t would be required for the shear band to propagate the distance of $l_f \approx 11$ km if the excess pressure developed not only in the shear band, but also in the sliding layer. In general, this analysis indicates that the upslope growth of the shear band in the open cut conditions is probabaly rare and, if at all possible, it probably occurs for relatively short slides a few hundred meters long (< 1 km).

An alternative scenario to that of *Prior et al.* [1986] (i.e., Slide 1 developed prior to Slide 2 and, perhaps, triggered the latter) could be the opposite sequence of events. That is, Slide 2 developed first by the translational mechanism of the shear band growth *downslope* from the initial weakness zone located below the Slide 2 headscarp (Figure 16a and Figure 16b). In the area under this headscarp, the slope is slightly steeper (≈ 4.5° [*Prior et al.*, 1986]) than the average slope of 4° of Slide 2 (Figure 16b). Hence, it seems plausible that the band started growing downslope from this area, bypassed the future Slide 1 headscarp, and continued downhill. *Prior et al.* [1986] and *Locat et al.* [2009] suggest that the slope of the upper boundary of Slide 1 is also ≈ 4°. So it seems feasible that the shear band continued parallel to the slope along the length of Slide 1 as shown in Figure 16b. We name this event *Slide A* (Figure 16b) to distinguish from the conventional terms Slides 1 and 2. A similar sequence of events was also considered by *Mulder and Cochonat* [1996] (Figure 16c).

Since in the scenario of Slide A, all stresses are compressive and because the Currituck slide clays are most likely normally-consolidated [*Locat et al.*, 2009], we adopted the baseline parameters (Table 6), but with a slope $\alpha = 4°$ and slide thickness $h = 180$ m. As expected, we found that the shear band would not propagate because the slope angle is too low. We then assumed an excess pressure in the band and found that $\Delta P = 0.181\ \sigma'_v = 0.26$ MPa ($\sigma'_v = 1.41$ MPa) is required for the band to propagate a distance of $l_f = 28.6$ km, which is close to the 28.5 km of combined length of Slides 1 and 2 [*Prior et al.*, 1986; *Locat et al.*, 2009]. In this case, $\lambda_* = 0.577$, the slide velocity at failure is 1.78 m/s, and the length of the corresponding static slide is $L_f = 15.1$ km ($\kappa = l_f/L_f = 1.9$). The initial velocity (K.10) of Slide A is $v_0 = \bar{\eta} = 1.53$ m/s.

An excess pressure of 18% of σ'_v is much lower than the 50% required for the scenario of Slide 2 with a shear band developing upslope.

After Slide A transports the upper 180 m of sediments downhill (Figure 16b), a part or the entire remaining material could also be removed by another translational slide, which we term *Slide B* (Figure 16b). For the geometry of the Currituck slide complex [*Prior et al.*, 1986; *Locat et al.*, 2009], this remaining material constitutes a wedge of $\approx$ 470 m thickness at the headscarp (Figure 16b) that gradually reduces downslope to essentially zero. The slope of the top surface of the wedge remains $\alpha \approx 4°$ (Figure 16b) while the bottom surface (potential slip plane), along which the shear band would propagate, slopes at 2°.

Strickly speaking, our model is not applicable to this case and needs to be adjusted for variable thickness. Yet, because the wedge thickness changes gradually, as a first order estimate, we approximate it by an average value of h = 235 m and consider a layer of constant thickness, h, on the slope of α = 2°.

We assume that the Slide B sediments were also normally-consolidated at the time of failure. Then, the baseline sediment properties (Table 6) are applicable to Slide B as well. As can be seen in Table 6, the excess pore pressure $\Delta P = 0.778\sigma'_v = 1.43$ MPa ($\sigma'_v = 1.84$ MPa) on the rupture surface of Slide B is added to let this slide happen for the basal surface angle of 2°. Using (7.8), we compute l_f = 17.5 km for Slide B. This is in good agreement with the value of 17.5 km inferred from the field observations [*Prior et al.*, 1986]. The static analysis (7.11) provides an estimate of the failure length as 9.2 km (κ = 1.90 in (7.11)) for Slide B. The initial velocity of this slide is $v_0 = \bar{\eta}$ = 2.06 m/s.

The excess pressure for Slide B is greater than for Slide A since the slide surface angle is more acute (2° instead of 4°). Depending upon how the excess pressure $\Delta P = 0.778\sigma'_v = 1.43$ MPa was accumulated, Slide B could have happened a significant time after Slide A. Alternatively, Slide B could have been triggered by Slide A, if, for example, the weight of the 180 m of sediments, overlying Slide B, had been removed as a result of Slide A (Figure 16b). This is seen by assuming that the excess pressure at the bottom of Slide 1 (which coincides with the bottom of Slide B), before Slide A took place, is $\Delta P = 0.524\sigma'_v = 1.43$ MPa ($\sigma'_v = 2.75$ MPa) where σ'_v is evaluated based on the new effective overburden, i.e., based on the seafloor surface of

the Slide 1 (which coincides with the seafloor surface of Slide A). Such excess pore pressure is not sufficient to cause Slide 1 to occur before Slide A. Assuming that the excess pressure, ΔP, at the base of Slide B does not change during the relatively short time of Slide A, it can be expressed as $\Delta P = 0.778\sigma'_v = 1.43$ MPa, where σ'_v reduces to $\sigma'_v = 1.84$ MPa (because of the removed overburden) and, therefore, is taken with respect to the position of the new slope (i.e., the base of Slide A). This level of excess pressure is sufficient for failure and the shear band would propagate if there was an initial zone of weakness at that depth (l_0 in Table 6). The excess pressure may be even lower if we take into account that the friction force from Slide A may have acted as a drag force that increased the longitudinal load τ_* (Figure 2), which drove the shear band growth. A model with two propagating shear bands (upper and lower) can be devised in a manner similar to the case of one band, but a more detailed analysis of the nature of excess pressure still would be required. This is beyond the scope of this work, however.

Finally, it is worth noting that the scenario of Slide A following Slide B agrees with the fact that Slide 2 'envelopes' Slide 1, at least, on the southern side (Figure 16a). The southern part of the Slide 2, next to the southern side of Slide 1 (Figure 16a), can also be interpreted as the slip surface of Slide A.

Table 6. The dynamic shear band model parameters for Currituck slides. The first column shows the baseline parameters.

Parameters	Currituck Slide 2 (upslope)	Currituck Slide A	Currituck Slide B
Slope angle, α	4°	4°	2°
Thickness, h (m)	180	180	235
Density, ρ_0 (kg/m^3)	1800	1800	1800
Characteristic slip, $\bar{\delta}$ (cm)	10	10	10
$k_p = \tau_p / \sigma'_v$	0.57*	0.25	0.25
$k_r = \tau_r / \tau_p$	0.4*	0.4	0.4
$k_E = E / \tau_p$	133	350	350
$k_0 = p_0 / \sigma'_v$	0.5	0.6	0.6
$\mu = \tau_r / \sigma'_v$	0.231	0.1	0.1
Cohesion, $C = \sigma_t$ (MPa)	1.1	0	0
Elastic modulus, E (MPa)	200	62	81
Excess pore pressure ratio, $\Delta P / \sigma'_v$	0.5	0.181	0.778
Active failure strain, ε_a (%)	–0.73	–0.11	–0.11
Passive failure strain, ε_p (%)	–0.18**	1.03	1.03
Fracture energy, J_0 (kPa·m)	119.1	13.5	6.1
Surface friction coefficient, C_S	0.002	0.002	0.002
Fracture strain, γ_0 (%)	0.257	0.156	0.080
$T_0 = (\tau_g - \tau_r)/E$	1.9×10^{-4}	1.4×10^{-4}	2.9×10^{-4}
Strain ratio, λ_*	3.172	0.577	0.413
Critical length, l_0 (km)	0.77	3.57	1.57
l_0/h	4.3	19.8	6.7
Dynamic failure length, l_f (km)	12.0	28.6	17.5
$\lambda_f = l_f / l_0$	15.7	8.0	11.2
Static failure length, $L_f = l_f / \kappa$ (km)	5.2	15.1	9.2
Failure length ratio, κ	2.32	1.90	1.90
Water resistance coefficient, β	6.1×10^{-6}	1.7×10^{-5}	3.0×10^{-6}
Slide velocity, $\bar{\eta} = v_0$ (m/s)	0.67	1.53	1.90
Slide velocity when $\beta = 0$, $\bar{\eta} = v_0$ (m/s)	1.40	1.78	2.06

*In this case, $k_p = (\tau_p - C) / (\sigma'_v + \Delta P) = \tan\phi_p$ and $k_r = \tan\phi_r / \tan\phi_p = \tan\phi_r / k_p$, where $\phi_p = 30°$ and $\phi_r = 13°$ are the peak and residual friction angle, respectively.
**Strain corresponding to zero effective stress at $x = 0$ (Figure 24 in Section 10.1).

Table 7. Static analysis (based on equation (7.9)) applied for the Currituck Slides A and B. Varying parameters are denoted by the bold font. Quantities that changed as a result of parameter variation are given in blue font.

Parameters	Currituck Slide A			Currituck Slide B		
	varying ΔP	varying τ_r	varying τ_p	varying ΔP	varying τ_r	varying τ_p
Slope angle, α	4°	4°	4°	2°	2°	2°
Thickness, h (m)	180	180	180	235	235	235
Density, ρ_0 (kg/m^3)	1800	1800	1800	1800	1800	1800
Characteristic slip, $\bar{\delta}$ (cm)	10	10	10	10	10	10
$k_p = \tau_p / \sigma'_v$	0.25	0.25	**0.47**	0.25	0.25	**0.48**
$k_r = \tau_r / \tau_p$	0.4	**0.417**	0.213	0.4	**0.51**	0.208
$k_E = E / \tau_p$	350	350	350	350	350	350
$k_0 = p_0 / \sigma'_v$	0.6	0.6	0.6	0.6	0.6	0.6
$\mu = \tau_r / \sigma'_v$	0.1	0.104	0.1	0.1	0.128	0.1
Elastic modulus, E (MPa)	62	62	116	81	81	155
Excess pore pressure ratio, $\Delta P / \sigma'_v$	0.167	0.181	0.181	0.717	0.778	0.778
Active failure strain, ε_a (%)	–0.11	–0.11	–0.33	–0.11	–0.16	–0.33
Passive failure strain, ε_p (%)	1.03	1.03	0.82	1.03	1.44	0.81
Fracture energy, J_0 (kPa·m)	14.1	13.1	33.3	7.8	5.0	15.5
Surface friction coefficient, C_S	0.002	0.002	0.002	0.002	0.002	0.002
Fracture strain, γ_0 (%)	0.159	0.154	0.179	0.091	0.073	0.092
$T_0 = (\tau_g - \tau_r)/E$	7.2×10^{-5}	7.4×10^{-5}	7.2×10^{-5}	1.5×10^{-4}	1.5×10^{-4}	1.5×10^{-4}
Strain ratio, λ_*	0.583	0.574	0.353	0.443	0.389	0.217
Critical length, l_0 (km)	6.81	6.49	12.72	3.16	2.88	6.56
l_0 / h	37.8	36.1	70.7	13.5	12.3	27.9
Dynamic failure length, l_f (km)	54.0	52.6	49.1	33.5	33.4	30.1
$\lambda_f = l_f / l_0$	7.9	8.1	3.9	10.6	11.6	4.6
Static failure length, $L_f = l_f / \kappa$ (km)	**28.4**	**27.7**	**28.7**	**17.6**	**17.6**	**17.6**
Failure length ratio, κ	1.90	1.90	1.71	1.90	1.90	1.71
Water resistance coefficient, β	3.4×10^{-5}	3.1×10^{-5}	7.0×10^{-5}	6.8×10^{-6}	4.9×10^{-6}	1.4×10^{-5}
Slide velocity, $\bar{\eta} = v_0$ (m/s)	1.52	1.53	1.34	1.88	1.92	1.74
Slide velocity when $\beta = 0$, $\bar{\eta} = v_0$ (m/s)	1.78	1.78	1.68	2.05	2.06	1.96

8.3. Gaviota slide

The Gaviota slide (Figure 1 and Figure 17) is located on the northern slope of the Santa Barbara basin (34°22'N, 120°06'W). The slide is relatively well studied [*Lee and Edwards*, 1986; *Edwards et al.*, 1993; *Edwards et al.*, 1995; *Hampton et al.*, 1996; *Greene et al.*, 2006; *Schwehr et al.*, 2006; *Dingler*, 2007; *Schwehr et al.*, 2007; *Blum*, 2010; *Blum et al.*, 2010] and composed of silty clay sediments [*Lee and Edwards*, 1986]. Analysis of the gravity cores collected in the slide area suggests that the Gaviota slide occurred between AD 1715 and AD 1840 [*Schwehr et al.*, 2006]. The *M*7.1 earthquake of 21 December 1812 in Santa Barbara, California is often attributed as the slide trigger [e.g., *Lee et al.*, 2004; *Greene et al.*, 2006; *Blum et al.*, 2010]. Slope failure occurred on a 4° slope, and the main body of the material displaced by the slide is 12 m thick, 1.65 km wide, and 1 km long [*Lee et al.*, 2004] (Table A.1).

The depth of the Gaviota slide headwall is approximately 400 m. Adjacent to the Gaviota slide, a large fracture traverses the intact slope at the same depth (Figure 1 and Figure 17). The fracture is approximately 8 km long eastward [*Lee and Edwards*, 1986; *Edwards et al.*, 1995; *Hampton et al.*, 1996; *Greene et al.*, 2006; *Schwehr et al.*, 2007; *Blum et al.*, 2010] and resembles a headwall of the Gaviota slide [*Blum*, 2010]. According to *Dingler* [2007], this fracture formed concurrently with the Gaviota slide.

Properties of the sediment from the Gaviota slide area were studied by *Lee and Edwards* [1986] and *Edwards et al.* [1995] based on the gravity cores taken in 6 locations in the slide area. Their results do not show considerable difference between the locations with the average overconsolidation ratio [e.g., *Lambe and Whitman*, 1986, page 297] of 1.5 [*Lee and Edwards*, 1986]. Such a value is relatively low and indicates that the sediment is lightly overconsolidated [*Bjerrum*, 1972]. The mean value of the peak shear strength for this sediment is $\tau_p \approx 0.48\sigma'_v$ [*Lee and Edwards*, 1986, eq. (1)] where the average sensitivity $\tau_p / \tau_r \approx 2.7$ [*Edwards et al.*, 1995]. Hence, the characteristic residual strngth is given by $\tau_r \approx 2.7\tau_p = 0.18\sigma'_v$. Since the data on the elastic modulus, E, and cohesion, C, of the Gaviota slide sediment are not available, we simply used the value of $E = 500\tau_p$ and $C = 0$, which are the typical values that are characteristic for lightly-overconsolidated sediments [e.g., *Bjerrum*, 1972; *Mayne et al.*, 2001].

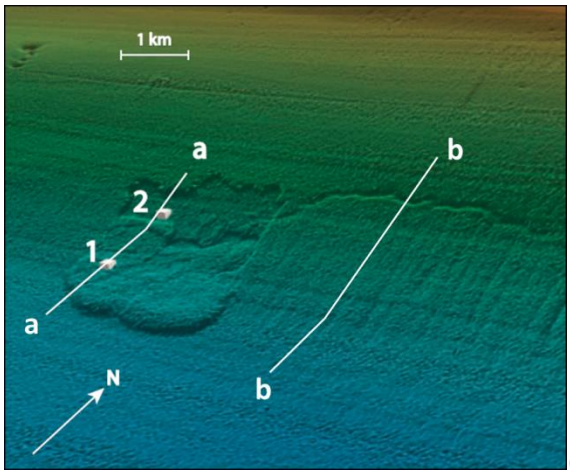

(a)

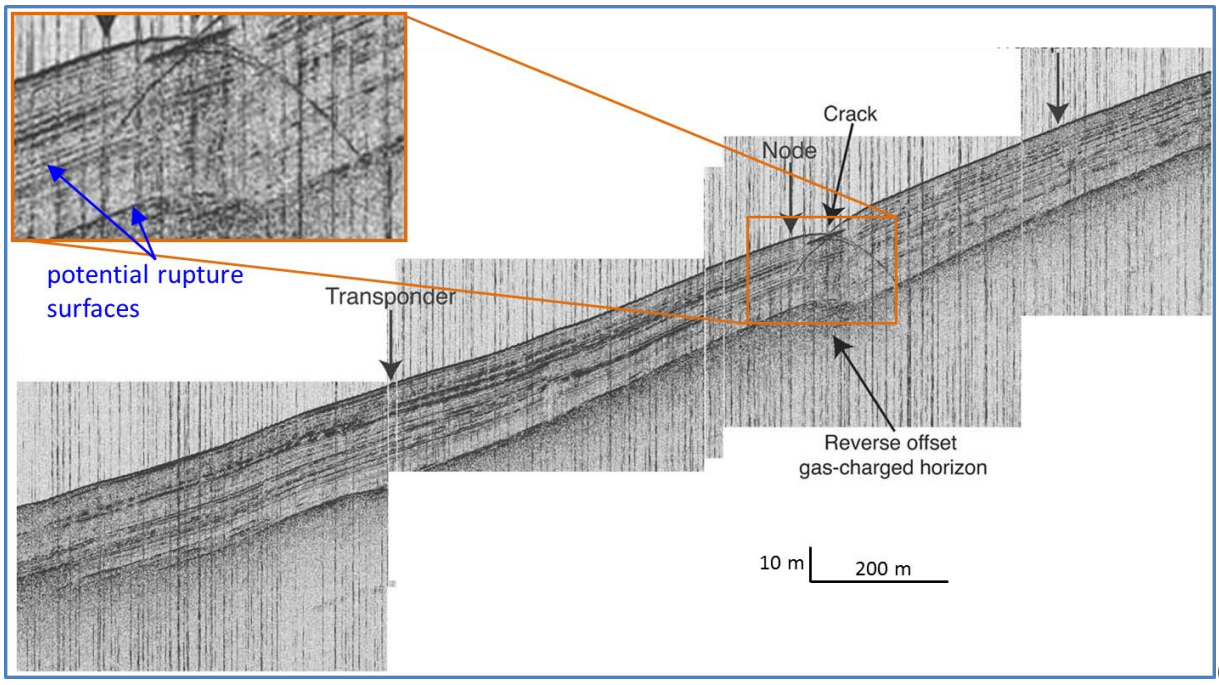

(b)

Figure 17. (a) Gaviota slide on the northern slope of the Santa Barbara basin [modified after *Schwehr et al.*, 2006]. (b) A CHIRP [*Schock et al.*, 1989] seismic profile image along line b-b (figure (a)) west to the slide in the area with the sub-horizontal fracture [modified after *Blum et al.*, 2010]. The profile along line a-a (figure (a)) is shown in Figure 1b.

The gravity cores sampled only ≈ 1.5 m of the upper sediment layer, which is deeper than the ≈ 0.5 m thick drape, accumulated after the slide [e.g., *Greene et al.*, 2006], but much shallower than the thickness of 12 m of the Gaviota slide body. As noted by *Lee and Edwards* [1986], in the absence of geological information, it is difficult to conclude that all 12 meters of the displaced materials were over-consolidated (albeit lightly). We, therefore, also consider the case of the Gaviota slide sediment being normally-consolidated (similar to many other

submarine deposits). This is consistent with the nearly constant regional sedimentation rate during the last 136 ky [*NIicholson et al.*, 2006] including the most recent 500 to 1000 years when the Gaviota slide have occurred [*Lee et al.*, 2004].

Although the Gaviota slide is sometimes interpreted as being retrogressive [*Lee and Edwards*, 1986; *Edwards et al.*, 1995], recent multibeam bathymetric and backscatter data [*Eichhubl et al.*, 2002; *Greene et al.*, 2006; *Schwehr et al.*, 2006; *Schwehr et al.*, 2007] as well as seismic profiles [*Schwehr et al.*, 2006; *Schwehr et al.*, 2007; *Blum et al.*, 2010] do not show surface morphology characteristic for retrogressive sliding [e.g., *Kvalstad et al.*, 2005; *Quinn et al.*, 2011b]. The slide rupture surface appears to be fairly smooth (Figure 1a and Figure 17a) and can be interpreted as a result of the downslope rupture (shear band) propagation, which started from the upper headwall (Figure 2a).

Considering the Gaviota slide clays as being normally-consolidated and adopting the baseline sediment properties (Table 6 and Table 8), we find that because the slope angle is low ($\alpha = 4°$), some excess pressure in the shear band is required to trigger its propagation. Specifically, $\Delta P = 0.413\sigma'_v$ for the band to propagate the observed distance of $l_f = 1$ km (Table A.1). In this case, $\lambda_* = 0.835$, the slide velocity at failure is relatively small $v_0 = \bar{\eta} = 0.21$ m/s (as expected for a small slide), and the length of the corresponding static slide is $L_f = 0.5$ km (so $\kappa = l_f/L_f = 1.9$).

Similar to Table 7, static analysis of the Gaviota slide with normally-consolidated sediments could also explain the observed failure length of $l_f = 1$ km. In static interpretation, the excess pressure $\Delta P = 0.360\sigma'_v = 34$ kPa ($\sigma'_v = 94$ kPa) in the band or $k_r = \tau_r/\tau_p = 0.436$ would also result in the failure length of $L_f = 1$ km. The increased value of $k_p = \tau_p/\sigma'_v = 0.470$ leads to $L_f = 1.0$ km as well, but in this case, the residual friction needs to be decreased to $\tau_r = 0.213\tau_p$ to maintain the same value of $\tau_r/\sigma'_v = 0.1$ as in the dynamic case (Table 8). Compared to the dynamic analysis (Table 8), the excess pore pressure, ΔP, and coefficient, $k_r = \tau_r/\tau_p$, do not significantly change, while coefficient $k_p = \tau_p/\sigma'_v$ nearly doubles. The corresponding critical lengths, l_0, are 630 m, 590 m, and 870 m, respectively, which are 2 to 3 times larger than the value in the dynamic slide ($l_0 = 320$ m; Table 8). These conditions are consistent with the results for the Gaviota slide complex of lightly-overconsolidated sediments (Table 6) and for the Currituck

Slides A (Table 7) and B (Table 8). The parameter k_p differs the most between the dynamic and static analyses.

The fracture on the slope to the right (east) of the Gaviota slide can be interpreted [*Martel*, 2004] as produced by the developing rupture surface when the fracture represents the future location of the headscarp of the potential slide. A similar interpretation was offered by *Bernander* [2011] who described the formation of long cracks on the ground surface with no generation of global slope failure. *Bernander* [2011] termed such cases 'unfinished landslides', which are also referred to as 'confined failures' [*Hutchinson*, 1988]. This interpretation is consistent with the image in Figure 17b, which shows the vertical seismic cross-section along the profile line b-b in Figure 17a. We hypothesize that this landslide did not take place at the time of the Gaviota slide because of the difference in the slope and/or subsurface geometry below the headscarp fracture. Indeed, assuming the same sediment properties in the two areas (since they are adjacent each other), we slightly change the slope angle from $\alpha = 4°$ to 3.7°. This results in the increase of the critical lengths from $l_0 = 320$ m to 600 m in the case of normally-consolidated sediments (Table 8). Hence, it could have been that when the initial rupture surface (shear band) reached the critical length of l_0 under the sediment displaced by the Gaviota slide, it was shorter than the value of l_0 corresponding to the adjacent east slope. As a result, the unstable shear band growth did not occur to the east of the Gaviota slide. Therefore, the slight difference in slope angle (although visible in Figure 17b), may have caused a drastically different behavior of the shear band (i.e., unstable, dynamic growth versus stable, static development). If the shear band keeps propagating progressively below the headscarp fracture, it may start propagating dynamically and will cause the corresponding landslides. Parameters of this potential landslide are given in Table 8.

We interpret the curved lines in the inset on Figure 17a as shear bands that appeared as a result of active failure. Resolution of this image is insufficient to conclude whether the basal rupture surface initiated or did not initiate. Possible locations of this surface are indicated based on the locations of the lower ends of the curved shear band and the sub-horizontal slope crack (Figure 1a and Figure 17a). The latter appears to end at the depth of 20 m, where the sub-horizontal shear band may emerge. In this scenario, we keep the same slope angle of $\approx 4°$,

but increase the depth of the shear band from 12 m to 20 m. The critical shear band length, l_0, increases again, from l_0 = 320 m to l_0 = 400 m for normally-consolidated slope sediments (Table 8). Similar to the case of different slope angle, that the slide did not take place may be indicative of the current shear band length being smaller than the critical length, l_0. If the band reaches this value, it will cause the slide, which is characterized by parameters given in Table 8.

Results for lightly-oversonsolidated slope sediments are given in Table 6. Except the excess pore pressure magnitude, they are similar to the case of normally-consolidated sediments (Table 8). This difference is important, however, since the required overpressure exceeds the value of $\Delta P = k_0\sigma'_v$ ($k_0 \approx 0.6$) and, therefore, hydraulic fracturing will occur prior to the slide taking place. Since the Gaviota slide did happen, we concluded that the sediment at the time of slide may have been normally-consolidated. In this scenario, the magnitude of the excess pore pressure does not exceed the hydro-fracturing threshold of $\approx k_0\sigma'_v$ (Table 8).

Table 8. The shear band model parameters for the Gaviota slide and adjacent slope fracture on the slope composed of a normally-consolidated sediment. Quantities that changed as a result of parameter changes are given in blue font. The slide associated with the fracture on the slope (adjacent to the Gaviota slide) has not taken place yet, but the expected parameters are computed and presented in parenthesis.

Parameters	Gaviota slide (dynamic analysis)	Gaviota slide (static analysis)			Adjacent slope fracture (dynamic analysis)	
		varying ΔP	varying τ_r	varying τ_p	milder slope	thicker slide
Slope angle, α	4°	4°	4°	4°	**3.7°**	4°
Thickness, h (m)	12	12	12	12	12	**20**
Density, ρ_0 (kg/m^3)	1800	1800	1800	1800	1800	1800
Characteristic slip, $\bar{\delta}$ (cm)	10	10	10	10	10	10
$k_p = \tau_p / \sigma'_v$	0.25	0.25	0.25	**0.470**	0.25	0.25
$k_r = \tau_r / \tau_p$	0.4	0.4	**0.436**	0.213	0.4	0.4
$k_E = E / \tau_p$	350	350	350	350	350	350
$k_0 = p_0 / \sigma'_v$	0.6	0.6	0.6	0.6	0.6	0.6
$\mu = \tau_r / \sigma'_v$	0.1	0.1	0.109	0.1	0.1	0.1
Elastic modulus, E (MPa)	4.1	4.1	4.1	7.7	4.1	7
Excess pore pressure ratio, $\Delta P / \sigma'_v$	0.413	**0.360**	0.413	0.413	0.413	0.413
Active failure strain, ε_a (%)	–0.11	–0.11	–0.11	–0.33	–0.11	–0.11
Passive failure strain, ε_p (%)	1.03	1.03	1.03	0.82	1.03	1.03
Fracture energy, J_0 (kPa·m)	0.825	0.900	0.776	2.036	0.825	1.376
Surface friction coefficient, C_S	0.002	0.002	0.002	0.002	0.002	0.002
Fracture strain, γ_0 (%)	0.579	0.604	0.561	0.663	0. 579	0.448
$T_0 = (\tau_g - \tau_r)/E$	2.6×10^{-4}	1.4×10^{-4}	1.4×10^{-4}	1.4×10^{-4}	1.4×10^{-4}	2.6×10^{-4}
Strain ratio, λ_*	0.835	0.841	0.831	0.669	0.835	0.797
Critical length, l_0 (km)	0.32	0.63	0.59	0.87	(0.60)	(0.40)
l_0/h	26.8	52.3	48.8	72.4	(49.8)	(21.7)
Dynamic failure length, l_f (km)	1.0	1.9	1.89	1.7	(1.9)	(1.7)
$\lambda_f = l_f / l_0$	3.1	3.0	3.2	2.0	(3.1)	(3.9)
Static failure length, $L_f = l_f / \kappa$ (km)	0.5	**1.0**	**1.0**	**1.0**	(1.0)	(0.9)
Failure length ratio, κ	1.90	1.90	1.90	1.71	(1.90)	(1.90)
Water resistance coefficient, β	8.9×10^{-5}	1.8×10^{-4}	1.5×10^{-4}	2.7×10^{-4}	(1.6×10^{-4})	(5.4×10^{-5})
Slide velocity, $\bar{\eta} = v_0$ (m/s)	0.21	0.19	0.21	0.10	(0.21)	(0.34)
Slide velocity when $\beta = 0$, $\bar{\eta} = v_0$ (m/s)	0.39	0.38	0.39	0.26	(0.39)	(0.54)

Table 9. The shear band model parameters for the Gaviota slide and the adjacent fracture on the slope composed of a lightly-overconsolidated sediment. The slide associated with the fracture on the slope (adjacent to the Gaviota slide) has not taken place yet, but the expected parameters are computed and presented in the parenthesis.

Parameters	Gaviota slide (dynamic analysis)	Gaviota slide (static analysis)			Adjacent slope fracture (dynamic analysis)	
		varying ΔP	varying τ_r	varying τ_p	midler slope	thicker slide
Slope angle, α	4°	4°	4°	4°	**3.7°**	4°
Thickness, h (m)	12	12	12	12	12	**20**
Density, ρ_0 (kg/m^3)	1800	1800	1800	1800	1800	1800
Characteristic slip, $\bar{\delta}$ (cm)	10	10	10	10	10	10
$k_p = \tau_p / \sigma'_v$	0.475	0.475	0.475	**0.81**	0.475	0.475
$k_r = \tau_r / \tau_p$	0.37	0.37	**0.43**	0.217	0.37	0.37
$k_E = E / \tau_p$	500	500	500	500	500	500
$k_0 = p_0 / \sigma'_v$	0.6	0.6	0.6	0.6	0.6	0.6
$\mu = \tau_r / \sigma'_v$	0.176	0.176	0.204	0.176	0.176	0.176
Elastic modulus, E (MPa)	11.4	11.4	11.4	19.4	11.4	19.0
Excess pore pressure ratio, $\Delta P / \sigma'_v$	0.714	**0.668**	0.714	0.714	0.714	0.714
Active failure strain, ε_a (%)	–0.23	–0.23	–0.23	–0.30	–0.30	–0.23
Passive failure strain, ε_p (%)	0.57	0.57	0.57	0.50	0.57	0.57
Fracture energy, J_0 (kPa·m)	0.821	0.953	0.744	1.741	0.821	1.368
Surface friction coefficient, C_S	0.002	0.002	0.002	0.002	0.002	0.002
Fracture strain, γ_0 (%)	0.35	0.37	0.33	0.39	0.35	0.27
$T_0 = (\tau_g - \tau_r)/E$	1.6×10^{-4}	9.5×10^{-5}	9.6×10^{-5}	9.6×10^{-5}	1.2×10^{-4}	1.6×10^{-4}
Strain ratio, λ_*	0.599	0.617	0.588	0.562	0.599	0.537
Critical length, l_0 (km)	0.42	0.76	0.70	0.75	(0.58)	(0.61)
l_0/h	35.3	63.4	58.4	71.7	(48.3)	(30.6)
Dynamic failure length, l_f (km)	1.0	1.7	1.7	1.6	(1.4)	(1.7)
$\lambda_f = l_f / l_0$	2.4	2.3	2.4	1.9	(2.4)	(2.7)
Static failure length, $L_f = l_f/\kappa$ (km)	0.59	**1.0**	**1.0**	**1.0**	(0.80)	(1.0)
Failure length ratio, κ	1.71	1.71	1.71	1.62	(1.71)	(1.71)
Water resistance coefficient, β	6.8×10^{-5}	1.3×10^{-4}	1.1×10^{-4}	1.5×10^{-4}	(9.3×10^{-5})	(4.6×10^{-5})
Slide velocity, $\bar{\eta} = v_0$ (m/s)	0.14	0.13	0.16	0.11	(0.14)	(0.25)
Slide velocity when $\beta = 0$, $\bar{\eta} = v_0$ (m/s)	0.29	0.28	0.30	0.25	(0.29)	(0.42)

8.4. Humboldt slide

Humboldt slide is located in the Eel River basin on the Northern California continental margin, about 50 km of Cape Mondecino [*Field et al.*, 1980; *Field and Barber*, 1993]. Sediments in the slide area are primarily Late Pleistocene and Holocene clayey silts with abundant evidence of gas in the sediments [*Field and Barber*, 1993; *Yun et al.*, 1999]. *Gardner et al.* [1999] interpret the Humboldt slide as a large slope failure with a length of 10 km, and thickness of 65 m. The origin of the Humboldt slide has created a controversy [*Lee et al.*, 2007; *Schwehr et al.*, 2007]. *Gardner et al.* [1999] interpreted the Humboldt slide as a submarine slope failure deposit. *Lee et al.* [2007], however, concluded that the Humboldt slide is a field of migrating current-controlled sediment waves. The controversy steams out of the same data set used for both interpretations [*Lee et al.*, 2007; *Schwehr et al.*, 2007].

These two alternative hypothesis (slope failure and sediment waves) predict different sediment fabric that can be evaluated using measurements of anisotropy of magnetic susceptibility [e.g., *Rees*, 1961; *Marino and Ellwood*, 1978; *Schwehr and Tauxe*, 2003]. Using this technique, *Schwehr et al.* [2007] concluded that the top 8 m of the sediment have not experienced post-depositional deformation, but rather formed by primary deposition associated with downslope currents [*Schwehr et al.*, 2007]. Measurements of the sediment strata deeper than 8 m are not available. Nevertheless, the general morphology of the Humboldt slide suggests minimal downslope thickening or upslope thinning [*Schwehr et al.*, 2007]. In addition, there is no evidence in the seismic data of a basal surface coming out to the slope surface in the tow of the slide [*Lee et al.*, 2007]. These arguments are important in support of the sediment wave hypothesis of the Humboldt slide origin. For example, the seismic cross-section along the Gaviota slide (Figure 1) does exhibit both upslope thinning (in the excavation region) and downslope thickening (in the deposition region), and the slide is, therefore, interpreted as a part of the slope failure process.

The hypotheses of slope failure and sediment waves can be reconciled by recognizing that the sediment waves in the Humboldt slide area could be a shallow phenomenon (up to $\approx$ 10 m depth), while the basal rupture surface has been developing much deeper, at the depth of $\approx$ 65 m (Figure 18). In this scenario, the rupture surface (shear band) has been propagating

progressively and the catastrophic propagation is yet to take place. In other words, so far, the Humboldt slide has been in the pre-failure slope, which is to be followed by the failure stage in the future (Appendix A). This would explain minimal downslope displacements in the Humboldt slide area and why the basal rupture surface has not daylight yet at the slide tow area. Because previous slope failure (and possibly slides) have been interpreted beneath the Humboldt slide [*Field et al.*, 1980; *Gardner et al.*, 1999], it is worthwhile evaluating the slide potential in mass movement and generating tsunamis.

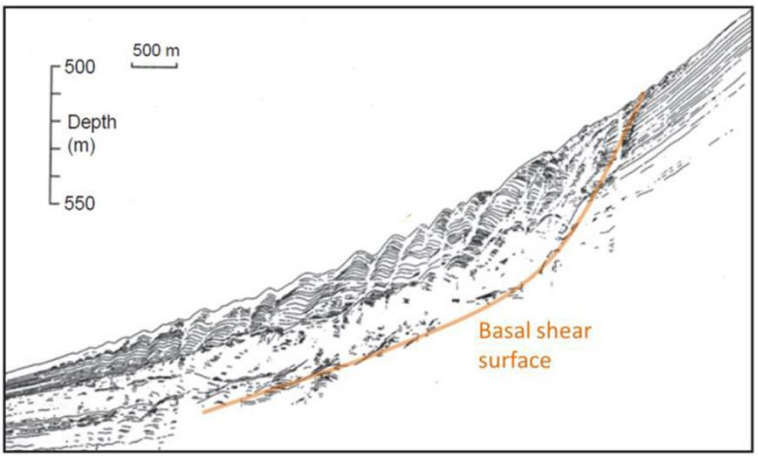

Figure 18. Seismic profile of the Humboldt slide on the Northern California continental margin (≈50 km north of Cape Mendocino) [*Gardner et al.*, 1999; *Lee et al.*, 2007]. Orange line shows the structural interpretation of *Gardner et al.* [1999].

Based on the basal shear surface interpretation of *Gardner et al.* [1999] (Figure 18), we first assume that the current length of the basal rupture of $l \approx 4.5$ km (Figure 18) is close to the critical value, l_0, of the sub-surface shear band. The Humboldt slide sediments are probabaly overconsolidated [*Lee et al.*, 1999; *Lee et al.*, 2002; *Lee et al.*, 2007], so far this first-order analysis we use the same sediment properties as for Currituck Slide 1 (Table 6). For these properties, $l_0 = 4.5$ km, $\alpha = 2°$, and $h = 65$ m, the shear band will propagate catastrphicaly if the overpressure $\Delta P = 0.670\sigma'_v = 342$ kPa. While some overpressure may be a result of the sediment pressurization by the existing gas, for example, by the gas dissociating from the methane hydrates, abundant in the Humboldt slide area [*Brooks et al.*, 1991; *Gardner et al.*, 1999], the overpressure is unlinkely to reach such a high level as before that, the sediment will be hydro-fractured at $\Delta P = k_0\sigma'_v$ ($k_0 \approx 0.6$). Therefore, currently, $l < l_0$. Nevertheless, $\Delta P > k_0\sigma'_v$ may be generated, at least in principle, by an earthquake. Given earthquake activity in the

Northern California area, we also computed the landslide parameters for $\Delta P = 0.670\sigma'_v$. The slope failure then would occur at $l_f = 32.5$ km, which roughly doubles the value of $L_f = 17.1$ km, obtained in the static approximation. The results of our analysis are summarized in Table 10.

8.5. Storegga slide

The Storegga Slides (offshore Norway, North Sea, 5 to 30 ka) were originally interpreted as three separate slides [*Bugge et al.*, 1988; *Dawson et al.*, 1988], but more recent work [*Haflidason et al.*, 2004; *Masson et al.*, 2006; *De Blasio*, 2011] suggests that there may have been a larger number of smaller events. Yet it is believed [*Haflidason et al.*, 2004; *Bondevik et al.*, 2005; *Haflidason et al.*, 2005; *Lovholt et al.*, 2005] that a large tsunami was generated by one of the Storegga Slides with the size of ~100 km. This hypothesis is supported by the tsunami deposits found in onshore lakes in Norway [*Bondevik et al.*, 2005] and in inland mudflats in Scotland [*Dawson et al.*, 1988]. In Table 10, we presented the results of modeling of such a slide. Given the uncertainty in dating and geometry, we refer to this event simply as Storegga Slide. *Bondevik et al.* [2005] and *Kvalstad et al.* [2005] used a retrogressive (uphill) slope failure model to analyze the Storegga Slide and the magnitude of the resulting tsunami. Here we use an alternative model of the slide (Figure 2a) associated with the downhill shear band propagation [*Saurer*, 2009].

Following *Bugge et al.* [1988], *Harbitz* [1992], *Bondevik et al.* [2005], and *Kvalstad et al.* [2005], we consider $h = 144$ m and $\alpha = 0.5°$ as the average thickness and slope angle for the Storegga Slide. *Bugge et al.* [1988] argue that in the area of Storegga Slide, most of the clayey sediments were normally-consolidated at the slide time. Therefore, we use again the baseline parameters (Table 6), but add the excess pore pressure of $\Delta P = 0.925\sigma'_v$. Such a high pore pressure is required because of the small slope angle of $\alpha = 0.5°$. The limiting equilibrium approach also results in highly elevated pressure [*Kvalstad et al.*, 2005]. However, since $\Delta P > k_0\sigma'_v$ ($k_0 = 0.6$), hydraulic fracturing is likely to take place before the excess pressure reaches the level of $\Delta P = 0.925\sigma'_v$. Nevertheless, since such a high overpressure may be generated by an earthquake [*Kvalstad et al.*, 2005], we computed the slide parameters for this overpressure (Table 10). Expression (7.8) and (7.11) give $l_f = 111.5$ km and $L_f = 58.7$ km ($\kappa = 1.90$)

for dynamic and static analyses, respectively. The initial slide velocity is estimated as $v_0 = 1.61$ m/s (per (K.10) in Appendix K).

Alternatively, the same values of failure lengths $l_f = 111.5$ km and $L_f = 58.7$ km can also be achieved when the residual friction coefficient drops from $k_r = \tau_r / \tau_p = 0.4$ to 0.03. The lowered value of $k_r = \tau_r / \tau_p$ can be justified by high sensitivity of the sediments in Storegga area [e.g., *Kvalstad et al.*, 2005]. In this case, excess pore pressure does not need to be added on the rupture surface ($\Delta P = 0$).

8.6. Subaerial slides

Quinn et al. [2011a; 2012] suggested using the original model by *Palmer and Rice* [1973] (Figure 24, Section 10.1) to study low-angle subaerial landslides such as those at river banks in Quebec, Canada. Specifically, they suggested that shear bands propagating upslope in conditions similar to an open-cut in an infinite slope (Figure 24, Section 10.1) may be an important mechanism of progressive failure in sensitive clay. For their quantitative analysis, *Quinn et al.* [2011a; 2012] used the properties of the Saint-Alban slide (Quebec, Canada) clay. These properties are given in Table 10. In their model, the slope angle and slide thickness were $\alpha = 0.5°$ and $h = 30$ m, respectively.

As mentioned above, for an open-cut with a shear band propagating upslope (Figure 24, Section 10.1), the sediment must have at least some cohesion (tensile strength) to counterbalance the weight of the slab separated from the substrata by the shear band. *Quinn et al.* [2011a; 2012] suggested that the slab grows to such a length that the tensile strength along the slab is exceeded, resulting in the sediment failure at the higher end of the slab. They used, however, the value of the active load characteristic to compressive stress regime. Numerically, their "active load" corresponds to cohesion or tensile strength of the sediment material. For the sake of comparison, we, therefore, used the value of their "active" load as cohesion to failure length in static analysis. Instead we used the length given by L_f in (7.9) with γ_p replaced by $\gamma_t = (\sigma_t + p_0)/E$ and λ_* given by equation (10.2) in Section 10.1. This value of L_f is a result of the static analysis. Since the residual friction for the Saint-Alban clay is 80 times smaller than its peak value [*Quinn et al.*, 2011a; 2012], no excess pressure is required for the

slip to develop, even in such a low angle as $\alpha = 0.5°$.

To compare the results of static and dynamic analyses, we use parameters defined by *Quinn et al.* [2011a; 2012] (we do not introduce any additional parameters). As can be seen in Table 10, the critical band size is $l_0 = 220$ m, which is the same as in *Quinn et al.* [2011a; 2012]. The failure lengths for static and dynamic analyses are 730 m and 2.05 km, respectively. Therefore, the dynamic analysis suggests that after reaching the length of $l_0 = 220$ m, the shear band would grow not until it reaches a length of 730 m, but until a significantly greater length of 2,050 m is reached. In other words, the dynamic analysis indicates that the slide three times as large as in the static analysis.

Table 10. The shear band model parameters for two submarine (Humboldt [*Field et al.*, 1980; *Gardner et al.*, 1999] and Storegga [*Bugge et al.*, 1988; *Dawson et al.*, 1988]) slides and one subaerial [*Quinn et al.*, 2011a] slide.

Parameters	Humboldt slide	Storegga Slide	Storegga Slide	Saint-Alban
		varying ΔP	varying τ_r	
Slope angle, α	2°	0.5°	0.5°	0.5°
Thickness, h (m)	65	144	144	30
Density, ρ_0 (kg/m^3)	1800	1800	1800	1800
Characteristic slip, $\bar{\delta}$ (cm)	10	10	10	50
$k_p = \tau_p / \sigma'_v$	0.25	0.25	0.25	0.15
$k_r = \tau_r / \tau_p$	0.4	0.4	**0.03**	0.013
$k_E = E / \tau_p$	350	350	350	250
$k_0 = p_0 / \sigma'_v$	0.6	0.6	0.6	0.5
$\mu = \tau_r / \sigma'_v$	0.1	0.1	0.0075	0.002
Cohesion, $C = \sigma_t$ (MPa)	0	0	0	0.090
Elastic modulus, E (MPa)	22	49	49	10
Excess pore pressure ratio, $\Delta P / \sigma'_v$	0.670	0.925	0	0
Active failure strain, ε_a (%)	–0.11	–0.11	–0.11	–2.25
Passive failure strain, ε_p (%)	1.03	1.03	1.03	–1.35*
Fracture energy, J_0 (kPa·m)	2.524	1.3	27.4	40.0
Surface friction coefficient, C_S	0.002	0.002	0.002	subaerial
Fracture strain, γ_0 (%)	0.187	0.060	0.277	–1.633
$T_0 = (\tau_g - \tau_r)/E$	4.3×10^{-5}	2.8×10^{-5}	2.8×10^{-5}	3.7×10^{-4}
Strain ratio, λ_*	0.620	0.343	0.708	5.773
Critical length, l_0 (km)	4.50	8.95	20.1	0.22
l_0/h	69.3	62.1	139.7	7.6
Dynamic failure length, l_f (km)	32.5	111.5	111.5	2.0
$\lambda_f = l_f / l_0$	7.2	12.5	5.5	8.9
Static failure length, $L_f = l_f / \kappa$ (km)	17.1	58.7	58.7	0.73
Failure length ratio, κ	1.9	1.90	1.90	2.81
Water resistance coefficient, β	7.2×10^{-5}	2.1×10^{-5}	2.2×10^{-4}	subaerial
Slide velocity, $\bar{\eta} = v_0$ (m/s)	0.89	1.52	1.18	1.81
Slide velocity when $\beta = 0$, $\bar{\eta} = v_0$ (m/s)	1.07	1.61	1.56	1.81

*Strain corresponding to zero effective stress at $x = 0$ (Figure 24 in Section 10.1)

CHAPTER 9. TSUNAMI WAVE MAGNITUDE

9.1. Submarine slide on a mild slope

A common approach to modeling tsunamis generated by submarine landslides is to represent the slide by a solid body moving along the slope with a constant angle [*Harbitz*, 1992; *Pelinovsky and Poplavsky*, 1996; *Watts*, 1998; 2000; *Liu et al.*, 2003; *Grilli and Watts*, 2005]. In this scenario, however, the slide would never stop and eventually disintegrate. In many real cases, the finite run-out distance of a submarine slide is identified by seafloor observations [*McAdoo et al.*, 2000; *Haflidason et al.*, 2005]. A slide can stop for different reasons such as increasing friction coefficient on the sliding surface or decreasing slope magnitude as the slide moves [*De Blasio et al.*, 2004; *Bozzano et al.*, 2009; *De Blasio*, 2011]. Since accurate modeling of landslide-generated tsunamis is beyond the scope of this work, to compare the tsunamigenic potentials of different slides, we utilize the latter possibility. We assume that the friction coefficient μ is constant, but not necessarily equal to that on the propagating shear band. We also assume that the slide thickness and volume do not change, as its shape adjusts to the shape of the slope surface, along which the slide moves.

Let the ocean depth be $H(x)$, with $H(0) = H_0$ being the depth of the left (upper) slide end, $x = 0$, before it starts moving (Figure 19a). Note that, above we used notation x for the coordinate along the slope to describe the shear band propagation. In this chapter, $x > 0$ is the horizontal distance the left side end moves as the result of the slide motion along the slope (Figure 19a). The difference in notation, however, does not create any confusion since we do not describe both processes at the same time. As common in the literature on tsunamis and tsunamigenic landslides, the same notation, x, is used for both the horizontal coordinate and sliding distance.

As in Figure 2a, frictional load τ_r acts at the slide bottom while the water resistance τ_w is applied at its surface. The gravitational load τ_g is the driving force, and we consider two cases of a slide with (*i*) zero and (*ii*) non-zero initial velocity $v_0 = \bar{\eta}(l_f)$ (equations (6.14) and (K.10), respectively). Once the layer above the shear band separates from the substrata and begins sliding downslope, the coefficient of friction, μ, changes and typically reduces compared to that in the shear band because of such effects as hydroplaning and lubrication in the boundary layer

between the slide and the slope [*De Blasio et al.*, 2004; *Talling*, 2013]. In reality, it may take time for the seawater to percolate underneath the moving slide. For simplicity, however, we ignore this time scale and assume that μ changes as soon as the slide begins moving away from the trough (Figure 19b).

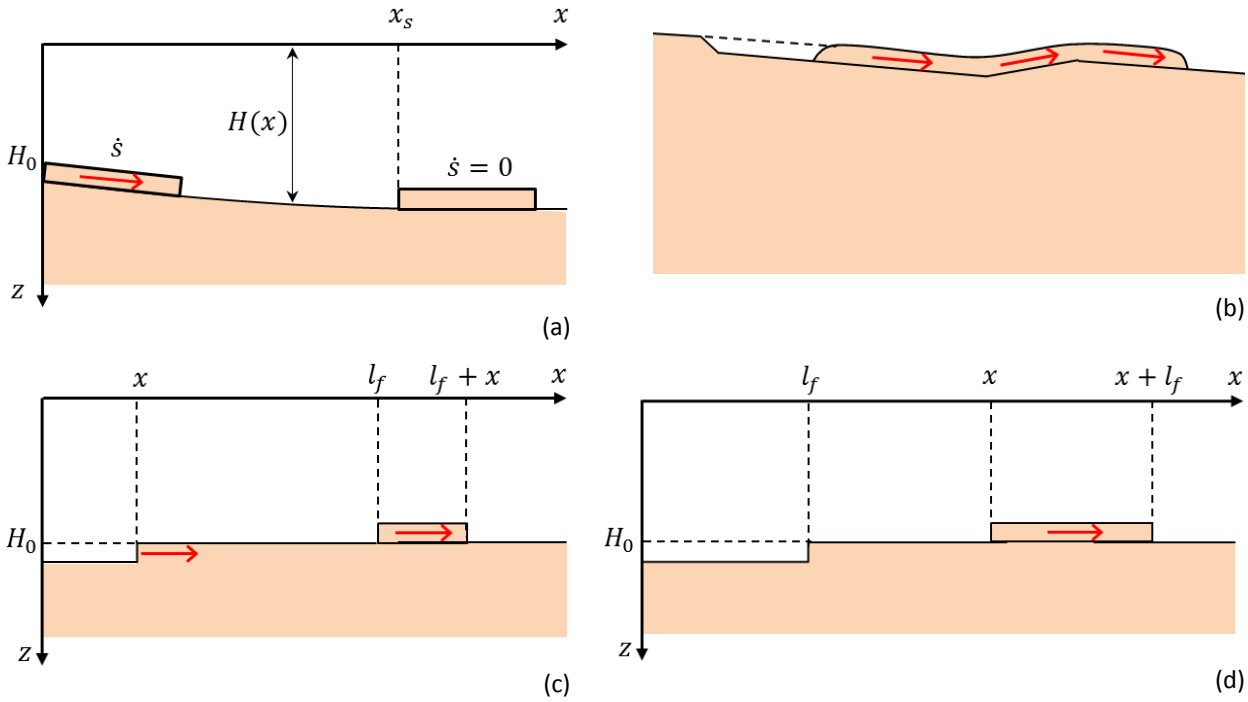

Figure 19. Schematics of a submarine slide. (a) Slide at the initial position (when its upper end is at $x = 0$) and final position (when its upper end is at $x = x_s$ where it arrived at $t = t_s$). Initially, the upper end of the slide is at depth H_0. (b) Development of the topographic depression (trench) and seafloor uplift as the slide moves. (c) A model of scenario (b) before the final depression is formed. (d) Slide movement after the final depression (trench) is formed.

Most works on tsunamigenic landslides adopt $\mu = 0.0025 - 0.005$ [*Harbitz*, 1992; *Pelinovsky and Poplavsky*, 1996; *Grilli and Watts*, 2005; *Geist et al.*, 2009]. For the sake of comparison of the tsunamigenic potential of different landslides, we, therefore, adopt a typical value of $\mu = 0.0025$ for slides moving downslope [*Geist et al.*, 2009].

Although not all, most of submarine slides have occurred on slopes with small angles [*McAdoo et al.*, 2000; *Hühnerbach and Masson*, 2004; *Masson et al.*, 2006; *Lee et al.*, 2007; *Clarke et al.*, 2011; *De Blasio*, 2011], and this is the case for all slides in Table 6 through Table 10. Therefore, we consider only small slope angles such that

$$\tan\alpha = H'(x) < \varepsilon << 1 \quad (\varepsilon = \text{const},\ \alpha > 0) \tag{9.1}$$

and keep only the leading terms with respect to $\varepsilon > 0$ in the momentum balance condition. Specifically, we *first* solve the momentum balance equation written for the arbitrary $\alpha(x) > 0$ and *then* consider the limit of $\alpha \to 0$ in all but friction terms in the obtained solution (Appendix M). This order is essential since making *first* the limit transition of $\alpha \to 0$ leads to the slope of constant α, on which the slide with constant μ would not stop.

As a result, the slide velocity can be expressed as (Appendix M)

$$v(x) = \left[e^{-A_w x/l_f} v_0^2 + 2(g/l_f)(1-\rho_w/\rho_0) \int_0^x [H(s+l_f) - H(s) - \mu l_f] e^{-A_w(x-s)/l_f} ds \right]^{1/2} \qquad (9.2)$$

Constant A_w is given by

$$A_w = \frac{1}{2} \frac{\rho_w}{\rho_0} \left(C_S \frac{l_f}{h} + C_D \right) \qquad (9.3)$$

which includes (in contrast to (K.8)) the drag coefficient, C_D, because of the "front" (Stokes-like) resistance to the slide motion [*Harbitz*, 1992; *Pelinovsky and Poplavsky*, 1996; *Watts*, 1998; *De Blasio et al.*, 2004; *De Blasio*, 2011].The dependence of $x(t)$ is then given in the implicit form of

$$t = \int_0^x \frac{dx}{v(x)} \qquad (9.4)$$

where time t is counted from the slide failure. At time t_s, the slide stops at $x = x_s$ defined from (9.2) with $v(x) = 0$.

Typically, submarine slides stop at a distance of 2 to 4 times the slide length [*McAdoo et al.*, 2000; *Haflidason et al.*, 2004; *Haflidason et al.*, 2005; *Geist et al.*, 2009], although this distance can be both smaller (Figure 1b) and greater [e.g., *Locat et al.*, 2009]. The stopping distances, x_s, shorter than run-out distance by slide length, for the Currituck slides and the Storegga slides were inferred as roughly 50 km ($\approx 2l_f$) [*Geist et al.*, 2009] and 400 km ($\approx 3.7l_f$) [*Haflidason et al.*, 2004], respectively (Table 11). *Harbitz* [1992] and *Geist et al.* [2009] reported the depth profiles consisted of two approximately linear segments of the seafloor (i.e., with two different slope angles) for Storegga slide and Currituck Slide B. Currituck Slide A includes one more segment, also approximately linear [*Geist et al.*, 2009]. In line with these observations, we adopt the simplest depth profile

Table 11. Parameters for the seafloor profile and tsunami wave magnitudes.

Parameters	Currituck Slide A	Currituck Slide B	Storegga slide	Baseline
Dynamic failure length, l_f (km)	28.7	17.3	111.5	10.5
Static failure length, L_f (km)	15.1	9.1	58.7	5.5
Slide thickness, h (m)	180	235	150	50
Initial velocity of dynamic slide, $v_0 = \bar{\eta}$ (m/s)	1.86	2.28	1.81	0.78
Initial depth, H_0 (km)	0.5	0.5	0.4	0.5
Shallow water wave velocity, c_w (m/s)	137.4	65.3	162.1	176.0
Characteristic time, $\tau = l_f/c_w$ (s)	211	268	688	60
Slope (shear band) angle for $x < x_0$, α_0	4°	2°	0.5°	6°
Slope angle for $x > x_0$, α_1	2°	0.6°	0.1°	0°
Slope angle for $x > x_1$, α_2	0.6°			
Stopping distance, x_s (km)	47.11	1.96	420	30
Distance where slope angle changes from α_0 to α_1, x_0 (km)	28.7	32.5	250	30
Distance where slope angle changes from α_1 to α_2, x_1 (km)	50			
Bottom friction coefficient for a mobile slide, μ	0.03524	0.03524	0.0025	0.075
Outgoing wave height, h_w (dynamic slide, crest/trough, m)	29.70/–24.30	3.38/–0.64	12.53/–12.49	1.42/–3.72
Outgoing wave height, h_w (static slide, crest/trough, m)	22.64/–15.40		7.05/–9.73	0.81/–2.76
Dynamic-to-static ratio of outgoing wave height, h_w (crest/trough)	1.31/1.57		1.78/1.28	1.75/1.34
Backgoing wave height, h_w (dynamic slide, crest/trough, m)	8.79/–11.86	0.59/–3.20	1.92/–6.04	1.89/–0.88
Backgoing wave height, h_w (static slide, crest/trough, m)	5.09/–7.20		1.48/–3.98	1.46/–0.57
Dynamic-to-static ratio of backgoing wave height, h_w (crest/trough)	1.73/1.65		1.30/1.52	1.29/1.54

$$H(x) = \begin{cases} x\tan\alpha_0 + H_0 & \text{if} \quad 0 \le x < x_0 \\ (x - x_0)\tan\alpha_1 + x_0\tan\alpha_0 + H_0 & \text{if} \quad x_0 \le x < x_1 \\ (x - x_1)\tan\alpha_2 + (x_1 - x_0)\tan\alpha_1 + x_0\tan\alpha_0 + H_0 & \text{if} \quad x \ge x_1 \end{cases} \tag{9.5}$$

which accommodates both cases. Here $0 \le \alpha_2 \le \alpha_1 < \alpha_0$ and α_0 represent the initial slope where the shear band developed (denoted by α in the preceding text). For the Currituck Slides A and B (Figure 16c), for example, the slope angles are $\alpha_0 = 4°$, $\alpha_1 = 2°$, $\alpha_2 = 0.6°$ and $\alpha_0 = 2°$, $\alpha_1 = \alpha_2 = 0.6°$, respectively, while the corresponding values of x_0 and x_1 in (9.5) are $x_0 = 28.7$ km,

$x_1 = 50$ km and $x_0 = x_1 = 32.5$ km, respectively. For Storegga slide, $\alpha_0 = 0.5°$, $\alpha_1 = \alpha_2 = 0.1°$, and $x_0 = x_1 = 250$ km (Table 11). The moving slides stop because of the reducing gravitational load along the slide paths.

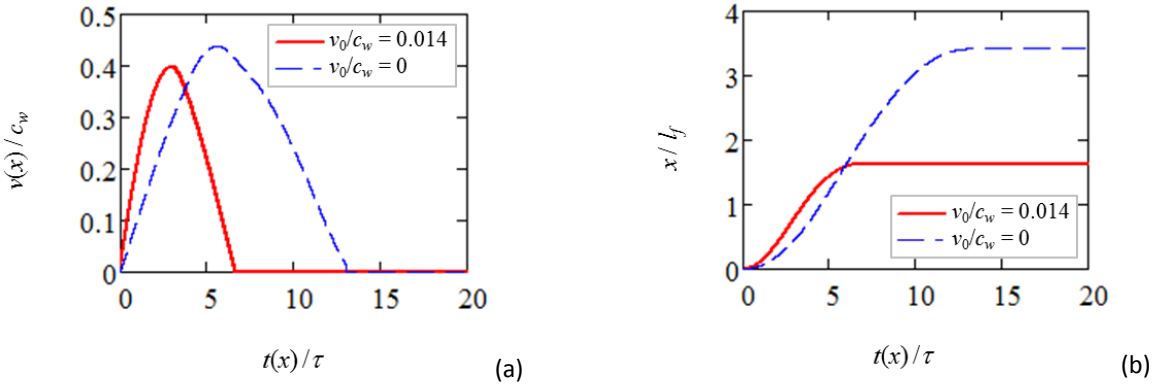

Figure 20. Sediment motion as a result of the Currituck Slide A. (a) Dimensionless slide velocity, $V(x) = v(x)/c_w$, and (b) dimensionless sliding distance $S = x/l_f$, as functions of the dimensionless time, t/τ, for initial velocity $V_0 = 0.014$ (red, solid lines) in the dynamic case (Table 11) and $V_0 = 0$ (blue, dashed lines) in the static case (Table 11). Quantity, $v(x)$ and $t(x)$ were computed with (9.2) and (9.4), respectively, using distance x as parameter.

For the calculations described below, we used the geometry (e.g., failure length, l_f, slope angle, $\alpha = \alpha_0$, and dynamic to static failure length ratio, κ) and the initial slide velocity, $v_0 = \bar{\eta}$, given in Table 6. Dimensionless slide motion distance, x/l_f, and velocity, $v(x)/c_w$, are plotted in Figure 20a and Figure 20b, respectively, as functions of dimensionless time $t(x)/t_0$ for the Slide A of the Currituck slide complex. Here $c_w = (g\bar{H})^{1/2}$ is the shallow water wave velocity, $\bar{H}$ is the averaged water depth while the slide is in motion, and $t_0 = l_f/c_w$ is the characteristic time. As can be seen in Figure 20a, the value of v/c_w does not exceed 0.5. The results for other slides in Table 6 are similar.

9.2. Tsunami height

Relation between the landslide and generated surface waves (tsunamis) is characterized by the landslide and wave velocities. A landslide motion on the seafloor results in perturbations of the water surface. If the slide moves with the velocity v close to the long gravitational (shallow water) wave velocity, c_w, the waves cannot depart sufficiently fast from the source region, where the wave build-up takes place. As a result, if v approaches c_w, the wave resistance to the landslide motion sharply increases and so does the wave amplitude [*Pelinovsky et al.*, 2001;

Ward, 2001; *Didenkulova et al.*, 2010]. The resonance occurs when the corresponding Froude number, $Fr = v/c_w$, becomes equal to one. The Froude number changes as the slide separates from the strata and moves downhill (Figure 20a) since both v and c_w are generally not constant. Yet, for the Currituck Slide A, the Froude number does not exceed 0.5, which indicates the subcritical flow regime ($Fr < 1$) [*Munson et al.*, 2006]. The flow regime remains subcritical as the slide moves. This statement is valid for other slides in Table 11 and, in general, for submarine slides with low slope angles.

Because of the small slope angle under consideration, we follow others [*Tinti and Bortolucci*, 2000a; b; *Tinti et al.*, 2001; *Pelinovsky*, 2003] and consider tsunami height in the ocean of the constant, average depth ($H = \bar{H} = \text{const}$). Comparison of the results between the cases of horizontal seafloor and a small slope showed that the difference is not significant [*Didenkulova et al.*, 2010]. In the case of $l_f >> H$, which is of interest here, we use the linearized, shallow-water asymptotic approximation [*Tinti and Bortolucci*, 2000b]

$$\frac{\partial \xi}{\partial t_1} + \frac{\partial u}{\partial x_1} = \frac{\partial \eta_s}{\partial t_1}, \qquad \frac{\partial u}{\partial t_1} + \frac{\partial \xi}{\partial x_1} = 0 \tag{9.6}$$

and assume that in the initially static ocean,

$$\xi(x_1, 0) = 0, \qquad u(x_1, 0) = 0 \tag{9.7}$$

where $\xi = h_w/h$, $\eta_s = h_s/h$, $u = u_x H/(hc_w)$, $h_w(x_1, t_1)$ is the water level relative to the undisturbed ocean surface, $h_s(x_1, t_1)$ is the bottom uplift due to the slide motion, $t_1 = t/t_0$ and $x_1 = x/l_f$ are the dimensionless time and sliding distance, respectively, $c_w = (gH)^{1/2}$ is the shallow water wave velocity, $t_0 = l_f/c_w$ is the characteristic time, u_x is the velocity of the fluid flow along the x axis, and h is the slide height (or, in general, a characteristic slide thickness).

The solution

$$\xi(x,t) = \frac{1}{2}\int_{x-t}^{x+t} \frac{\partial \eta_s}{\partial t}(y,0)dy + \frac{1}{2}\int_0^t dq \int_{x-t+q}^{x+t-q} \frac{\partial^2 \eta_s}{\partial t^2}(y,q)dy \tag{9.8}$$

of (9.6) with initial conditions (9.7) is well known [e.g., *Tinti and Bortolucci*, 2000a; b; *Tinti et al.*, 2001; *Pelinovsky*, 2003]. Unless otherwise stated, hereafter, we omit subscript "1" in the notations of dimensionless parameters for the sake of briefness. Changing the order of integration, (9.8) can be written as

$$\xi(x,t)=\frac{1}{2}\int_{x}^{x+t}\frac{\partial\eta_s}{\partial t}(y,-y+x+t)dy+\frac{1}{2}\int_{x-t}^{x}\frac{\partial\eta_s}{\partial t}(y,y-x+t)dy \tag{9.9}$$

Below we model the slide as shown in Figure 21a. As the slide moves horizontally, it leaves a depression of the depth h behind and creates a surface uplift of approximately the same height. The created depression spreads until the slide moves the distance of l_f (Figure 19c), and it does not change its shape after that. Similarly, the uplift does not change its size after the slide moves distance l_f and continues to move as a solid body (Figure 19d). Taking into account that the slide eventually stops (at $t = t_s$ and $x = x_s$), its motion can be described by perturbing the seafloor level by

$$\eta_s(x,t)=h_s/h=\theta(x-1)-\theta(x)+\theta(x-S(t))-\theta(x-1-S(t)) \tag{9.10}$$

where $\theta(x)$ is the Heaviside function ($\theta(x) = 1$ if $x \ge 0$ and $\theta(x) = 0$ if $x < 0$), $S(t) = x(t)/l_f$ is the dimensionless sliding distance, and $x(t)$ is defined by (9.4), written in the dimensionless form of

$$t=\int_{0}^{S(t)}\frac{dt}{V(t)} \tag{9.11}$$

Taking into account that $\theta'(x) = \delta(x)$ (Dirac's δ-function), we obtain by differentiating (9.10) with respect to time that

$$\frac{\partial\eta_s}{\partial t}(x,t)=V(t)[\delta(x-1-S(t))-\delta(x-S(t)] \tag{9.12}$$

where $V(t) = v/c_w$ is the dimensionless slide velocity. Together with (9.10), equation (9.12) gives the sought tsunami wave magnitude

$$\begin{aligned}\xi(x,t)=\frac{1}{2}\int_{0}^{t}V(u)[\delta(x+t-u-1-S(u))-\delta(x+t-u-S(u))]du+\\+\frac{1}{2}\int_{0}^{t}V(u)[\delta(x-t+u-1-S(u))-\delta(x-t+u-S(u))]du\end{aligned} \tag{9.13}$$

The development of the tsunami wave in the source region corresponds to $t < t_s$ in (9.13). For $u > t_s$, $V(u) = 0$ and (9.13) reads

$$\xi(x,t)=\xi_{-}(x+t)+\xi_{+}(x-t)\qquad(t>t_s,\ -\infty<x<\infty) \tag{9.14}$$

where

$$\xi_{-}(x+t)=\frac{1}{2}\int_{0}^{t_s}V(u)[\delta(x+t-u-1-S(u))-\delta(x+t-u-S(u))]du \tag{9.15}$$

and

$$\xi_{+}(x-t)=\frac{1}{2}\int_{0}^{t_s}V(u)[\delta(x-t+u-1-S(u))-\delta(x-t+u-S(u))]du \tag{9.16}$$

are the waves of constant magnitude propagating with velocity c_w (in dimensional coordinates) in the direction of $x < 0$ (backgoing wave, propagating opposite to the landslide direction) and $x > 0$ (outgoing wave, propagating in the landslide direction), respectively. In other words, at $t = t_s$, the initial perturbation of the ocean level splits onto two waves, which then propagate independently in the opposite directions.

The generated tsunami waves are plotted for the Currituck Slide A at times $t = 0.1t_s$, $t = t_f = 0.533t_s$, and $t = t_s$ in Figure 21b and at times $t = t_s$, $t = 2t_s$, and $t = 3t_s$ in Figure 21c and Figure 21d. As expected, while the slide is still in motion ($t < t_s$), the magnitudes and shapes of the waves are changing with time (Figure 21b). After the slide fully stops, however, the backgoing and outgoing waves show constant amplitude and do not change shape for $t \geq t_s$ (Figure 21c and Figure 21d). The outgoing wave ($x > 0$) has higher amplitude and shorter "wavelength" than the backgoing ($x < 0$) wave. The dimensionless amplitudes, $\xi = h_w/h$, for the outgoing wave are 0.165 and –0.136 for crest and trough, respectively. For the backgoing wave, the amplitudes are reduced to 0.049 and –0.060, respectively. The corresponding dimensionless wavelength is approximately $6l_f$ and $10l_f$ for the outgoing and backgoing waves, respectively. The described wave characteristics are similar to the Currituck Slide B, Storegga slide, and the baseline slide in Table 11.

It appears that the landslides analyzed by the static approach have slightly higher maximum velocity than in the dynamic approach, because the static slides accelerate faster from zero initial velocity (Figure 20a). However, the landslide volume (or the failure length) calculated with the static analysis is roughly a half that obtained with dynamic analysis (Table 11). As a result, the tsunami wave generated by the initially static slide is smaller than that created by the dynamic slide (Table 11). The dynamic effect on the tsunami wave height is shown in Figure 22 for the Currituck Slides A and B and in Figure 23 for the Storegga and baseline slides. The

calculated “wavelengths” are comparable for the static and dynamic slides (Figure 22 and Figure 23), but the amplitudes of tsunamis differ by as much as 78% for the outgoing wave of the Storegga slide (Table 11). The dynamic analysis results in the initial velocity of the Currituck Slide A of only 2 m/sec. Yet, because the slide volume (or failure length) is 1.9 times larger than for the static slide (Table 6), the generated wave height is 31% to 73% larger (Table 11).

It is worth mentioning that it may not be possible to evaluate the slide motion in the static analysis because the slide has zero initial velocity. For example, the Currituck Slide B does not move when initial velocity is zero (Table 11). Therefore, the static analysis in this case cannot identify the slide motion and the resulting tsunami height, although the dynamic analysis results in more than 3 m of the tsunami height (Table 11, Figure 22c, and Figure 22d).

Finally, although the dynamic effect leads to a non-zero initial slide velocity, its magnitude is typically not sufficient to affect the tsunami wave magnitude significantly. The effect of the increased slide size is much more important.

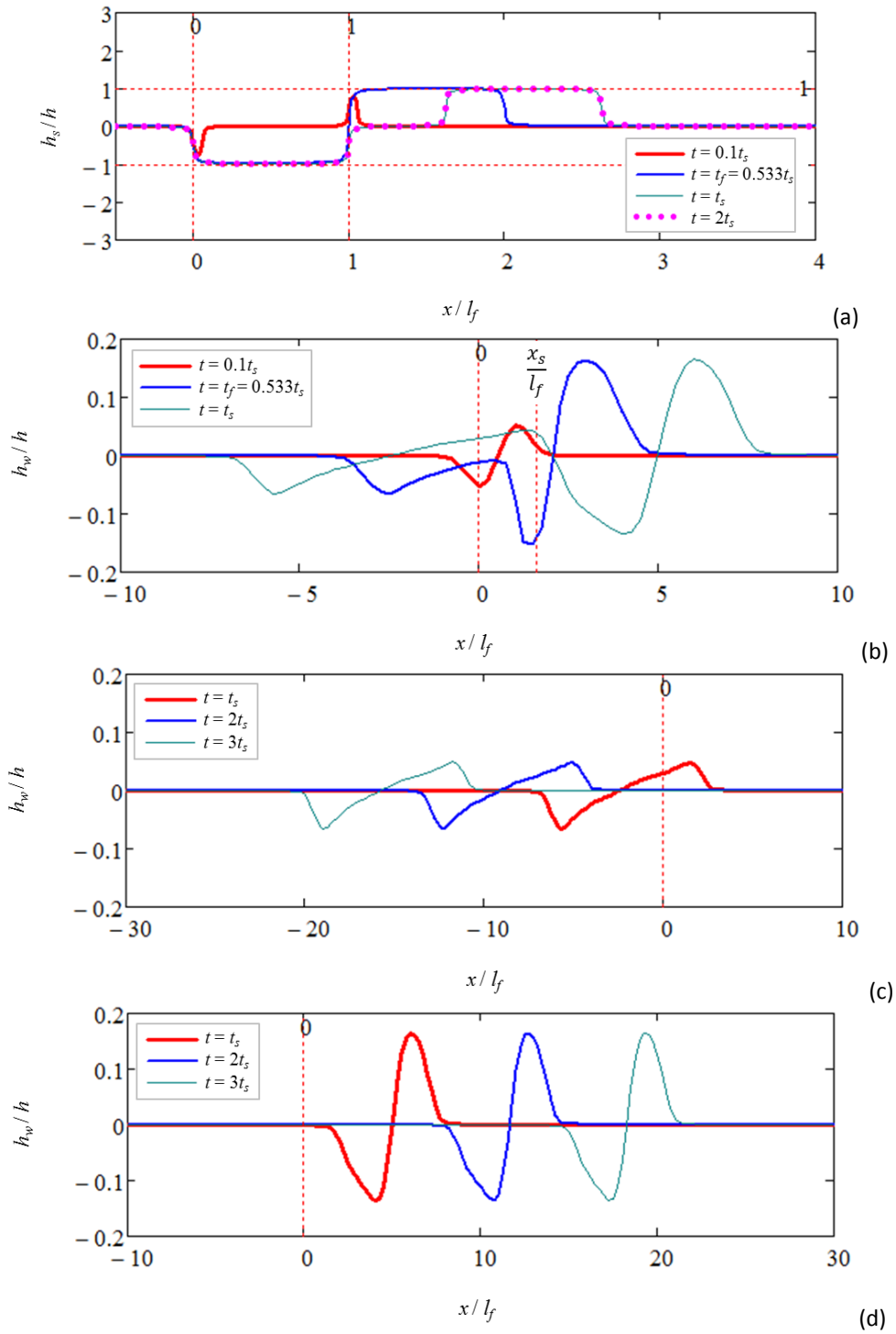

Figure 21. (a) Seafloor profile (uplift), h_s/h, at times $t = 0.1t_s$ (red ,bold line), $t = t_f = 0.533t_s$ (blue, solid line), $t = t_s$ (green, thin line), and $t = 2t_s$ (pink, dotted line) describing the Currituck Slide A movement. (b) Tsunami wave magnitude, h_w/h, at times $t = 0.1t_s$ (red ,bold line), $t = t_f = 0.533t_s$ (blue, solid line), and $t = t_s$ (green, thin line). (c, d) Water wave propagation (c) to the left (backgoing wave, $x < 0$) and (d) to the right (outgoing wave, $x > 0$) directions at times $t = t_s$ (red, bold lines) and $t = 2t_s$ (blue, solid lines), and $t = 3t_s$ (green, thin lines).

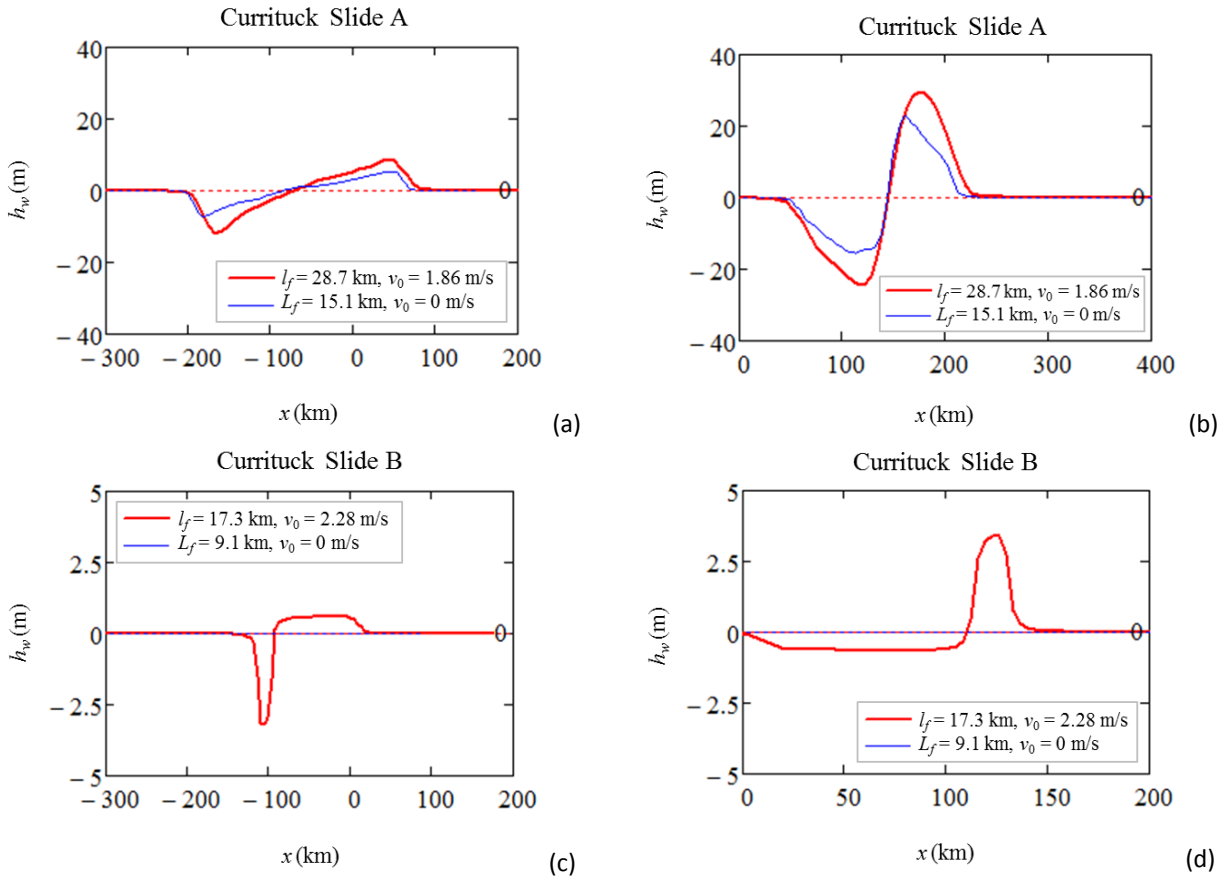

Figure 22. Tsunami wave amplitude, h_w, at times $t = t_s$ is plotted for the dynamic and static analyses for (a, b) the Slide A and (c, d) Currituck Slide B. Both (a, c) backgoing ($x < 0$) and (b, d) outgoing ($x > 0$) waves are shown. The failure lengths of the Currituck Slide A are $l_f = 28.7$ km and $L_f = 15.1$ km for the dynamic and static analyses, respectively, and the corresponding initial velocities are $v_0 = 1.86$ m/s and $v_0 = 0$ m/s (Table 11). For the Currituck Slide B, the failure lengths are $l_f = 17.3$ km and $L_f = 9.1$ km for the dynamic and static analyses, respectively, and the corresponding initial velocities are $v_0 = 2.28$ m/s and $v_0 = 0$ m/s (Table 11).

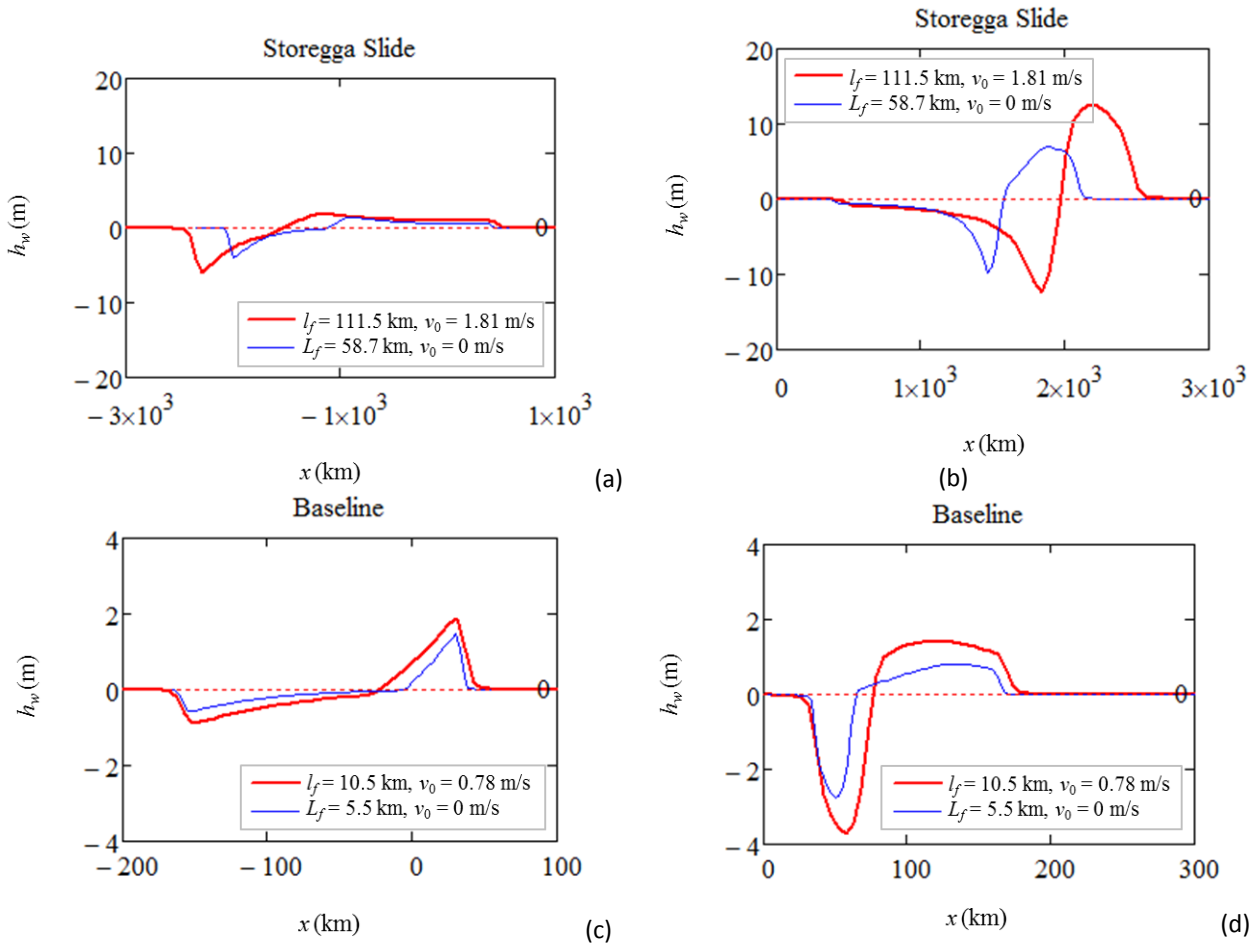

Figure 23. Tsunami wave amplitude, h_w, at times $t = t_s$ is plotted for the dynamic and static analyses for (a, b) Storegga and (c, d) baseline slides. Both (a, c) backgoing ($x < 0$) and (b, d) outgoing ($x > 0$) waves are shown. The failure lengths of the Storegga are $l_f = 11.5$ km and $L_f = 58.7$ km for the dynamic and static analyses, respectively, and the corresponding initial velocities are $v_0 = 1.81$ m/s and $v_0 = 0$ m/s (Table 11). For the baseline slide, the failure lengths are $l_f = 10.5$ km and $L_f = 5.5$ km for the dynamic and static analyses, respectively, and the corresponding initial velocities are $v_0 = 0.78$ m/s and $v_0 = 0$ m/s (Table 11).

CHAPTER 10. DISCUSSION

10.1. Dynamic version of the *Palmer and Rice* [1973] model

In their celebrated paper, *Palmer and Rice* [1973] analyzed general conditions for the propagation of a shear band and, in particular, a static shear band in an open-cut slope (Figure 24) in over-consolidated sediments. Here we consider a dynamically growing shear band. Similar to our model (Figure 2), we consider a slope in the submerged or subaerial condition. Therefore, the hydrostatic pressure, p_h, of water acts at the bottom of the slope (Figure 24) which corresponds to zero effective stress (i.e., $\sigma = -p_h$) at $x = 0$. Then, per (2.2), $\gamma_h = p_0/E > 0$ is the strain that corresponds to p_h. This is consistent with *Palmer and Rice* [1973], who studied the subaerial case of $p_h = 0$. Since the strain increases uphill (from $x = 0$ to $x = l$), condition $0 < \gamma_h < \gamma_0 < \gamma_a$ should be satisfied as it would be in the original static model [*Palmer and Rice*, 1973].

Mathematically, *Palmer and Rice*'s [1973] (Figure 24) and our (Figure 2) models differ by the relative direction of τ_* and the x-axis, which is now pointing uphill (Figure 24), and by p_h acting at $x = 0$ instead of p_a. Hence, the dynamic version of *Palmer and Rice*'s [1973] model follows directly from the results obtained in this work. Specifically, keeping both τ_* and T positive, we simply need to replace the signs of these quantities in (2.3), (2.4), (3.1), (4.1) and adjust other equations accordingly.

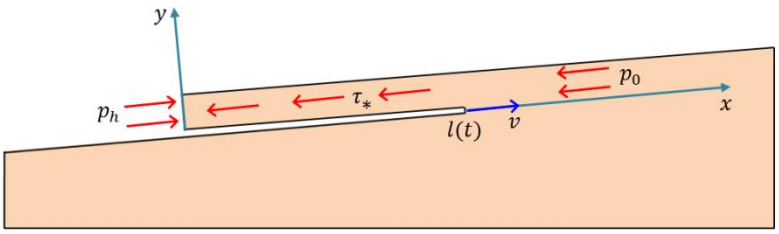

Figure 24. *Palmer and Rice*'s [1973] model

In particular, the sign before T in (4.2) needs to be changed, and the static strain, defined in (3.4) and (4.8), now becomes

$$\gamma_s(l) = \gamma_h + \frac{l}{h}\bar{T}(l) = \gamma_0 + I(l), \qquad \bar{T}(l) = \frac{1}{l}\int_0^l T(x)dx, \qquad I(l) = \frac{1}{h}\int_{l_0}^l T(x)dx \tag{10.1}$$

Expressions (4.7) and (4.18) for the band propagation velocity, (4.9) and (4.22) for the strain

and material velocity at the tip, and (6.11) and (6.12) for the average slide velocity remain the same, but they should be used with the adjusted static strain (10.1).

The position of the crack tip is still defined by (4.6) and (4.17) (both with using (10.1) for $\gamma_s(l)$), and the location of point *E* of the discontinuity arrival at the band tip (Figure 6), is defined by (4.20). Whether the discontinuity reaches the tip after the first or second reflection from the slide end, $x = 0$, can still be determined from (F.2) and (F.4) (Appendix F), respectively, both used with (10.1) for the static strain.

Similarly, for the homogeneous distribution (5.1), $T = T_0 = \bar{T}(l_0) = \text{const} > 0$, equations (5.5) - (5.11), (6.14), (F.4) (Appendix F), (G.13) - (G.22) (Appendix G) all remain valid, but with λ_* defined by

$$\lambda_* = \frac{\gamma_0 h}{T_0 l_0} = \frac{\gamma_0}{\gamma_0 - \gamma_h} \tag{10.2}$$

instead of (4.29) and with the static strain (5.2) replaced by

$$\gamma_s(l) = \gamma_0 + T_0(l - l_0)/h \tag{10.3}$$

The initial band length (5.3) is now given by

$$l_0/h = (\gamma_0 - \gamma_h)/T_0 \tag{10.4}$$

which agrees with *Palmer and Rice* [1973] for $\gamma_h = 0$. Because $l_0 >> h$ in *Palmer and Rice*'s [1973] model, equation (10.4) implies that

$$\gamma_0 - \gamma_h >> T_0 \tag{10.5}$$

The recurrence relations presented in Appendix E (equations (E.1) – (E.21)) are also all valid for the dynamic *Palmer and Rice*'s [1973] model, which employs definition (10.1) of the static strain. This means that in *Palmer and Rice*'s [1973] case, the general dynamic solution, when the discontinuity reflects at the band tip arbitrary number of times, is given directly by Appendix E.

The definition of λ_* is, in fact, the main difference between *Palmer and Rice*'s [1973] and our formulations. It affects the range of λ_*, which depends upon the value of γ_h (or p_h) in (10.2). For $\gamma_h > 0$ (tensile strain), $\gamma_h < \gamma_0$, and the range is $\lambda_* > 1$. For this range, the chance of the discontinuity reaching the band tip after the first reflection from $x = 0$ is higher (Figure F.1b in Appendix F) than for the range of $0 < \lambda_* < 1$ (Figure F.1a). Indeed, for any *n* from $1 < n < 2$, the

discontinuity does reach the tip if $\lambda_* > 1.605$. For $1 < n < 1.43$, the discontinuity reaches the tip for any $\lambda_* > 1$. This means that in most practical cases, it is expected that the discontinuity will reflect at least once from the band tip. This can be explained by a shorter initial band length l_0 in (10.2) than in (5.3) (when $\gamma_h > 0$). For a shorter initial band length, the discontinuity will travel more frequently between $x = 0$ and the band tip, so in general, more reflections will happen.

The dynamic version of the *Palmer and Rice*'s [1973] model can be used for analyzing the uphill growth of the shear bands in submerged slopes, which has been inferred from some observations [*Kvalstad et al.*, 2005]. We first note that $\gamma_0 < \gamma_a$, since the shear band propagates until the strain at the tip reaches the active failure strain, γ_a. Further analysis is similar to that in Section 6.1, so equations (6.1) – (6.3), and (6.4) – (6.5) remain valid when γ_p is replaced with $\gamma_a = (p_0 - p_a)/E$ and the static strain is replaced by (10.3) where $l = l_f$.

10.2. Direction of band growth

Above, we have considered downhill (Chapters 2–7) and uphill (Section 10.1) propagation of the shear band. In the developed models, the shear band has one tip ($x = l$), which can only propagate in one direction. The initial discontinuity, however, may have two tips [*Puzrin and Germanovich*, 2005a; *Viesca*, 2011; *Viesca and Rice*, 2012] as shown in Figure 25. To understand which tip begins propagating first, we consider here a quasi-static shear band at the onset of dynamic (catastrophic) propagation, i.e., at the end of the stable (progressive) stage of the band growth.

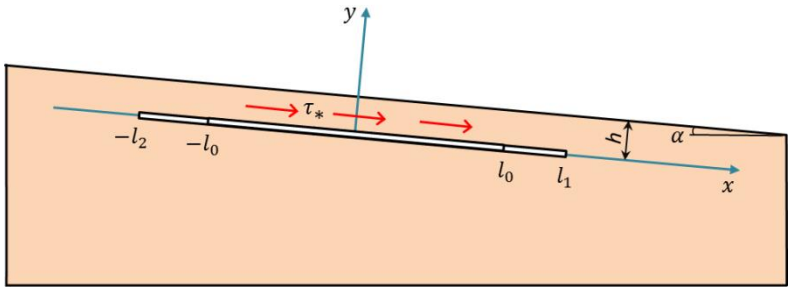

Figure 25. Static band propagation with two tips at $x = -l_2$ and $x = l_1$ (after [*Puzrin and Germanovich*, 2005a]).

In general, for a static band of length $l = l_1 + l_2$ with tips located at $x = -l_2$ and $x = l_1$, equation (2.4) is reduced to the equilibrium condition

$$d^2u/dx^2 = -T(x)/h \qquad (0 < x < l) \tag{10.6}$$

Boundary conditions (2.7) are now specified at both tips as $u(-l_2) = u(l_1) = 0$, so integrating (10.6) results in the static strain

$$\gamma_s(x) = -\frac{1}{h}\int_{-l_2}^{x} T(s)ds + \frac{1}{hl}\int_{-l_2}^{l_1}(l_1 - s)T(s)ds \tag{10.7}$$

which can also be written as

$$\gamma_s(x) = \frac{1}{h}\int_{x}^{l_1} T(s)ds - \frac{1}{hl}\int_{-l_2}^{l_1}(l_2 + s)T(s)ds \tag{10.8}$$

Expressions (10.7) and (10.8) are valid for the arbitrary (static) shear band $-l_2 < x < l_1$. Let $l_1 = l_2 = l_0$ at the onset of dynamic propagation of one of the band tips (or both). Without the loss of generality, the y-axis can always be placed in the middle of the band (Figure 25) at that moment. Substituting $x = l_0$ in (10.7) and $x = -l_0$ in (10.8) leads to

$$\Delta\gamma_s = -\gamma_s(l_0) - \gamma_s(-l_0) = \frac{1}{hl_0}\int_{-l_0}^{l_0} sT(s)ds \tag{10.9}$$

and condition (2.12) of band growth now holds at either band tip. The shear band begins propagating at the upper end, $x = -l_0$, if $\gamma_s(-l_0) > -\gamma_s(l_0)$. If $\gamma_s(-l_0) < -\gamma_s(l_0)$, the propagation begins at the lower end, $x = l_0$. Hence, according to (10.9) and (2.12), at the onset of band growth,

$$\gamma_0 = \begin{cases} -\gamma_s(l_0) & \text{if} \quad \Delta\gamma_s > 0 \\ \gamma_s(-l_0) & \text{if} \quad \Delta\gamma_s < 0 \end{cases} \tag{10.10}$$

Theoretically, for a load distribution $T(s)$ such that $\Delta\gamma_s = 0$, propagation begins simultaneously at both ends $x = l_0$ and $x = -l_0$. This would occur, for example, when $T(s)$ is an even function ($T(s) = T(-s)$); in particular, for the homogeneous distribution (5.1) when $T(s) = T_0 = \text{const}$. In this case, (10.10) results in the critical length

$$2l_0 = \frac{2h\gamma_0}{T_0} = \frac{2h}{T_0}\sqrt{\frac{2J_0}{hE}} \tag{10.11}$$

which agrees with *Puzrin and Germanovich* [2005a] if $E = E_l = E_u$, i.e., the material moduli in loading and unloading (Section 2.1) are the same.

If $E_l \neq E_u$,

$$T(s) = \begin{cases} \tau_1/E_l & \text{if} \quad x_0 < x < l_0 \\ \tau_1/E_u & \text{if} \quad -l_0 < x < x_0 \end{cases} \tag{10.12}$$

When $x = x_0$, strain $\gamma_s(x)$ changes sign. Adding (10.7) and (10.8) with $l_1 = l_2 = l_0$ and solving equation $2\gamma(x_0) = 0$ in the case of (10.12), we obtain the root

$$x_0 = \frac{(E_u / E_l)^{1/2} - 1}{(E_u / E_l)^{1/2} + 1} l_0 \tag{10.13}$$

of function $\gamma_s(x)$. Substituting (10.12) (with (10.13)) in (10.9), we find that

$$\Delta\gamma_s = \frac{2\tau}{h\sqrt{E_u E_l}} x_0 \tag{10.14}$$

In soil and sediment materials, typically $E_u > E_l$ [*Desai and Siriwardane*, 1984; *Wood*, 1990; *Puzrin and Germanovich*, 2005a; *Budhu*, 2007]. Hence, $x_0 > 0$ in (10.13), and, accordingly, $\Delta\gamma_s > 0$ in (10.14). Comparing to (10.10), we conclude that the band growth would occur first downhill at the lower end of $x = l_0$.

Note that although (10.14) is equivalent to the corresponding result of *Puzrin et al.* [2004] and *Puzrin and Germanovich* [2005], they used the energy balance condition for the entire sliding layer (rather than for individual band tips) and, therefore, could not determine which tip of the shear band would propagate first at the onset of dynamic growth.

10.3. Slides with varying slope and finite width

So far, we have been considering slopes with constant angles (Figure 2). If the slope angle, α, varies along the slope, but the angle is small ($0 \le \alpha(x) << 1$) (Figure N.1 in Appendix N; note that x-axis is now horizontal), the momentum balance condition can be written in the form of (2.4) or the second equation in (3.1) with $T = (\tau_0 - h\,\partial p/\partial x)/E = \tau_*/E = [(\rho_0 - \rho_w)(\tan\alpha - \mu)gh - \tau_w]/E$ (Appendix N). The boundary and initial conditions (3.2) - (3.5) remain valid (Appendix N).

Since the solution obtained in Chapter 4 is valid for the general case of $T(x)$, it is also valid for the above interpretation of $T(x)$. In particular, when $p_0(x)$ is independent of x, $T(x)$ remains the same as in the preceding chapters.

It should be noted that using (2.4) in the case of a varying angle represents an asymptotic case (for $0 \le \alpha << 1$), and changing the angle affects mainly the term of $T(x)$ in (2.4) or (3.1). This is significant, however, since for α reducing with x, components $\tau_g - \tau_b$ and τ_r of load τ_* reduce and increase, respectively, so the shear band may eventually stop before the slope failure takes

place. This can be seen, for example, from (4.7), which suggests that the shear band stops growing when it reaches the length of l_s such that $\gamma_s(l_s) = -\gamma_c$. Using (4.8), this condition can be written as

$$I(l_s) = \frac{1}{h}\int_{l_0}^{l_s} T(x)dx = \gamma_c - \gamma_0 \tag{10.15}$$

where $T(x)$ decreases (and even becomes negative) with decreasing α. According to (4.9), both $\eta_1(l_s) = 0$ and $\partial\eta_1(l_s)/\partial t = 0$ if (10.15) is satisfied. Hence, both the material velocity and acceleration equal zero at the shear band tip when it reaches the length of l_s. This indeed means the full stop of the band growth and the slide motion ceases at that moment.

Using (4.8), equation (10.15) can be written as

$$l_s\bar{T}(l_s) - l_0\bar{T}(l_0) = (\gamma_c - \gamma_0)h \tag{10.16}$$

and a lower bound of l_s is obtained by setting $\gamma_0 = \gamma$ in (10.15) or (10.16). This bound is independent of n and is close to l_s if n is close to 1 (i.e., if γ_c is close to γ). Note that $I(l) = 0$ has another (trivial) solution, $l = l_0$, which is not of interest here.

Finally, many slides have an elongated shape (Figure 26), which typically depends upon the topographic features in the slide region. Yet the characteristic slide width, b, is usually much greater than the thickness, h, of the sliding layer. In most cases (e.g., Table A.1), the overall resistance to the slide movement (per unit area) at its margins (e.g., side scars) is comparable to the bottom (shear band) friction (also per unit area), although it may be much more complex in detail [e.g., *Farrell*, 1984; *Martel*, 2004]. Therefore, if $b >> h$, the edge resistance at the side scars can be ignored to the first order, and the obtained solution can also be used for such slides of finite width (if b does not change too much along the slide).

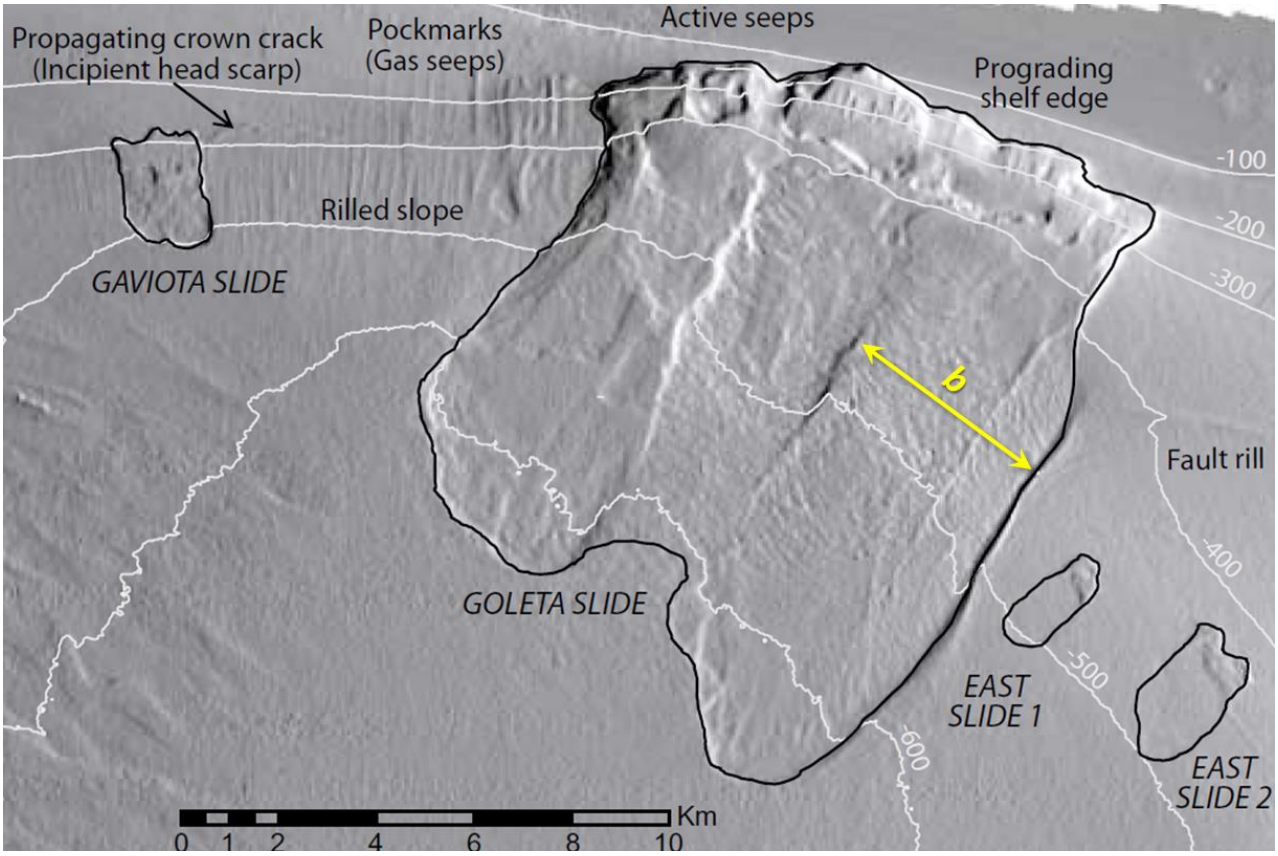

Figure 26. Map view of the Goleta slide [after *Greene et al.*, 2006]. The Goleta slide is centered at 34.34°N, 119.97°W (offshore Santa Barbara, California), with the headscarp at ≈ 150 m water depth. The slide age and the sediment characteristics are currently unknown. The Goleta slide has a width $b \approx 4$ km, a thickness $h \approx 50$ m, and an averaged slope angle $\alpha \approx 2°$ (Table A.1) [e.g., *Greene et al.*, 2006].

CHAPTER 11. CONCLUSIONS

In this work, landslide failure is considered as a dynamic process when a shear band emerges along a length of the potential rupture surface. Within this band, the shear strength drops due to the softening behaviour of the particulate material. The material above the band moves downwards, causing the band to propagate. This propagation may first be stable (progressive), but eventually becomes dynamic (catastrophic), which produces an initial landslide velocity before the slide reaches the post-failure stage and separates from the substrata. For tsunamigenic landslides, therefore, the resulting tsunami is expected to be larger than in the case of zero initial velocity.

In this work, we considered the dynamic elastic problem for the shear band propagating parallel to the slope surface. The problem is formulated within the framework of the *Palmer and Rice*'s [1973] approach, which is generalized to the dynamic case. Using the method of characteristics, we found the exact, closed-form solution for the shear band and landslide velocities as well as for the distributions of strain and slip rate in space and time. The solution allows assessing when the slide separates from the substrata once the failure condition is satisfied at the propagating tip of the shear band. The obtained solution is valid for the general case of an arbitrary distribution of shear and gravitational forces along the slide; for example, in the case of a varying slope angle. The case of the uniform distribution of these forces is considered in detail.

To understand the shear band evolution, we employed different surface energies for static and dynamically-propagating shear bands. This simplified approach captures, to the first order, the friction dependence on the velocity of the relative motion. It results, however, in a discontinuity that appears initially at the band tip and propagates back and forth along the band between reflections from the slide end and the band tip. We analyzed the behavior of this discontinuity and showed that its magnitude decreases after each reflection from the band tip. In addition, this magnitude of the discontinuity is always small in the relative sense. The developed simplified model, therefore, appears to be physically acceptable.

Using the developed model we showed that the shear band accelerates, and the band tip velocity, v, reaches the order of the speed c of elastic waves (yet being smaller than c) after it

propagates only approximately three lengths of the initial band. The slide body velocity also grows with the band length. By the time the slide separates from the substrata, when the band increases its initial length roughly by one to two orders of magnitude, slide velocity can become $\sim 0.1c$, or even $\sim c$ (still remaining smaller than v), depending upon the value of γ_0.

The band tip velocity, v, strain, γ, and slip rate, η, are controlled by the "bluntness" parameter, n, initial deformation, γ_0, and strain ratio, $\lambda_* = \gamma_0/(\gamma_a + \gamma_0)$. It turns out that γ and η are simply proportional to γ_0, while the effect of n and λ_* is more complex. The value of λ_* belongs to the relatively narrow range of $0 < \lambda_* < 1$ and is is relatively well constrained by field measurements. The value of n, however, is currently uncertain, except that $n > 1$. Yet, we showed that for n only slightly larger than unity, dependency of the solution on n becomes very weak. In fact, γ and η are close to their asymptotic values for $n \to \infty$ already at $n \sim 1.001$.

For a sufficiently long band length, the distribution of slip rate along the slope becomes asymptotically uniform. This occurs in both the exact solution, when $v = v(l)$, and in the asymptotic solution with $n \to \infty$, when $v = c$ starting from $t = 0$. Treating the slip rate as a constant (along the slope, but not in time) enables the introduction of water resistance to the motion of the submerged slope, which is a function (typically, quadratic) of the relative velocity. Our results show that the water resistance reduces the slide velocity only by up to $\sim 10\%$ compared to the case of no water resistance.

The simple asymptotic solution was compared to the exact solution and used in landslide analyses. The slide body velocity was also obtained in a closed form, which was further simplified in the case of uniform loads (gravitational and frictional) acting along the slide. Our model indicates that while the shear band propagation velocity is slower than thought previously [*Puzrin et al.*, 2010], the landslide accelerates much faster. Even more importantly, our results suggest that the conventional static approach to the slope stability analysis leads to a significant underestimation of the slide size. In most cases, the volumes of catastrophic slides are roughly twice the volumes of progressive slides. The obtained results may be useful for assessing the potential of the landslide to generate a tsunami.

REFERENCES

Baba, T., H. Matsumoto, K. Kashiwase, T. Hyakudome, Y. Kaneda, and M. Sano (2012), Micro-bathymetric evidence for the effect of submarine mass movement on tsunami generation during the 2009 Suruga bay earthquake, Japan, in *Submarine Mass Movements and Their Consequences, 5th International Symposium, Advances in Natural and Technological Hazards Research*, edited by Y. Yamada et al., pp. 485-496, Springer Science+Business Media B.V., doi:10.1007/978-94-007-2162-3_43.

Bardet, J.-P., C. E. Synolakis, H. L. Davies, F. Imamura, and E. A. Okal (2003), Landslide tsunamis: recent findings and research directions, *Pure and Applied Geophysics*, *160*, 1793-1809.

Barenblatt, G. I. (1962), The mathematical theory of equilibrium cracks in brittle fracture, *Advances in Applied Mechanics*, *7*, 55-129.

Beget, J. (2007), Earthquake, Landslide and Tsunami Hazards in the Port Valdez area, Alaska: Consultation to the Prince William Sound Regional Citizen's Advisory Council*Rep.*, Alaska Beget Consulting.

Bernander, S. (2011), *Progressive landslides in long natural slopes: Formation, potential extension and configuration of finished slides in strain-softening soils*, Doctoral thesis, 240 pp., Luleå University of Technology, Luleå, Sweden.

Bernander, S., and I. Olofsson (1981), On formation of progressive failures in slopes, *Proceedings of the International Conference on Soil Mechanics and Foundation Engineering*, *3*, 357-362.

Bertini, T., F. Cugusi, B. D'Elia, and M. Rossi-Doria (1986), Lenti movimenti di versante nell'Abruzzo Adriatico: caratteri e criteri di stabilizzazione, *Proc 16th Convegno Nazionale di Geotecnica, Bologna*, *1*, 91-100.

Bjerrum, L. (1967), Engineering geology of Norwegian normally-consolidated marine clays as related to settlements of buildings, *Ge´otechnique*, *17*(2), 83-118.

Bjerrum, L. (1972), Embankments on soft ground, in *Proceedings of the Specialty Conference on Performance of Earth and Earth-Supported Structures, Volume II*, edited, pp. 1-54, American Society of Civil Engineers, New York, NY.

Blackman, D. K., J. A. Karson, D. S. Kelley, J. R. Cann, G. L. Früh-Green, J. S. Gee, S. D. Hurst, B. E. John, J. Morgan, S. L. Nooner, D. K. Ross, T. J. Schroeder, and E. A. Williams (2002), Geology of the Atlantis Massif (Mid-Atlantic Ridge, 30° N): Implications for the evolution of an ultramafic oceanic core complex, *Marine Geophysical Researches*, *23*, 443-469.

Blum, J. (2010), *Development of Sensors and Techniques to Assess Earthquake Hazards and Submarine Slope Stability*, 171 pp., University of California, San Diego.

Blum, J. A., C. D. Chadwell, N. Driscoll, and M. A. Zumberge (2010), Assessing slope stability in the Santa Barbara Basin, California, using seafloor geodesy and CHIRP seismic data, *Geophysical Research Letters*, *37*(L13308), doi:10.1029/2010GL043293.

Blum, J. A., and M. A. Zumberge (2006), Monitoring Potential Slope Failure in the Santa Barbara Basin Using Optical Fibers, in *American Geophysical Union, Fall Meeting 2006, Abstract*, edited, AGU.

Bondevik, S., F. Lovholt, C. Harbitz, J. Mangerud, A. Dawson, and J. I. Svendsen (2005), The Storegga Slide tsunami - comparing field observations with numerical simulations, *Marine and Petroleum Geology*, *22*(1-2), 195-208.

Bonzanigo, L. (1997), Rheological particularities and artesian heads in a large landslide: Successful reclaiming using of underground drainage, *Engineering Geology and the Engnvironment*, *1-3*, 525-528.

Booth, J. S., D. W. O'Leary, P. Popenoe, and W. W. Danforth (1993), U.S. Atlantic continental slope landslides: their distribution, general attributes, and implications, in *Submarine Landslides: Selected Studies in the U.S. Exclusive Economic Zone*, edited by W. C. Schwab and D. C. Twichell, pp. 14-22, Bulletin 2002, U.S. Geological Survey., Reston, VA.

Borrero, J. C., J. F. Dolan, and C. E. Synolakis (2001), Tsunamis within the Eastern Santa Barbara Channel, *Geophysical Research Letters*, *28*(4), 643-646.

Bozzano, F., P. Mazzanti, M. Anzidei, C. Esposito, M. Floris, G. Fasani, and A. Esposito (2009), Slope dynamics of Lake Albano (Rome, Italy): insights from high resolution bathymetry, *Earth Surface Processes and Landforms*, *34*, 1469-1486, doi:10.1002/esp.1832.

Bradshaw, A. S., D. R. Tappin, and D. Rugg (2010), The kinematics of a debris avalanche on the Sumatra margin, in *Submarine Mass Movement and Their Consequences, 4th International Symposium, Advances in Natural and Technological Hazards Research*, edited by D. C. Mosher et al., pp. 117-126, Springer Science + Business Media B.V., Switzerland.

Broberg, K. B. (1999), *Cracks and Fracture*, 752 pp., Academic Press, San Diego, California.

Brooks, J. M., M. E. Field, and M. C. Kenicutt II (1991), Observations of gas hydrates offshore northern California, *Marine Geology*, *96*, 103-109.

Bryant, E. (2008), *Tsunami: The Underrated Hazard, Second Edition*, 330 pp., Springer, Berlin, Germany.

Bryn, P., K. Berg, R. Lien, and A. Solheim (2005), Submarine slides on the Mid-Norwegian Continental Margin - A challenge to the oil industry, in *Onshore-Offshore Relationships on the North Atlantic Margin*, edited by B. T. G. Wandas et al., Elsevier, The Neterlands.

Bryn, P., T. J. Kvalstad, T. R. Guttormsen, P. A. Kjaernes, J. K. Lund, F. Nadim, and J. Olsen (2004), Storegga slide risk assessment, in *Offshore Technology Conference*, edited.

Budhu, M. (2007), *Soil Mechanics and Foundations, Second edition*, 634 pp., John Wiley & Sons, Inc., Hoboken, NJ.

Bugge, T., R. H. Belderson, and N. H. Kenyon (1988), The Storegga slide, *Philosophical Transactions of the Royal Society of London A: Mathematical and Physical Sciences*, *325*(1586), 357-388.

Bunn, A. R., and B. A. McGregor (1980), Morphology of the North Carolina continental slope, western North Atlantic, shaped by deltaic sedimentation and slumping, *Marine Geology*, *37*, 253-266.

Burguete, J., P. Garcia-Navarro, J. Murillo, and I. Garcia-Palacin (2007), Analysis of the friction term in the one-dimensional shallow-water model, *Journal of Hydraulic Engineering*, *133*(9), 1048-1063, doi:10.1061/(ASCE)0733-9429(2007)133:9(1048).

Burridge, R., and J. B. Keller (1978), Peeling, slipping and cracking - some one-dimensional free-boundary problems in mechanics, *SIAM Review*, *20*(1), 31-61.

Canals, M., G. Lastras, R. Urgeles, J. L. Casamor, J. Mienert, A. Cattaneo, M. De Batist, H. Haflidason, Y. Imbo, J. S. Laberg, J. Locat, D. Long, O. Longva, D. G. Masson, N. Sultan, F. Trincardi, and P. Bryn (2004), Slope failure dynamics and impacts from seafloor and shallow sub-seafloor geophysical data: case studies from the COSTA project, *Marine Geology*, *213*, 9-72.

Carson, P. R. (1978), Holocene slump on continental shelf off Malaspina Glacier, Gulf of Alaska, *American Association of Petroleum Geologists Bulletin*, *62*(12), 2412-2426.

Cartier, G., and P. Pouget (1988), ´ tude du comportement d'un remblai construit sur un versant instable, le remblai de

Salle`des (Puy-de-Dome)*Rep.*, Res. Rep. No 153, Laboratoire Central des Ponts et Chausse`es.

Cecinato, F. (2009), *The Role of Frictional Heating in the Development of Catastrophic Landslides*, 221 pp., University of Southampton.

Chai, M. F., T. L. Lau, and T. A. Majid (2014), Potential impacts of the Brunei Slide tsunami over East Malaysia and Brunei Darussalam, *Ocean Engineering*, *81*, 69-76.

Chang, K.-J., A. Taboada, and Y.-C. Chan (2005), Geological and morphological study of the Jiufengershan landslide triggered by the Chi-Chi Taiwan earthquake, *Geomorphology*, *71*, 293-309.

Chen, W. F., and G. Y. Baladi (1985), *Soil Plasticity, Theory and Implementation*, Developments in Geotechnical Engineering 231 pp., Elsevier, Amsterdam, The Netherlands.

Cherepanov, G. P. (1979), *Mechanics of Brittle Fracture*, 939 pp., McGraw-Hill, New York, NY.

Chowdhury, R. (1978), Propagation of failure surfaces in natural slopes, *Journal of Geophysical Research*, *83*(B12), 5983-5988.

Chowdhury, R., P. Flentje, and G. Bhattacharya (2010), *Geotechnical Slope Analysis*, 737 pp., CRC Press/Balkema, London, UK.

Clare, M. A., P. J. Talling, P. Challenor, G. Malgesini, and J. Hunt (2014), Distal turbidites reveal a common distribution for large (>0.1 km^3) submarine landslide recurrence, *Geology*, doi:10.1130/G35160.1.

Clarke, S., D. W. Airey, P. Yu, and T. Hubble (2011), Submarine landslides on the South-Eastern Australian Margin, paper presented at Australian Geomechanics Society Sydney Chapter Symposium, October 2011.

Coleman, J. M., and D. B. Prior (1988), Mass wasting on continental margins, *Annual Review of Earth and Planetary Sciences*, *16*, 101-119.

Cornforth, D. H. (2005), *Landslides in Practice: Inverstications, Analysis, and Remedial/Preventative Options in Soils*, 596 pp., John Wiley & Sons, Inc., Hoboken, NJ.

Courant, R., and K. O. Friedrichs (1948), *Supersonic Flow and Shock Waves, Mathematics Subject Classification*, 467 pp., Springer, New York, NY.

Craig, R. F. (1997), *Soil Mechanics, Sixth edition*, 485 pp., Chapman & Hall, New York, NY.

Crozier, M. J. (2010), Deciphering the effect of climate change on landslide activity: A review, *Geomorphology*, *124*(3), 260-267, doi:10.1016/j.geomorph.2010.04.009.

D'Elia, B., L. Picarelli, S. Leroueil, and J. Vaunat (1998), Geotechnical characterisation of slope movements in structurally complex clay soils and stiff jointed clays, *Italian Geotechnical Journal*, *Anno XXXII*(3), 5-32.

Das, B. M. (1994), *Principles of Geotechnical Engineering, Third Edition*, 672 pp., PWS Publishing Company, Boston, MA.

Davis, R. O., and A. P. S. Selvadurai (1996), *Elasticity and Geomechanics*, 201 pp., Cambridge University Press, Cambridge, UK.

Davison, L. (2008), *Fundamentals of Shock Wave Propagation in Solids*, Shock Wave and High Pressure Phenomena, 433 pp., Springer, Berlin, Germany.

Dawson, A. G., D. Long, and D. E. Smith (1988), The Storegga slides: Evidence from eastern Scotland for a possible tsunami, *Marine Geology*, *82*(8), 271-276.

De Blasio, F. V. (2011), *Introduction to the Physics of Landslides*, 408 pp., Springer, New York.

De Blasio, F. V., L. Engvik, C. B. Harbitz, and A. Elverhoi (2004), Hydroplaning and submarine debris flows, *Journal of Geophysical Research*, *109*(C01002), doi:10.1029/2002JC001714.

Denlinger, R., and R. M. Iverson (1990), Limiting equilibrium and liquefaction potential in infinite submarine slopes, *Marine Geotechnology*, *9*(4), 299-312.

Desai, C. S., and H. J. Siriwardane (1984), *Constituitive Laws for Engineering Materials with Emphasis on Geologic Materials*, 468 pp., Prentice-Hall, Inc., Englewood Cliffs, NJ.

Detournay, E., and A. H.-D. Cheng (1993), Fundamentals of Poroelasticity, in *Comprehensive Rock Engineering: Principles, Practice and Projects, Vol. II, Analysis and Design Method*, edited by C. Fairhurst, pp. 113-171, Pergamon Press.

Dey, R., B. Hawlader, R. Phillips, and K. Soga (2012), Effects of shear band propagation on submarine landslide, in *Proceedings of the Twenty-second (2012) International Offshore and Polar Engineering Conference (ISOPE)*, edited by J. S. Chung et al., pp. 766-772, Rhodes, Greece.

Didenkulova, I., I. Nikolkina, E. Pelinovsky, and N. Zahibo (2010), Tsunami waves generated by submarine landslides of variable volume: analytical solutions for a basin of variable depth, *Natural Hazards and Earth System Sciences*, *10*, 2407-2419.

Dieterich, J. (1979), Modeling of rock friction: 1. Experimental results and constitutive equations, *Journal of Geophysical Research*, *84*(B5), 2161-2168.

Ding, Y., Y. Jia, and S. S. Y. Wang (2004), Identification of Manning's roughness coefficients in shallow water flows, *Journal of Hydraulic Engineering*, *130*(6), 501-510, doi:10.1061/(ASCE)0733-9429(2004)130:6(501).

Dingemans, M. W. (1997), *Water Wave Propagation Over Uneven Bottoms*, Advanced Series on Ocean Engineering: Volume 13 World Scientific Pub., The Netherlands.

Dingle, R. V. (1977), The anatomy of a large submarine slump on a sheared continental margin (SE Africa), *Journal of the Geological Society of London*, *134*, 293-310.

Dingler, J. A. (2007), *New Geophysical Approaches to Study Neotectonics and Associated Geohazards*, 170 pp., University of California, San Diego.

Dominey-Howes, D., and J. A. Goff (2013), Tsunami risk management in Pacific Island Countries and Territories (PICTs) – some issues, challenges and ways forward, *Pure and Applied Geophysics*, *170*, 1397-1413.

Dott, R. H. (1963), Dynamics of subaqueous gravity depositional process, *Bulletin of the American Association of Petroleum Geologists*, *47*(1), 104-128.

Dugan, B., and P. B. Flemings (2000), Overpressure and fluid flow in the New Jersey continental slope: implications for slope failure and cold seeps, *Science*, *289*, 288-291.

Dugan, B., and J. Stigall (2010), Origin of overpressure and slope failure in the Ursa region, Northern Gulf of Mexico, in *Submarine Mass Movements and Their Consequences, 4th International Symposium, Advances in Natural and Technological Hazards Research*, edited by D. C. Mosher et al., pp. 167-178, Springer Science + Business Media B.V., Switzerland.

Duncan, J. M., and S. G. Wright (2005), *Soil Strength and Slope Stability*, 297 pp., John Wiley & Sons, Inc., Hoboken, NJ.

Dyskin, A. V., L. N. Germanovich, and K. B. Ustinov (2000), Asymptotic analysis of crack interaction with free boundary, *Int. J. Solids Struct.*, *37*(6), 857-886.

Edwards, B. D., H. J. Lee, and M. E. Field (1993), Seismically induced mudflow in Santa Barbara Basin, California, in *Submarine landslides: Selected studies in the US Exclusive Economic Zone*, edited by W. C. Schwab et al., pp. 167-183, US Geological Survey Bulletin 2002.

Edwards, B. D., H. J. Lee, and M. E. Field (1995), Mudflow generated by retrogressive slope failure, Santa Babara Basin, California continental borderland, *Journal of Sedimentary Research A*, *65*, 57-68.

Eichhubl, P., H. G. Greene, and N. Maher (2002), Physiography of an active transpressive margin basin: high-resolution bathymetry of the Santa Barbara basin, Southern California continental borderland, *Marine Geology*, *184*, 95-120.

Erismann, T. (1977), Der Bimsstein von Köfels, Impaktit oder Friktionit?, *Material und Technik*, *5*(4), 190-196.

Farrell, S. G. (1984), A dislocation model applied to slump structures, Ainsa Basin, South Central Pyrenees, *Journal of Structural Geology*, *6*(6), 727-736.

Field, M. E., and J. H. Barber (1993), A submarine landslide associated with shallow seafloor gas and gas hydrates off northern California, in *Submarine Landslides: Selected Studies in the U.S. Exclusive Economic Zone. U.S. Geol. Surv. Bull. 2002*, edited by W. C. Schwab et al., pp. 151–157.

Field, M. E., S. H. Clarke, and M. E. White (1980), *Geology and geologic hazards of offshore Eel River Basin, northern California continental margin*, U.S. Geol. Surv. Open-File Rep. 80-1080, 80 pp.

Field, M. E., J. V. Gardner, A. E. Jennings, and B. D. Edwards (1982), Earthquake-induced sediment failures on a 0.25° slope, Klamath River delta, California, *Geology*, *10*, 543-546.

Fine, I. V., A. B. Rabinovich, B. D. Bornhld, R. E. Thomson, and E. A. Kulikov (2005), The Grand Banks landslide-generated tsunami of November 18, 1929: preliminary analysis and numerical modeling, *Marine Geology*, *215*, 45-57.

Fine, I. V., A. B. Rabinovich, R. E. Thomson, and E. A. Kulikov (2003), Numerical modeling of tsunami generation by submarine and subaerial landslides., in *Submarine Landslides and Tsunamis*, edited, pp. 69-88, Kluwer Academic Publishers.

Fisher, M. A., W. R. Normark, H. G. Greene, H. J. Lee, and R. W. Sliter (2005), Geology and tsunamigenic potential of submarine landslides in Santa Barbara Channel, Southern California, *Marine Geology*, *224*, 1-22.

Flemings, P. B., C. John, and J. Behrmann (2012), Expedition 308 synthesis: overpressure, consolidation, and slope stability on the continental slope of the of the Gulf of Mexico. In Flemings, P.B., Behrmann, J.H., John, C.M., and the Expedition 308 Scientists, Proc. IODP, 308: College Station TX (Integrated Ocean Drilling Program Management International, Inc.), doi:10.2204/iodp.proc.308.215.2012.

Flemings, P. B., H. Long, B. Dugan, J. Germaine, C. M. John, J. H. Behrmann, D. Sawyer, and IODP Expedition 308 Scientists (2008a), Pore pressure penetrometers document high overpressure near the seafloor where multiple submarine landslides have occurred on the continental slope, offshore Louisiana, Gulf of Mexico, *Earth and Planetary Science Letters*, *269*(3-4), 309–325, doi:10.1016/j.epsl.2007.12.005.

Flemings, P. B., H. Long, B. Dugan, J. Germaine, C. M. John, J. H. Behrmann, D. Sawyer, and IODP Expedition 308 Scientists (2008b), Erratum to “Pore pressure penetrometers document high overpressure near the seafloor where multiple submarine landslides have occurred on the continental slope, offshore Louisiana, Gulf of Mexico” [Earth and Planetary Science Letters 269/3–4 (2008) 309–32], *Earth and Planetary Science Letters*, *274*(1-2), 269-283, doi:10.1016/j.epsl.2008.06.027.

Freund, L. B. (1998), *Dynamic Fracture Mechanics*, 584 pp., Cambridge University Press, Melbourne, Australia.

Fryer, G. J., P. Watts, and L. F. Pratson (2004), Source of the great tsunami of 1 April 1946: a landslide in the upper Aleutian forearc, *Marine Geology*, *203*, 201-218.

Fæseth, R. B., and B. H. Sætersmoen (2008), Geometry of a major slump structure in the Storegga slide region offshore western Norway, *Norweigian Journal of Geology*, *88*, 1-11.

Garagash, D. I., and L. N. Germanovich (2012), Nucleation and arrest of dynamic slip on a pressurized fault., *Journal of Geophysical Research*, *117*, doi:10.1029/2012JB009209.

Gardner, J. V., D. B. Prior, and M. E. Field (1999), Humboldt Slide - a large shear-dominated retrogressive slope failure, *Marine Geology*, *154*, 328-338.

Garziglia, S., N. Sultan, A. Cattaneo, S. Ker, B. Marsset, V. Riboulot, M. Voisset, J. Adamy, and S. Unterseh (2010), Identification of shear zones and their causal mechanisms using a combination of cone penetration tests and seismic data in the Eastern Niger Delta, in *Submarine Mass Movement and Their Consequences, 4th International Symposium, Advances in Natural and Technological Hazards Research*, edited by D. C. Mosher et al., pp. 55-65, Springer Science + Business Media B.V., Switzerland.

Gauer, P., T. J. Kvalstad, C. F. Forsberg, P. Bryn, and K. Berg (2005), The last phase of the Storegga Slide: simulation of retrogressive slide dynamics and comparison with slide-scar morphology, *Marine and Petroleum Geology*, *22*, 171-178, doi:10.1016/j.marpetgeo.2004.10.004.

Gee, M. J. R., H. S. Uy, J. Warren, C. K. Morley, and J. J. Lambiase (2007), The Brunei slide: A giant submarine landslide on the North West Borneo Margin revealed by 3D seismic data, *Marine Geology*, *246*, 9-23.

Geist, E. (2000), Origina of the 17 July 1998 Papua New Guinea tsunami: earthquake or landslide?, *Seismological Research Letters*, *71*, 344-351.

Geist, E. L., P. J. Lynett, and J. D. Chaytor (2009), Hydrodynamic modeling of tsunamis from the Currituck landslide, *Marine Geology*, *264*, 41-52, doi:10.1016/j.margeo.2008.09.005.

Goren, L., E. Aharonov, and M. H. Anders (2010), The long runout of the Heart Mountain landslide: Heating, pressurization, and carbonate decomposition, *Journal of Geophysical Research*, *115*(B10210), doi:10.1029/2009JB007113.

Greene, H. G., L. Y. Murai, P. Watts, N. A. Maher, M. A. Fisher, C. E. Paull, and P. Eichhubl (2006), Submarine landslides in the Santa Barbara Channel as potential tsunami sources, *Natural Hazards and Earth System Sciences*, *6*, 63-88.

Grilli, S. T., and P. Watts (2005), Tsunami generation by submarine mass failure. I: Modeling, experimental validation, and sensitivity analyses, *Journal of Waterway, Port, Coastal, and Ocean Engineering*, *131*(6), 283-297, doi:10.1061/(ASCE)0733-950X(2005)131:6(283).

Grozic, J. L. H. (2010), Interplay between gas hydrates and submarine slope failure, in *Submarine Mass Movement and Their Consequences, 4th International Symposium, Advances in Natural and Technological Hazards Research*, edited by D. C. Mosher et al., pp. 11-30, Springer Science + Business Media B.V., Switzerland.

Gutenberg, B. (1939), Tsunamis and earthquakes, *Bulletin of the Seismological Society of America*, *29*(4), 517-526.

Hühnerbach, V., and D. G. Masson (2004), Landslides in the North Atlantic and its adjacent seas: an analysis of their morphology, setting and behaviour, *Marine Geology*, *213*, 343-362.

Haeussler, P. J., T. Parsons, D. P. Finlayson, P. Hart, J. D. Chaytor, H. Ryan, H. Lee, K. Labay, A. Peterson, and L. Liberty (2014), New imaging of sumarine landslides from the 1964 earthquake near Whittier, Alaska, and a comparison to failures in other Alaskan fiords, in *Submarine Mass Movements and Their Consequences, 6th International Symposium, Advances in Natural and Technological Hazards Research*, edited by S. Krastel et al., pp. 361-370, Springer Internaltional Publishing, Switzerland, doi:10.1007/978-3-319-00972-8_1.

Haflidason, H., R. Lien, H. P. Sejrup, C. F. Forsberg, and P. Bryn (2005), The dating and morphometry of the Storegga Slide, *Marine and Petroleum Geology*, *22*, 123-136, doi:10.1016/j.marpetgeo.2004.10.008.

Haflidason, H., H. P. Seijrup, I. M. Berstad, A. Nygard, T. Richter, P. Bryn, R. Lien, and K. Berg (2003), A weak layer feature on the Northern Storegga Slide escarpment, in *European Margin Sediment Dynamics*, edited by J. Minert and P. Weaver, pp. 55-62, Springer, Berlin.

Haflidason, H., H. P. Sejrup, A. Nygard, J. Minert, P. Bryn, R. Lien, C. F. Forsberg, K. Berg, and D. Masson (2004), The Storegga Slide: architecture, geometry and slide development, *Marine Geology*, *213*, 201-234, doi:10.1016/j.margeo.2004.10.007.

Hammack, J. L. (1973), A note on tsunamis: their generation and propagation in an ocean of uniform depth, *Journal of Fluid Mechanics*, *60*(4), 769-799.

Hampton, M. A., H. J. Lee, and J. Locat (1996), Submarine landslides, *Reviews of Geophysics*, *34*(1), 33-59.

Harbitz, C. B. (1992), Model simulations of tsunamis generated by the Storegga slides, *Marine Geology*, *105*, 1-21.

Harbitz, C. B., F. Lovholt, G. Pedersen, and D. G. Masson (2006), Mechanicsms of tsunami generation by submarine landslides: a short review, *Norwegian Journal of Geology*, *86*, 255-264.

Hasegawa, H. S., and H. Kanamori (1987), Source mechanism of the magnitude 7.2 Grand Banks earthquake of November 1929: double couple or submarine landslide?, *Bulletin of the Seismological Society of America*, *77*(6), 1984-2004.

Haugen, K. B., F. Lovholt, and C. B. Harbitz (2005), Fundamental mechanicsms for tsunami generation by submarine mass flows in idealised geometries, *Marine and Petroleum Geology*, *22*, 209-217.

Heinrich, P., A. Piatanesi, E. A. Okal, and H. Hebert (2000), Near-field modeling of the July 17, 1998 tsunami in Papua New Guinea, *Geophysical Research Letters*, *27*, 3037-3040.

Hellan, K. (1984), *Introduction to Fracture Mechanics*, 302 pp., McGraw-Hill Inc.,US, NY, NY.

Hidayat, D., J. S. Barker, and K. Satake (1995), Modeling the seismic source and tsunami generation of the December 12, 1992 Flores Island, Indonesia, earthquake, *Pure and Applied Geophysics*, *144*(3/4), 537-554.

Hutchinson, J. N. (1988), Morphological and geotechnical parameters of landslides in relation to geology and hydrogeology, paper presented at Landslides: Proceedings of the Fifth International Symposium on Landslides, Lausanne, 10-15 July 1988.

Huvenne, V. A., P. F. Croker, and J.-P. Henriet (2002), A refreshing 3D view of an ancient sediment collapse and slope failure, *Terra Nova*, *14*, 33-40.

Ida, Y. (1972), Cohesive force across the tip of a longitudinal-shear crack and Griffith's specific surface energy, *Journal of Geophysical Research*, *77*(20), 3796-3805.

Imamura, F., E. Gica, T. Takahashi, and N. Shuto (1995), Numerical simulation of the 1992 Flores tsunami: interpretation of tsunami phenomena in Northeastern Flores island and damage at Babi island, *Pure and Applied Geophysics*, *144*(3-4), 556-568.

Imamura, F., and K. Hashi (2002), Re-examination of the tsunami source of the 1998 Papua New Guinea earthquake tsunami, *Pure and Applied Geophysics*, *160*, 2071-2086.

Jajam, K. C., and H. V. Tippur (2012), Quasi-static and dynamic fracture behavior of particulate polymer composites: A study of nano- vs. micro-size filler and loading-rate effects, *Composites Part B: Engineering*, *43*(8), 3467-3481.

Jansen, E., S. Befring, T. Bugge, T. Eidvin, H. Holtedahl, and H. P. Sejrup (1987), Large submarine slides on the Norwegian continental margin: Sediments, transport, and timing, *Marine Geology*, *78*, 77-107.

Joseph, G. (2011), *Tsunamis, 1st Edition, Detection, Monitoring, and Early-Warning Technologies*, 448 pp., Academic Press.

Kanamori, H. (1972), Mechanism of tsunami earthquakes, *Phys. Earth Planet. Interiors 6*, 346-359.

Kostrov, B. V., and S. Das (1975), *Principles of earthquake source mechanics*, 286 pp., Cambridge University Press, New York, NY.

Kovacevic, N., R. J. Jardine, D. M. Potts, C. E. Clukey, J. R. Brand, and D. R. Spikula (2012), A numerical simulation of underwater slope failures generated by salt diapirism combined with active sedimentation, *Ge´otechnique*, *62*(9), 777-786.

Kulikov, E. A., A. B. Rabinovich, R. E. Thomson, and B. D. Bornhld (1996), The landslide tsunami of November 3, 1994, Skagway Harbor, Alaska, *Journal of Geophysical Research*, *101*(C3), 6609-6615.

Kvalstad, T. J., L. Andresen, C. F. Forsberg, K. Berg, P. Bryn, and M. Wangen (2005), The Storegga slide: evaluation of triggering sources and slide mechanics, *Marine and Petroleum Geology*, *22*, 245-256, doi:10.1016/j.marpetgeo.2004.10.019.

L'Heureux, J.-S., O. Longva, L. Hansen, and M. Vanneste (2014), The 1930 landslide in Orkdalsfjorden: Morphology and failure mechanism, in *Submarine Mass Movements and Their Consequences, 6th International Symposium, Advances in Natural and Technological Hazards Research*, edited by S. Krastel et al., pp. 239-247, Springer Internaltional Publishing, Switzerland, doi:10.1007/978-3-319-00972-8_21.

L'Heureux, J. S., M. Vanneste, L. Rise, J. Brendryend, C. F. Forsberg, F. Nadim, O. Longva, S. Chand, T. J. Kvalstad, and H. Haflidason (2013), Stability, mobility and failure mechanism for landslides at the upper continental slope off Vesterålen, Norway, *Marine Geology*, *346*, 192-207.

L'Heureux, J.-S., L. Hansen, O. Longva, A. Emdal, and L. Grande (2010), A multidisciplinary study of submarine landslides at the Nidelva fjord delta, Central Norway - implications for geohazards assessments, *Norweigian Journal of Geology*, *90*, 1-20.

L'Heureux, J.-S., M. Vanneste, L. Rise, J. Brendryen, C. F. N. Forsberg, F., O. Longva, S. Chand, T. J. Kvalstad, and H. Haflidason (2013), Stability, mobility and failure mechanism for landslides at the upper continental slope off Vesterålen, Norway, *Marine Geology*, *346*, 192-207.

Lambe, T. W., and R. V. Whitman (1986), *Soil Mechanics*, 553 pp., John Wiley & Sons, Inc., Hoboken, NJ.

Lastras, G., M. Canals, R. Urgeles, J. E. Hughes-Clarke, and J. Acosta (2004), Shallow slides and pockmark swarms in teh Eivissa Channel, western Mediterranean Sea, *Sedimentology*, *51*, 837-850, doi:10.1111/j.1365-3091.2004.00654.x.

Lax, P. D. (2006), *Hyperbolic Partial Differential Equations*, Courant Lecture Notes, 217 pp., Courant Institute of Mathematical Sciences, New York, NY.

Lee, H., J. Locat, P. Dartnell, K. Israel, and F. Wong (1999), Regional variability of slope stability: application to the Eel margin, California, *Marine Geology*, *154*, 305-321.

Lee, H., J. Locat, P. Desgagne´s, J. Parson, B. McAdoo, D. Orange, P. Puig, F. Wong, P. Dartnell, and E. et Boulanger (2007), Submarine Mass Movements, in *Continental-margin Sedimentation: Transport to Sequence Stratigraphy*, edited by C. Nittrouer, pp. 213-275, Special Publication No. 37 of the International Association of Sedimentologists.

Lee, H. J. (2009), Timing of occurrence of large submarine landslides on the Atlantic Ocean margin, *Marine Geology*, *264*, 53-64, doi:10.1016/j.margeo.2008.09.009.

Lee, H. J., and B. D. Edwards (1986), Regional method to assess offshore slope stability, *Journal of Geotechnical Engineering*, *112*, 489-509.

Lee, H. J., W. R. Normark, M. A. Fisher, H. G. Greene, B. D. Edwards, and J. Locat (2004), Timing and extent of submarine landslides in sourthern California, in *Offshore Technology Conference*, edited, OTC 16744, Houston, TX.

Lee, H. J., J. P. M. Syvitski, G. Parker, D. Orange, J. Locat, E. W. H. Hutton, and J. Imran (2002), Distinguishing sediment waves from slope failure deposits: field examples, including the 'Humboldt slide', and modelling results, *Marine Geology*, *192*, 79-104.

Legros, F. (2002), The mobility of long-runout landslides, *Engineering Geology*, *63*(3-4), 301-331.

Levin, B., and M. Nosov (2009), *Physics of Tsunamis*, 327 pp., Springer, Berlin, Germany.

Lewis, K. B. (1971), Slumping on a continental slope inclined at 1°~ 4°, *Sedimentology*, *16*, 97-110.

Leynaud, D., J. Mienert, and F. Nadim (2004), Slope stability assessment of the Helland Hansen area offshore the mid-Norwegian margin, *Marine Geology*, *213*, 457-480, doi:10.1016/j.margeo.2004.10.019.

Liu, P. L.-F., P. Lynett, and C. E. Synolakis (2003), Analytical solutions for forced long waves on a sloping beach, *Journal of Fluid Mechanics*, *478*, 101-109, doi:10.1017/S0022112002003385.

Locat, A., S. Leroueil, S. Bernander, D. Demers, J. Locat, and L. Quehb (2008), Study of a lateral spread failure in an eastern Canada clay deposit in relation with progressive failure: The Saint-Barnabe-Nord slide, in *Proceedings of the 4th Canadian Conference on Geohazards: From Causes to Management, Quebec, Que., 20-24 May 2008*, edited by J. Locat et al., pp. 89-96, Presses de l'Universite Laval, Quebec, Que.

Locat, J., and D. Demers (1988), Viscosity, yield stress, remolded strength, and liquidity index relationships for sensitive clays, *Canadian Geotechnical Journal*, *25*, 799-806.

Locat, J., and H. Lee (2009), Submarine mass movements and their consequences: and overview, in *Landslides - Disaster Risk Reduction.*, edited by K. Sassa and P. Canuti, pp. 115-142, Springer-Verlag, Berlin, Heidelberg.

Locat, J., H. Lee, U. S. ten Brink, D. Twichell, E. Geist, and M. Sansoucy (2009), Geomorphology, stability and mobility of the Currituck slide, *Marine Geology*, *264*, 28-40, doi:10.1016/j.margeo.2008.12.005.

Locat, J., and H. J. Lee (2002), Submarine landslides, advances and challenges, *Canadian Geotechnical Journal*, *39*(1), 193-212.

Locat, J., S. Leroueil, A. Locat, and H. Lee (2014), Weak layers: Their definition and classification from a geotechnical perspective, in *Submarine Mass Movements and Their Consequences, 6th Int. Symp., Advances in Natural and Technological Hazards Research*, edited by S. Krastel et al., pp. 3-12, Springer Internaltional Publishing, Switzerland, doi:10.1007/978-3-319-00972-8_1.

Lovholt, F., C. B. Harbitz, and K. B. Haugen (2005), A parametry study of tsunamis generated by submarine slides in the Ormen Lange/Storegga area off western Norway, *Marine and Petroleum Geology*, *22*, 219-231, doi:10.1016/j.marpetgeo.2004.10.017.

Lu, N., and J. W. Godt (2013), *Hillslope Hydrology and Stability*, 458 pp., Cambridge University Press, New York, NY.

Lurie, A. I. (2010), *Theory of Elasticity*, Foundations of Engineering Mechanics, 1054 pp., Springer, The Netherlands.

Ma, K.-F., K. Satake, and H. Kanamori (1991), The origin of the tsunami excited by the 1989 Loma Prieta earthquake -Faulting or slumping?, *Geophysical Research Letters*, *18*(4), 637-640.

Marino, R., and B. Ellwood (1978), Anomalous magnetic fabric in sediments which record an apparent geomagnetic field excursion, *Nature*, *274*, 581-582.

Martel, S. J. (2004), Mechanics of landslide initiation as a shear fracture phenomenon, *Marine Geology*, *203*, 319-339.

Martinsen, O. (1994), Mass movements, in *The Geological Deformation of Sediments*, edited by A. Maltman, pp. 127-165, Chapman and Hall.

Marur, P. R., R. C. Batra, G. Garcia, and A. C. Loos (2004), Static and dynamic fracture toughness of epoxy/alumina composite with submicron inclusions, *Journal of Materials Science*, *39*, 1437-1440.

Masson, D. G., C. B. Harbitz, R. B. Wynn, G. Pedersen, and F. Lovholt (2006), Submarine landslides: processes, triggers and hazard prediction, *Phil. Trans. R. Soc. A*, *364*(1845), 2009-2039.

Mayne, P. W. (2014), edited.

Mayne, P. W., B. R. Christopher, and J. DeJong (2001), *Subsurface Investigations (Geotechnical Site Characterization)*, National Highway Institute Publication No. FHWA NHI-01-031, 305 pp., Federal Highway Administration, Washington, DC.

McAdoo, B. G., L. F. Pratson, and D. L. Orange (2000), Submarine landslide geomorphology, US continental slope, *Marine Geology*, *169*, 103-136.

McClung, D. M. (1979), Shear fracture precipitated by strain softening as a mechanism of dry slab avalanche release, *Journal of Geophysical Research*, *84*(B7), 3519-3526.

McClung, D. M. (2009), Dry sno slab quasi-brittle fracture initiation and verification from field tests, *Journal of Geophysical Research*, *114*(F01022), doi:10.1029/2007JF000913.

McGregor, B. A. (1981), Smooth seaward-dipping horizons - an important factor in sea-floor stability?, *Marine Geology*, *39*, M89-M98.

Micallef, A., D. G. Masson, C. Berndt, and D. A. Stow (2007), Morphology and mechanics of submarine spreading: A case study from the Storegga Slide, *Journal of Geophysical Reserach*, *112*(F03023), doi:doi:10.1029/2006JF000739.

Miller, D. J. (1960), The Alaska earthquake of July 10, 1958: giant wave in Lituya bay., *Bulletin of the Seismological Society of America*, *50*(2), 253-266.

Mitchell, R. J., and A. R. Markell (1974), Flow slides in sensitive soils, *Canadian Geotechnical Journal*, *11*(1), 11-31.

Miyazawa, K., K. Goto, and F. Imamura (2012), Re-evaluation of the 1771 Meiwa tsunami source model, southern Ryukyu Islands, Japan, in *Submarine Mass Movements and Their Consequences, 5th International Symposium, Advances in Natural and Technological Hazards Research*, edited by Y. Yamada et al., pp. 497-506, Springer Science+Business Media B.V., doi:10.1007/978-94-007-2162-3_44.

Moore, D. G. (1961), Submarine slumps, *Journal of Sedimentary Petrology*, *31*, 343-357.

Moore, D. G. (1977), Submarine slides, in *Rockslides and Avalanches, 1. Natural Phenomena*, edited by B. Voight, pp. 563-604, Elsevier Scientific Pub. Co., New York.

Mosher, D. C., and D. J. W. Piper (2007), Analysis of multibeam seafloor imagery of the Laurentian fan and the 1929 Grand Banks landslide area, in *Submarine Mass Movements and Their Consequences*, edited by V. Lykousis et al., pp. 77-88, Springer.

Mulder, T., and P. Cochonat (1996), Classification of offshore mass movements, *Journal of Sedimentary Research*, *66*(1), 43-57.

Munson, B. R., D. F. Young, and T. H. Okiishi (2006), *Fundamentals of Fluid Mechanics*, Fifth Edition ed., 790 Pages pp., John Wiley & Sons, Inc., New York, NY.

Murty, T. S. (2003), Tsunami wave height dependence on landslide volume, *Pure and Applied Geophysics*, *160*(10-11), 2147-2153.

Nadim, F., G. Biscontin, and A. M. Kaynia (2007), Seismic triggering of submarine slides, paper presented at Offshore Technology Conference, 30 April-3 May 2007, Offshore Technology Conference, Houston, Texas.

Neuffer, D. P., and R. A. Schultz (2006), Mechanisms of slope failure in Valles Marineris, Mars, *Quarterly Journal of Engineering Geology and Hydrogeology*, *39*(3), 227-240.

Newmark, N. (1965), Effects of earthquakes on dams and embankments, *Géotechnique*, *15*(2), 139-160.

NIicholson, C., J. Kennett, C. Sorlien, S. Hopkins, R. Behl, W. Normark, R. Sliter, T. Hill, D. Pak, A. Schimmelmann, and K. Cannariato (2006), Santa Barbara basin study extends global climate record, *EOS Transactions*, *87*(21), 205-212.

Nisbet, E. G., and D. J. W. Piper (1998), Giant submarine landslides, *Nature*, *392*, 329-330.

O'Leary, D. W. (1991), Structure and morphology of submarine slab slides: clues to origin and behaviour, *Marine Geotechnology*, *10*, 53-69.

Okal, E. A., G. Plafker, C. E. Synolakis, and J. C. Borrero (2003), Near-field survey of the 1946 Aleutian tsunami of Unimak and Sanak islands, *Bulletin of the Seismological Society of America*, *93*(3), 1226-1234.

Okal, E. A., and C. E. Synolakis (2004), Source discriminants for near-field tsunamis, *Geophysical Journal of International*, *158*, 899-912.

Palmer, A. C., and J. R. Rice (1973), The growth of slip surfaces in the progressive failure of over-consolidated clay, *Proc. R. Soc. A*, *332*(1591), 527-548.

Pelinovsky, E. (2003), Analytical models of tsunami generation by sumarine landslides, in *Submarine Landslides and Tsunamis*, edited by A. C. Yalciner et al., pp. 111-128, Kluwer Academic Publishers, Netherlands.

Pelinovsky, E., and A. Poplavsky (1996), Simplified model of tsunami generation by submarine landslides, *Physics and Chemistry of The Earth*, *21*(1-2), 13-17.

Pelinovsky, E., T. Talipova, A. Kurkin, and C. Kharif (2001), Nonlinear mechanism of tsunami wave generation by atmospheric disturbances, *Natural Hazards and Earth System Sciences*, *1*, 243-250.

Picarelli, L., C. Russo, and G. Urciuoli (1995), Modelling earthflow movement based on experiences, paper presented at The Interplay between Geotechnical Engineering and Engineering Geology: Proceedings of the Eleventh European Conference on Soil Mechanics and Foundation Engineering, Copenhagen, 28 May - 1 June, 1995.

Picarelli, L., G. Urciuoli, and C. Russo (2000), Mechanics of slope deformation and failure in stiff clays and clay shales as a consequence of pore pressure fluctuation., paper presented at Proc. 8th Int. Symp. on Landslides, Thomas Telford Ltd., Cardiff, Wales.

Pinyol, N. M., and E. E. Alonso (2010), Fast planar slides. A closed-form thermo-hydro-mechanical solution, *Int J Numer Anal Met Geomech*, *34*, 27-52, doi:10.1002/nag.795.

Plafker, G., R. Kachadoorian, E. B. Eckel, and L. R. Mayo (1969), *Effects of the earthquake of March 27, 1964 on various communities*, US Geol. Surv. Prof. Paper 542-G, US Geological Survey, Washington, DC.

Prior, D. B. (1984), Subaqueous landslides, paper presented at Fourth International Symposium on Landslides, University of Toronto, Downsview, Ont. Canada.

Prior, D. B., and J. M. Coleman (1978), Disintegrative retrogressive landslides on very-low-angle subaqueous slopes, Mississippi delta, *Marine Geotechnology*, *3*, 37-60.

Prior, D. B., and J. M. Coleman (1979), Submarine landslides - geometry and nomenclatue, *Zeitschift fur Geomorphologie. Annals of Geomorphology.*, *23*(4), 415-426.

Prior, D. B., and J. M. Coleman (1984), Submarine slope instability, in *Slope Instability*, edited by D. Brunsden and D. B. Prior, pp. 419-455, Wiley, New York.

Prior, D. B., E. H. Doyle, and T. Neurauter (1986), The Currituck Slide, mid-Atlantic continental slope - revisited, *Marine Geology*, *73*, 25-45.

Prior, D. B., and J. N. Suhayda (1979), Application of infinite slope analysis to subaqueous sediment instabitlity, Mississippi delta, *Engineering Geology*, *14*, 1-10.

Puzrin, A., S. Frydman, and M. Talesnick (1995), Normalized non-degrading behaviour of soft clay under cyclic simple shear loading, *ASCE Journal of Geotechnical Engineering*, *121*(12), 836-843.

Puzrin, A., S. Frydman, and M. Talesnick (1997), Effect of degradation of soil properties on seismic response of soft clay strata, *ASCE Journal of Geotechnical Engineering*, *123*(2), 85-93.

Puzrin, A. M. (2014), Personal Communication, edited.

Puzrin, A. M., and L. N. Germanovich (2005a), The growth of shear bands in the catastrophic failure of soils, *Proc. R. Soc. A*, *461*(2056), 1199-1228.

Puzrin, A. M., and L. N. Germanovich (2005b), The Mechanism of Tsunamigenic Landslides, *Geotechnical Special Publications 143*, 421-428, doi:10.1061/40797(172)24.

Puzrin, A. M., L. N. Germanovich, and S. Kim (2004), Catastrophic failure of submerged slopes in normally consolidated sediments, *Géotechnique*, *54*(10), 631-643.

Puzrin, A. M., E. Saurer, and L. N. Germanovich (2010), A dynamic solution of the shear band propagation in submerged landslides, *Granular Matter*, *12*, 253-265.

Quinn, P. E., M. S. Diederichs, R. K. Rowe, and D. J. Hutchinson (2011a), A new model for large landslides in sensitive clay using a fracture mechanics approach, *Canadian Geotechnical Journal*, *48*, 1151-1162.

Quinn, P. E., M. S. Diederichs, R. K. Rowe, and D. J. Hutchinson (2012), Development of progressive failure in sensitive clay slopes, *Canadian Geotechnical Journal*, *49*, 782-795.

Quinn, P. E., D. J. Hutchinson, M. S. Diederichs, and R. K. Rowe (2011b), Characteristics of large landslides in sensitive clay in relation to susceptibility, hazard, and risk, *Canadian Geotechnical Journal*, *48*, 1212-1232, doi:10.1139/T11-039.

Rees, A. I. (1961), The effect of water currents on themagnetic remanence and anisotropy of susceptibility of some sediments, *Geophysical Journal of the Royal Astronomical Society*, *6*, 235-251.

Reid, W. T. (1972), *Riccati Differential Equations*, Academic Press, New York.

Rice, J. R. (1968), Mathematical analysis in the mechanics of fracture, in *Fracture: An advanced treatise, Mathematical Fundamentals*, edited by H. Liebowitz, pp. 191-311, Academic Press, New York, NY.

Rice, J. R. (1973), The initiation and growth of shear bands, paper presented at Plasticity and soil mechanics, Cambridge University Engineering Department, Cambridge.

Rice, J. R. (1980), The mechanics of earthquake rupture, in *Physics of the Earth's Interior*, edited by A. Dziewonski and E. Boschi, North-Holland, Amsterdam, 555-649.

Ruff, L. J. (2003), Some aspects of energy balance and tsunami generation by earthquakes and landslides, *Pure and Applied Geophysics*, *160*, 2155-2176, doi:10.1007/s00024-003-2424-y.

Ruina, A. (1983), Slip instability and state variable friction laws, *J. Geophys. Res.*, *88*(10), 359-370.

Ryan, H. F., H. J. Lee, P. J. Haeussler, C. R. Alexander, and R. E. Kayen (2010), Historic and paleo-submarine landslide deposits imaged beneath Port Valdez, Alaska: Implications for tsunami generation in a glacial fiord, in *Submarine Mass Movements and Their Consequences, 4th International Symposium, Advances in Natural and Technological Hazards Research*, edited by D. C. Mosher et al., pp. 411-421, Springer Science + Business Media B.V., Switzerland.

Sansoucy, M., J. Locat, and H. J. Lee (2007), Geotechnical considerations of submarine canyon formation: The case of Cap de Creus canyon, in *Submarine Mass Movements and Their Consequences, 3rd Int. Symp., Advances in Natural and Technological Hazards Research*, edited by V. Lykousis et al., pp. 221-230, Springer, Netherlands.

Satake, K. (2012), Tsunamis generated by submarine landslides, in *Submarine Mass Movements and Their Consequences, 5th International Symposium, Advances in Natural and Technological Hazards Research*, edited by Y. Yamada et al., pp. 475-484, Springer Science+Business Media B.V., doi:10.1007/978-94-007-2162-3_42.

Saurer, E. (2009), *Shear Band Propagation in Soils and Dynamics of Tsunamigenic Landslides*, Doctor of Sciences thesis, 168 pp., ETH Zurich.

Saurer, E., and A. M. Puzrin (2011), Validation of the energy-balance approach to curve-shaped shear-band propagation in soil, *Philosophical Transactions of the Royal Society of London A: Mathematical and Physical Sciences*, *467*, 627-652, doi:10.1098/rspa.2010.0285.

Sayago-Gil, M., D. Long, L.-M. Fernández-Salas, K. Hitchen, N. López-González, V. Díaz-del-Río, and P. Durán-Muñoz (2010), Geomorphology of the Talismán Slide (Western slope of Hatton Bank, NE Atlantic Ocean), in *Submarine Mass Movements and Their Consequences, 4th International Symposium, Advances in Natural and Technological Hazards Research*, edited by D. C. Mosher et al., pp. 289-300, Springer Science + Business Media B.V., Switzerland.

Schock, S. G., L. R. LeBlanc, and L. A. Mayer (1989), Chirp subbottom profiler for quantitative sediment analysis, *Geophysics*, *54*(4), 445-450.

Scholz, N. A., M. Riedel, G. D. Spence, R. D. Hyndman, T. James, K. Naegeli, B. Dugan, J. Pohlman, and T. Hamilton (2011), Do dissociating gas hydrates play a role in triggering submarine slope failures? A case study from the Northern Cacadia Marin, paper presented at Proceedings of the 7th International Conference on Gas Hydrates (ICGH 2011), Edinburgh, United Kingdom, July 17-21, 2011.

Schwehr, K., N. Driscoll, and L. Tauxe (2007), Origin of continental margin morphology: Submarine-slide or downslope current-controlled bedforms, a rock magnetic approach, *Marine Geology*, *240*, 19-41.

Schwehr, K., and L. Tauxe (2003), Characterization of soft sediment deformation: detection of crypto-slumps using magnetic methods, *Geology*, *31*(3), 203-206.

Schwehr, K., L. Tauxe, N. Driscoll, and H. Lee (2006), Detecting compaction disequilibrium with anisotropy of magnetic susceptibility, *Geochemistry Geophysics Geosystems*, *7*(11), doi:10.1029/2006GC001378.

Schwing, F. B., and J. G. Norton (1990), Earthquake and bay, *Eos Transaction Americal Geophysical Union*, *71*(6), 250-251, 262.

Screaton, E. J., D. R. Wuthrich, and S. J. Dreiss (1990), Permeabilities, fluid pressures, and flow rates in the Barbados Ridge Complex, *Journal of Geophysical Research*, *95*(B6), 8997-9007.

Seed, H. B. (1979), Considerations in the earthquake-resistant design of earth and rockfill dams, *Géotechnique*, *29*(3), 215-263.

Segur, H. (2007), Waves in shallow water, with emphasis on the tsunami of 2004, in *Tsunami and Nonlinear Waves*, edited by A. Kundu, p. 315, Springer, Berlin.

Shukla, A. (1983), Comparison of static and dynamic energy release rate for different fracture specimens *Engineering Fracture Mechanics*, *18*(5), 725-730.

Skempton, A. W. (1985), Residual strength of clays in landslides, folded strata and the laboratory, *Ge´otechnique*, *35*(1), 3-18.

Skempton, A. W., and J. N. Hutchinson (1969), Stability of natural slopes and embankment foundation, in *Proc. 7th Conf. Soil Mechan. and Foundation Engr.*, edited, pp. 291-340, Mexico.

Solheim, A., K. Berg, C. F. Forsberg, and P. Bryn (2005), The Storegga Slide complex: repetitive large scale sliding with similar cause and development, *Marine and Petroleum Geology*, *22*, 97-107.

Stein, S., and E. A. Okal (2005), Speed and size of the Sumatra earthquake, *Nature*, *434*, 581-582, doi:10.1038/434581a.

Steiner, A., J.-S. L'Heureux, A. Kopf, M. Vanneste, O. Longva, M. Lange, and H. Haflidason (2012), An in-situ free-fall piezocone penetrometer for characterizing soft and sensitive clays at Finneidfjord (norther Norway), in *Submarine Mass Movement and Their Consequences, 5th International Symposium, Advances in Natural and Technological Hazards Research*, edited by Y. Yamada et al., pp. 99-110, Springer Science + Business Media B.V., doi:10.1007/978-94-007-2162-3_9.

Strasser, M., S. Stegmann, F. Bussmann, F. S. Anselmetti, R. B., and A. Kopf (2007), Quantifying subaqueous slope stability during seismic shaking: Lake Lucerne as model for ocean margins, *Marine Geology*, *240*, 77-97.

Sultan, N., P. Cochonat, J. P. Foucher, and J. Mienert (2004), Effect of gas hydrates melting on seafloor slope instability, *Marine Geology*, *213*(1-4), 379-401.

Sweet, S., and E. A. Silver (2003), Tectonics and slumping in the source region of the 1998 Papua New Guinea tsunami from seismic reflection images, *Pure and Applied Geophysics*, *160*, 1945-1968.

Synolakis, C. E., J.-P. Bardet, J. C. Borrero, H. L. Davies, E. A. Okal, E. A. Silver, S. Sweet, and D. R. Tappin (2002), The slump origin of the 1998 Papua New Guinea Tsunami, *Proceedings of the Royal Society of London, Series A*, *458*, 763-789.

Synolakis, C. E., and E. N. Bernard (2006), Tsunami science before and beyond boxing day 2004, *Philosophical Transactions: Mathematical, Physical and Engineering Sciences*, *364*(1845), 2231-2265.

Talling, P. J. (2013), Hybrid submarine flows comprising turbidity current and cohesive debris flow: Deposits, theoretical and experimental analyses, and generalized models, *Geosphere*, *9*, 460-488, doi:10.1130/GES00792.1.

Tappin, D. R., P. Watts, G. M. McMurtry, Y. Lafoy, and T. Matsumoto (2001), The Sissano, Papua New Guinea tsunami of July 1998 - Offshore evidence on the source mechanism, *Marine Geology*, *175*(1-4), 1-23.

ten Brink, U. S., D. Twichell, E. Geist, J. Chaytor, J. Locat, H. Lee, B. Buczkowski, and M. Sansoucy (2007), *The Current State of Knowledge Regarding Potential Tsunami Sources Affecting U.S. Atlantic and Gulf Coasts*, A Report to the Nuclear Regulatory Commission, 156 pp., USGS.

Thakur, V., S. A. Degago, F. Oset, B. K. Dolva, and R. Aaboe (2013), A new approach to assess the potential for flow slide in sensitive clays, *Proceedings of the 18th International Conference on Soil Mechanics and Geotechnical Engineering*, 2265-2268.

Timoshenko, S. P., and J. N. Goodier (1970), *Theory of Elasticity, 3rd Ed.*, 567 pp., McGraw-Hill, Singapore.

Tinti, S., and E. Bortolucci (2000a), Analytical investigation on tsunamis generated by submarine slides, *Annali Di Geofisica*, *43*(3), 519-536.

Tinti, S., and E. Bortolucci (2000b), Energy of water waves induced by submarine landslides, *Pure and Applied Geophysics*, *157*, 281-318.

Tinti, S., E. Bortolucci, and C. Chiavettieri (2001), Tsunami excitation by submarine slides in shallow-water approximation, *Pure and Applied Geophysics*, *158*, 759-797.

Trenter, N. A., and C. D. Warren (1996), Further investigations at the Folkestone Warren landslide, *Ge´otechnique*, *46*(4), 589-620.

Troncone, A. (2005), Numerical analysis of a landslide in soils with strain-softening behaviour, *Géotechnique*, *55*(8), 585-596.

Twichell, D. C., J. D. Chaytor, U. S. ten Brink, and B. Buczkowski (2009), Morphology of late Quaternary submarine landslides along the U.S. Atlantic continental margin, *Marine Geology*, *264*, 4-15, doi:10.1016/j.margeo.2009.01.009.

Urciuoli, G., L. Picarelli, and S. Leroueil (2007), Local soil failure before general slope failure, *Geotechnical and Geological Engineering*, *25*, 103-122, doi:10.1007/s10706-006-0009-0.

Vanneste, M., N. Sultan, S. Garziglia, C. F. Forsberg, and J. S. L'Heureux (2014), Seafloor instabilities and sediment deformation processes: The need for integrated, multi-disciplinary investigations, *Marine Geology*, *352*(183-214).

Vardoulakis, I. (2002), Dynamic thermo-poro-mechanical analysis of catastrophic landslides, *Géotechnique*, *52*(3), 157-171.

Varnes, D. J. (1978), Slope movement types and processes, in *Landslides: Analysis and Control*, edited by R. L. Schuster and R. J. Krizek, pp. 11-33, National Academy of Science, Washington D.C.

Viesca, R. C. (2011), *The near and far of pore pressure during landslide and earthquake ruptures*, Ph.D thesis, 149 pp., Harvard University, Cambridge, MA.

Viesca, R. C., and J. R. Rice (2012), Nucleation of slip-weakening rupture instability in landslides by localized increase of pore pressure, *Journal of Geophysical Research*, *117*(B03104), doi:10.1029/2011JB008866.

Voight, B., and C. Faust (1982), Frictional heat and strength loss in some rapid landslides, *Géotechnique*, *32*(1), 43-54.

Walder, J. S., P. Watts, O. E. Sorensen, and J. Janssen (2003), Tsunamis generated by subaerial mass flows, *Journal of Geophysical Reserach*, *108*(B5), 2236, doi:10.1029/2001JB000707.

Wang, H. F. (2000), *Theory of Linear Poroelasticity with Applications to Geomechanics and Hydrogeology*, 276 pp., Princeton University Press.

Wang, W.-N., M. Chigira, and T. Furuya (2003), Geological and geomorphological precursors of the Chiu-fen-erh-shan landslide triggered by the Chi-chi earthquake in central Taiwan, *Engineering Geology*, *69*, 1-13.

Ward, S. N. (2001), Landslide tsunami, *Journal of Geophysical Research*, *106*(6), 11201-11215.

Watts, P. (1998), Wavemaker curves for tsunamis generated by underwater landslides, *Journal of Waterway, Port, Coastal, and Ocean Engineering*, *124*(3), 127-137.

Watts, P. (2000), Tsunami features of solid block under water landslides, *Journal OF Waterway, Port, Coastal, and Ocean Engineering*, *126*(3), 144-152.

Watts, P. (2012), Tsunami hazards for nuclear power plants: mass failures, uncertainty, and warning, in *Submarine Mass Movements and Their Consequences, 5th International Symposium, Advances in Natural and Technological Hazards Research*, edited by Y.

Yamada et al., pp. 525-538, Springer Science+Business Media B.V., doi:10.1007/978-94-007-2162-3_47.

Watts, P., S. T. Grilli, D. R. Tappin, and G. J. Fryer (2005), Tsunami generation by submarine mass failure. II: Predictive Equations and case studies, *Journal of Waterway, Port, Coastal, and Ocean Engineering 131*(6), 298-310.

Whitham, G. B. (1999), *Linear and Nonlinear Waves*, 660 pp., Wiley, Hoboken, NJ.

Wiemer, G., A. Reusch, M. Strasser, S. Kreiter, D. Otto, T. Mörz, and A. Kopf (2012), Static and cyclic shear strength of cohesive and non-cohesive sediments, in *Submarine Mass Movements and Their Consequences, 5th International Symposium, Advances in Natural and Technological Hazards Research*, edited by Y. Yamada et al., pp. 111-121, Springer Science+Business Media B.V., doi:10.1007/978-94-007-2162-3_10.

Wilson, C. K., D. Long, and J. Bulat (2004), The morphology, setting and processes of the Afen Slide, *Marine Geology*, *213*, 149-167, doi:10.1016/j.margeo.2004.10.005.

Wood, D. M. (1990), *Soil Behaviour and Critical State Soil Mechanics*, 462 pp., Cambridge University Press, New York, NY

Woodcock, N. H. (1979), Sizes of submarine slides and their significance, *Journal of Structural Geology*, *1*(2), 137-142.

Wright, S. G., and E. M. Rathje (2003), Triggering mechanisms of slope instability and their relationship to earthquakes and tsunamis, *Pure and Applied Geophysics*, *160*, 1865-1877.

Xu, W., and L. N. Germanovich (2006), Excess pore pressure resulting from methane hydrate dissociation in marine sediments: A theoretical approach, *J. Geophys. Res.*, *111*(B01104), doi:10.1029/2004JB003600.

Xu, W., and L. N. Germanovich (2007), Reply to comment by Nabil Sultan on "Excess pore pressure resulting from methane hydrate dissociation in marine sediments: A theoretical approach", *J. Geophys. Res.*, *112*(B02104), doi:10.1029/2006JB004722.

Yalciner, A. C., B. Alpar, Y. Altinok, I. Ozbay, and F. Imamura (2002), Tsunamis in the Sea of Marmara Historical documents for the past, models for the future, *Marine Geology*, *190*, 445-463.

Yun, J. W., D. L. Orange, and M. E. Field (1999), Subsurface gas offshore of northern California and its link to submarine geomorphology, *Marine Geology*, *154*, 357-368.

APPENDIX A. LANDSLIDE TYPES AND MECHANISMS

Although we mainly discuss below submarine landslides, we focus on such features and processes that are also common for subaerial landslides.

Many, if not most, submarine landslides take place on mild slopes [e.g., *Lewis*, 1971; *Bugge et al.*, 1988; *McAdoo et al.*, 2000; *Masson et al.*, 2006; *Micallef et al.*, 2007; *Twichell et al.*, 2009; *L'Heureux et al.*, 2013], which can be as small as 0.5° (continental shelf off the Malaspina glacier, Alaska [*Carson*, 1978]), 0.25° (Klamath river delta, California [*Field et al.*, 1982]), or even 0.01° (Mississippi river delta, Gulf of Mexico [*Prior and Coleman*, 1978]). As a result of analysis of more than 260 landslides on both margins of the North Atlantic Ocean and adjacent seas, *Hühnerbach and Masson* [2004] concluded that landslides on the ocean slopes occur on virtually every angle, although the majority takes place on slopes between 2° and 20° with mean values of 5° and 3° on the open continental margins in the western and eastern North Atlantic, respectively. Most landslides and seafloor failures on the Southeastern Australian Margin took place on slopes between 1° and 7° [*Clarke et al.*, 2011]. Nearly 90 % of the landslides documented on the North America Atlantic Margin [*Masson et al.*, 2006; *Lee et al.*, 2007] and on the continental slope in the Gulf of Mexico [*McAdoo et al.*, 2000] occurred on slopes smaller than 10°. The available seafloor data [e.g., *McAdoo et al.*, 2000; *Hühnerbach and Masson*, 2004; *Masson et al.*, 2006] indicate that the largest landslides take place on the lowest slopes. Dimensions of the region excavated by a landslide range from less than 1 km [e.g., *Woodcock*, 1979; *Canals et al.*, 2004; *Blum et al.*, 2010; *L'Heureux et al.*, 2013] to more than 10^2 km [e.g., *Nisbet and Piper*, 1998; *Twichell et al.*, 2009] both along the slope (landslide length) and in horizontal direction (landslide width). Submarine landslides occur on both passive and active margins [e.g., *McAdoo et al.*, 2000; *Locat et al.*, 2009], and active margins show the presence of low-angle landslides as large as those found on passive margins (e.g., 120-km Brunei slide, Northwest Borneo Margin, South China Sea [*Gee et al.*, 2007]).

Typical types of the submarine mass movements [*Dott*, 1963; *Varnes*, 1978; *Prior and Coleman*, 1979; *Coleman and Prior*, 1988; *Martinsen*, 1994; *Mulder and Cochonat*, 1996; *Locat and Lee*, 2002; *Masson et al.*, 2006; *Micallef et al.*, 2007; *Locat and Lee*, 2009] include falls, slides, spreads, debris flows, avalanches, mudflows, and turbidity currents. Slides are further

categorized as *rotational* or *translational* [e.g., *Varnes*, 1978; *Prior and Coleman*, 1979; *Locat and Lee*, 2002]. They take place by rotational or translational downslope movements, respectively, of a sediment mass on a thin zone of large shear strain gradients, which is often recognized as a rupture surface [e.g., *Hampton et al.*, 1996; *Locat and Lee*, 2002; *Masson et al.*, 2006], a slide (slip) surface [*Coleman and Prior*, 1988; *Hampton et al.*, 1996; *D'Elia et al.*, 1998], or a shear band [e.g., *Chowdhury et al.*, 2010; *Dey et al.*, 2012; *Quinn et al.*, 2012]. Rotational slides develop along a concave upward, scoop-shaped rupture surface and exhibit noticeable deformation in the slide material. Translational slides (also called planar slides [*Prior and Coleman*, 1979]) show much less internal deformation and move on a relatively planar surface of rupture that usually parallels the slope surface (Figure A.1a) [*Varnes*, 1978; *Bernander and Olofsson*, 1981; *Hampton et al.*, 1996; *Lu and Godt*, 2013]. It is commonly accepted that translational slides take place in sediments where the rupture process is controlled by such morphological features as bedding planes or thin, weak layers susceptible to failure and sub-parallel to the seafloor [*Bjerrum*, 1967; *Varnes*, 1978; *Bunn and McGregor*, 1980; *Cartier and Pouget*, 1988; *O'Leary*, 1991; *Picarelli et al.*, 1995; *Hampton et al.*, 1996; *D'Elia et al.*, 1998; *Haflidason et al.*, 2003; *Wang et al.*, 2003; *Haflidason et al.*, 2004; *Lastras et al.*, 2004; *Wilson et al.*, 2004; *Chang et al.*, 2005; *Troncone*, 2005; *Fæseth and Sætersmoen*, 2008; *Cecinato*, 2009; *Garziglia et al.*, 2010; *Grozic*, 2010; *Locat et al.*, 2014]. Generally, the observed depth-to-length ratio of rotational and translational slides is greater and less than 15%, respectively [*Skempton and Hutchinson*, 1969; *Prior and Coleman*, 1979; *Masson et al.*, 2006].

Rotational and translational slides are also called *slumps* and *slides* (i.e., omitting modifier 'translational'), respectively [e.g., *Masson et al.*, 2006; *Fæseth and Sætersmoen*, 2008]. As noted by *Prior and Coleman* [1979], many slumps should be reclassified as varieties of translational slides because rotational shear surfaces tend to coalesce at a relatively shallow depth to form a planar basal rupture (or detachment) boundary, inclined at low angles and paralleling the regional slope over long distances (Figure A.1a). For example, *Fæseth and Sætersmoen* [2008] report that a giant, intact slump (155 by 35 km), contemporary to the latest Storegga Slide (released approximately 8100 ya) [*Bugge et al.*, 1988; *Haflidason et al.*, 2005; *Solheim et al.*, 2005] and located along the southern margin of the Storegga Slide scar, consists

of rotational movement closer to the break-away fault while the detachment boundary is bedding-parallel below a major part of the slump. *Prior and Coleman* [1979; 1984] further note that translational slides, in which the rupture surface is planar and inclined approximately parallel to the slope surface, appear to be the most common form of seafloor instability. In particular, ≈57% of slides on the U.S. Atlantic continental slope are translational, which includes 17% of coherent slab slides [*Booth et al.*, 1993]. Incidentally, the majority of the identified submarine slides have the thickness-to-length ratio of less than 0.1 and often less than 0.01 [e.g., *Woodcock*, 1979; *Hühnerbach and Masson*, 2004; *Masson et al.*, 2006; *Lee et al.*, 2007; *ten Brink et al.*, 2007; *L'Heureux et al.*, 2013].

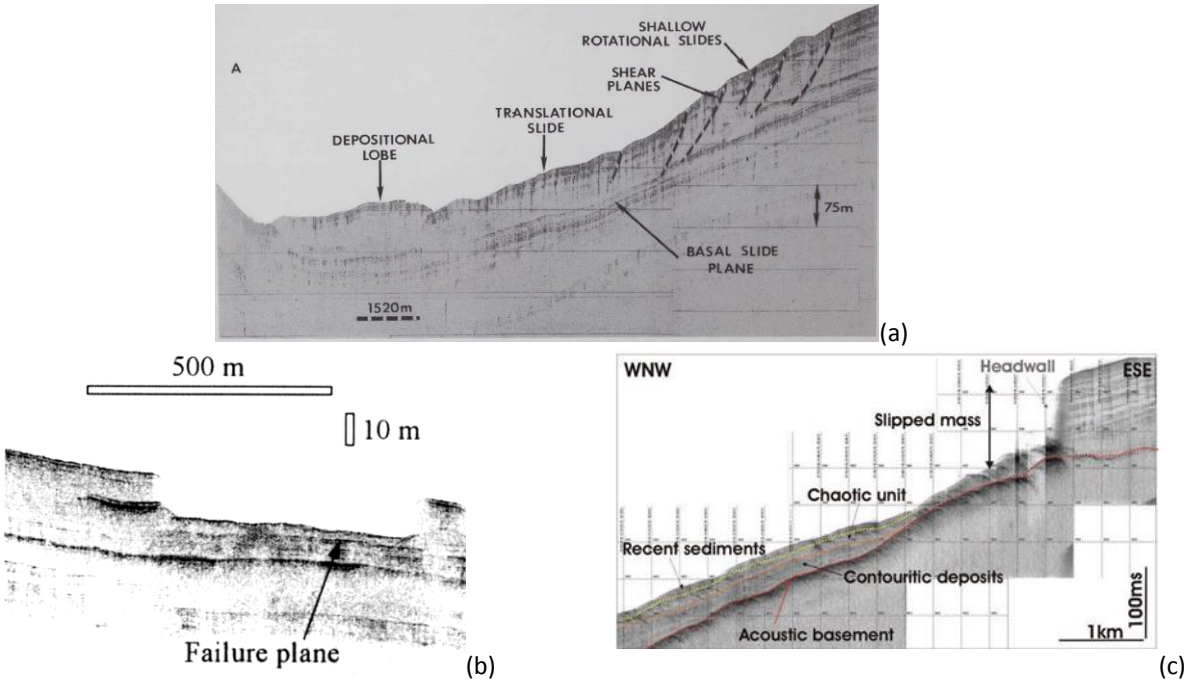

Figure A.1. (a) Seismic profile from the continental slope in the Gulf of Mexico [*Prior*, 1984]. (b) Volume removed as a result of landslide in the Saguenay Fjord, Quebec, Canada [*Locat et al.*, 2014]. (c) Longitudinal seismic section of the Talismán Slide [*Sayago-Gil et al.*, 2010].

In actuality, translation and rotational slides represent two end-members of the slide variety [e.g., *Martinsen*, 1994]. For example, both translational and rotational elements are present in slides shown in Figure A.1a and Figure 18. An important translational feature of these slides is *the basal shear surface* (called basal slide plane in Figure A.1a), which we represent below by a shear band (discontinuity). This rupture surface separates the slide material from the relatively undeformed substrata. Because slip on this surface was limited (for

both slides in Figure A.1a and Figure 18), the slide material is relatively coherent, and it is possible to see the details of the rupture surface development. When the slip distances are sufficiently large, the slide material is completely removed from its original position (Figure 1b, Figure A.1b, and Figure A.1c).

Conceptually, a slide develops from the (quasi-) equilibrium state of the intact (or creeping) slope material and involves *failure* (Figure A.2a) and *post-failure* (Figure A.2b) stages [e.g., *D'Elia et al.*, 1998; *Locat and Lee*, 2002]. During the failure stage, also called the slide initiation stage, a continuous shear band, which constitutes the rupture surface, develops in the slope material and separates the sliding mass from the underlying sediment (Figure A.2a). The moment when this separation is completed is called *global failure* or *slope failure* [e.g., *D'Elia et al.*, 1998]. Active (extensional) and passive (compressional) failures [e.g., *Budhu*, 2007; *Locat et al.*, 2008], taking place at the upper and lower slide ends, respectively (Figure A.2a), can be viewed as global failure mechanisms, although in 3-D, details can be more complex [e.g., *Farrell*, 1984; *Martel*, 2004]. The direction of the slide development during the failure stage (Figure A.2a) is not clear *a priory*. In the case of the Humboldt slide (Figure A.2b), for example, the shallow rotational failure began in the middle of the 'slide' and progressed simultaneously upslope and downslope [*Gardner et al.*, 1999], but the basal shear surface probably propagated downslope. Note that the *pre-failure* stage, distinguished in some works [e.g., *D'Elia et al.*, 1998; *Locat and Lee*, 2002], is a part of the *failure* stage introduced here. A relatively small but distinct basal shear band emerges as a result of pre-failure processes such as viscous creep, elasto-plastic yielding, and, possibly, small-scale rotational shearing or faulting (Figure A.1a and Figure 18). During the failure stage, this initial discontinuity (Figure A.2a) develops into the basal shear (rupture) surface.

The sliding mass, separated from the substrata by the basal rupture surface (developed during the failure stage), moves outward and downhill during the post-failure stage (Figure A.2b). In slide development, therefore, the moment of global failure separates the failure and post-failure stages, which end and begin, respectively, with the global failure. Without special instrumentation, the slide becomes visible to an observer (if one were present) only during the post-failure stage, when some slides mobilize into flows, while others take place as movements

of relatively intact, coherent bodies (Figure A.2b) [e.g., *Erismann*, 1977; *Locat and Lee*, 2002; *Masson et al.*, 2006], for example, as shallow slab slides [*Prior and Coleman*, 1979; *Coleman and Prior*, 1988]. In particular, ≈36% of submarine landslides on the US Atlantic continental slope remained coherent bodies during sliding and ≈64% disintegrated [*Booth et al.*, 1993]. As the excavated slide material moves downhill (Figure 1 and Figure 17a), it displaces a large water volume and may generate a tsunami (Figure A.2b) [*Yalciner et al.*, 2002; *Bardet et al.*, 2003; *Haugen et al.*, 2005; *Harbitz et al.*, 2006; *Levin and Nosov*, 2009; *Chai et al.*, 2014].

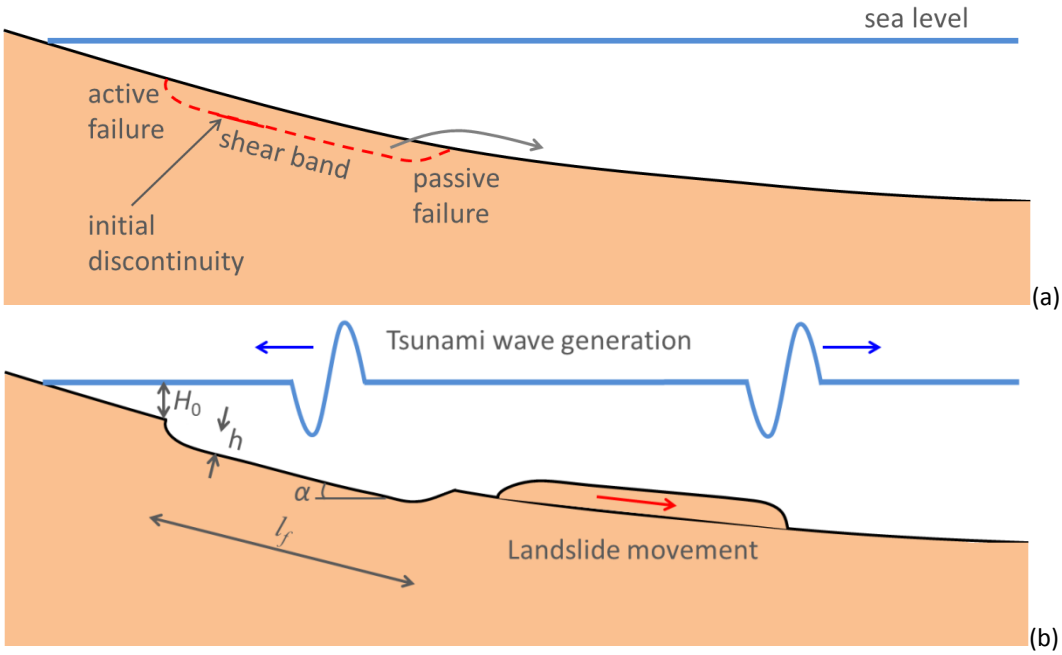

Figure A.2. A submarine slide scenario. (a) Failure (initiation) stage. This stage ends by the global slope failure (Section 6.1), when the basal shear band (rectilinear part of the dashed line), developing sub-parallel to the slope boundary, is linked with the boundary by the processes of active and passive failures), creating a continuous rupture (slip) surface. (b) Post-failure stage. This stage begins with the global slope failure (Section 6.1), when a relatively intact and coherent excavated mass starts moving outward and downhill. It first moves along the freshly created slip surface and then along the slope boundary until it stops (Section 9.1) or mobilizes into a sediment flow (not shown). Except for the effect of the seawater on the sediment flow (if it occurs), failure and post-failure stages are similar for submarine and subaerial landslides [e.g., *Locat and Lee*, 2002].

Examples of historic submarine, tsunamigenic landslides are given in Table A.1. One of these landslides, the Gaviota slide [*Lee and Edwards*, 1986; *Edwards et al.*, 1995; *Hampton et al.*, 1996; *Greene et al.*, 2006; *Schwehr et al.*, 2007; *Blum et al.*, 2010] is shown in Figure 1 and Figure 17a. This is a translational slide with a sub-horizontal crack on the slope west to the slide. In Figure 1a and Figure 17a, the slope is interpreted as to be undeformed to the left (west) of

the slide, while the fracture (≈8 km long [*Schwehr et al.*, 2006]) to the right (east) of the slide (marked by arrows spaced by ≈4 km) is produced by the developing rupture surface and represents the future location of a head scarp [*Martel*, 2004]. This interpretation is consistent with the image in Figure 17b, which shows the vertical seismic cross-section along profile line b-b in Figure 17a. We interpret the curved lines in the inset on Figure 17a as shear bands that appeared as a result of active failure. Resolution of this image is insufficient to conclude whether the basal rupture surface initiated or did not initiate. Possible locations of this surface are indicated based on the locations of the lower ends of the curved shear band and the sub-horizontal slope crack (Figure 1a and Figure 17b).

Table A.1. Historical submarine tsunamigenic landslides. In this table, h, l_f, and b are the thickness, length (along the slope), and width (in horizontal direction), respectively (Figure A.2b and Figure 26), of the displaced sediment body of volume V, α is the slope angle (Figure A.2b), and H_0 is the depth of the slide headwall scarp, i.e., the upper slide point (Figure A.2b and Figure 19).

Source Location	Date	Tsunami runup (m)	Deposit	Geometry					
				h (m)	l_f (km)	b (km)	V (km^3)	α (deg)	H_0 (m)
Currituck, North Carolina[1]	40,000-24,000 BP	3*	normally-consolidated clay	350	30	20	128	4	500
Storegga, Norway[2]	30,000-5,000 BP	19	clay	160	340	100	5580	0.6	500
Goleta slide, California[3]	200 BP	10**	stiff clay	48	14.6	10.5	1.51	2	150
Gaviota slide, California[4]	1812	1.5***	stiff clay	12	2.6	1.65	0.02	4	400
Grand Banks, New Foundland[5]	1929 Nov.18	13	unconsolidated muddy sediment	10	250	150	200	3	730
Ugamak Slide, Alaska[6]	1946 Apr.1	40	glacial sediment	250	40	25	250	4.3	1600
Port Valdez, Alaska[7]	1964 Mar.27	65	under-consolidated fine-grain sediment	32	1.3	0.18	0.05	2	141
Loma Prieta, California[8]	1989, Oct.17	0.2	mud and silt	0.35	3.4	10	0.01	0.8	25
Papua New Guinea[9]	1998 Jul.17	15	marine clay	30	4.6	2.5	4.2	10	760
Izmit Bay, Turkey[10]	1999 Aug.17	20	stiff clay	50	5	5	12.5	5	220

[1] *Prior et al.* [1986], *Geist et al.* [2009], *Locat et al.* [2009]
[2] *Bugge et al.* [1988]
[3] *Borrero et al.* [2001], *Fisher et al.* [2005], *Greene et al.* [2006]
[4] *Edwards et al.* [1995], *Lee et al.* [2004], *Greene et al.* [2006]

[5] *Hasegawa and Kanamori* [1987], *Nisbet and Piper* [1998], *Fine et al.* [2005], *Mosher and Piper* [2007]
[6] *Okal et al.* [2003], *Fryer et al.* [2004], *Watts et al.* [2005]
[7] *Beget* [2007], *Ryan et al.* [2010], *Haeussler et al.* [2014]
[8] *Schwing and Norton* [1990], *Ma et al.* [1991]
[9] *Synolakis et al.* [2002], *Sweet and Silver* [2003], *Watts et al.* [2005]
[10] *Yalciner et al.* [2002], *Watts et al.* [2005]
[*] *Geist et al.* [2009]
[**] *Borrero et al.* [2001]
[***] *Blum and Zumberge* [2006]

APPENDIX B. MOMENTUM BALANCE CONDITION

Consider an infinite slope $y < h$ with x-axis located along the potential shear band ($y = 0$, $0 < x < l$), which is parallel to the slope surface $y = h$ (similar to Figure 2a). The surface has the angle of α with the horizontal, and we assume that the pressure $P(x, y)$ in the slope body can be represented as hydrostatic plus the overpressure, $\Delta P(y)$, which depends only on depth. This assumption is reasonable for mild slopes, and we have

$$P(x,y) = P_0 + \rho_w g(x\sin\alpha - y\cos\alpha) + \Delta P(y) \qquad \text{(B.1)}$$

where $P_0 = P(0, 0)$ is the pore pressure at $x = 0$, $y = 0$, and $\Delta P(h) = 0$, so that the pressure is hydrostatic on the slope surface. The equilibrium conditions in terms of the total stresses s_x, s_y, and s_{xy} read [*Timoshenko and Goodier*, 1970]

$$\frac{\partial s_x}{\partial x} + \frac{\partial s_{xy}}{\partial y} = -\rho_0 g\sin\alpha, \qquad \frac{\partial s_{xy}}{\partial x} + \frac{\partial s_y}{\partial y} = \rho_0 g\cos\alpha \qquad \text{(B.2)}$$

Even through the stress field in the slope body can be non-uniform [e.g., *Picarelli et al.*, 2000], the conventional assumption made for infinite slopes is that the effective stress, $s'_x = s_x + P$ and $s'_y = s_y + P$, are independent of x and are functions of depth only [e.g., *Davis and Selvadurai*, 1996]. With this assumption, equations (B.2) become

$$\frac{\partial s_{xy}}{\partial y} = -(\rho_0 - \rho_w)g\sin\alpha, \qquad \frac{\partial s_{xy}}{\partial x} + \frac{\partial s'_y}{\partial y} = (\rho_0 - \rho_w)g\cos\alpha + \frac{\partial(\Delta P)}{\partial y} \qquad \text{(B.3)}$$

and should be integrated with the boundary conditions $s_{xy} = 0$, $s_y = -P(x, h)$ (or $s'_y = 0$) at the slope surface, $y = h$. We then have

$$s_{xy}(y) = -(\rho_0 - \rho_w)gy\sin\alpha, \quad s'_y(y) = (\rho_0 - \rho_w)g(y-h)\cos\alpha + \Delta P(y) \qquad \text{(B.4)}$$

Stress s'_x cannot be defined in the infinite slope model.

When the shear band appears, the motion of the sliding layer, overlying the shear band, is described in terms of the averaged values in (2.1). For the arbitrary layer segment between $x = a$ and $x = b$ ($0 < a < b < l$), the momentum balance (Second Law) condition $F_x = d(mv_x)/dt$ in the x direction (along the slope) can be written as

$$\int_0^h [\sigma_x(b,y,t) - \sigma_x(a,y,t)]dy - \int_a^b (\tau_r + \tau_w)dx + g\sin\alpha \int_a^b dx \int_0^h \rho_0 dy = \frac{d}{dt}\int_a^b dx \int_0^h \rho_0 v_x dy \qquad \text{(B.5)}$$

where $v_x = \partial u_x/\partial t$, m is the layer mass in segment (a, b), and F_x is the x-component of the resultant force acting on segment (a, b). Pressure at the bottom of the sliding layer is either zero (if the ambient water does not infiltrate the shear band) or it does not contribute to F_x (since it acts in the y-direction perpendicular to the layer). Taking into account that ρ_0 is constant (homogeneous sediment) and using (2.1), equation (B.5) rewrites as

$$\int_a^b \frac{\partial \sigma}{\partial x}dx + \frac{1}{h}\int_a^b \tau_0 dx = \rho_0 \int_a^b \frac{\partial^2 u}{\partial t^2}dx \qquad \text{(B.6)}$$

where $\tau_0 = \tau_g - \tau_r - \tau_w$ with $\tau_g = \rho_0 g h \sin\alpha$. Given that a and b are arbitrary, equation (B.6), is equivalent to (2.3).

Until this point, we used assumptions of constant α, h, and ρ_0, but did not use any constitutive relations. We now specify that the layer material is poroelastic, so that the constitutive relation along the layer can be written as [*Detournay and Cheng*, 1993; *Wang*, 2000]

$$2G\partial u_x/\partial x = (1-\nu)(\sigma_x' - s_x') - \nu(\sigma_y' - s_y') + (\alpha - 1)(1-2\nu)\delta P \qquad \text{(B.7)}$$

where $G = (E_0/2)/(1 + \nu)$ is the shear modulus, α is the Biot coefficient, δP is the pressure change with respect to the initial pressure, P, in (B.1), and, as discussed in the main text, strains are considered zero at the initial state of the infinite slope (when $\sigma_x' = s_x'$, $\sigma_y' = s_y'$, and $\delta P = 0$). Typically, soils and soft sediment materials, Biot coefficient $\alpha = 1$ [e.g., *Detournay and Cheng*, 1993; *Wang*, 2000]. Hence, the last term in (B.7) is negligible.

For a long, thin sliding layer (Figure 2), we further assume, as common in landslide models based on the shear band concept [*Palmer and Rice*, 1973; *Chowdhury*, 1978; *Puzrin and Germanovich*, 2005a; *Puzrin et al.*, 2010; *Quinn et al.*, 2011a; *Dey et al.*, 2012], that

$$\sigma_y' = s_y' \qquad \text{(B.8)}$$

in the layer above the shear band. Averaging (B.7) across the layer and using (2.1) gives

$$\sigma + p = \frac{E_0}{1-\nu^2}\frac{\partial u}{\partial x} - p_0, \qquad p_0 = \frac{1}{h}\int_0^h s'_x(y)dy = \text{const} \tag{B.9}$$

which aggress with (2.2).

Substituting (B.9) in (2.3) results in

$$\rho_0 \frac{\partial^2 u}{\partial t^2} = \frac{\tau_0}{h} + E\frac{\partial^2 u}{\partial x^2} - \frac{\partial p}{\partial x} \tag{B.10}$$

so taking into account that due to (B.1),

$$p(x) = \frac{1}{h}\int_0^h P(x,y)dy = P_0 + \rho_w g\left(x\sin\alpha - \frac{h}{2}\cos\alpha\right) + \Delta p \tag{B.11}$$

where

$$\Delta p = \frac{1}{h}\int_0^h P(y)dy \tag{B.12}$$

is the thickness-averaged excess pore pressure, we finally arrive at (2.4).

On the shear band (except a small tip zone), $\tau_r = -\mu\sigma'_y(0)$, where μ is the coefficient of residual friction between the shear band sides. Hence, due to (B.8) and (B.4),

$$\tau_r = -\mu s'_y(0) = -\mu(\rho_0 - \rho_w)\, g\, (y-h)\cos\alpha - \mu\Delta P(0) \tag{B.13}$$

so that

$$\tau_* = (\rho_0 - \rho_w)(g\sin\alpha - \mu\cos\alpha)h - \tau_w + \mu\Delta P(0) \tag{B.14}$$

in (2.4), (2.5). Therefore, the hydrostatic part of the initial pore pressure, $P(x, y)$ in (B.1), is the source of the buoyancy term $\tau_b = \rho_w g h\sin\alpha$ in (2.5). Equation (2.5) follows from (B.10) in the absence of the overpressure ($\Delta P(0) = 0$) on the shear band.

APPENDIX C. PROPAGATION CONDITION AT THE BAND TIP

In plane strain, the energy flux to the shear band tip [*Cherepanov*, 1979; *Freund*, 1998]

$$F(\Gamma) = \int_\Gamma \left[\sigma_{ij}n_j\frac{\partial u_i}{\partial t} + (U+K)vn_x\right]ds \tag{C.1}$$

where v us the propagation velocity of the band tip, Γ is the arbitrary, simple, closed contour surrounding the tip (solid line in Figure C.1), u_i and σ_{ij} are the displacement and stress

components, respectively, in the x, y coordinate set aligned with the propagation direction (Figure 2b), $i, j = x, y$, n_i is the external normal to contour, U and K are the elastic and kinetic energy densities (per unit volume), respectively, the integration direction in (C.1) is counter-clockwise, and repeating indices indicate summation of x and y components. Quantity F is the total energy flux through contour Γ per unit width in the direction perpendicular to the plain of drawing in Figure C.1. In dynamics, integral F in (C.1) is path dependent, but when Γ is shrunk to the fracture tip, it gives the total energy flux to the tip [*Kostrov and Das*, 1975]. In the 1-D case under consideration, instead of shrinking Γ, we pass to the limit of $x \to l - 0$, which results in the outer asymptote for F considered as a function of the small parameter h/l. The inner asymptote is given by the corresponding semi-infinite crack is the half-plane. The inner and outer asymptotes differ by higher order terms with respect to $h/l << 1$ [*Dyskin et al.*, 2000], so below we consider the 1-D sliding layer (above the shear band) and the limit of $x \to l - 0$ in evaluating F. The energy release rate is then defined by $J = F/v$.

As in *Palmer and Rice* [1973], we choose contour Γ with the upper boundary at $y = h$, while the other three boundaries are located far (compared to h), but not too far (compared to l) from the band tip (dashed line in Figure C.1). The left vertical line below the band and the right vertical line do not contribute to the integral in (C.1) because on these lines, $\partial u_i/\partial t = 0$ and $U = K = 0$. The lower horizontal line (below the band) does not contribute to (C.1) because $\partial u_i/\partial t = 0$ and $n_x = 0$ on this line. The top horizontal part of Γ (located on the slide surface) also does not contribute to (C.1) as $\sigma_{ij} n_j = 0$ and $n_x = 0$ there. Hence, the leading term in integral (C.1) is due to the left vertical, dashed line above the shear band (Figure C.1). Because on this line, $n_x = 1$, (C.1) simplifies to

$$F(\Gamma) = \int_h^0 \left[\sigma_{xx} \frac{\partial u_x}{\partial t} + (U + K) v \right] dy \qquad \text{(C.2)}$$

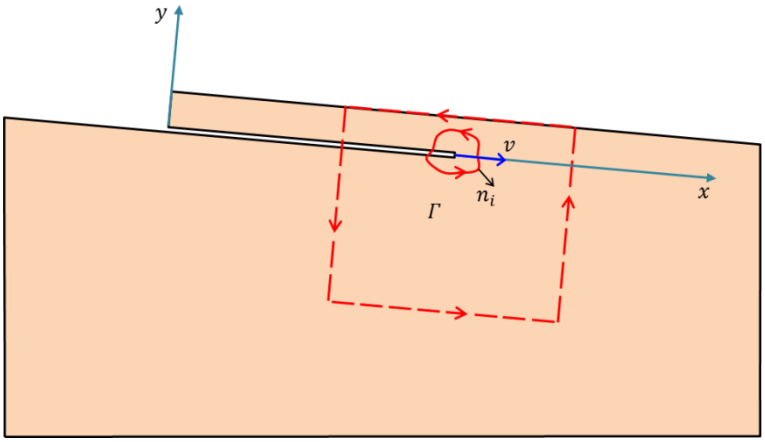

Figure C.1. Integration contours for deter-mining the energy flux (C.1) to the tip of a propagating shear band.

For the sliding 1-D layer (Figure 2 and Figure C.1), $\sigma_{xx} = \sigma$, $u_x = u$, and (C.2) reads as

$$F = -h\sigma\eta - hv(U + K) \tag{C.3}$$

where

$$U(x,t) = \int_0^\gamma \sigma d\gamma = \int_0^\gamma (E\gamma - p_0)d\gamma = \frac{E\gamma^2}{2} - p_0\gamma, \quad K(x,t) = \frac{\rho_0\eta^2}{2} \tag{C.4}$$

strain $\gamma(x, t) = \partial u/\partial x$, material velocity $\eta(x, t) = \partial u/\partial t$, and we took into account that $\rho_0 c^2 = E$. Finally, applying in (C.2) Hooke's law (2.2), boundary condition (2.7), and (C.3) yields

$$F = -h(E\gamma - p_0)\eta - hv\left(\frac{E\gamma^2}{2} - p_0\gamma + \frac{\rho_0\eta^2}{2}\right) = v\frac{hE}{2}\gamma^2\left(1 - \frac{\rho_0}{E}v^2\right) \tag{C.5}$$

where p_0 cancelled out due to (2.7).

That integral in (C.1) is path dependent can be seen directly from (C.5) where F is a function of x. Yet, as mentioned above, F is the total energy flux through contour Γ, so that, the energy release rate J is obtained using (C.5) (in the limit of $x \to l$) and the definition of $J = F/v$. Given $J = J_c$, this results in condition (2.9) at the tip of a propagating band. In obtaining (C.5) and $J = J_c$, we only accounted for the displacement of the upper side of the shear band because for $l/h >> 1$, displacement of the lower side only contributes to the higher terms in J. *Dyskin et al.* [2000] showed this for a static fracture parallel to the half-space surface, but their result also holds in the dynamic case. Hence, we followed others [*Palmer and Rice*, 1973; *Chowdhury*, 1978; *Hellan*, 1984; *Freund*, 1998; *Dyskin et al.*, 2000; *Chowdhury et al.*, 2010; *Quinn et al.*, 2011a; *Dey et al.*, 2012; *Quinn et al.*, 2012] and ignored displacement of the lower band side.

Accordingly, in this work, we also employ the earthquake (fault rupture) mechanics terminology and refer to u as relative displacement or slip and to $\eta = \partial u/\partial t$ as slip velocity or slip rate.

The local energy balance condition (2.9) can also be obtained by employing the global energy balance criterion [*Palmer and Rice*, 1973; *Rice*, 1973; *Puzrin and Germanovich*, 2005a] for the moving (or "growing") 1-D layer (slide). Let $u(x, t)$ be the longitudinal displacement when the shear band has length $l = l(t)$ (Figure 2a). When time changes from t to $t + \Delta t$, the band length changes from l to $l + \Delta l$, and for small Δt, the displacement change is

$$\Delta u = u\left(x,t+\Delta t\right)-u\left(x,t\right)=\Delta t\frac{\partial u(x,t)}{\partial t}+O(\Delta t^2) \qquad (0<x<l) \tag{C.6}$$

The increments of work done on the layer above the band over Δu by $\tau = \tau_g - \tau_r - \tau_w$ and by p_a (at $x = 0$) are

$$\Delta W_\tau = \int_0^{l+\Delta l} \tau(x,t)\Delta u\, dx\,, \quad \Delta W_a = hp_a\eta(0,t)\Delta t \tag{C.7}$$

where $\Delta l = v\Delta t$. Taking into account that at time t, there is no displacement outside the interval of $(0, l)$ and using (C.6) yields

$$\begin{aligned}\int_0^{l+\Delta l} \tau(x,t)\Delta u\, dx &= \int_0^{l} \tau(x,t)\Delta u\, dx + \int_l^{l+\Delta l} \tau(x,t)u(x,t+\Delta t)\, dx \\ &= \Delta t\int_0^{l} \tau(x,t)\frac{\partial u(x,t)}{\partial t}\, dx + \tau(l,t)u(l,t)\Delta l + O(\Delta t)^2\end{aligned} \tag{C.8}$$

Considering then (C.7) and (C.8) results in work

$$\Delta W = \Delta W_\tau + \Delta W_a = \Delta t\int_0^{l} \tau(x,t)\eta(x,t)\, dx + hp_a\eta(0,t)\Delta t + O(\Delta t)^2 \tag{C.9}$$

done by τ over Δu.

Because at time t, $\partial u/\partial t = 0$ for $x \in (l, l + \Delta l)$, the corresponding change of the kinetic energy of the sliding layer can be expressed as

$$\begin{aligned}\Delta K &= \frac{\rho_0 h}{2}\int_0^{l+\Delta l}\left(\frac{\partial u(x,t+\Delta t)}{\partial t}\right)^2 dx - \frac{\rho_0 h}{2}\int_0^{l}\left(\frac{\partial u(x,t)}{\partial t}\right)^2 dx \\ &= \frac{\rho_0 h}{2}\int_0^{l}\left[\left(\frac{\partial u(x,t+\Delta t)}{\partial t}\right)^2 - \left(\frac{\partial u(x,t)}{\partial t}\right)^2\right] dx + \frac{\rho_0 h}{2}\int_l^{l+\Delta l}\left(\frac{\partial u(x,t+\Delta t)}{\partial t}\right)^2 dx\end{aligned} \tag{C.10}$$

Here

$$\left(\frac{\partial u(x,t+\Delta t)}{\partial t}\right)^2=\left(\frac{\partial u(x,t)}{\partial t}\right)^2+2\Delta t\frac{\partial u(x,t)}{\partial t}\frac{\partial^2 u(x,t)}{\partial t^2}+O(\Delta t)^2 \tag{C.11}$$

and

$$\int_l^{l+\Delta l}\left(\frac{\partial u(x,t+\Delta t)}{\partial t}\right)^2 dx=\left(\frac{\partial u(l,t)}{\partial t}\right)^2\Delta l+O(\Delta t)^2 \tag{C.12}$$

so substituting (C.11) and (C.12) into (C.10) gives

$$\Delta K=\rho_0 h\Delta t\int_0^l\frac{\partial u(x,t)}{\partial t}\frac{\partial^2 u(x,t)}{\partial t^2}dx+\frac{\rho_0 h}{2}\left(\frac{\partial u(l,t)}{\partial t}\right)^2\Delta l+O(\Delta t)^2 \tag{C.13}$$

Inserting then (C.9) and the equation of motion (2.3) in (C.13) leads to

$$\begin{aligned}\Delta K&=h\Delta t\int_0^l\eta(x,t)\left[\frac{\tau(x,t)}{h}+\frac{\partial\sigma(x,t)}{\partial x}\right]dx+\frac{\rho_0 h}{2}\eta^2(l,t)v\Delta t+O(\Delta t)^2\\&=\Delta t\int_0^l\tau(x,t)\eta(x,t)dx+h\Delta t\int_0^l\eta(x,t)\frac{\partial\sigma(x,t)}{\partial x}dx+\frac{\rho_0 h}{2}\eta^2(l,t)v\Delta t+O(\Delta t)^2\end{aligned} \tag{C.14}$$

The change of the elastic (internal) energy can be represented as

$$\begin{aligned}\Delta W_i&=h\int_0^{l+\Delta l}dx\int_0^{\gamma(x,t+\Delta t)}\sigma(\gamma)d\gamma-h\int_0^l dx\int_0^{\gamma(x,t)}\sigma(\gamma)\,d\gamma\\&=h\int_0^l dx\int_{\gamma(x,t)}^{\gamma(x,t+\Delta t)}\sigma(\gamma)\,d\gamma+h\int_l^{l+\Delta l}dx\int_0^{\gamma(x,t+\Delta t)}\sigma(\gamma)\,d\gamma\end{aligned} \tag{C.15}$$

where

$$\int_l^{l+\Delta l}dx\int_0^{\gamma(x,t+\Delta t)}\sigma(\gamma)\,d\gamma=\Delta l\int_0^{\gamma(l,t)}\sigma(\gamma)d\gamma+O(\Delta t)^2 \tag{C.16}$$

and

$$\int_{\gamma(x,t)}^{\gamma(x,t+\Delta t)}\sigma(\gamma)d\gamma=\sigma(\gamma(x,t))\frac{\partial\gamma(x,t)}{\partial t}\Delta t+O(\Delta t)^2 \tag{C.17}$$

Substituting further (C.16) and (C.17) in (C.15) results in

$$\Delta W_i=h\Delta t\int_0^l\sigma(\gamma(x,t))\frac{\partial\gamma(x,t)}{\partial t}dx+hv\Delta t\int_0^{\gamma(l,t)}\sigma(\gamma)\,d\gamma+O(\Delta t)^2 \tag{C.18}$$

Integrating the first and the second integrals in (C.18) by parts, we obtain

$$\int_0^l \sigma(\gamma(x,t))\frac{\partial\gamma(x,t)}{\partial t}dx = \int_0^l \frac{\partial\eta(x,t)}{\partial x}\sigma(x,t)\,dx$$

$$= \eta(l,t)\sigma(l,t) - \eta(0,t)\sigma(0,t) - \int_0^l \eta(x,t)\frac{\partial\sigma(x,t)}{\partial x}dx \qquad \text{(C.19)}$$

$$= -v\gamma(l,t)\sigma(l,t) - \eta(0,t)(-p_a) - \int_0^l \eta(x,t)\frac{\partial\sigma(x,t)}{\partial x}dx$$

and

$$\int_0^{\gamma(l,t)} \sigma(\gamma)\,d\gamma = \sigma(l,t)\gamma(l,t) - \int_{p_0}^{\sigma(l,t)} \gamma(\sigma)d\sigma \qquad \text{(C.20)}$$

respectively, where we applied in (C.19) the boundary conditions (2.7) and $\sigma(0, t) = -p_a$ at the layer ends. Substituting next (C.19) and (C.20) into (C.18) yields

$$\Delta W_i = h\Delta t\left[\eta(0,t)p_a - v\int_{-p_0}^{\sigma(l,t)} \gamma(\sigma)d\sigma - \int_0^l \eta(x,t)\frac{\partial\sigma(x,t)}{\partial x}dx\right] + O(\Delta t)^2 \qquad \text{(C.21)}$$

Finally, the energy dissipated at the tip of the shear band (Figure 3b) when it propagates distance Δl is given by

$$\Delta U_S = \Delta l\int_0^{\delta_r}[\tau(\delta) - \tau_r]d\delta = J_c\Delta l \qquad \text{(C.22)}$$

The energy conservation suggests that the work done on the body by external forces equals to the energy change. In the absence of heat transfer and pressure dissipation processes, the energy balance condition

$$\Delta W_i + \Delta K + \Delta U_S = \Delta W_\tau + \Delta W_a \qquad \text{(C.23)}$$

can be rewritten combining energy terms (C.9), (C.14), and (C.21) as

$$\underbrace{\Delta t\int_0^l \tau(x,t)\eta(x,t)\,dx + h\Delta t p_a \eta(0,t)}_{\Delta W_\tau + \Delta W_a}$$
$$\underbrace{-h\Delta t\left\{\eta(0,t)\,p_a - v\int_{-p_0}^{\sigma(l,t)}\gamma(\sigma)d\sigma - \int_0^l \eta(x,t)\frac{\partial\sigma(x,t)}{\partial x}dx\right\}}_{\Delta W_i} \qquad \text{(C.24)}$$
$$\underbrace{-\Delta t\left\{\int_0^l \tau(x,t)\eta(x,t)dx + h\int_0^l \eta(x,t)\frac{\partial\sigma(x,t)}{\partial x}dx + v\frac{\rho h}{2}\eta^2(x,t)\right\}}_{\Delta K} + O(\Delta t)^2 = \underbrace{\Delta l J_c}_{\Delta U_S}$$

Collecting terms in (C.24) and taking into account that $\Delta l = v\Delta t$ reveals the condition

$$h\int_{-p_0}^{\sigma(l,t)}\gamma(\sigma)d\sigma - \frac{\rho_0 h}{2}\eta^2(l,t) = J_c \qquad \text{(C.25)}$$

at the tip of dynamically propagating shear band. This condition is valid both for linear (2.2) and nonlinear constitutive laws $\gamma(\sigma)$. In the linear case, using Hooke's law (2.2) and the boundary condition (2.7) in (C.25) results in

$$\frac{hE}{2}\gamma^2(l,t) - \frac{\rho_0 h}{2}v^2\gamma^2(l,t) = J_c \qquad \text{(C.26)}$$

which, given that $E/\rho_0 = c^2$, is equivalent to (2.9).

APPENDIX D. POSSIBILITY OF CONTINUOUS SOLUTION

It may appear that it is possible to illuminate the discontinuity by simply allowing $n = 1$ in (2.12), which corresponds to $\gamma_c = \gamma_0$. We then have $\gamma^-(B) = \gamma(B)$ and $\eta^-(B) = \eta(B)$, so that (4.2) with (4.3) result in

$$\gamma(D) - \frac{\eta(D)}{c} - \gamma_s(x_B) = -\frac{1}{h}\int_{x_B}^{l} T(x, t_B + (x-l)/c)dx \qquad \text{(D.1)}$$

where $D(l, t)$ corresponds to the propagating tip (Figure 4). Substituting the dynamic fracture condition in (3.4) together with (4.4) in (4.2), results in equation

$$\sqrt{\frac{1+v_1/c}{1-v_1/c}} = -\frac{\gamma_s(l)}{\gamma_0} \qquad \text{(D.2)}$$

for the band tip velocity v_1. From here,

$$v_1(l) = \frac{dl}{dt} = c\frac{\gamma_s^2(l) - \gamma_0^2}{\gamma_s^2(l) + \gamma_0^2} \qquad \text{(D.3)}$$

which can also be formally obtained by replacing γ_c with γ_0 in (4.7).

It is impossible, however, to make the next step and integrate (D.3) in order to obtain $t(l)$ using (4.6). Indeed, the integral in (4.6) diverges for any $l > l_0$ when $\gamma_c = \gamma_0$, which indicates the infinite time required for the shear band to reach velocity $v_1(l)$. The reason for this effect is that both $dl/dt = 0$ and $d^2l/dt^2 = 0$ at $t = 0$ for dl/dt defined by (D.3). Because both the velocity and acceleration are zeroes at the initial moment, the shear band effectively does not grow and the infinite time is required to propagate the band to any length $l > l_0$.

Therefore, while the continuous solution can be formally written as a function of l, it does not exist on the (x, t) plane when $\gamma_c = \gamma_0$ (or $n = 1$). The obtained solution with propagating discontinuities, however, is stable and models reasonably well the dynamic propagation of a shear band.

APPENDIX E. RECURRENCE SOLUTION

Consider the general case of the shear band propagation starting at time of t_A when it has the length of l_A, that is, at point A in Figure E.1, where the discontinuity reflects or initiates from the band tip. Let the limits of $\gamma(x, t)$ and $\eta(x, t)$ when (x, t) approaches line AC (Figure E.1a) from below be $\gamma^-(x, t)$ and $\eta^-(x, t)$, respectively. Our goal is to express all unknown quantities in domain $ACFE$ through values of γ^- and η^- on AC. Then, quantities in domain $EFXL$, which is above $ACFE$ (Figure E.1a), will be found by using the solution for line EF (when approaching this line from CEF) and considering E instead of A as a starting point. Domain above line XL can be treated similarly.

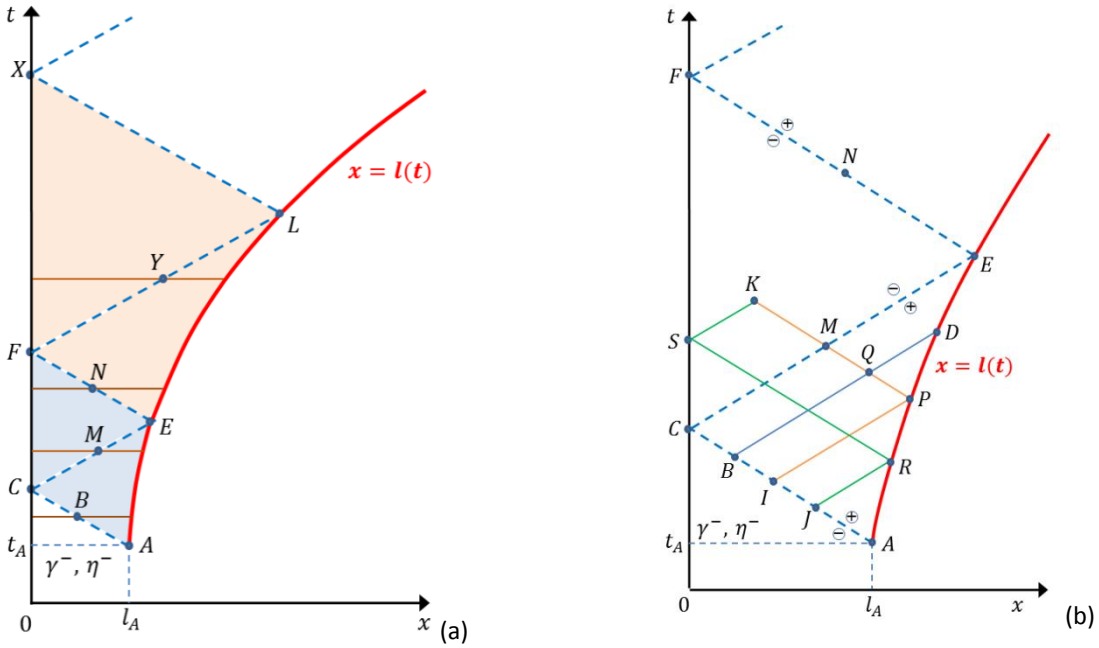

Figure E.1. (a) Discontinuity (dashed line) reflected from or initiated at point $A(l_A, t_A)$ at the band tip and reflected consequently from points *C*, *E*, *F*, *L*, and *X*. (b) Magnified view of domains *ACE* and *CEF* in (a). *Q* and *K* are the arbitrary points in *ACE* and *CEF*, respectively. Points *P*, *R*, *D* on the tip line *AE* and points *B*, *I*, *J* on the discontinuity line *AC* are connected to *Q* and *K* by the corresponding characteristics.

The discontinuity jump condition (3.5) at the arbitrary point $B(x_B, t_B)$ (Figure E.1b) on the characteristic line *AC* reads

$$\frac{\eta^+(B)}{c} - \gamma^+(B) = \frac{\eta^-(B)}{c} - \gamma^-(B) \tag{E.1}$$

Similar to (4.2), integrating (4.1) along the characteristic line *BD* and using (E.1) results in

$$\gamma(D) - \frac{\eta(D)}{c} - \gamma^-(B) + \frac{\eta^-(B)}{c} = -\frac{1}{h}\int_{x_B}^{l_D} T(x)dx \tag{E.2}$$

Using then (3.3) (second equation), (3.4) (dynamic condition) in (E.2) gives an equation for the band tip velocity, v_1, between points *A* and *E* (Figure E.1b). Similar to (4.5), (4.8), we have

$$\sqrt{\frac{1+v_1(l)/c}{1-v_1(l)/c}} = -\frac{\delta(l,B)}{\gamma_c} \tag{E.3}$$

where

$$\delta(l,B) = \gamma_s(l) - \gamma_s(x_B) + \gamma^-(B) - \eta^-(B)/c \tag{E.4}$$

and x_B is related to t_B by

$$l_A - x_B = c(t_B - t_A) \qquad (0 \le x_B \le l_A, \;\; t_A \le t_B \le t_A + l_A/c) \tag{E.5}$$

Solving (E.3) for the band tip velocity, we arrive at

$$\frac{v_1(l)}{c}=\frac{\delta^2(l,B)-\gamma_c^2}{\delta^2(l,B)+\gamma_c^2} \tag{E.6}$$

and the band length, $l(t)$, is defined by the implicit relation

$$t=t_A+\int_{l_A}^{l}\frac{dl}{v_1(l)} \tag{E.7}$$

obtained by integrating (E.6).

Strain and material velocity at the tip can be found from (E.2), using (E.6) and (3.3), as

$$\gamma_1(l)=\frac{\gamma_c^2+\delta^2(l,B)}{2\delta(l,B)},\qquad \frac{\eta_1(l)}{c}=\frac{\gamma_c^2-\delta^2(l,B)}{2\delta(l,B)} \tag{E.8}$$

In particular, for point $A(l_A, t_A)$ in Figure E.1, inserting $l = l_A$ in (E.8) yields

$$\gamma_1(l_A)=\frac{\gamma_c^2+[\gamma^-(A)-\eta^-(A)/c]^2}{2[\gamma^-(A)-\eta^-(A)/c]},\quad \frac{\eta_1(l_A)}{c}=\frac{\gamma_c^2-[\gamma^-(A)-\eta^-(A)/c]^2}{2[\gamma^-(A)-\eta^-(A)/c]} \tag{E.9}$$

If point A is the initial point where the band starts propagating and discontinuity initiates, then $t_A = 0$, $l_A = l_0$, and $\gamma^-(B)$, $\eta^-(B)$ are given by (4.3). In this case, (E.4) becomes

$$\delta(l,B)=\gamma_s(l) \tag{E.10}$$

so that expression (E.6), (E.8), and (E.9) reduce to equation (4.7), (4.9), and (4.14), respectively, while (E.7) reduces to (4.6).

Now consider the arbitrary point $Q(x, t)$ in domain ACE in Figure E.1b. Integrating (4.1) along PQ and BQ delivers

$$\begin{cases}\gamma(Q)+\dfrac{\eta(Q)}{c}-\gamma(P)-\dfrac{\eta(P)}{c}=-\dfrac{1}{h}\displaystyle\int_{l_P}^{x}T(x)dx\\[2ex] \gamma(Q)-\dfrac{\eta(Q)}{c}-\gamma^+(B)+\dfrac{\eta^+(B)}{c}=-\dfrac{1}{h}\displaystyle\int_{x_B}^{x}T(x)dx\end{cases} \tag{E.11}$$

where $\gamma(P) = \gamma_1(l_p)$, $\eta(P) = \eta_1(l_p)$, and point $P(l_P, t_P)$ is located at the crack tip line $x = l(t)$ (Figure E1.b). Using (E.1) and (E.8) with (E.11), we have for point $Q(x, t)$

$$\begin{cases}\gamma(x,t)=\eta(x,t)/c+\delta(x,B)\\[2ex] 2\dfrac{\eta(x,t)}{c}=\dfrac{\gamma_c^2}{\delta(l_P,I)}-\delta(l_P,B)\end{cases} \tag{E.12}$$

where $\delta(x, B)$ and $\delta(l_P, I)$ are defined by (E.4) with $l \to x$, $l \to l_P$, and $B \to I$. In (E.11), points B and P are related to point $Q(x, t)$ by

$$c(t - t_B) = x - x_B, \qquad c(t_B - t_A) = l_A - x_B \tag{E.13}$$

and

$$c(t_P - t) = x - l_P, \qquad t_P = t_A + \int_{l_A}^{l_P} \frac{dl}{v_1(l)} \tag{E.14}$$

respectively. Point $I(l_I, t_I)$ is obtained from

$$c(t_P - t_I) = l_P - x_I\,, \qquad c(t_I - t_A) = l_A - x_I \tag{E.15}$$

Next, consider the arbitrary point $K(x, t)$ in domain CEF and the corresponding point $P(l_P, t_P)$ at the crack tip $x = l(t)$ (Figure E.1b). The characteristic line PK crosses line CE of the reflected discontinuity at point $M(x_M, t_M)$. Since the strain and material velocity and their derivatives have continuous values in the regions above and below CE, it is permissible to integrate (4.1) from P to M and from M to K separately and then sum up the resulting equations. This yields

$$\gamma(K) + \frac{\eta(K)}{c} - \gamma(P) - \frac{\eta(P)}{c} + \gamma^+(M) - \gamma^-(M) + \frac{\eta^+(M) - \eta^-(M)}{c} = -\frac{1}{h}\int_{l_P}^{x} T(x)dx \tag{E.16}$$

Using then condition (3.5) on discontinuity CE (i.e., $dt/dx = 1/c$) results in

$$\gamma(K) + \frac{\eta(K)}{c} - \gamma(P) - \frac{\eta(P)}{c} = -\frac{1}{h}\int_{l_P}^{x} T(x)dx \tag{E.17}$$

which shows that the discontinuity does not contribute to the result of the integration. In other words, crossing the discontinuity line does not affect the characteristic equation.

Therefore, for point S ($x = 0$), where the wave, started from R ($x = l(t)$), reflects back to arrive at K, it is possible to simply integrate (4.1) along RS. We then find the material velocity at S

$$\frac{\eta(S)}{c} = \frac{\gamma_c^2}{\delta(l_R, J)} - \gamma_s(l_R) \tag{E.18}$$

where point J is defined from (E.14) and (E.15) with (t_P, l_P) and (t_I, l_I) replaced by (t_R, l_R) and (t_J, l_J), respectively, while $\delta(l_R, J)$ is given by (E.4) with $l \to l_R$, $B \to J$. Then, for the arbitrary point $K(x, t)$ in CEF, integrating (4.1) along characteristics PK and SK yields

$$\begin{cases} 2\gamma(x,t) = \dfrac{\gamma_c^2}{\delta(l_P, I)} - \gamma_s(l_P) + \gamma_s(l_R) - \dfrac{\gamma_c^2}{\delta(l_R, J)} + 2\gamma_s(x) \\ 2\dfrac{\eta(x,t)}{c} = \dfrac{\gamma_c^2}{\delta(l_P, I)} - \gamma_s(l_P) + \dfrac{\gamma_c^2}{\delta(l_R, J)} - \gamma_s(l_R) \end{cases} \tag{E.19}$$

When point A coincides with the initial position of the crack tip (i.e., $t_A = 0$, $l_A = l_0$), per (E.10), $\delta(l_R, J) = \gamma_S(l_R)$, $\delta(l_P, I) = \gamma_S(l_P)$, and equations (E.12) and (E.19) reduce to (4.13) and (4.15), respectively.

Equation (E.1) through (E.19) are valid until the discontinuity, propagating along CE, reaches the band tip at point $E(l_E, t_E)$. The position of E is given by

$$t_E = t_A + \int_{l_A}^{l_E} \frac{dl}{v_1(l)}, \qquad c(t_E - t_A) = l_E + l_A \tag{E.20}$$

Solution (E.19) enables finding γ and η at the arbitrary point $K(x, t)$ in CEF. Hence, considering the limits of $l_P \to l_E$ and $l_I \to l_C$ for the arbitrary point N on the discontinuity line EF (Figure E.1b), we find

$$\begin{cases} 2\gamma^-(N) = \dfrac{\gamma_c^2}{\delta(l_E, C)} - \gamma_s(l_E) + \gamma_s(l_R) - \dfrac{\gamma_c^2}{\delta(l_R, J)} + 2\gamma_s(x_N) \\ 2\dfrac{\eta^-(N)}{c} = \dfrac{\gamma_c^2}{\delta(l_E, C)} - \gamma_s(l_E) + \dfrac{\gamma_c^2}{\delta(l_R, J)} - \gamma_s(l_R) \end{cases} \tag{E.21}$$

where $\delta(l_E, C)$ is given by (E.4) with l and B replaced by l_E and C, respectively.

Equations (E.21) can now be utilized as the "initial" conditions to find the solution in domain $EFXL$ (Figure E.1a) directly from (E.6), (E.8), (E.9), (E.12), and (E.19) simply by renaming the unknowns. The initial values of γ^- and η^- (when $l_A = l_0$, $t_A = 0$) are given by (4.3). This establishes the recurrence relations for finding the solution everywhere (Figure E.1a).

APPENDIX F. ARRIVAL OF THE DISCONTINUITY AT THE SHEAR BAND TIP

If the discontinuity propagating along CE in Figure 4 reaches the shear band tip, it reflects and propagates again towards $x = 0$. Whether this indeed happens can be characterized by considering the difference

$$\Delta t(x) = \frac{2}{c}\left[l_0 - \gamma_c^2 \int_{l_0}^{x} \frac{dl}{\gamma_s^2(l) - \gamma_c^2} \right] \tag{F.1}$$

between the arrival times of the discontinuity ($t = (l_0 + x)/c$) and the band tip ($t(x)$ in (4.6) with $l = x$) to a given location x (Figure 4a and Figure 4b). Because $\gamma_s^2(l) - \gamma_c^2$ monotonically increases with l, $\Delta t(x)$ in (F.1) monotonically decreases. Hence, the necessary and sufficient condition for *AE* and *CE* to intersect (Figure 4) is given by

$$\delta t = \lim_{x\to\infty} \Delta t(x) = \frac{2}{c}\left[l_0 - \gamma_c^2 \int_{l_0}^{\infty} \frac{dl}{\gamma_s^2(l) - \gamma_c^2} \right] < 0 \tag{F.2}$$

If condition (F.2) is not satisfied (e.g., for $\Delta t \to 0$ as $x \to \infty$), the discontinuity will never reach the band tip (Figure 6a). In this case, while the tip remains slower ($v < c$), its velocity, v, approaches the discontinuity velocity, c, and it has the head start, $x = l_0$, large enough to always remain ahead the discontinuity (Figure 4b). For this to happen, the integral in (F.2) must converge, which depends, essentially, on the distribution of $T(x, t)$. For example, for the integral to converge, it is sufficient if $|\gamma_1(l)|$ increases with l faster than $\sqrt{l}$ as $l \to \infty$. This is probably typical for many practical cases, but not sufficient for (F.2) to be satisfied. Then the discontinuity always lags behind the band tip.

In the case of the homogeneous distribution (5.1), the dimensionless form $\delta\tau = (c/l_0)\delta t$ of (F.2) is given by using (5.6) (with $\lambda = \xi$) and $\Gamma_s(\lambda)$ from (5.7). In this case,

$$\delta\tau = \lim_{\xi\to\infty} \Delta\tau(\xi) = 2 - \frac{\lambda_*}{\sqrt{n}} \ln\left(1 + \frac{2}{\sqrt{n} - 1} \right) \tag{F.3}$$

where $\delta\tau \geq 0$ corresponds to the case of the discontinuity reflected from $x = 0$ that would never catch up with the band tip. This depends upon two parameters, λ_* and n. As discussed in Section 4.4, $0 \leq \lambda_* \leq 1$, and $1 < n < 2$ is the range of primary interest in applications.

Contours of $\delta\tau(n, \lambda_*)$ for the domain of $0 \leq \lambda_* \leq 1$ and $1 < n < 2$ are shown in Figure F.1a. We observe that the region of $\delta\tau \geq 0$ (above the line of $\delta\tau = 0$) occupies most of this domain. In particular, $\delta\tau \geq 0$ for $n \geq 1.4392$, and the entire range of $0 \leq \lambda_* \leq 1$, for $n \geq 1.231$ and $0 \leq \lambda_* \leq 0.75$, and for $n \geq 1.067$ and $0 \leq \lambda_* \leq 0.5$. For $\lambda_* = 0.75$ and $n = 1.23$, the lines of discontinuity and band tip intersect, but only at $\xi = 259$. In most practical cases, such lines can

be considered not intersecting since the band propagation will probably end before it reaches the length of $259l_0$ for other reasons such as the passive failure near the band tip.

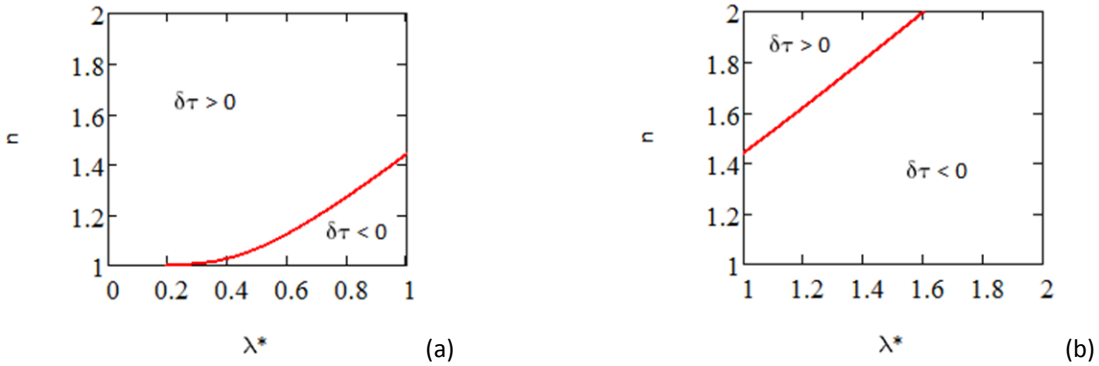

Figure F.1 Contours of $\delta\tau(n, \lambda_*)$ for the domain of $1< n < 2$, and (a) $0 \le \lambda_* \le 1$ and (b) $1 \le \lambda_* \le 2$ (Section 10.1). Region $\delta\tau \ge 0$ corresponds to the case of reflected discontinuity that would be "chasing" the shear band tip, but would never catch up with it (Figure 4b). The discontinuity would not ever reach the band tip also for the points on line $\delta\tau = 0$. For a smaller region $\delta\tau < 0$ below the line of $\delta\tau = 0$ in (a), the shear band does reach the band tip (Figure 4), but this may happen too far in the propagation process (e.g., at $\xi = l/l_0 = 259$ for $\lambda_* = 0.75$ and $n = 1.230$) to be physically unrealistic. In (b), this region of $\delta\tau < 0$ is considerably larger, however.

If the reflected discontinuity catches up with the band tip E (Figure 4), it reflects and propagates back to the slope end $x = 0$ where it reflects again and starts once more "chasing" after the band tip (Figure 6). To characterize the possibility for the discontinuity to actually reach the tip for the second time, we follow the above approach and consider the difference between the second arrival time of the discontinuity ($t = t_E + (l_E + x)/c$) and the band tip ($t(x)$ in (4.6) with $l = x$) to a given location x (where l_E is found from (4.20) and l_R from (4.16) or (4.23)). In dimensionless form, this difference writes as

$$\Delta\tau(\xi) = 2\left[\xi - \lambda_E - \int_{\lambda_E}^{\xi} \frac{d\lambda}{n[\Gamma_s(\lambda_R) + \Gamma_s(\lambda) - 1/(n\Gamma_s(\lambda_R))]^2 - 1}\right] \qquad \text{(F.4)}$$

with $\Gamma_s(\lambda) = -1 - (\lambda - 1)/\lambda_*$ from (5.7) in the case of the homogeneous loading (5.1). Parameters $\lambda_R(\lambda, \tau) = l_R/l_0$ and $\lambda_E = l_E/l_0$ are defined from (G.18) and (G.16) (Appendix G), respectfully, and λ and τ are related by $\tau = \tau_E + \lambda_E + \lambda$ with τ_E from (G.16) (Appendix G).

Numerical integration in (F.4) represents no difficulty. The ranges of λ_* and n, satisfying condition $\Delta\tau(\xi) > 0$ in (F.4), which implies that the discontinuity does not arrive at the band tip, cover a broader domain than $\Delta\tau > 0$ in (F.2) for the first reflection at the band tip. In particular,

if $n \geq 1.04$, $\Delta\tau \geq 0$ for the entire range of $0 \leq \lambda_* \leq 1$ and $0 \leq \lambda \leq 10^3$ as long as $\xi \leq 10^3$. We chose this upper limit because for all intents and purposes, it can be considered that the shear band propagation will end (with global failure) before its length reaches $\lambda = 10^3$. Similarly, $\Delta\tau \geq 0$ for $0 \leq \lambda_* \leq 0.75$ when $1 \leq \xi \leq 10^3$, if $n \geq 1.02$, for $0 \leq \lambda_* \leq 2$ if $n \geq 1.195$, and for $0 \leq \lambda_* \leq 1.5$ if $n \geq 1.10$.

For the dynamic version of *Palmer and Rice*'s [1973] model (Section 10.1), the range of λ_* is broader as in this case, it can be both $0 \leq \lambda_* \leq 1$ and $\lambda_* \geq 1$. The possibility of the discontinuity to arrive at the band tip for the first time is still described by (F.4), however. In particular, Figure F.1a still covers the case of $0 \leq \lambda_* \leq 1$. The case of $\lambda_* \geq 1$ is shown in Figure F.1b. As can be observed, the domain of discontinuity reaching the band tip ($\Delta\tau < 0$) is considerably larger than that of not reaching ($\Delta\tau \geq 0$). For example, if the discontinuity does not arrive to the tip ($\delta\tau \leq 0$) prior to $\xi = 10^3$ for $\lambda_* > 1.605$, and the entire range of $1 < n < 2$ used in Figure F.1b, or for $1 < n < 1.43$, and any $\lambda_* > 1$.

APPENDIX G. FIRST TWO TERMS IN THE RECURRENCE SOLUTION

Appendix E offers the recurrence solution to the dynamic problem under consideration (Figure 2). Using the solution for domain *ACFE*, we obtain below explicit expressions for $\gamma(x, t)$ and $\eta(x, t)$ in domain *EFXL* (Figure E.1a) with the initial conditions (4.3). These expressions are given in Section 4.3 and used in examples presented in Section 5.3.

Domain *EFXL* can also be seen in Figure G.1b (point *X* is not shown in Figure G.1a). Domain *ACFE* in Figure E.1a corresponds to domain *ACFE* in Figure G.1a, where $A(l_0, 0)$ is the point where the dynamic growth initiates. Line *AE* represents the band tip locations before the discontinuity, initiated at *A*, first arrives at the band tip at *E*. The solution in *ACFE* is simply the "zero term" in the recurrence solution (Appendix E), which corresponds to the initial conditions (4.3) and described in Section 4.3. Tip line *EL* in Figure G.1a is between the first and second arrivals of the discontinuity to the band tip. Band velocities, strains, and material velocities on the tip lines *AE* and *EL* (Figure G.1a) are denoted by v_1, γ_1, η_1 and v_2, γ_2, η_2, respectively.

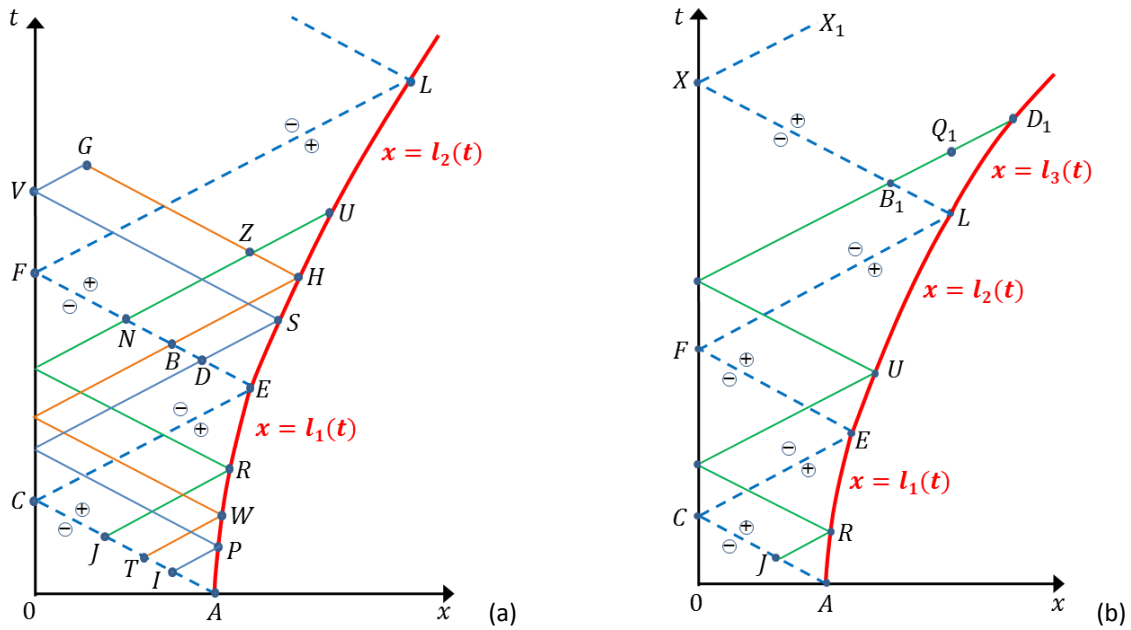

Figure G.1. (a) First two reflections of the discontinuity from the band tip. *AE* is the band tip line, $x = l(t)$, before the discontinuity arrives to the tip for the first time at *E*, and *EL* is the tip line after the first arrival of the discontinuity at *E*, but before the second arrival at *L*. *U* is the arbitrary point on the tip line *EL*, while *N*, *R*, and *I* are the corresponding points on the discontinuity line *EF*, on the tip line *AE* and on the characteristic line *AC*, respectively. *G* and *Z* are the arbitrary points (with *Z* located in domain *EFL*) above and below the discontinuity line *FL*, respectively. They are related to points *H*, *S* on *EL*, points *N*, *B*, *D* on *EF*, points *R*, *W*, *P* on *AC*, and points *J*, *T*, *I* on *AC* by the corresponding characteristic lines. Points *N*, *B*, *D* on *EF* correspond to points *I*, *T*, *I* on *AE*, respectively. (b) Location of the shear band tip, $x = l_3(t)$, after the second reflections of the discontinuity from the band tip. After the discontinuity, propagating from the band tip at *L* is reflected back from the slide end, $x = 0$, at *X*, it is approaching to the moving band tip, $x = l_3(t)$, again. In this case, X_1 can be an infinite point or point that the discontinuity arrives the third times at the band tip. Point D_1 is on $x = l_3(t)$ above *L*, and corresponds to wave reflected from $x = l_2(t)$ at point *U* and $x = l_1(t)$ at point *R*.

The crack velocity at *EH* is obtained from (E.6) by changing $v_1 \to v_2$ and $B \to N$. Then,

$$\frac{v_2(l)}{c} = \frac{\delta^2(l,N) - \gamma_c^2}{\delta^2(l,N) + \gamma_c^2} \tag{G.1}$$

where point $N(x_N, t_N)$ is the arbitrary point on the discontinuity line *EF*, function $\delta(l,N)$ is defined by (E.4), and x_N and t_N are related through

$$l_E - x_N = c(t_N - t_E) \qquad (0 \le x_N \le l_E, \;\; t_E \le t_N \le t_E + l_E / c) \tag{G.2}$$

Using (E.21) with the initial condition (4.3), we obtain

$$\delta(l,N) = \gamma_s(l) + \gamma_s(l_R) - \gamma_c^2 / \gamma_s(l_R) \tag{G.3}$$

where function $\delta(l, N)$ is defined in (E.4). Equation (G.24) with (G.1) gives the tip velocity

$$\frac{v_2(l)}{c} = \frac{[\gamma_s(l) + \gamma_s(l_R) - \gamma_c^2 / \gamma_s(l_R)]^2 - \gamma_c^2}{[\gamma_s(l) + \gamma_s(l_R) - \gamma_c^2 / \gamma_s(l_R)]^2 + \gamma_c^2} \tag{G.4}$$

at *EL*, that is, after the tip is reached by the discontinuity. Here $l_R(l)$ is defined from the solution of the initial value problem in (4.19) (with l_{RU} replace by l_R) and related to point *N* by

$$\frac{l_R + x_N}{c} + \int_{l_0}^{l_R} \frac{dl}{v_1(l)} = t_N, \qquad t_N - t_E = \frac{l_E - x_N}{c} \tag{G.5}$$

The strain and material velocity at the band tip on *EL* (Figure G.1a) are obtained from (E.8) as

$$\gamma_2(l) = \frac{\gamma_c^2 + \delta^2(l,N)}{2\delta(l,N)}, \qquad \frac{\eta_2(l)}{c} = \frac{\gamma_c^2 - \delta^2(l,N)}{2\delta(l,N)} \tag{G.6}$$

Using (G.24), (G.6) can be written as

$$\begin{cases} \gamma_2(l) = \dfrac{\gamma_c^2 + [\gamma_s(l) + \gamma_s(l_R) - \gamma_c^2/\gamma_s(l_R)]^2}{2[\gamma_s(l) + \gamma_s(l_R) - \gamma_c^2/\gamma_s(l_R)]} \\ \dfrac{\eta_2(l)}{c} = \dfrac{\gamma_c^2 - [\gamma_s(l) + \gamma_s(l_R) - \gamma_c^2/\gamma_s(l_R)]^2}{2[\gamma_s(l) + \gamma_s(l_R) - \gamma_c^2/\gamma_s(l_R)]} \end{cases} \tag{G.7}$$

which results in (4.22). Taking into account (4.9), equations (G.4) and (G.7) result in (4.18) and (4.22), respectively.

Solution (E.12) can now be used for the arbitrary point *Z*(*x*, *t*) in domain *EFL* (Figure G.1a), which yields

$$\begin{cases} \gamma(x,t) = \eta(x,t)/c + \delta(x,N) \\ 2\dfrac{\eta(x,t)}{c} = \dfrac{\gamma_c^2}{\delta(l_H,B)} - \delta(l_H,N) \end{cases} \tag{G.8}$$

where the relation between point *B* on line *EF* and point *H* on the band tip line *EL* is obtained by considering $l_R \to l_W$ and $x_N \to x_B$ in (G.5). Using (E.21) with the initial condition (4.3) and substituting (G.24) into (G.8) gives

$$\begin{cases} 2\gamma(x,t) = \dfrac{\gamma_c^2}{\gamma_s(l_H) + \gamma_s(l_W) - \gamma_c^2/\gamma_s(l_W)} - \gamma_s(l_H) + \gamma_s(l_R) - \dfrac{\gamma_c^2}{\gamma_s(l_R)} + 2\gamma_s(x) \\ 2\dfrac{\eta(x,t)}{c} = \dfrac{\gamma_c^2}{\gamma_s(l_H) + \gamma_s(l_W) - \gamma_c^2/\gamma_s(l_W)} - \gamma_s(l_H) - \gamma_s(l_R) + \dfrac{\gamma_c^2}{\gamma_s(l_R)} \end{cases} \tag{G.9}$$

which is reduced to (4.21) by employing (4.9) and (G.7). Here points *R*, *H*, and *W* are on the band tip line *AC* (Figure G.1a), they are defined in (4.23) and (4.24).

For the arbitrary point *G*(*x*, *t*) above line *FL* (Figure G.1a), (E.19) results in

$$\begin{cases} 2\gamma(x,t) = \dfrac{\gamma_c^2}{\delta(l_H, B)} - \gamma_s(l_H) + \gamma_s(l_S) - \dfrac{\gamma_c^2}{\delta(l_S, D)} + 2\gamma_s(x) \\ 2\dfrac{\eta(x,t)}{c} = \dfrac{\gamma_c^2}{\delta(l_H, B)} - \gamma_s(l_H) + \dfrac{\gamma_c^2}{\delta(l_S, D)} - \gamma_s(l_S) \end{cases} \tag{G.10}$$

where points D on the discontinuity line EF and S on the band tip line EL (Figure G.1a) are related through (G.5) with $l_R \to l_S$ and $x_N \to x_D$. Then, (G.10) reduces to (4.25) by using (4.9) and (G.7). Points H is given by (4.23) (second equation), while points S and P are defined by

$$t + \frac{x + l_S}{c} = t_E + \int_{l_E}^{l_S} \frac{dl}{v_2(l, l_{RS}(l))}, \qquad t = \frac{2l_S + l_P + x}{c} + \int_{l_0}^{l_P} \frac{dl}{v_1(l)} \tag{G.11}$$

respectively. Function $l_{RS}(l)$ in (G.11) is obtained by replacing l_{RU} with l_{RS} in (4.19) and solving the obtained equation.

Solutions (G.4), (G.7), (G.9), and (G.10) are valid until the discontinuity reaches the band tip for the second time at point $L(l_L, t_L)$ given by

$$t_L = t_E + \int_{l_E}^{l_L} \frac{dl}{v_2(l)}, \qquad c(t_L - t_E) = l_L + l_E \tag{G.12}$$

In the normalized form (4.28), equation (4.18) for the band tip velocity simplifies to

$$V_2(\lambda, \lambda_{RU}) = \frac{[\Gamma_s(\lambda) + 2\Omega_1(\lambda_{RU})]^2 - 1/n}{[\Gamma_s(\lambda) + 2\Omega_1(\lambda_{RU})]^2 + 1/n} \quad (\lambda \ge \lambda_E,\ 1 \le \lambda_{RU}(\lambda) < \lambda_E) \tag{G.13}$$

while equations (4.22) for strain and material velocity at the fracture tip become

$$\begin{cases} \Gamma_2(\lambda) = \dfrac{1}{2} \dfrac{[\Gamma_s(\lambda) + 2\Omega_1(\lambda_{RU})]^2 + 1/n}{\Gamma_s(\lambda) + 2\Omega_1(\lambda_{RU})} \\ \Omega_2(\lambda) = \dfrac{1}{2} \dfrac{[\Gamma_s(\lambda) + 2\Omega_1(\lambda_{RU})]^2 - 1/n}{\Gamma_s(\lambda) + 2\Omega_1(\lambda_{RU})} \end{cases} \quad (\lambda \ge \lambda_E,\ 1 \le \lambda_{RU}(\lambda) < \lambda_E) \tag{G.14}$$

In (G.13), (G.14), $\lambda_{RU}(\lambda)$ is found by solving (4.19) written in the dimensionless form as

$$\frac{d\lambda_{RU}}{d\lambda} = \left[\frac{1}{V_2(\lambda, \lambda_{RU})} - 1\right]\left[1 + \frac{1}{V_1(\lambda_{RU})}\right]^{-1}, \quad \lambda_{RU}(\lambda_E) = 1 \quad (\lambda \ge \lambda_E,\ 1 \le \lambda_{RU}(\lambda) < \lambda_E) \tag{G.15}$$

Parameter λ_E is obtained from (4.20), which becomes

$$\tau_E = \lambda_E + 1, \quad \tau_E = \int_1^{\lambda_E} \frac{d\lambda}{V_1(\lambda)} \tag{G.16}$$

Normalized strain and material velocity at the arbitrary point (ξ, τ) above the discontinuity

line *EF* (Figure 6) are obtained from (4.21) as

$$\begin{cases}\Gamma(\xi,\tau) = -\Omega_2(\lambda_H) + \Omega_1(\lambda_W) + \Omega_1(\lambda_R) + \Gamma_s(\xi) \\ \Omega(\xi,\tau) = \Omega_2(\lambda_H) - \Omega_1(\lambda_W) + \Omega_1(\lambda_R)\end{cases} \tag{G.17}$$

Functions $\lambda_H(\xi, \tau)$, $\lambda_W(\xi, \tau)$, $\lambda_R(\xi, \tau)$ are given by (4.23) and (4.24), expressed in the dimensionless form as

$$\tau = \xi + \lambda_R + \int_1^{\lambda_R} \frac{d\lambda}{V_1(\lambda)}, \quad \tau + \xi - \lambda_H = \tau_E + \int_{\lambda_E}^{\lambda_H} \frac{d\lambda}{V_2(\lambda, \lambda_{RH}(\lambda))} \tag{G.18}$$

and

$$\tau = 2\lambda_H + \lambda_W - \xi + \int_1^{\lambda_W} \frac{d\lambda}{V_1(\lambda)} \tag{G.19}$$

respectively. Here $\lambda_{RH}(\lambda)$ is defined by solving (G.15) with λ_{RU} replaced by λ_{RH}. Function $\lambda_R(\xi, \tau)$ is computed from the first equation in (G.18), while $\lambda_H(\xi, \tau)$ is found from the second equation. Once $\lambda_H(\xi, \tau)$ is determined, $\lambda_W(\xi, \tau)$ is obtained from (G.19), and the propagation length as a function of time (or vice versa) is found from (4.17) written in dimensionless form as

$$\tau = \tau_E + \int_{\lambda_E}^{\lambda} \frac{d\lambda}{V_2(\lambda, \lambda_R(\lambda))} \tag{G.20}$$

Finally, for point (ξ, τ) above line *FL* in Figure 6, the distributions of Γ and Ω above line *FE* in Figure 6 are given by (4.25), which in the normalized form reads as

$$\begin{cases}\Gamma(\xi,\tau) = -\Omega_2(l_H) + \Omega_2(l_S) + \Omega_1(l_W) - \Omega_1(l_P) + \Gamma_s(x) \\ \Omega(\xi,\tau) = \Omega_2(l_H) + \Omega_2(l_S) - \Omega_1(l_W) - \Omega_1(l_P)\end{cases} \tag{G.21}$$

Here $\lambda_H(\xi, \tau)$ and $\lambda_W(\xi, \tau)$ are defined above (equations (G.18), (G.19)), while $\lambda_U(\xi, \tau)$, is computed from

$$\tau + \xi + \lambda_S = \tau_E + \int_{\lambda_E}^{\lambda_S} \frac{d\lambda}{V_2(\lambda, \lambda_{RS}(\lambda))}, \qquad \tau = 2\lambda_S + \lambda_P + \xi + \int_1^{\lambda_P} \frac{d\lambda}{V_1(\lambda)} \tag{G.22}$$

with $\lambda_{RS}(\lambda)$ being the solution of (G.15) when λ_R is replaced by λ_{RS}. In the case of homogeneous load (5.1), the elementary expressions (5.5) – (5.8) are to be used in (G.19) – (G.22).

The crack velocity $v_3 = dl_3/dt$ after point *L* (i.e., in domain LXX_1, in Figure G.1b) is obtained from (G.1) by replacing v_2 with v_3 and *R* with *U*. Then,

$$\frac{v_3(l)}{c}=\frac{\delta^2(l,B_1)-\gamma_c^2}{\delta^2(l,B_1)+\gamma_c^2} \tag{G.23}$$

where similar to (G.24), using (E.4) and (E.21)

$$\delta(l,B_1)=\gamma_s(l)+2\eta_1(l_R)/c-2\eta_1(l_U)/c \tag{G.24}$$

and $l_U(l)$ is defined from the solution of the initial value problem

$$\frac{dl_U}{dl}=\left[\frac{c}{v_3(l,l_U)}-1\right]\left[\frac{c}{v_2(l_U)}+1\right]^{-1},\quad l_U(l_L)=l_E\quad (l\ge l_L,\ l_E\le l_U(l)<l_L) \tag{G.25}$$

The strain and material velocity at the band tip after point *L* (Figure G.1b) are obtained by rewriting (E.8) as

$$\begin{cases}\gamma_3(l)=\dfrac{[\gamma_s(l)+2\eta_1(l_R)/c-2\eta_1(l_U)/c]^2+\gamma_c^2}{2[\gamma_s(l)+2\eta_1(l_R)/c-2\eta_1(l_U)/c]}\\ \dfrac{\eta_3(l)}{c}=\dfrac{\gamma_c^2-[\gamma_s(l)+2\eta_1(l_R)/c-2\eta_1(l_U)/c]^2}{2[\gamma_s(l)+2\eta_1(l_R)/c-2\eta_1(l_U)/c]}\end{cases}\quad (l\ge l_L,\ l_E\le l_U(l)<l_L) \tag{G.26}$$

APPENDIX H. DISONTINUITY MAGNITUDE

The attractive features of the landslide model presented in this work are its simplicity and the possibility of obtaining closed-form solutions for the dynamic formulation. The appearance of the discontinuity in this model is a result of the simplified description (2.12) of the static-to-dynamic transition of the shear band. Such discontinuities are typical for one-dimensional models of this type [*Burridge and Keller*, 1978; *Hellan*, 1984; *Freund*, 1998; *Whitham*, 1999], and the obtained solutions can be reasonably acceptable if the discontinuities are not too large and do not grow as the shear band propagates.

To assess the evolution of the discontinuity, consider the limit of $Q(x, t)\to B$ in Figure 4a and use (4.13) (with $l_P\to l_0$), which results in

$$\gamma^+(B)=\gamma_s(x_B)+\eta_1(l_0)/c,\qquad \eta^+(B)=\eta_1(l_0) \tag{H.1}$$

Therefore, taking (4.4) and (4.14) into account, we find that the value of

$$\Delta_0=\gamma^+(B)-\gamma^-(B)=\frac{\eta^+(B)-\eta^-(B)}{c}=\frac{\eta_1(l_0)}{c}=\gamma_0\frac{n-1}{2n} \tag{H.2}$$

of the discontinuity remains constant as the discontinuity moves along line *AC* in Figure 4.

When the discontinuity reflects from $x = 0$, it simply changes its sign, which can formally be seen by considering the arbitrary point (x, t) and the limit of $(x, t) \to M$ on line CE in Figure 4a. Depending on which side of CE this limit is taken, we use either (4.13) or (4.15) (with $l_R \to l_0$) to obtain

$$\gamma^+(M) = \gamma_s(x) + \eta_1(l_P)/c, \qquad \eta^+(M) = \eta_1(l_P) \tag{H.3}$$

and

$$\gamma^-(M) = \frac{\eta_1(l_P)}{c} - \frac{\eta_1(l_0)}{c} + \gamma_s(x), \qquad \eta^-(M) = \eta_1(l_P) + \eta_1(l_0) \tag{H.4}$$

respectively. Hence

$$\gamma^-(M) - \gamma^+(M) = -\frac{\eta^-(M) - \eta^+(M)}{c} = -\frac{\eta_1(l_0)}{c} = -\gamma_0 \frac{n-1}{2n} \tag{H.5}$$

which is independent of M and has the same magnitude as (H.2), but the opposite sign. Note that we used here $\gamma^- - \gamma^+$ and $\eta^- - \eta^+$ (compare to (H.2)) because this corresponds to our choice of signs in Figure 4b, where the discontinuity does not reach the band tip and its magnitude remains constant.

In the case of Figure 4a, the discontinuity is also described by (H.5) and maintains the same constant magnitude (H.2) until it reflects from the band tip at point E. Indeed, considering the limit of $(x, t) \to N$ on line EF in Figure 6 and using either (4.15) (with $l_P \to l_E$) or (4.21) (with $l_H \to l_E$ and $l_W \to l_0$) results in

$$\gamma^-(N) = \frac{\eta_1(l_E)}{c} - \frac{\eta_1(l_R)}{c} + \gamma_s(x), \qquad \eta^-(N) = \eta_1(l_E) + \eta_1(l_R) \tag{H.6}$$

and

$$\begin{cases} \gamma^+(N) = \dfrac{\eta_2(l_E) - \eta_1(l_0) - \eta_1(l_R)}{c} + \gamma_s(x) \\ \eta^+(N) = \eta_2(l_E) - \eta_1(l_0) + \eta_1(l_R) \end{cases} \tag{H.7}$$

respectively. We then obtain the discontinuity value

$$\Delta_1 = \gamma^+(N) - \gamma^-(N) = \frac{\eta^+(N) - \eta^-(N)}{c} = \frac{\gamma_0^2}{n\gamma_s^2(l_E)} \frac{\Delta_0 \gamma_s(l_E)}{\gamma_s(l_E) - 2\Delta_0} \tag{H.8}$$

after the first reflection from the band tip. This value is independent of point N and, hence, does not change when the discontinuity propagates from the band tip E back to the slide end F,

where $x = 0$. The value (H.8) of the discontinuity is positive because the static strain, $\gamma_s(l_E)$, at point E is negative. Furthermore, because per (H.2), $0 < 2\Delta_0 < \gamma_0$ (since $n > 1$) and because $\gamma_0 < -\gamma_s(l_E)$, we obtain from (H.8) that

$$\Delta_1 < \Delta_0 \frac{1/n}{\gamma_s^2(l_E)/\gamma_0^2} < \Delta_0 \tag{H.9}$$

which means that the magnitude of the discontinuity decreases after it reflects from the band tip E.

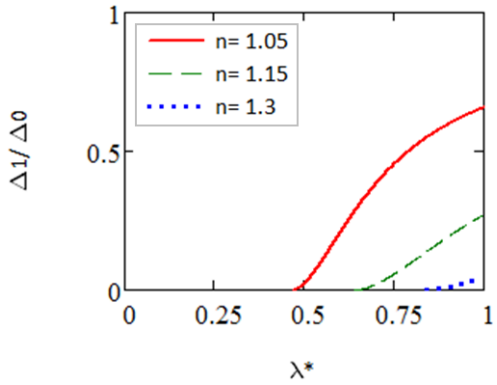

Figure H.1. Relative discontinuity magnitude Δ_1/Δ_0 as a function of λ_* for $n = 1.05$ (red solid line), 1.15 (green dashed line), and 1.3 (blue dotted line).

It turns out that each reflection from the band tip reduces the discontinuity magnitude (e.g., by an order in Figure 7 and by two orders in Figure 9). Furthermore, because n is relatively close to 1 (Section 5.2), this magnitude is only a small fraction of γ_0 (the strain required for the shear band to start growing dynamically), even prior to the first reflection from the tip (equations (H.2) and (H.5)), after the discontinuity just appears. As the discontinuity propagates, it may retain constant magnitude, if it does not reach the band tip, or keep reducing the magnitude so long as it continues to reflect from the tip. This somewhat justifies the discontinuities in our model. This can also be seen in Figure H.1, where the dependence of the relative discontinuity change Δ_1/Δ_0 (after the first reflection from the band tip) is shown as a function of λ_*. The discontinuity change is more significant for smaller λ_* and for greater n, but in all cases $\Delta_1/\Delta_0 < 1$.

APPENDIX I. COMPARISON TO *PUZRIN ET AL.* [2010]

To compare this work with *Puzrin et al.* [2010], we rewrite their eq. (29) for the shear band

propagation velocity, $v = [2\tau(l - l_0)/(3\rho\gamma_0 h)]^{1/2}$, and eq. (30) for the corresponding landslide velocity, $\bar{\eta} = v\gamma_0 = [2\tau\gamma_0(l - l_0)/(3\rho h)]^{1/2}$, using the dimensionless formulation (4.28) as a single relation

$$\frac{v}{c} = \frac{\bar{\eta}}{c\gamma_0} = \sqrt{\frac{2(\lambda - 1)}{3\lambda_*}} \tag{I.1}$$

where we took into account that in both works, the initial shear band length (i.e., under static conditions), l_0, is the same and given by (5.3). The comparison is shown in Figure I.1. The shear band velocity (5.5) is plotted in Figure I.1a as a function of λ for $n = 1.1$ and $\lambda_* = 1$ (blue, bold, solid line), 0.5 (blue, thin, solid line), and 0.1 (blue, dashed line). Velocity (I.1) is plotted for the same λ_* of 1 (red, bold, solid line), 0.5 (red, thin, solid line), and 0.1 (red, dashed line). According to (I.1) and Figure I.1a (blue lines), the shear band accelerates from zero velocity, and the velocity grows faster than in our work (eq. (5.5)). In both works, it already reaches the level of c at $\lambda \approx 2$, but then the velocity (I.1) grows unboundedly becoming as high as $\approx 2.5c$ at $\lambda = 10$ (Figure I.1a). *Puzrin et al.* [2010] indicated that in reality, the slope would fail much before the band velocity reaches c as, indeed, happened in the analysis of the several real slides they analyzed.

The band velocity (5.5), obtained in this work, remains bounded ($v < c$), but in the beginning of its growth, the band accelerates at the rate comparable to *Puzrin et al.* [2010] (Figure I.1a). It should be noted that this acceleration occurs not from zero velocity, but from the initial velocity, v_0, given by (4.5). Although this is a consequence of our model being one-dimensional (and so is the model of *Puzrin et al.* [2010]), such a velocity jump could be interpreted as fast acceleration during the short initial stage when the dynamic mechanism of the band growth is being engaged.

The average landslide velocity (6.14) is plotted with (I.1) in Figure I.1b (see also Figure 12) for the same parameters ($n = 1.1$ and $\lambda_* = 0.1$, 0.5, 1) as in Figure I.1a. As can be observed, the slide velocity (6.14) increases much faster than that given by (I.1). For example, when $\lambda = 100$, $\bar{\eta}/(\gamma_0 c)$ in (6.14) grows from 50.6 to 99.0 as λ_* decreases from 1 to 0.5, and for $\lambda_* = 0.1$, $\bar{\eta}/(\gamma_0 c)$ reaches 100 when $\lambda = 21.8$. In contrast, v / c in (I.1), ranges only from 8.1 to 25.7 with λ_* decreasing from 1 to 0.1. Hence, using (I.1) may result in a considerable underestimation of

the slide velocity and, consequently, the tsunami magnitude.

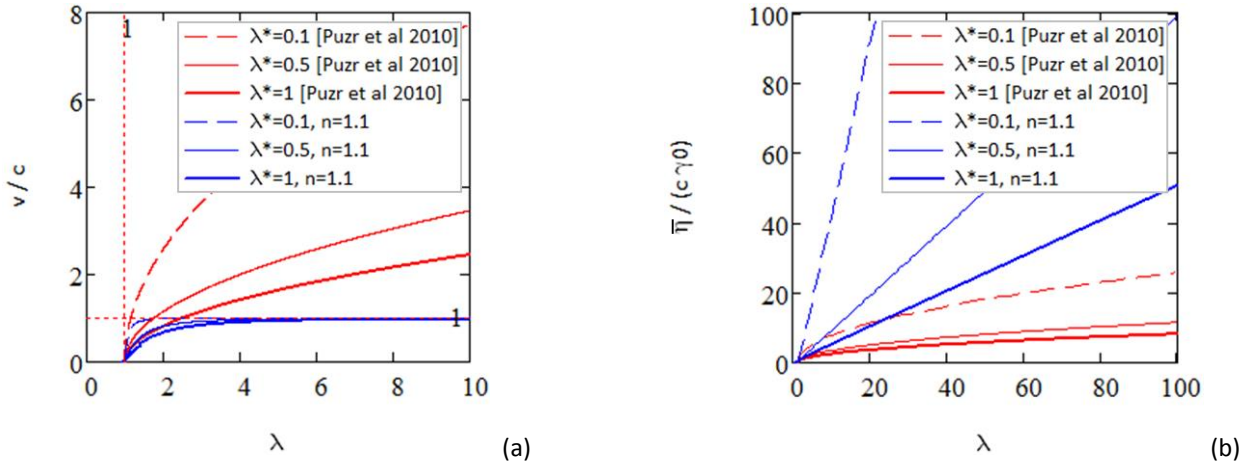

Figure I.1. (a) Dimensionless shear band velocities (5.5) (blue lines, this work) and (I.1) (red lines, *Puzrin et al.* [2010]) and (b) dimensionless slide velocities (6.14) (blue lines, this work) and (I.1) (red lines, *Puzrin et al.* [2010]) for $n = 1.1$ and $\lambda_* = 0.1$ (dashed lines), $\lambda_* = 0.5$ (thin, solid lines), and $\lambda_* = 1$ (bold, solid lines). (c) Legend to Figures (a) and (b).

APPENDIX J. RECURRENCE RELATIONS FOR SLIDE VELOCITY

The recurrence solution obtained in Appendix E is now used to find the recurrence relations for the slide velocity, $\bar{\eta}$. As in Appendix E, consider point $A(l_A, t_A)$ where the discontinuity imitates, when the band begins growing at $t = 0$, or reflects from the tip at time t_A, when it has the length of l_A (Figure E.1). The objective is to express the slide velocity in domain *ACFE* (Figure E.1) through the solution valid below the discontinuity line *AC*. Then, the slide velocity in domain *EFXL* will also be found by using the solution in *ACFE*, which is just below *EFXL* (Figure E.1).

Slide velocity is defined as the average material velocity (6.7). To evaluate this velocity, we first integrate the second equation in (3.1) with respect to x for constant t from $t_A < t < t_A + l_A / c$ (Figure E.1). We obtain

$$\frac{1}{c^2}\int_0^{x_B(t)}\frac{\partial \eta}{\partial t}dx+\frac{1}{c^2}\int_{x_B(t)}^{l(t)}\frac{\partial \eta}{\partial t}dx=\int_0^{x_B}\frac{\partial \gamma}{\partial x}dx+\int_{x_B}^{l}\frac{\partial \gamma}{\partial x}dx+\frac{1}{h}\int_0^{l}T(x)dx \qquad \text{(J.1)}$$

where $x_B(t) = l_A - c(t - t_A)$. Changing the order of integration and differentiation in the left hand side integrals and taking into account that both l and x_B are functions of time, we rewrite (J.1) as

$$\frac{\partial}{\partial t}\int_0^{l}\eta dx=\eta_1(l)v_1(l)+c[\eta^+(x_B,t)-\eta^-(x_B,t)]+c^2[\gamma_1(l)-\gamma_s(l)-\gamma^+(x_B,t)+\gamma^-(x_B,t)] \qquad \text{(J.2)}$$

where we used (2.11), (4.8), $v_1(l)$ is defined by (E.6), and $\gamma(l, t) = \gamma_1(l)$, $\eta(l, t) = \eta_1(l)$ given by (E.8). Using next the jump condition (4.4) and integrating (J.2) with respect to time, we arrive at

$$\int_0^l \eta dx = \int_0^{l_A} \eta dx + \int_{l_A}^{l} \left[\eta_1(l) + c^2 \frac{\gamma_1(l) - \gamma_s(l)}{v_1(l)} \right] dl \tag{J.3}$$

where $dl = v\, dt$.

Finally, substituting (J.3) into (6.7), we obtain

$$\frac{\bar{\eta}(l)}{c} = -\frac{l_A}{l}\frac{\bar{\eta}(l_A)}{c} + \frac{1}{l}\int_{l_A}^{l} \left[\frac{\eta_1(l)}{c} + c\frac{\gamma_1(l) - \gamma_s(l)}{v_1(l)} \right] dl \tag{J.4}$$

which is valid for $t_A / c > t > t_A + l_A / c$.

Determining $\bar{\eta}(l)$ for $t_A + l_A / c > t > t_A + (l_A + l_E)/ c$ is similar (Figure E.1), but with point M ($x_M(t) = l_A + c(t - t_A)$; Figure E.1) instead of B and l_E defined by (E.20). Since the discontinuity travels towards $x = 0$ with the speed of c, we have

$$\frac{\partial}{\partial t}\int_0^l \eta dx = \eta_1(l)v_1 - c[\eta^+(x_M, t) - \eta^-(x_M, t)] + c^2[\gamma_1(l) - \gamma_s(l) - \gamma^+(x_M, t) + \gamma^-(x_M, t)] \tag{J.5}$$

instead of (J.2). Using the jump condition (4.4) and integrating (J.5) with respect to time, yields

$$\int_0^l \eta dx = \int_0^{l_C} \eta dx + \int_{l_C}^{l} \left[\eta_1(l) + c^2 \frac{\gamma_1(l) - \gamma_s(l)}{v_1(l)} \right] dl \tag{J.6}$$

which is similar to (J.3). Here, $l_C = l(t_C)$ is the shear band length when the discontinuity is at point $C(0, t_C)$ being reflected at $x = 0$ for the first time. Although equation (J.6) is nearly identical to (J.3), the integration intervals now have l_C. The first integral in (J.6) can be expressed from (J.3) as

$$\int_0^{l_C} \eta dx = \int_0^{l_A} \eta dx + \int_{l_A}^{l_C} \left[\eta_1(l) + c^2 \frac{\gamma_1(l) - \gamma_s(l)}{v_1(l)} \right] dl \tag{J.7}$$

With (J.7) in (J.6), the average, slide, velocity for $t_A + l_A / c < t < t_A + (l_A + l_E)/ c$ becomes the same as (J.4).

Solution (J.4) is valid from point A ($t = t_A$) through the moment t_E when the discontinuity reaches the band tip at point E. This establishes the recurrence sequence for finding the slide velocity everywhere at $t > t_A$ in Figure E.1 since at each "step" the next term, $\bar{\eta}(l_A)$, is found during the previous "step". Initially, $l_A = l_0$, $t_A = 0$, and $\bar{\eta}(l_0) = 0$.

Substituting strain and material velocity (4.9) at the tip together with $\bar{\eta}(l_0) = 0$ into (J.4) results in (6.11), which, therefore, is valid not only for $t < l_0/c$, but also for $l_0/c < t < (l_0 + l_E)/c$ (since (J.4) is applicable for $t_A < t < t_A + (l_A + l_E)/c$).

For the integration interval of *EFXL* above point *E* but below point *L* (Figure E.1), that is, for $(l_0 + l_E)/c < t < (l_0 + 2l_E + l_L)/c$, the slide velocity is obtained directly from (J.4) by changing $l_A \to l_E$, $v_1 \to v_2$, $\gamma_1 \to \gamma_2$, and $\eta_1 \to \eta_2$, which yields

$$\frac{\bar{\eta}(l)}{c} = -\frac{l_E}{l}\frac{\bar{\eta}(l_E)}{c} + \frac{1}{l}\int_{l_E}^{l}\left[\frac{\eta_2(l)}{c} + c\frac{\gamma_2(l) - \gamma_s(l)}{v_2(l)}\right]dl \qquad (t_E < t < t_L) \tag{J.8}$$

where $v_2(l)$ is defined in (G.4). In the case of $l_A = l_0$, $t_A = 0$, and $\bar{\eta}(l_E)$ is also given by (6.12). In the case of $l = l_E$, (6.11) and (6.12) give the same result, which implies that the slide velocity is continuous function of t (or l).

APPENDIX K. EFFECT OF WATER RESISTANCE

For both the exact and asymptotic solutions, the distribution of material velocity becomes flat for large enough τ or λ (Figure 14b). Hence, in this case, the material velocity can be reasonably assumed uniform along the slope. Accordingly, we evaluate the effect of water resistance to the landslide by letting the resistance also be uniform.

The resistance is usually a function $\tau_w(\bar{\eta})$ of the sliding velocity, $\bar{\eta}$, so $T(x, t)$ can be expressed as

$$T(x, \bar{\eta}) = T_1(x) - T_w(\bar{\eta}), \qquad \bar{\eta} = \bar{\eta}(t) \tag{K.1}$$

where $T_1(x) = \tau_1(x)/E$, $T_w(\bar{\eta}) = \tau_w(\bar{\eta})/E$, and $\tau_1 = \tau_g - \tau_r$ is defined in (2.5).

Substituting (K.1) into the second equation in (3.1) and integrating with respect to x yields

$$\frac{1}{c^2}\int_{x_B}^{l}\frac{\partial \eta}{\partial t}dx = \int_0^l \frac{\partial \gamma}{\partial x}dx + \frac{1}{h}\int_0^l T_1(x)dx - \frac{l}{h}T_w(\bar{\eta}) \tag{K.2}$$

which has an additional (last) term compared to (6.8). Expression (6.9) is still valid in this case and (6.10) is also valid with the same additional term in (K.2) with c^{-2}, and it is convenient to express static strain (4.8) as

$$\gamma_s(l) = \gamma_s(l_0) - \frac{1}{h}\int_{l_0}^{l} T_1(x)dx \tag{K.3}$$

which contains $T_1(x)$ instead of $T(x)$. Assuming $v(l) = c$ (for long bands), then, similar to (6.11), the average material velocity

$$\frac{\bar{\eta}(l)}{c} = -\frac{1}{l}\int_{l_0}^{l} \gamma_s(l)dl - \frac{1}{hl}\int_{l_0}^{l} lT_w(\bar{\eta})dl \qquad \text{(K.4)}$$

Note the additional term (related to τ_w) in (K.4) compared to (6.11).

Differentiating (K.4) with respect to l, and using (K.3) results in

$$\frac{h}{l}\frac{d}{dl}\left(\frac{\bar{\eta}}{c}l\right) = \frac{1}{l}\int_{l_0}^{l} T_1(x)dx - T_w(\bar{\eta}) \qquad (l > l_0) \qquad \text{(K.5)}$$

where $\bar{\eta}(l_0) = 0$ as the slope is initially at rest. This is clearly an approximation since, strictly speaking, (K.5) is obtained for $l >> l_0$, while the boundary condition, $\bar{\eta}(l_0) = 0$ is used for $l = l_0$. Nonetheless, (K.5) is asymptotically accurate for large l and small $T_w(\bar{\eta})$ because it coincides (up to the higher order terms) with (6.11) and (6.12) or with (J.4) and (J.8) when $l \to \infty$.

Equation (K.5) can be solved for the slide velocity, $\bar{\eta}(l)$, when function $T_w(\bar{\eta})$, is specified. In dimensionless form, (K.5) reads

$$\lambda_* \frac{d(\bar{\Omega}\lambda)}{d\lambda} = \lambda[S(\lambda) - F(\bar{\Omega})] - 1 \qquad (\lambda > 1) \qquad \text{(K.6)}$$

where $\bar{\Omega} = \bar{\eta}/(\gamma_0 c)$, $S(\lambda) = \bar{T}_1(\lambda l_0)/T_0$, $F(\bar{\Omega}) = T_w(\bar{\eta})/T_0 = T_w(\gamma_0 c\bar{\Omega})/T_0$, $T_0 = \bar{T}_1(l_0)$,

$$\bar{T}_1(l) = \frac{1}{l}\int_0^l T_1(x)dx \qquad \text{(K.7)}$$

and $\lambda_* = h\gamma_0/(T_0 l_0)$ which is consistent with (4.29) because T_w (or τ_w) in (4.29) was assumed negligible and, hence, $\bar{T}(l_0) = \bar{T}_1(l_0) = T_0$.

For physically acceptable functions $T_w(\bar{\eta})$ (or $F(\bar{\Omega})$) and condition $\bar{\Omega}(1) = 0$, the first order ordinary differential equation (K.6) has a unique solution, finding which represents no numerical difficulty. Note that equation (K.6) is not singular if $\lambda_* \to 0$. Indeed, for $\lambda_* \to 0$, it reduces to the algebraic equation (generally, transcendental) $F(\bar{\Omega}) = S(\lambda) - 1/\lambda$ for $\bar{\Omega}(\lambda)$. Hence, for $\lambda \to 1$, $F(\bar{\Omega}) \to F(0) = S(1) - 1 = 0$ (since $\bar{\eta}(1) = 0$), which is equivalent to $T_w(0) = 0$. This condition is satisfied because the water resistance is zero for zero velocity.

Water resistance is often assumed to be proportional to $\bar{\eta}^2$ [*Harbitz*, 1992; *Pelinovsky and Poplavsky*, 1996; *Watts*, 1998; *De Blasio*, 2011]. The coefficient of proportionality, however,

depends upon several factors such as the slide geometry, character of flow (turbulent or laminar), and slide surface material (e.g., sand or clay). Typically, for a slide moving downhill after it is separated from the substrata, the main resistance component is due to the Stokes drag [*Pelinovsky and Poplavsky*, 1996; *Watts*, 1998; *De Blasio*, 2011], which is proportional to the cross-sectional area of the sliding body (in the direction perpendicular to sliding). In our notations, the Stokes drag can be written in the form of the effective dimensionless longitudinal load, $T_D(\bar{\eta}) = C_D \rho_w h \bar{\eta}^2/(2El)$, in the slide, where C_D is the drag coefficient and ρ_w is the water density. The shear load acting on the top surface of the slide is also proportional $\bar{\eta}^2$ [*Harbitz*, 1992; *Ding et al.*, 2004; *Burguete et al.*, 2007; *De Blasio*, 2011], and can be written in the same form as $T_S(\bar{\eta}) = C_S \rho_w \bar{\eta}^2/(2E)$, where the surface friction coefficient C_S may be two to three orders of magnitude smaller than C_D [*De Blasio*, 2011]. Then the combined water resistance load $T_w(\bar{\eta}) = T_D(\bar{\eta}) + T_S(\bar{\eta})$, and if h/l is not too small (say, $h/l > 10^{-3}$), $T_S(\bar{\eta})$ is considered to be much smaller than $T_D(\bar{\eta})$ and is usually omitted in the submarine landslide models [*Pelinovsky and Poplavsky*, 1996; *Watts*, 1998; *Grilli and Watts*, 2005]. In our case, however, before the global failure occurs and the slide separates (or at least begins separating) from the substrata, the seafloor surface is flat and the Stokes drag is not significant. In this case, $T_S(\bar{\eta})$ becomes the leading term, and we have

$$T_w(\bar{\eta}) \approx T_S(\bar{\eta}) = \frac{\beta h}{l_0 \gamma_0 c^2} \bar{\eta}^2, \qquad \beta = \frac{C_w \rho_w \gamma_0}{2\rho_0} \frac{l_0}{h} \tag{K.8}$$

where $\rho_0 c^2 = E$.

For the submarine landslide conditions, *De Blasio et al.* [2004] estimated that $C_S \approx 0.03 - 0.05$, so here we consider the range of $C_S \sim 10^{-3}$–10^{-2} in (K.8). We further note that for most soils and submarine sediments, $\rho_0/(2\rho_w) \sim 1$. Since in many observed landslides, $l_f/h \sim 10^1$–10^2 [*Bugge et al.*, 1988; *Ma et al.*, 1991; *Kulikov et al.*, 1996; *Yalciner et al.*, 2002; *Sweet and Silver*, 2003], and because $l_0/l_f < 1$, we further assume that $10^1 < l_0/h < 10^2$, where the lower bound is due to the condition $l_0/h >> 1$, which needs to be satisfied for the 1-D shear band (landslide) model to be valid. Finally for most sediments we expect γ_0 range from 10^{-4} to 10^{-2} (Chapter 8). Hence, coefficient β in (K.8) ranges as

$$10^{-7} < \beta < 10^{-3} \tag{K.9}$$

In the case of homogeneous loading (5.1), $\overline{T}_1(l) = \overline{T}_1(l_0) = T_0$, so that $S(\lambda) = 1$, $F(\overline{\Omega}) = \beta\lambda_*\overline{\Omega}^2$, and (K.6) is reduced to the Riccati equation [*Reid*, 1972]

$$\frac{dy(\lambda)}{d\lambda} + \beta\frac{y^2(\lambda)}{\lambda} = \frac{\lambda - 1}{\lambda_*} \qquad (\lambda > 1) \tag{K.10}$$

where $y = \overline{\Omega}\lambda$, and $y(1) = 0$. The dimensionless slide velocity is recovered from $y = \overline{\Omega}(\lambda) = y/\lambda$.

Function $\overline{\Omega}(\lambda)$ is plotted in Figure K.1 for $\lambda_* = 0.25$ (solid line) and $\lambda_* = 0.75$ (dashed line). The selected values of β are 10^{-4} (red line), 10^{-5} (blue line), and 0 (green line). Without water resistance ($\beta = 0$), $\overline{\Omega}(\lambda)$ was calculated based on the exact solution (6.11), (6.12) for $n = 1.1$. For $\lambda_* = 0.25$ and $n = 1.1$, the discontinuity does not reach the band tip, so (6.11) was used to compute $\overline{\Omega}(\lambda)$. For $\lambda_* = 0.75$ and $n = 1.1$, (6.11) was used before the discontinuity arrives at the tip, and (6.12) was used after that. This procedure resulted in $\overline{\Omega}(50) = 97.02$ and 32.99 for $\lambda_* = 0.25$ and 0.75, respectively (Figure K.1a). Accounting for the water resistance reduces $\overline{\Omega}(\lambda)$. For example, $\overline{\Omega}(50)$ is reduced by 11.0% ($\beta = 10^{-4}$) and 2.1% ($\beta = 10^{-5}$) for $\lambda_* = 0.25$ and by 6.6% ($\beta = 10^{-4}$) and 3.3% ($\beta = 10^{-5}$) for $\lambda_* = 0.75$. Therefore, the effect of water resistance is relatively small for these values of β, λ, and λ_*. For smaller values of λ, however, the difference between accounting and not accounting for the water resistance can be more significant (Figure K.1b). For example, $\overline{\Omega}(5)$ is reduced by 11.12% ($\beta = 10^{-4}$) and 11.17% ($\beta = 10^{-5}$) for $\lambda_* = 0.25$ and by 26.01% ($\beta = 10^{-4}$) and 26.02% ($\beta = 10^{-5}$) for $\lambda_* = 0.75$. Hence, for relatively small values of λ, the effect of water resistance is stronger as λ_* increases, but it is almost insensitive to the value of β in this example. This can also be seen in Figure K.1b where the difference between $\beta = 10^{-5}$ (blue lines) and $\beta = 10^{-4}$ (red lines) is hardly noticeable for $\lambda < 10$. The difference, becomes visible in Figure K.1a roughly at $\lambda = 40$ when the band accelerates to higher velocities and the effect of water resistance becomes more significant. The exact solution (6.14) (green lines) differs noticeably from the asymptotic solutions (blue and red lines) for small values of λ, which characterizes not the effect of water resistance (negligible at this stage of propagation), but the accuracy of the asymptotic solution obtained for $\lambda >> 1$. Had we plotted $\overline{\Omega}(\lambda)$ in Figure K.1b based on the asymptotic solution of (K.10) for $\beta = 0$, it would have been hardly distinguishable from the plotted asymptotic solutions for $\beta = 10^{-5}$ and $\beta = 10^{-4}$.

At the moment of slope failure, the band size, l_f, is given by (7.8) (in the asymptotic solution) and is independent of β (and n) while the time, t_f, of the slope failure is a function of β. Similar to the exact solution, at any given time, the largest material velocity in the asymptotic solution is at the band tip (e.g., Figure 14). In turn, this velocity is smaller than c for $l < l_f$ (Chapter 8). Hence, the asymptotic slide velocity $\bar{\eta}$ is also smaller than c for $l < l_f$.

To evaluate the effect of water resistance on the failure length, we integrate (4.1) along the characteristic line BQ in Figure 13 (in the asymptotic case of $v = c$). We then arrive at equation (4.2) with point $D(l_d, t_d)$ replaced by the arbitrary point $Q(x, t)$ below line CE in Figure 13. Similar to (4.13) and (7.3), the strain at point $Q(x, t)$ can be obtained by using another integration from point $P(l_p, t_p)$ to $Q(x, t)$. If Q approaches point $P(l_p, t_p)$ at the propagating band tip, $x = l(t)$ (Figure 13), the tip strain at $P(l_p, t_p)$ can be obtained (such as $\gamma_1(l_p) = \gamma_s(l_p)/2$ for the case of no water resistance per (7.3)), which becomes equal to the passive strain at failure. Therefore, similar to (6.1) or (7.8), we obtain the equation

$$\gamma_1(l_f^w) = -\gamma_p = \frac{1}{2}\gamma_s(l_f^w) + \frac{1}{2h}\int_{l_0}^{l_f^w} T_w(\bar{\eta})dl \qquad \text{(K.11)}$$

for the strain at the tip $l = l_f^w$, which has an additional, second term (water resistance) in the right side in (K.11). This term is positive and reduces the magnitude of the tip strain (because the first term is negative). Thus, at the same length, the tip strain computed with accounting for the water resistance is smaller than the one without. As a result, the longer failure length is required to reach γ_p when the water resistance is accounted for. Therefore, the dynamic failure length is larger if water resistance is included. Therefore, (7.10) and (7.11) give the lower bound of λ_f and κ, respectively.

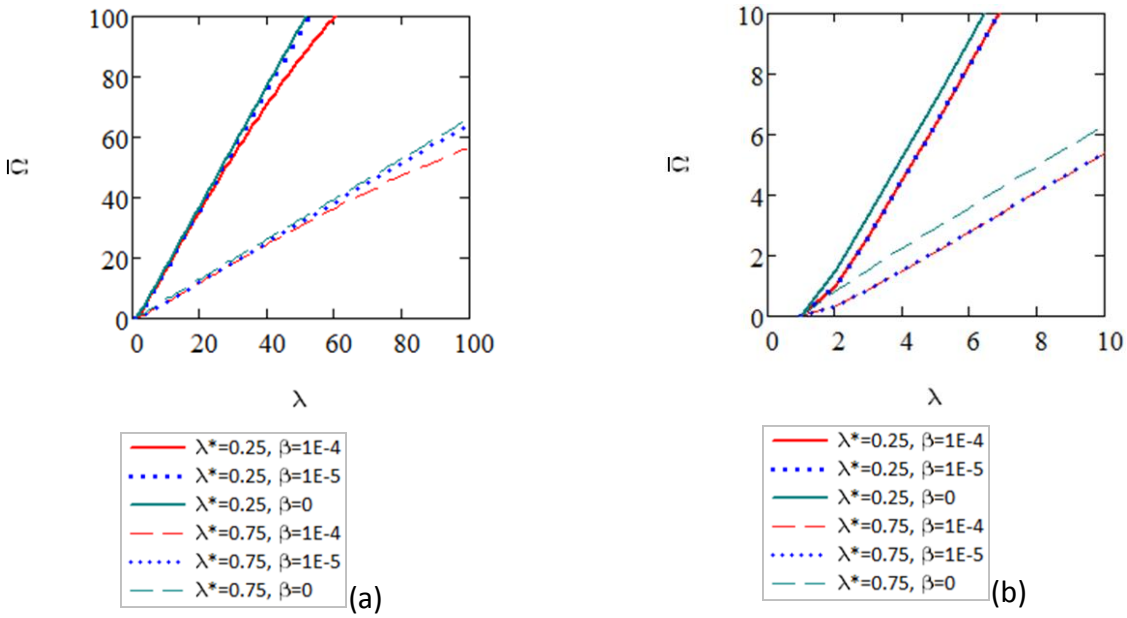

Figure K.1. Effect of water resistance on slide velocity, $\bar{\Omega} = \bar{\eta}/(\gamma_0 c)$. The same plots are given in (a) and (b) at different scales. Slide velocity, obtained by solving (K.10) (with boundary condition $y(1) = 0$), is plotted as a function of the dimensionless band length, $\lambda = l/l_0$ for $\lambda_* = 0.25$ (solid lines), $\lambda_* = 0.75$ (dashed lines) and $\beta = 10^{-4}$ (red lines), $\beta = 10^{-5}$ (blue lines). Slide velocity (6.14), which does not account for the water resistance ($\beta = 0$; green lines), is also plotted for same λ_*. Discontinuity reflects from the band tip at $\lambda_E = 1.881$ and $\tau_E = 2.881$ for $\lambda_* = 0.75$ and $n = 1.1$, while it does not reach the band for $\lambda_* = 0.25$ and $n = 1.1$.

APPENDIX L. NORMALLY-CONSOLIDATED SEDIMENTS

Sediment parameters usually depend upon depth, therefore, we use the average values with respect to the sliding layer thickness. For example, averaging (based on (2.1)) of the constitutive law $\sigma_x = E(y)(\partial u_x/\partial x) - P(x, y)$ (Appendix B) would result not in (2.2), but in

$$\sigma(x,t) + p = \frac{1}{h}\int_0^h E(y)\frac{\partial u_x}{\partial x}dy - p_0 \approx -\bar{E}\varepsilon(x,t) - p_0 \qquad \text{(L.1)}$$

where $\varepsilon(x, t) = -\gamma(x, t)$, p_0 is the thickness-averaged longitudinal effective stress ((B.9) in Appendix B), and $\bar{E}$ is the average modulus of the sliding layer ($0 < y < h$), or, more accurately, the overall elastic modulus in 1-D model. The estimate in (L.1) may be justified by noting that sufficiently away from the band tip, the character of the layer deformation is approximately one-dimensional [*Palmer and Rice*, 1973] and the distribution of strain, $\partial u_x/\partial x$, across the layer is relatively uniform. As an estimate, we assume a linear dependence of the relevant parameters on depth and employ the properties in the middle of the sliding layer (i.e., at the depth of $h/2$). We can then use the results obtained for homogeneous material by writing $\bar{E}$

rather than E everywhere. Alternatively, E can be understood as the average modulus. With this notation, (L.1) agrees with (2.2), and all obtained results are applicable.

Generally, properties of normally-consolidated sediments depend on the applied load and are not independent. Typical correlations [*Mayne*, 2014; *Puzrin*, 2014] suggest that in the undrained infinite slope condition,

$$\bar{\tau}_p = k_p \bar{\sigma}'_v, \qquad \bar{E} = k_E \bar{\tau}_p, \qquad p_0 = k_0 \bar{\sigma}'_v \tag{L.2}$$

for the average quantities (marked by the bar) in the sliding layer, and

$$\tau_p = k_p \sigma'_v, \qquad \tau_r = k_r \tau_p \tag{L.3}$$

at the shear band, which underlines this layer (Figure 2). Here, the coefficient ranges are $k_p = 0.2 - 0.3$, $k_E = 250 - 500$, $k_r = 0.3 - 0.5$, and $k_0 = 0.5 - 0.7$.

Failure of fully saturated, normally-consolidated sediments under fast (dynamic) loading can be described by the Von Mises criterion [e.g., *Desai and Siriwardane*, 1984; *Chen and Baladi*, 1985], which results in $p_a = \bar{\sigma}'_v - 2\bar{\tau}_p$, and $p_p = \bar{\sigma}'_v + 2\bar{\tau}_p$. Per (L.1), the corresponding average active and passive strains are $\varepsilon_a = (p_a - p_0)/\bar{E}$ and $\varepsilon_p = (p_p - p_0)/\bar{E}$, where $\varepsilon_a = -\gamma_a$ and $\varepsilon_p = \gamma_p$ in the notations of the preceding chapters. Using (L.2) then gives

$$\varepsilon_a = \frac{1 - 2k_p - k_0}{k_p k_E}, \qquad \varepsilon_p = \frac{1 + 2k_p - k_0}{k_p k_E} \tag{L.4}$$

Based on (L.2) and (L.3), representative properties of normally-consolidated sediments could be, for example, $\tau_p = 0.25\sigma'_v$ ($k_p = 0.25$), $\tau_r = 0.4\tau_p$ ($k_r = 0.4$), and $E = 350\tau_p = 17.1$ MPa ($k_E = 350$). Per (L.4), the corresponding active and passive strains are $\varepsilon_a = -0.114\%$ and $\varepsilon_p = 1.029\%$. Their properties are adopted in the main text to describe a representative (generic) landslides.

APPENDIX M. LANDSLIDE VELOCITY

The slide motion (Figure 19a) can be described by the momentum balance condition in the horizontal direction

$$\int_s^{s+l_f} (\tau_g - \tau_b - \tau_r - \tau_w)\cos\alpha ds - \tau_d h \cos\alpha_f = \frac{d}{dt}\int_s^{s+l_f} \rho_0 h \dot{s}\cos\alpha ds \tag{M.1}$$

where $\tau_g - \tau_b = (\rho_0 - \rho_w)gh\sin\alpha$ (Section 2.2 and Appendix B), $\tau_r = \mu[(\rho_0 - \rho_w)gh\cos\alpha + N]$,

$\tau_w = C_s\rho_w\dot{s}^2/2$ (Appendix K), $\tau_d = C_D\rho_w\dot{s}^2/2$ is the "front" drag resistance (neglected in Appendix K), $\alpha(x) = \arctan H'(x)$ is the slope angle, x is the horizontal coordinate (Figure 19a), s is the curvilinear coordinate along the slope, $\dot{s}$ is the slide velocity tangential to the slope surface ($\dot{s}$ = const along the slide body but varies with time), $H(x)$ is the depth profile (Figure 19a), $\alpha_f = \alpha(x + x_f)$ is the slope angle at the current position, $x + x_f$, of its right end, $N = \rho_0 g\dot{s}^2/r$ is the density of centripetal forces along the slope, $r(x) = 1/[\alpha'(x)\cos\alpha(x)]$ ($-\pi/2 < \alpha < \pi/2$) is the radius of the local slope curvature, and $\alpha'(x) = d\alpha(x)/dx$. Friction coefficient, μ, differs from that in Section 2.2. When the slide starts moving, it is likely that μ decreases as the slide material enters the ambient water (Figure 19b). Here we simply assume that $\mu = \mu_0$ over the surface of the propagated shear band and $\mu = \mu_1$ (typically $\mu_1 << \mu_0$) outside the original slide position (Figure 19b). Hence,

$$\mu = \begin{cases} \mu_0 & \text{if} \quad 0 < x \le x_f \\ \mu_1 & \text{if} \quad x \ge x_f \end{cases} \tag{M.2}$$

Taking into account that $\cos\alpha\, ds = dx$, the right side of (M.1) can be written as

$$\frac{d}{dt}\int_0^{x+l_f} \rho_0 h\dot{s}\cos\alpha\, ds = \frac{d(\dot{s}x_f)}{dt} = \frac{\ddot{x} + \dot{x}^2\alpha'(x)\tan\alpha(x)}{\cos\alpha(x)}x_f(x) + \frac{\dot{x}^2 x_f'(x)}{\cos\alpha(x)} \tag{M.3}$$

where function $x_f(x)$ is defined from

$$l_f = \int_x^{x+x_f} \frac{dx}{\cos\alpha(x)} \tag{M.4}$$

Replacing the right side in (M.1) by (M.3) and rearranging the terms leads to the ordinary differential equation

$$\ddot{x} + a_1(x)\dot{x}^2 + a_2(x) = 0 \tag{M.5}$$

where

$$a_1 = \alpha'\tan\alpha + \frac{x_f'}{x_f} + \frac{\rho_w}{2\rho_0 x_f\cos\alpha}\left(C_S\frac{x_f}{h} + C_D\cos\alpha_f\right) + \mu\frac{\sin\alpha_f - \sin\alpha}{x_f\cos\alpha} \tag{M.6}$$

and

$$a_2 = -g\frac{\cos\alpha}{x_f}\left(1 - \frac{\rho_w}{\rho_0}\right)\int_x^{x+x_f}\cos\alpha(\tan\alpha - \mu)dx \tag{M.7}$$

In (M.7), $\alpha' = d\alpha/dx$.

The solution (M.5) with initial conditions $x(0) = 0$ and $\dot{x}(0) = v_0 \cos\alpha(0)$ can be obtained, for example, by using the new unknown function $X(x) = \dot{x}^2$. As a result, we obtain the slide velocity

$$v(x) = \left[e^{-q(x)} v_0^2 \cos^2\alpha - \int_0^x a_2(s) e^{q(s)-q(x)} ds \right]^{1/2}, \quad q(x) = 2\int_0^x a_1(s) ds \tag{M.8}$$

When the angle $\alpha(x) \geq 0$ is small (condition (9.1)) and does not change too fast (say $|\alpha'(x)| < 1$ or $|H''(x)| < 1$), we further substitute $\cos\alpha \approx 1$ and $\sin\alpha \approx 0$. We also take into account that in this (asymptotic) approximation, $x_f \approx l_f$ and that $\tan\alpha \approx 0$ in expression (M.8) for $a_1(x)$ (but not in (M.7) where $\tan\alpha$ cannot be neglected). Integrating then in (M.7) (with $\tan\alpha = H'(x)$), we arrive at (9.2) in Section 9.1.

The same asymptotic result can be obtained by considering the slide as moving along the constant slope $\alpha = \text{const}$, but accounting for the frictional resistance (M.2) at the slide bottom for varying slope angle $\alpha(x)$. This is essentially a version of the Boussinesq approximation [*Dingemans*, 1997], when the dependence of α on x is neglected everywhere except in the frictional load terms.

APPENDIX N. MOMENTUM BALANCE FOR SLIDES WITH VARYING SLOPE ANGLE

In the case of gradually varying slope angle, α, a consideration of the momentum balance in the 1-D sliding layer could follow Appendix B by introducing an infinite slope in the orthogonal curvilinear coordinates r, s such that the slope surface would be a line of $r = \text{const}$. If the angle of the slope varies, but remains small ($0 \leq \alpha << 1$), it seems reasonable to assume that the effective stresses, s'_{rr} and s'_{ss}, are independent of coordinate s. The analysis, which is more cumbersome, but in essence identical to that in Appendix B, then leads to (2.4) with the same T. This analysis is applicable at least when the Jacobian of the coordinate transformation $r = r(x, y)$, $s = s(x, y)$ (x and y are the horizontal and vertical coordinates, respectively) is not equal to zero for any x and y, and when the Lame's coefficients of this transformation are not equal to zero identically [e.g., *Lurie*, 2010].

For the sake of simplicity, below we illustrate this statement by assuming that in the sliding layer (Figure N.1), all relevant quantities across the layer are uniform and equal to their average

values. Then, the momentum balance condition (in the horizontal direction) for a slide segment between $x = a$ and $x = b$ (Figure N.1) can be written as

$$[\sigma(a,t)\cos\alpha(a)-\sigma(b,t)\cos\alpha(b)]h+\int_{s(a)}^{s(b)}\tau_0\cos\alpha(s)ds=\frac{d}{dt}\int_{s(a)}^{s(b)}\rho_0 h\frac{\partial}{\partial t}\cos\alpha(s)ds \qquad (N.1)$$

where x is the horizontal coordinate, $s(x)$ is the curvilinear coordinate along the shear band, which parallels the slope at the constant depth, h, and $\alpha(x) \geq 0$ is the varying slope angle. In (N.1), the left side is the horizontal component of the resultant force acting on the slide segment (a, b), and the right side is the rate of change of the horizontal component of the momentum of this segment. Taking into account that $ds \cos\alpha = dx$, (N.1) can be written as

$$\int_a^b\left[\frac{\partial(\sigma\cos\alpha)}{\partial x}+\frac{\tau_0}{h}\right]dx=\int_a^b\rho_0\frac{\partial^2 u}{\partial t^2}dx \qquad (N.2)$$

which, given that a and b are arbitrary, results in

$$\frac{\partial(\sigma\cos\alpha)}{\partial x}+\frac{\tau_0}{h}=\rho_0\frac{\partial^2 u}{\partial t^2} \qquad (N.3)$$

where

$$\tau_0=(\rho_0-\rho_w)(\tan\alpha-\mu)gh\cos\alpha+\rho_w gh\cos\alpha-\tau_w \qquad (N.4)$$

Using Hooke's law (B.9) in (N.3) then gives

$$\rho_0\frac{\partial^2 u}{\partial t^2}=E\frac{\partial}{\partial x}\left(\cos\alpha\frac{\partial u}{\partial x}\right)-\frac{\partial}{\partial x}[(p-p_0)\cos\alpha]+\frac{\tau_0}{h} \qquad (N.5)$$

Although angle α varies along the slope, for many subaerial and most submarine slides, this angle is relatively small (e.g., see Table A.1 in Appendix A). Hence, we further assume that $0 < \alpha << 1$. In this case, $\cos\alpha \approx 1$, which leads to the equations identical to (2.3), (2.4), or the second equation in (3.1), but with

$$\tau_0=\rho_0 gh\tan\alpha-\mu(\rho_0-\rho_w)gh-\tau_w \qquad (N.6)$$

In particular, using $0 < \alpha << 1$ and (B.10) in (N.5) leads to

$$\frac{1}{c_0^2}\frac{\partial^2 u}{\partial t^2}=\frac{\partial^2 u}{\partial x^2}+\frac{T}{h},\quad T=\frac{\tau_*}{h} \qquad (N.7)$$

where

$$\tau_*=(\rho_0-\rho_w)(\tan\alpha-\mu)gh-\tau_w \qquad (N.8)$$

Finally, for small slope angles, the initial and boundary conditions for equation (N.7) remain the same as in Chapter 2 and Chapter 3.

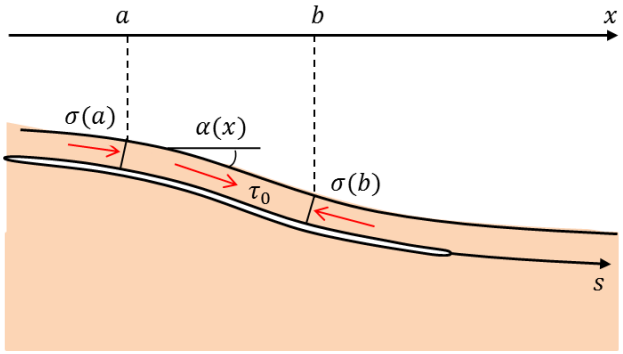

Figure N.1. Cross-sectional view of a curvilinear slope with changing angle $\alpha(x)$.